Mechanical response of glassy materials: theory and simulation

Michel Tsamados

N° d'ordre : 105-2008 Année 2009

THÈSE

présentée devant l'Université Claude Bernard - Lyon I

pour l'obtention du

Diplôme de Doctorat

(arrêté du 25 Avril 2002)

soutenue publiquement le 14 Décembre 2009

par

Michel Tsamados

Mechanical response of glassy materials : theory and simulation

---

sous la direction du Pr. Jean-Louis Barrat et Dr Anne Tanguy

devant le jury formé de :

Mr Y. BRECHET (Pr, INPG)	Examinateur
Mr D. VANDEMBROUCQ (CR, CNRS)	Rapporteur
Mr L. CIPELLETI (Pr, Montpellier 2)	Rapporteur
Mr P. SOLLICH (Pr, King's College London)	Examinateur
Mr J.-L. BARRAT (Pr, Université Lyon 1)	Directeur de Thèse
Mme A. TANGUY (MCF, Université Lyon 1)	Directeur de Thèse

Contents

Acknowledgements

I would like to acknowledge my supervisors Prof. Jean-Louis Barrat and Dr. Anne Tanguy for their help and guidance during my PhD study, without them this thesis would not have been possible. I would like to thank Prof. Peter Sollich who also supervised me during my stay in London.

I was honored to have Prof. Yves Bréchet, Prof. Luca Cipelletti, Dr. Damien Vandembroucq and Prof. Peter Sollich as members of the jury for the examination of my PhD.

I would also like to thank my fellow colleagues at LPMCN in Lyon who have helped me with useful discussions during my PhD in particular, Prof. Thierry Biben, Dr. Anatoli Mokshin, Dr. Samy Merabia, Dr. Laurent Joly, Dr. Tristan Albaret, Dr. Mina Talati, Prof. Lydéric Bocquet, Dr. Claus Heussinger, Dr. Pinaki Chaudhury and to all the staff of the LPMCN.

My thoughts go also to the underworld of the present and past PhD students Micho, Emmanuel, Diego, Boris, David, Félix, Walter, Jérémie, Raphael, Patrick, Daniel, Nicolas as well as to all my friends with whom I shared some nice moments in Lyon. Finally I am indebted to my family who have supported me constantly throughout all my studies culminating in my successful PhD, the belief of my mother Daphné, my father Yiannis, my grand-parents Jeanine, Toula and Dinos and sister Feya in my abilities has been invaluable. I must also thank Odette, Stamati, Irini, Maria, Iona, Vassili, Nikos, Yasmin, Constantin, Alexandra, Andreas, Dimitri but also Dionisis and Jean-Louis. At last I cannot forget my new English family Hazel, David, Wendy, Glenda, Cyril, John, Lise and Ela as well as Mme Athina for cooking the delicious greek buffet of my defense.

During my PhD I also became a father to little (big !) Marius which has further inspired me particularly in the difficult writing up period. I would also like to thank my partner Sarah for changing more than her fair share of nappies in his first 9 months and for making me happy.

Ευχαριστω ! Merci ! Thank you !

Chapter 1

Introduction

Contents

1.1 General context

Although glass has been used for thousands of years[1] and is nowadays of great industrial importance, questions associated to what is sometimes referred to naively as a fourth state of matter, in addition to solid, liquid and gas, are still puzzling scientists despite a large effort in the condensed and soft matter community over the last decades.

The first great challenge is to understand the formation of the glass itself, in other words why when a liquid is cooled below a certain temperature, referred to as glass transition temperature, at fast rate most substances rather than reaching a crystalline ordered final state remain in a metastable disordered configuration. Even more puzzling is the fact that this transition from liquid to glass does not seem to be associated to any simple structural change of the system. To the bare eye a snapshot of a glass looks exactly similar to a snapshot of the corresponding liquid. Yet one can somehow arbitrary define a glass transition temperature T_g as the temperature at which the viscosity of the liquid has increased by 13 orders of magnitude. Therefore this transition does not seem to be a structural one (in a first approximation as the structure undergoes in reality smooth and

[1] One of the earliest glass-making sites in ancient Egypt was uncovered in 2005 in the eastern Nile Delta and it was shown in Science [1] that glass was made there out of raw materials as early as 1250 BC.

weak changes with temperature) but rather a dynamical transition, referred to as dynamical arrest. Despite this apparent lack of a growing static structural length scale as temperature is lowered towards T_g (as would be the case in a 'normal phase transition'), evidences of such clusters or domains have been identified dynamically in several experiments and numerical simulations over the last decades and have provided a dynamical cooperativity length scale of a few inter-particle diameter just above T_g, i.e. in the supercooled liquid. In recent years these observations have lead to the generalization of the term glass not only to the hard, brittle, transparent silicate glasses used in windows and bottles, but to an entire class of materials that exhibit this type of dynamical arrest. In fact by glass we mean a system whose relaxation times diverge when an external parameter such as pressure, temperature, density or composition is tuned. Taking this definition allows to include in the class of glassy materials, materials as diverse as hard glasses such as silica glass, amorphous silicon, metallic glasses and polymeric glasses, soft glasses such as pastes, colloids, cells, foams, different complex fluids such as ketchup, mayonnaise, but also granular materials. In this thesis it is the generic physical behavior of these glassy material that we are aiming to describe.

The second great challenge for these glassy materials is to understand their peculiar physical properties. Here we are not interested in the properties pertaining to each type of materials due to their micro-structure, it is obvious for example that a polymeric substance will have specificities (reptation, entanglement,...) that are not present for example in granular materials, similarly grains have specificities (friction, inelastic collisions,...) that are not present in a Lennard-Jones glass. Rather we are interested in the properties that are associated with the actual physical process of going through or tending toward a glass transition. In fact such history dependent properties have been recently exemplified in different systems. A clear example was that shown by Falk in [2], where the mechanical response of a metallic glass well below T_g was shown to depend on the quench history of the liquid and supercooled liquid. The complex and history dependent state of matter is inherently associated to the rough energy landscape attached to the glass. In this energy landscape picture the dynamics of ageing or externally driven glasses is quite intuitive. The glass described by an energy of $\simeq d \times N$ coordinates (or distances), where d stands for dimension and N for the number of particles in the sample, is in a metastable state obtained from a quenching procedure. This state can evolve by activated processes in the case of thermal glass relaxation at $T \simeq T_g$ (ageing) or by an external drive in athermal quasi-static simulations. In both situations local rearrangements have been observed in simulations [3, 4, 5, 6, 7, 8] or more recently and less commonly in experiments [9, 10, 11, 12, 13, 14, 15]. These rearrangements, that correspond to the realization in coordinate space of an often irreversible change of local minima in the energy landscape of the glass, have been shown to be usually very localized involving the cooperative displacement of a few tens or hundreds of elementary particles or grains, therefore happening on a length scale of only a few inter-particle diameters. In ageing glasses they were shown to take the form of spring like cooperative chains [16], in sheared materials they have usually been described in terms of T1

events (foams), or STZ (metallic glasses) or quadrupolar events (Lennard-Jones glasses). These localized rearrangements have been recently postulated to be good microscopical candidates to be the elementary building blocks of the irreversible deformation mechanisms involved in disordered glassy materials. In fact to make a parallel with crystals these local events are now thought to be the equivalent in glassy materials of the dislocations present in lattice structures and one of the medium term aims (including in the present work) is to characterize the motion and interactions of these elementary units, in the spirit of what was initiated by Peierls, Nabarro, Friedel in the 50's and now well understood for defects and dislocations in crystals. Such knowledge could be included in a second stage in computer codes for a mesoscopic accurate modelization of the deformation mechanisms of amorphous materials. With this framework in mind we see how a multi-scale approach starting at the atomic (or grain) level with the use of numerical simulations such as Molecular Dynamics or Ab Initio techniques can emerge. Through this PhD thesis I will discuss of this topic of the mechanical response of disordered glassy materials that are well below the glass transition temperature, leaving aside the study of ageing supercooled liquids at finite temperatures near T_g.

1.2 Rheological and Mechanical properties of complex fluids

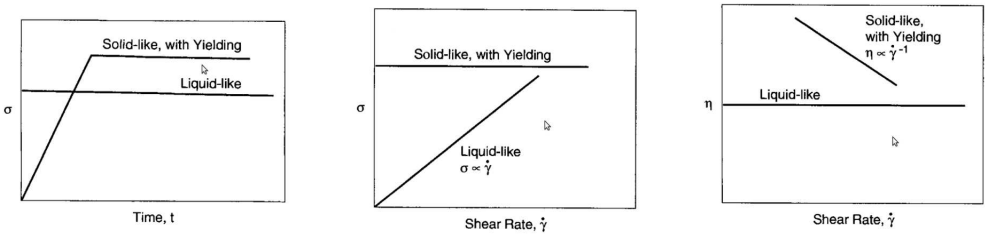

Fig. 1.1 : **Left :** Illustration of transient shear stress $\sigma(t)$ for 'liquid-like' and 'solid-like' materials. Illustration of shear-rate dependent, **middle :** shear stress σ and **right :** shear viscosity $\eta(\dot{\gamma}) \equiv \sigma/\dot{\gamma}$ for prototypical 'liquid-like' and 'solid-like' materials. [17]

In [17] Larson to characterize all the materials with a rheological behaviour intermediate between pure solids and pure liquids introduced the term *complex fluids*. Glassy materials enter this category and the dual terminology, glassy materials vs complex fluids, illustrates well the ambiguity to classify glasses as solids or as liquids. According to the classical definitions, a fluid is any substance that deforms continuously under the application of an arbitrarily small shearing stress, a solid has on the other hand shear rigidity and retains its shape when external forces are applied to it or rather returns to it when the external

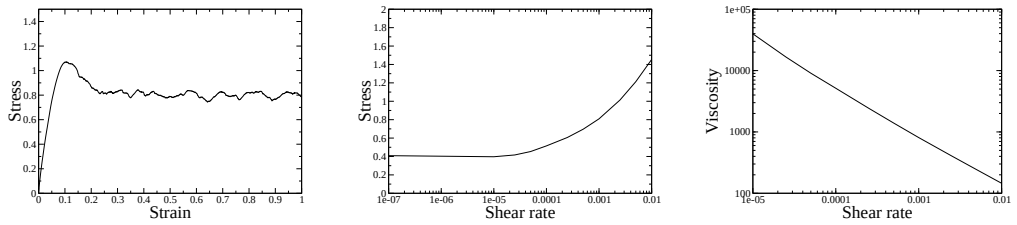

FIG. 1.2 : Parallel to figure 1.1 for the model Lennard-Jones glass system studied in this thesis. **Left :** Transient shear stress $\sigma(\gamma)$ at a shear rate of $\dot{\gamma} = 10^{-3}$ for a sample containing 10000 particles. Illustration of shear-rate dependent, **middle :** shear stress σ and **right :** shear viscosity $\eta(\dot{\gamma}) \equiv \sigma/\dot{\gamma}$ for the same Lennard-Jones glass at various shear rates ranging from 0 to 10^{-2}. For more details see chapters 5 and 6.

forces are removed. The typical mechanical/rheological behavior [2] of solids or liquids is illustrated in figure 1.1. While 'simple' Newtonian fluids are characterized by their viscosity and have a negligible elasticity, 'simple' Hookean solids do not flow and are characterized by their elastic moduli. These two limiting behaviors clearly cannot describe a vast number of substances that often show a behavior intermediate between the 'solid like' and 'liquid like' prototypes of figure 1.1, and are both viscous and elastic over the time scale at which they are probed.[3] Anticipating on the next sections figure 1.2 shows such an intermediate rheological behavior for the two dimensional poly-disperse Lennard-Glass mainly studied in this thesis and that has been widely used over the last years as a model system for different physical systems including disordered glassy materials. Here the rheology is considered in the athermal limit, and the system is shown to exhibit shear thinning, i.e. a fluid where the viscosity, defined as the average stress divided by the shear rate, decreases with shear rate. Another property of the Lennard-Jones glass shown in figure 1.2, also observed experimentally in many soft glassy materials such as pastes, dense colloidal suspensions, foams and granular systems is the presence of a yield stress and of a plateau stress at low shear rates where the behavior of the fluids deviates from the simple liquid's Newtonian law. Indeed like ketchup or mayonnaise these materials require a finite yield stress before they begin to flow. This is just an example of the many rheological characteristics that complex viscoelastic or viscoplastic fluids can exhibit. Experimentally and numerically in non-equilibrium molecular dynamics (NEMD) these global responses of the materials are obtained in various ways. For easily deformable substances ('fluid like') one usually applies in different possible geometries a shearing flow driven either by the movement of the boundaries or by a pressure gradient applied along the direction of the flow and records the stress at the boundaries resulting from this flow. For more rigid materials, ('solid like')

[2] To describe the response of solids one uses preferentially the term mechanical response, while the response of fluids is usually described by the term rheology. In what follows we will alternatively use both terminologies equivalently.

[3] Note that even the 'simple' behavior of Newtonian or Hookean systems is always confined to some frequency range

forces are usually applied on the systems and the resulting strains recorded. Another type of rheological experiment consists on applying a small-amplitude oscillatory shear (strain $\gamma(t) = \gamma_0 \sin(\omega t)$) and record the subsequent stress ($\sigma(t)$). These fields are related by the formula[4]

$$\sigma(t) = \gamma_0 \left[\mathrm{G}'(\omega) \sin(\omega t) + \mathrm{G}''(\omega) \cos(\omega t) \right] \ , \tag{1.1}$$

where the term proportional to the storage modulus $\mathrm{G}'(\omega)$ is in phase with strain and the term proportional to to the loss modulus $\mathrm{G}''(\omega)$ is in phase with strain rate $\dot{\gamma}(t)$. The storage modulus represents storage of elastic energy, while the loss modulus represents the viscous dissipation of that energy. The classical global rheology allows therefore to characterize the average flow properties in stationary or oscillatory regimes of the bulk materials [18], but does not inform on the structure and dynamics of the material at a local level. One question that someone might legitimately ask is if the flow is homogeneous in these complex systems or if the materials exhibit an heterogeneous response therefore requiring new experimental methods to probe the materials at the local level. This is precisely the origin of the growing experimental field that one can call micro-rheology or micro-mechanics (note that today in the age of extreme miniaturization one can replace the term micro by nano). Without detailing the ingenious experimental methods developed over the last years in this field we give in the following section some of the experimental evidences of heterogeneous flow or mechanical response of different glassy materials presenting them in decreasing order of stiffness.

1.3 Experimental and numerical evidence of heterogeneous response

At the top of the list of the stiffest glassy materials come (and by far) the *metallic glasses*. In fact this type of material first obtained at the California Institute of Technology (Caltech) by Duwez in 1960 and continuously perfected since then, even outgrows the hardest crystalline metals. This surprising result is due to the fact that the strength of even the latest alloys is far below their theoretical limit (see figure 1.3), this discrepancy stemming primarily from the existence in the crystals of defects such as dislocations. In the metallic glasses due to their inherently disordered nature such strength limiting defects are absent altogether. Hence, without the premature deformation of slip, elastic strain may regularly

[4] This equation is a generalisation of the Maxwell model of 1867 who was the first to propose a mathematical description of viscoelastic fluids. His model description combines the purely Hookean response of 'simple solids' to the purely Newtonian response 'simple fluids' through the simple constitutive equation $\dot{\gamma} = \dot{\sigma}/\mathrm{G} + \sigma/\eta$, where G is the elastic shear modulus, η is the viscosity and one can define a unique relaxation time $\tau = \eta/\mathrm{G}$. The general solution of this equation can be written $\sigma(t) = \eta/\tau \int_{-\infty}^{t} \exp\left[-(t-t')/\tau\right] \dot{\gamma}(t')dt'$. One can easily generalize this model to the case where there is a distribution of relaxation times to obtain the generalized constitutive equation, $\sigma(t) = \int_{-\infty}^{t} \mathrm{G}(t-t')\dot{\gamma}(t')dt'$ which precisely yields for a small amplitude oscillatory shear strain equation 1.1

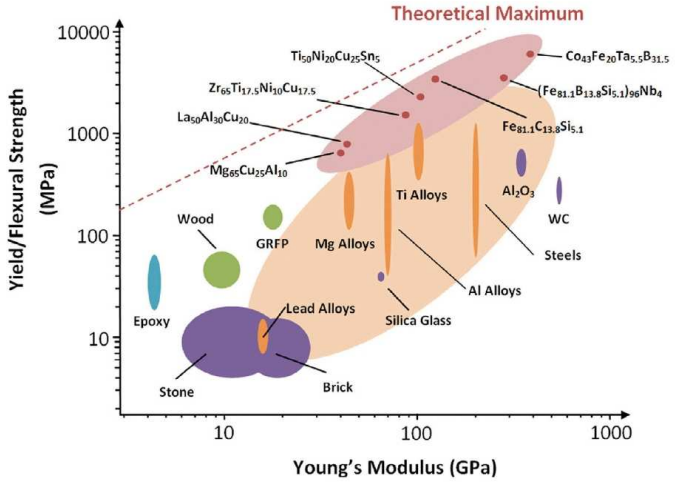

Fig. 1.3 : Schematic representation of room temperature yield (metals, composites and polymers) or flexural strength (ceramics) as a function of modulus. Note the increased strength of amorphous metals (light red) over conventional crystalline metals (light orange). [19] adapted from Greer[20].

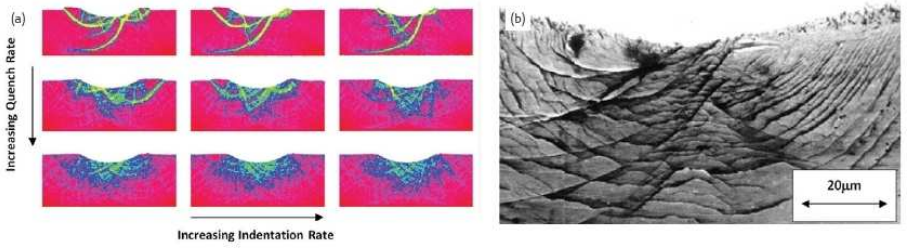

Fig. 1.4 : Sub-surface shear band morphologies resultant to indentation. (a) As simulated by the calculated local deviatoric strain field for a binary metallic glass (red is 0% strain and yellow 40%) [21] (b) As cast $Zr_{52.5}Al_{10}Ti_5Cu_{17.9}Ni_{14.6}$ using the clamped interface technique [22]

approach 2%, thereby facilitating strength and hardness values which are far beyond those of crystalline metals (figure 1.3). Further to such desirable mechanical properties, metallic glasses exhibit a full range of toughness values, low mechanical damping, good corrosion resistance and high magnetic permeability coupled with low coercivity to give superior soft magnetic properties, making them very promising candidates for future applications. Yet metallic glasses exhibit little plastic deformation prior to catastrophic failure and are usually relatively brittle at room temperature[5], such behavior severely limiting their functionality. Rather than stemming from an inherent lack of toughness, the brittle nature of these alloys has been found to arise primarily from a lack of strain hardening and the subsequent localization of strain into shear bands leading to premature failure. Such inhomogeneous flow was evidenced in both numerical simulations as shown in figure 1.4 (a) and in indentation experiments as shown in figure 1.4 (b).

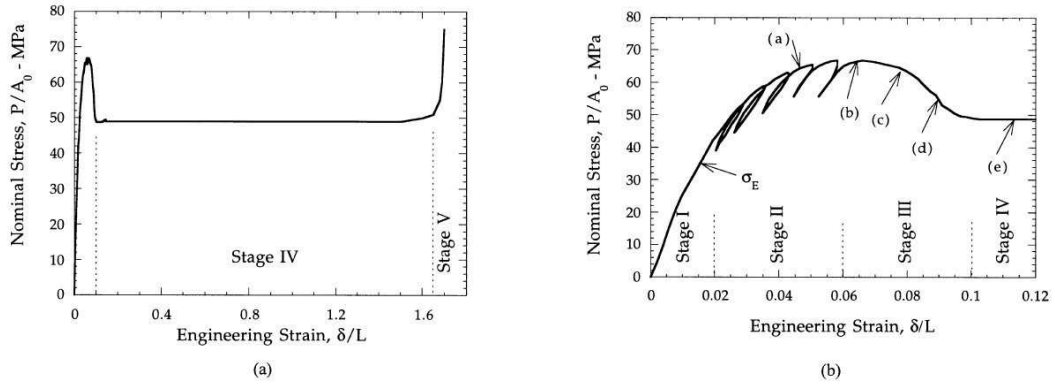

Fig. 1.5 : Nominal stress vs nominal extension of a polycarbonate specimen indicating the different stages in the deformation. (a) shows the full range and (b) shows an expanded view at small strain levels [23].

To obtain more tolerance to damage and enable structural use, mechanical properties need therefore to be enhanced by controlling shear band formation and propagation. A possible route consists in the design of amorphous/crystalline composites with increased plasticity. In any case it remains an important challenge to understand at a local level the nucleation and propagation of these shear bands.

Losing two orders of magnitude of stiffness with respect to typical metallic glasses (Young's modulus of about $\sim$ 1GPa vs $>$ 100GPa for metallic glasses), another class of materials that are widely used industrially, are the *polymer glasses*. Here we restrict the discussion to the polymers in the glassy state i.e. below their glass transition temperature ($T_g \sim 100°C$ for polymethyl methacrylate (PMMA) and $T_g \sim 150°C$ for polycarbonate (PC)) where their elasticity and strength are lost and the polymers become melt-like or, if

[5]Note that at high temperature, in their supercooled state, some metallic glasses are amenable to super-plastic deformation of up to 20000%

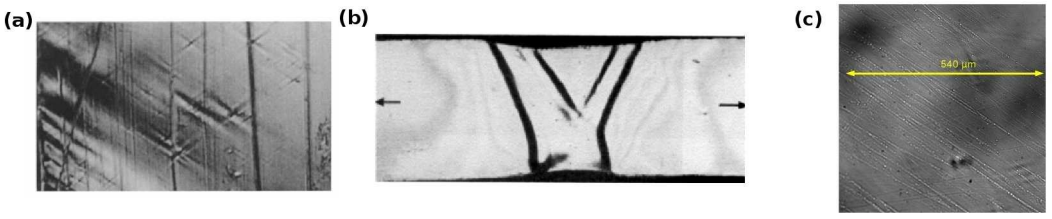

FIG. 1.6 : (a) Microscopic vue of the polycarbonate specimen taken during stage II of the deformation shown on figure 1.5(b) [23]. Formation of shear bands at the beginning of necking, observed for a sample of polycarbonate. The arrows indicate the direction of the applied tensile stress. Micrograph obtained by Morbitzer [24, 25]; (c) microscopic shear bands located inside the macroscopic shear bands of (a) [26].

they are cross-linked, turn into a rubber. Deformations of polymeric solids always include, in addition to the reversible part, an irreversible flow. Usually, as confirmed also in recent molecular dynamics simulation [7], this plastic flow sets in immediately when a sample is stretched and becomes very intensified when the yield point is reached. Upon further drawing this strain softening is often followed by a strain hardening (stage V in figure 1.5), which stabilizes the sample again and is associated to the stretching of the polymer chains. In addition polymers are viscoelastic solids and temperature as well as strain rate influence importantly their stress-strain response. The failure mechanisms in glassy polymers are of two types: crazing[6] and shear yielding; here we are mainly interested in the later. As shown by Ravi-Chandar *et al* [23] in their analysis of a shear yielding polymer (polycarbonate), different stages of the mechanical response correspond to different microscopical behaviors. Whilst the deformation in stage one (see figure 1.5) is to a first approximation homogeneous (in fact numerical simulations show that plasticity has already started at nano-metric level, i.e. outside of the microscopical resolution of [23]), in stage 2 micro shear bands measuring about $1\mu m$ in thickness and $100\mu m$ in length are observed distributed throughout the specimen particularly near surface defects. Remarkably their orientation appears dictated to some extent by the macroscopic stress state. As the load increases the density of the micro shear bands increases resulting in a reduction in the overall stiffness of the specimen, that eventually leads to a macroscopic localization at the end of stage III (figure 1.6 (b)). Once more this example shows that the understanding of the shear banding mechanism can have important potential applications even in daily life's materials such as poly-carbonates.

In *complex fluids* shear banding was first observed [27] with micelar solutions and has

[6]Crazing is a phenomenon that frequently precedes fracture in some glassy thermoplastic polymers. Crazing occurs in regions of high hydrostatic tension, or in regions of very localized yielding, which leads to the formation of inter-penetrating micro-voids and small fibrils. If an applied tensile load is sufficient, these bridges elongate and break, causing the micro-voids to grow and coalesce; as micro-voids coalesce, cracks begin to form.

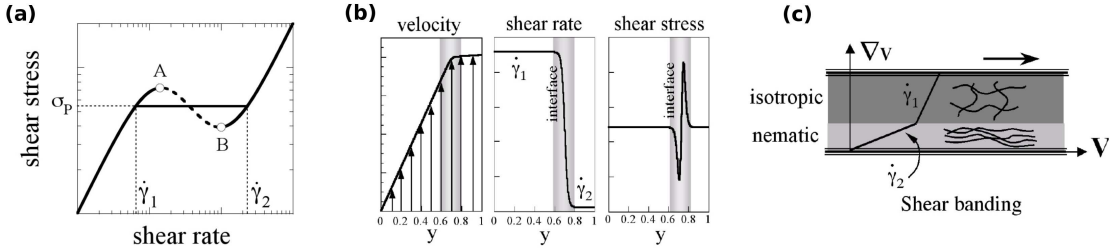

FIG. 1.7 : (a) Non monotonic constitutive equation assumed for wormlike micelles. The two stable branches at low and high shear rates are separated by an unstable portion [AB]. In the plateau region, the micellar solution demixes in bands of shear rate $\dot{\gamma}_1$ and $\dot{\gamma}_2$ (b) Velocity, shear rate and shear stress profiles calculated under the assumptions of shear banding and of non monotonic flow curve. (c) Schematic representation of the shear banding for system undergoing a shear induced isotropic-to-nematic transition.

since then generated an enormous interest due to numerous industrial applications[7] but also to the fundamental questions that are raised within these systems. As reviewed in numerous recent reviews [28, 29, 30, 31, 32, 33, 34], proof of the enormous interest in the field, shear localization has been widely observed and studied in worm-like and lamellar surfactants, side-chain liquid crystalline polymers, viral suspensions, telechelic polymers, soft glasses, polymer solutions, and colloidal suspensions. In a sense the prototypical example, giant micelles, is representative of the evolution of our understanding of shear localization in complex fluids. Initially macroscopic rheological studies of these surfractant solutions showed that the flow curve exhibits a plateau-like (figure 1.7) behavior under controlled shear rate experiments. Spatially resolved experiments followed exhibiting that for shear rates associated to the stress plateau region, the flow separates in two bands of different shear rates (figure 1.7) and associated to two different organizations of the material, an isotropic region, similar in structure to the original solution, and a strongly birefringent region, in which the micelles are aligned to a high degree with the flow direction (figure 1.7). Theoretical descriptions[8] attempted to capture the onset of this transition and the stability of the coexistence in terms of interfacial dynamics and mechanical instability [36]. This approach has provided some successful prediction concerning this heterogeneous flow, one of which is the lever rule to estimate the shear rates in each band. Nevertheless more detailed investigations of the birefringent phase have recently revealed strong spatial [37] and temporal [38] variations in the flow that are not encountered by the simple precedent theoretical approaches. A striking observation has been that the birefringent phase consists in fact of numerous transient, narrow zones of very large shear. The term 'fluid fracture'

[7] worm-like micelles have a widespread range of applications in every-day's life. Viscoelastic surfactant phases are already used in oil fields as fracturing fluids, in hydrodynamic engineering as drag reducing agents and in many home and personal care products.

[8] Here we follow the review made in [35].

[39] has been proposed to describe these individual events, which have been observed in different systems with similar rheological properties but different internal structures (connected micro-emulsions, copolymer cubic phase). The understanding of the shear-banding phenomenology has thus begun to shift from a phase transition picture to a fracture picture, and the interest is now focusing on the highly localized events (micro shear bands, quadrupolar events) that initiate the transition, and on their relation to the structural properties of the material. Another term used to coin this intermittent fluctuations of the velocity profile and of the stress response around the average value, is 'rheological chaos' or simply 'rheochaos', and many theoretical and experimental studies are devoted to the characterization of this flowing regime in glassy materials [40]. Of course numerical simulations are very useful to provide an atomistic insight and indeed some recent results (including the work presented in this thesis) in model glassy systems have exhibited this 'peculiar' shear banding phenomenon.

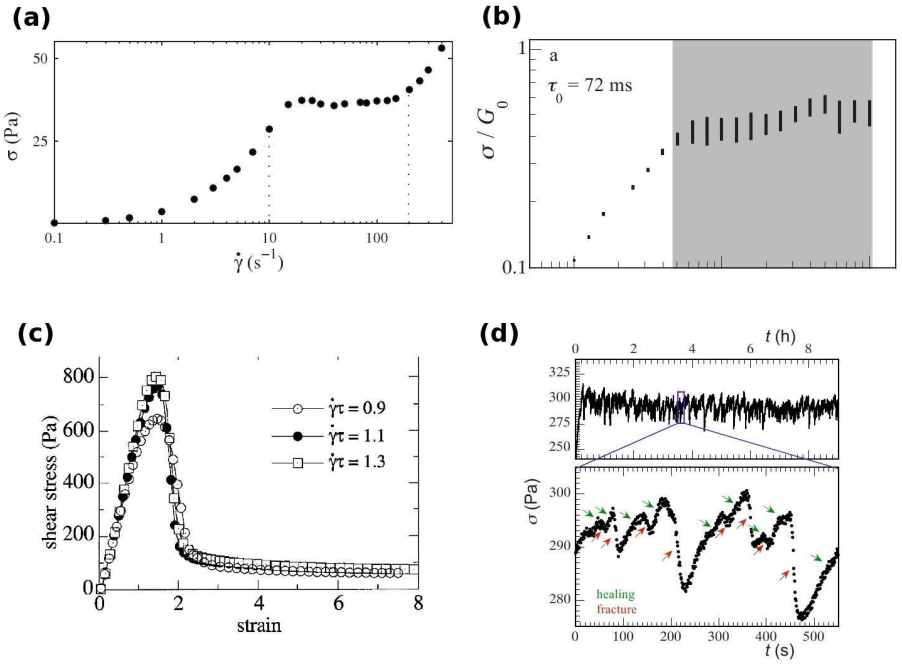

Fig. 1.8 : (a) Engineering flow curve (in the concentrated wormlike micellar system CTAB at 20% wt. in D_2O) $\sigma(\dot{\gamma})$ at T = 41°C under controlled shear rate obtained by averaging the shear stress over the last 100 s of each step [41].(b) Dimensionless shear stress σ/G_0 versus dimensionless $\dot{\gamma}\tau_0$ ($G_0 = 500$Pa, $\tau_0 = 72$ms) for a transient polymer network at 25 g/L at T = 5°C. The vertical bars indicate the range of stress fluctuations for a given shear rate. The grey region indicates where shear banding and fluctuating stresses are found [42, 43].(c) Transient stress measurements obtained from start-up experiments at various shear rates. (telechelich polymer network analysed in [39]) (d) Typical transient stress response in the banded regime, at a steady shear rate of $\dot{\gamma} = 1$, measured at T = 10°C ($\tau_0 = 36$ms). Note that at short time scales ($\simeq \tau_0$), at the start-up of the shear flow, the stress shows an overshoot, which is not visible here due to the longer sampling interval of $1s \approx 30\tau_0$ [42, 43].

Let us finally discuss two examples of glassy[9] materials that present the specificity to have elementary units that are macroscopic, namely foams and granular materials. The macroscopic nature of their elementary units makes these systems athermal and they are therefore ideal model systems to study the influence of external drive independantly of thermal effects, in addition their macroscopic size (human scale) allows for a direct visual observation and therefore tends to simplify the experimental procedures.

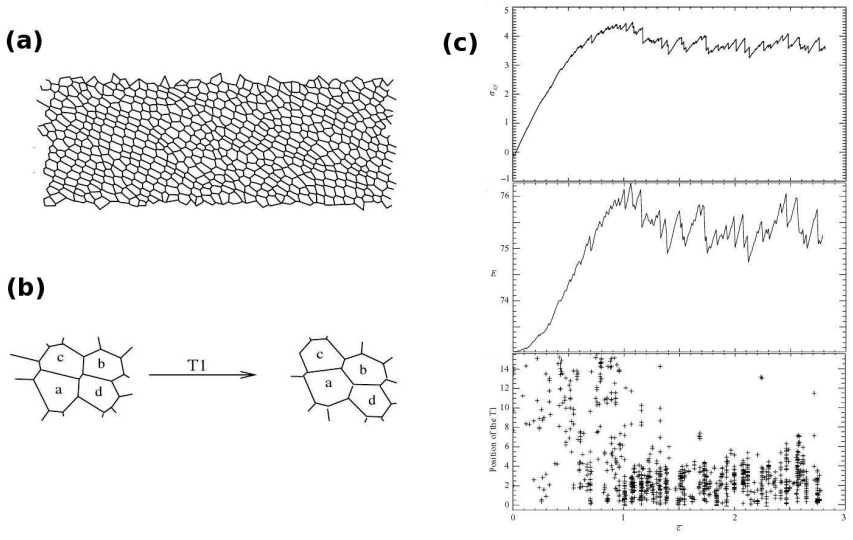

FIG. 1.9 : (a) Snapshot of a simulated foam with 16×48 bubbles. The polydispersity is 6%. The foam has periodic boundary conditions along the x direction. Films laying at upper and lower edges are fixed; shearing is obtained by moving the lower edge along the x direction. (b) Example of a topological change (T1 process) occurring inside the foam upon shearing.(c) Evolutions from top to bottom of the shear stress, the free energy and the positions of the T1 events within the gap as a function of the applied strain [11].

Liquid foams are dispersions of gaz bubbles in a liquid matrix. When the gas content of this emulsion becomes important (typically more than 70% of the total volume) the mechanical and rheological properties of the foams deviate strongly from those of the fluids phases (liquid and gas) that compose them, for example they have a higher shear modulus and only flow above a certain yield stress, behaving more in a 'solid like' manner. These properties combined with the lightness of their structure makes them widely used components in many industrial applications. In the agro-alimentary industry they are used for example to make ice creams and sauces more onctuous, to stop shaving foams and cleaning products from flowing too quickly. Many other industrial applications are also based on liquid foams that are fixed chemically once formed, one example is the use of polymer foams for car seats, not to mention the very wide variety of solid foams. In foams one observes two types of velocity profiles signalling shear localization, they can be continuous or not [44]. The continuous type appears usually in the form of an exponential

[9] The use of the word glassy to describe foams and grains remains a matter of debate, here we use it in the sense that these systems are non ergodic

profile [10, 45, 46] and has been attributed to either a drag effect [47] due to the confining plates or to stress fluctuations at the rotor that excite internal deformation modes in the bulk [10]. The second type, with discontinuous velocity profiles, has been recently observed for example in two dimensional buble rafts[10] [12] or in three dimensional foams. Once more with the example of foams we see that the same mechanisms appear to be at play in the heterogeneous response of glassy materials at low deformation rates.

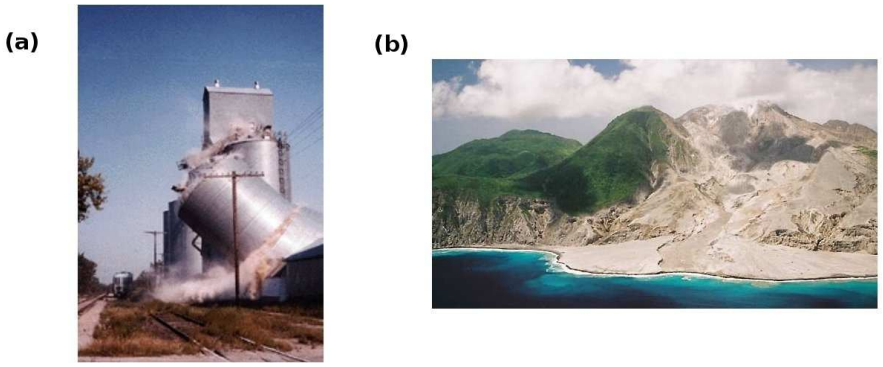

Fig. 1.10 : (a) Container collapse [48]. (b) Lava flowing to the sea in Montserrat island [49].

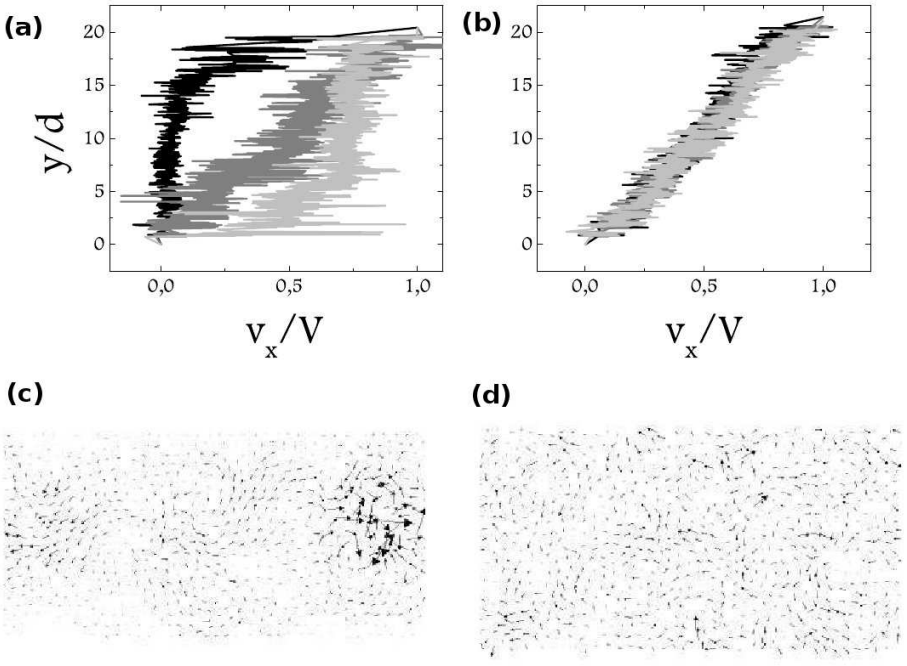

Fig. 1.11 : Instantaneous velocity profiles in simulation of dry granular material [49] for two different inertial numbers, in two dimensions defined as $I = \dot{\gamma}\sqrt{\frac{m}{P}}$, (a) $I = 10^{-3}$, (b) $I = 10^{-1}$. Non-affine velocity fluctuations in the quasistatic regime $I = 10^{-3}$ (c) and in the dynamic regime $I = 10^{-1}$ (c).

[10] A bubble raft consists of a single layer of bubbles floating on a fluid surface

At last let us mention the flows[11] of *granular materials*, again with a special focus on the question of the shear band formation and propagation. Here also, to understand the mechanical properties of these materials is of enormous industrial importance, with applications ranging from the storage (figure 1.10), transport and processing of grains to the understanding of natural phenomena such as for example dune migration, land slides (figure 1.10) or even earthquakes to name only a few. Detailed rheological studies at imposed stress or strain rate are reported for example in [49] and exhibit many common rheological features with micellar systems or foams (hysteresis, yield stress shear flow, localization of the deformation). Interestingly grains share many properties with complex fluids (and even solid glasses) in that they exhibit a flow threshold, although it is usually expressed in terms of friction instead of yield stress, but also in the fact that their flow is shear rate dependent, these combined properties help to classify them as visco-plastic materials. On a theoretical level a description of their mechanical response necessitates the definition of constitutive equations. This has been the focus of many theoretical studies in the last ten years and local constitutive laws in scalar and tensorial forms have been proposed [50]. Yet the particularly relevant for us quasistatic regime, again here, as we have already seen in previous examples of glassy materials, appears singular. In this regime the fluctuations of the velocity profile are very large (figure 1.11) and the flow appears intermittent, with localized burst of displacements of the grains (figure 1.11), and this mechanical response is not well described in the local viscoplastic framework of Pouliquen. There are different approaches to capture the correct flowing behavior in the quasi-static limit. We refer here the reader to the review of Pouliquen [50], let us simply mention, the Cosserat type approaches where one introduces an internal length scale and a rotational degree of freedom of the grains, models based on the definition of local plastic events, but also non-local continuum approaches motivated by the long-range fluctuation observed for example in the fluctuating velocity of slowly sheared grains (figure 1.11). Note that despite these efforts the question of a unified description of all flowing regimes remains open. In the next section we present some of the models of the rheology of glasses. Note that there are almost as many models of the rheology of glasses as there are of the glass transition[12] and we will only briefly present the most representative.

1.4 Models of rheology and plasticity of glassy materials

Non-ergodic glassy materials, such as the ones presented in the previous section, present as we have seen unusual rheological/mechanical properties. Understanding this peculiar flow represents a profound challenge to statistical physics. At a microscopical level work based on mode-coupling theory (MCT) is restricted (so far) to the case of monodisperse glasses near or above the glass transition temperature. Purely phenomenological models in which

[11] For a recent review of the flows of dense cohesionless granular materials see [50]

[12] In fact very often for each theory of the glass transition there is a derived model of the glass rheology.

a continuum stress or strain representation of the local state is supplemented by just one or two variables (e.g. 'fluidity') [51, 52, 53] are much simpler but of rather limited predictive power. Intermediate to these two types of approaches one finds various mesoscopic models. We present now some of these models. We introduce first the mean-field approaches and then continue with models that allow for a spatially heterogeneous response of the glasses.

1.4.1 Mean field approaches

Historical approach : Eyring's model. The simplest model that makes a prediction for the rate and temperature dependence of shear yielding is the rate-state Eyring model [54, 55, 17] of stress-biased thermal activation. Structural rearrangement is associated with a single energy barrier E that is lowered or raised linearly by an applied stress σ. This defines transition rates of the form,

$$\mathrm{R}_{\pm} = \nu_0 \exp\left[-\frac{\mathrm{E}}{k_\mathrm{B}\mathrm{T}}\right] \exp\left[\pm\frac{\mathrm{V}^*\sigma}{k_\mathrm{B}\mathrm{T}}\right] \ , \tag{1.2}$$

where ν_0 is an attempt frequency and V^* is a constant called the 'activation volume'. In glasses, the transition rates are negligible at zero stress. Thus, at finite stress one needs to consider only the rate R_+ of transitions in the direction aided by stress. The plastic strain rate $\dot{\varepsilon}_{pl}$ will be proportional to R_+, $\dot{\varepsilon}_{pl} = c\mathrm{R}_+$. Solving for the stress σ , one obtains

$$\sigma = \frac{\mathrm{E}}{\mathrm{V}^*} + \frac{k_\mathrm{B}\mathrm{T}}{\mathrm{V}^*} \ln\left[\frac{\dot{\varepsilon}_{pl}}{c\nu_0}\right] \ . \tag{1.3}$$

Equation 1.3 contains only a single relaxation time scale and predicts an apparent yield stress that varies logarithmically with the strain rate and where the logarithm has a prefactor that depends linearly on temperature. Despite its simplicity, experimental results are often fitted to equation 1.3, and the value V^* is associated with a typical volume required for a molecular shear rearrangement.

Modern phenomenological approaches pay tribute to the complexity of glassy systems through several extensions. First, it has been realized that assuming a single energy barrier for rearrangements is an oversimplified description of glassy materials. One can therefore introduce a distribution of barriers and add additional time scales. Second, any theory that attempts to predict a full stress-strain curve must contain some information about the internal state of the system as a function of time or strain. Extensions therefore consider dynamical internal state variables. The following models are particular realizations of these ideas.

Soft glassy rheology model. The SGR model is a mean field model based on Bouchaud's trap model [56]. The glassy nature of the material is accounted in Bouchaud's approach by a distribution of energy minima (density of states) taken to have an exponential tail

$\rho(\mathrm{E}) \sim \exp(-\mathrm{E}/x_g)$, where E is the depth of the trap and x_g a characteristic energy. A steady state (if it exists), is given by $\mathrm{P}_{eq}(\mathrm{E}) \sim \rho(\mathrm{E}) \exp(\mathrm{E}/x)$, where x is the temperature. These two terms, the density of states $\rho(\mathrm{E})$ and the Boltzmann factor $\exp(\mathrm{E}/x)$, exactly cancel at the glass transition temperature and the distribution is no longer normalizable and no steady state can exist : for $x < x_g$ the system ages in time, evolving in deeper and deeper traps.

The SGR model [57, 58] takes this picture and translates it from a global landscape to a mesoscopic one : the system is divided conceptually into many mesoscopic elements and the trap model is used to describe the distribution of the properties of all the elements. As new ingredients the SGR model incorporates deformation and flow in the following way : due to disorder the various mesoscopic elements possess a different strain l, away from their local equilibrium configuration. These small volume elements are assumed to yield with a rate $\Gamma_0 \exp\left[-(\mathrm{E} - kl^2/2)/x\right]$, where l is the local strain and k an elastic constant. The role of temperature is replaced by a 'noise' temperature x, which is assumed to describe the effect of structural rearrangements in a mean-field spirit. After yielding of a volume element, a new yield energy is drawn from $\rho(\mathrm{E})$ and the local strain l rises again from 0 according to the macroscopic shear rate $\dot{\gamma}$. The time evolution of the joint probability of finding an element with a yield energy E and a local strain l, $\mathrm{P}(\mathrm{E}, l, t)$ can be obtained from the following master equation,

$$\frac{\partial \mathrm{P}(\mathrm{E}, l, t)}{\partial t} = -\dot{\gamma}\frac{\partial \mathrm{P}(\mathrm{E}, l, t)}{\partial l} - \frac{\mathrm{P}(\mathrm{E}, l, t)}{\tau(\mathrm{E}, l)} + \int_0^\infty \frac{\mathrm{P}(\mathrm{E}', l', t)\rho(\mathrm{E})}{\tau(\mathrm{E}', l')} d\mathrm{E}' dl' \delta(l) \ , \tag{1.4}$$

where we have introduced $\tau(\mathrm{E}, l) = \left(\Gamma_0 \exp\left[-(\mathrm{E} - kl^2/2)/x\right]\right)^{-1}$ the average time spend in a trap of energy E. This model is simple enough to allow for the derivation of an exact constitutive relation linking stress and strain. The model was originally designed to describe the flow behavior of foams, dense emulsions, pastes, and slurries but its domain of application can reasonably be extended to the deformation and rheology of other 'harder' glassy materials such as metallic glasses. It covers not just linear but also nonlinear response, and is able to predict much of the complex rheological behaviour observed in experiments on soft materials. The predictions arising from the SGR equations are richer than the simple Eyring model. The exponential distribution of traps induces a dynamical glass transition, and the system exhibits ageing for $x < 1$. Analysis has mainly focused on the steady state situation under constant shear rate $\dot{\gamma}$, which is the generic experiment used to determine the mechanical properties of soft glassy materials. Salient predictions are: a Newtonian fluid flow $\sigma \propto \dot{\gamma}$ for $x > 2$ and a power law fluid $\sigma \propto \dot{\gamma}^{\tau-1}$ for $1 < x < 2$. In the glassy phase, $x < 1$, a scaling of the form $-\sigma_y \propto \dot{\gamma}^{1-x}$ is predicted. The nature of the noise temperature x (not the true thermodynamic temperature) and the pre-exponential factor Γ_0 remain largely unspecified. In a recent paper Fielding *et al* [59] extend the model, to capture the idea that the noise is largely caused by yield itself. The extended model can account for the viscosity-bifurcation and shear-banding effects reported recently in a wide

range of soft materials (as discussed in the previous section).

Shear transformation zone model. Falk and Langer, based on microscopic observations obtained with molecular dynamics simulations, formulated a theory of viscoplasticity [3] based on the concept of 'shear transformation zones (STZ), bistable (mesoscopic) regions that transform under shear between ± states. These ingredients of the STZ theory are based on earlier defect-flow theories of Turnbull, Cohen, Argon, Spaepen and others [60, 61, 62, 63]. Within the STZ model one considers the dynamics of an ensemble of STZ with number density n on a mean-field level, which determines the plastic strain rate

$$\dot{\varepsilon}_{pl} = \mathrm{A}_0 \left(\mathrm{R}_+ n_+ - \mathrm{R}_- n_-\right), \tag{1.5}$$

where A_0 is a constant and were the transition rates $\mathrm{R}_\pm$ from a (+)STZ to a (-)STZ and reciprocally, in contrast to the Eyring model are assumed to be free-volume (entropically) activated rather that termally activated. The authors also include a stress dependance in the following form,

$$\mathrm{R}_\pm = \mathrm{R}_0 \exp\left[-\frac{v_0 \exp\left[\sigma/\mu\right]}{v_f}\right] \tag{1.6}$$

where v_0 is a characteristic free volume required for a STZ flip and μ a characteristic stress scale required for a molecular rearrangement. The role of temperature is played by a 'free volume' v_f per particle. The authors motivate this with the observation that in a solid at very low temperature, energy barriers should be very large compared to thermal energies and thus, as in granular systems, thermal activation over these barriers should be negligible. The population densities themselves evolve according to the rate equation,

$$n_\pm = \mathrm{R}_\pm n_\pm - \mathrm{R}n + \sigma\dot{\varepsilon}(\mathrm{A}_c - \mathrm{A}_a n_\pm), \tag{1.7}$$

where the last term introduces creation and annihilation processes of STZ's proportional to the work of plastic deformation $\sigma\dot{\varepsilon}_{pl}$. By adding some dynamical rule for the free volume [64] the resolution of the non-linear system of the three equations so obtained leads to a yield stress, rheofluidification, and in some cases stick-slip. In addition to the mean-field approach used in this model the main limitation comes from the fact that the microscopic identification of the STZ remains elusive.

We now turn to the models that introduce explicitly in their approach the spatial dimension of the problem and aim at a precise description of the shear banding and heterogeneous deformation observed in various glassy materials (see 1.3).

1.4.2 Spatially resolved models

Elasto-plastic models. This class of models are inspired from geophysics [66] and from mechanics and are based on the following ideas [67]:

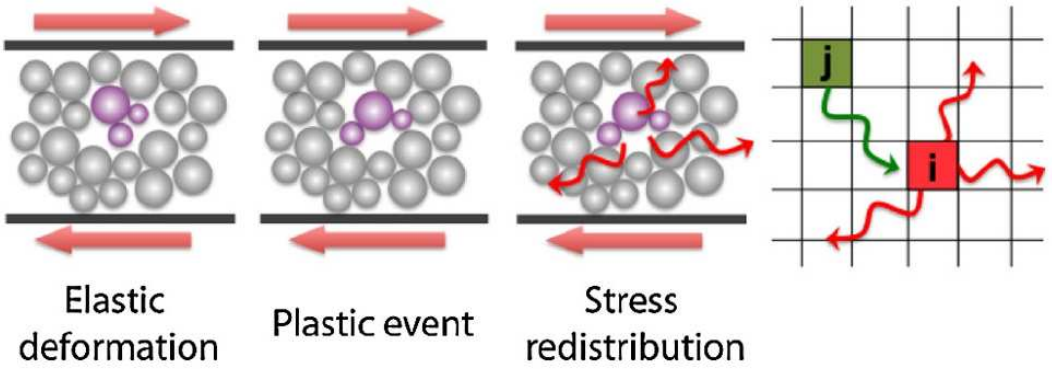

FIG. 1.12 : Sketch of plastic deformation in amorphous media. Deformation occurs via elastic deformation, localized plastic events, and nonlocal redistribution of the elastic stress, potentially triggering other plastic events [65].

- the macroscopic flow or deformation results from a collective organization of plastic rearrangements
- a plastic event is a local relaxation that occurs when a local yield criterion is attained
- a plastic event generates a perturbation of the entire medium through elastic propagation and can therefore generate new plastic events

This type of model allows therefore a mesoscopic approach of the appearance of heterogeneities based on elementary bricks, the plastic rearrangements. There are many elastoplastic models and the nature of the dynamics of the plastic events is different in each of these models [67, 68, 69, 70].

In the model of Picard *et al* [67, 71] (very similar in spirit to the earlier extremal model of Baret *et al* [68]) the local variables that are considered by the authors are the shear rate $\dot{\varepsilon}(\mathbf{r},t)$ and the shear stress $\sigma(\mathbf{r},t)$. The system is controled by the global shear $\dot{\gamma}$. The elastic shear modulus of the medium is noted μ. Under the simplifying assumptions of an infinite mdium and of a local plastic deformation with the same symmetry as the global deformation (here pure shear) one can write the expression of the shear stress field $\sigma(\mathbf{r},t)$ induced by a plastic deformation $\varepsilon_{pl}(\mathbf{r},t)$ as,

$$\sigma(\mathbf{r},t) = 2\mu \int d\mathbf{r}' \mathrm{G}^{\infty}(\mathbf{r}-\mathbf{r}')\varepsilon^{pl}(\mathbf{r}',t), \tag{1.8}$$

where the propagator is given by,

$$\mathrm{G}^{\infty}(r,\theta) = \frac{1}{\pi}\frac{2}{r^2}\cos(4\theta). \tag{1.9}$$

With these ingredients one can write the following evolution equation for the stress,

$$\frac{\partial \sigma(\mathbf{r},t)}{\partial t} = \mu\dot{\gamma} + 2\mu \int d\mathbf{r}' \mathrm{G}^{\infty}(\mathbf{r}-\mathbf{r}')\varepsilon^{pl}(\mathbf{r}',t), \tag{1.10}$$

where the first term corresponds to the global strain γ and the second term to the plastic shear.

To complete the model one needs to characterize the dynamics of the plastic deformation $\dot{\varepsilon}_{pl}$. To describe this dynamic a local yield criterion based on the existence of a local yield stress σ_c is implemented. In line with the extremal model of Baret *et al* the dynamics consists in the elastic deformation of the medium up to the point, where somewhere in the material the yield stress is attained. At this instant a plastic event is triggered that relaxes the local stress with the propagator 1.9. To describe this behaviour the authors introduce a new variable $n(\mathbf{r},t)$ that is equal to 1 if the local region at $\mathbf{r}$ is plastic or 0 if it is purely elastic. The dynamics of the plastic deformation is given by the following equations,

$$\dot{\varepsilon}^{pl}(\mathbf{r}',t) = \frac{1}{2\mu\tau} n(\mathbf{r}',t)\sigma(\mathbf{r}',t) \tag{1.11}$$

$$n(\mathbf{r}',t) : 0 \leftrightarrows 1. \tag{1.12}$$

The three equations 1.8, 1.10 and 1.11 provide a means of describing and model the rheology of the glass.

Kinetic theory of plastic flow. In a very recent paper Bocquet *et al* [65], develop a kinetic elasto-plastic model (KEP) based on the same ingredients as the extremal models of the previous paragraph. The KEP model is an extansion of a previous approach first proposed by Hébraud and Lequeux (HL) [72] that includes explicitly spatial interactions between plastic events. In the spirit of the SGR they divide, conceptually, the sample in mesoscopic blocks i to which they associate their own distribution of stress $\mathrm{P}_i(\sigma,t)$. In line with the elasto-plastic models of Baret [68] or Picard [71] the evolution of each distribution function $\mathrm{P}_i(\sigma,t)$ is driven by the three following mechanisms: an elastic response under the externally imposed shear rate $\dot{\gamma}_i^0$, a stress relaxation due to local plastic events, triggered at a given yield stress, and the modification of stress due to the plastic events occuring in other blocks, via the generated long-ranged elastic field (see figure 1.12). These processes can be condensed in the following master equation for the local stress distribution P_i,

$$\begin{aligned} \partial_t \mathrm{P}_i(\sigma,t) = & - \mathrm{G}_0\dot{\gamma}_i^0 \partial_\sigma \mathrm{P}_i(\sigma,t) - \frac{\Theta(|\sigma|-\sigma_c)}{\tau}\mathrm{P}_i(\sigma,t) \\ & + \Gamma_i(t)\delta(\sigma) + \mathcal{L}(\mathrm{P},\mathrm{P}), \end{aligned} \tag{1.13}$$

where $\dot{\gamma}_i^0$ is the imposed shear rate, G_0 is the elastic modulus, Θ the Heaviside function. The rate of plastic events, $\Gamma_i(t)$, is fixed by

$$\Gamma_i(t) = \int \frac{\Theta(|\sigma'|-\sigma_c}{\tau}\mathrm{P}_i(\sigma',t)d\sigma'. \tag{1.14}$$

In equation 1.13, the operator $\mathcal{L}(\mathrm{P},\mathrm{P})$ accounts for the stress redistributions due to the long-ranged elastic propagation. For example a block j can induce a nonlocal stress relaxation $\delta\sigma_i$ in block i given by $\delta\sigma_i = \Pi_{i,j}\delta\sigma_j$, with $\Pi_{i,j}$ the elastic stress propagator (see also 1.9). As discussed in [65], $\mathcal{L}(\mathrm{P},\mathrm{P})$ writes,

$$\begin{aligned}\mathcal{L}(\mathrm{P},\mathrm{P}) &= \sum_{j\neq i}\sigma'\frac{\Theta(|\sigma'|-\sigma_c)}{\tau} \\ &\times \left[\mathrm{P}_j(\sigma',t)\mathrm{P}_i(\sigma+\delta\sigma_i,t)-\mathrm{P}_j(\sigma')\mathrm{P}_i(\sigma)\right].\end{aligned} \tag{1.15}$$

Having formulated these 'microscopic' equations the authors derive in [65] their continuum hydrodynamic limit and deduce a set of constitutive nonlocal flow rules for the plastic flow. Switching to continuous space variables these two equations write,

$$\sigma = \frac{1}{f}\dot{\gamma}, \tag{1.16}$$

$$\Delta f - \frac{1}{\xi}(f-f_b) = 0. \tag{1.17}$$

In this equation f corresponds to the local fluidity of the material, intimately linked to the rate of plastic events, f_b is the bulk fluidity that satisfies, $f_b \propto (\sigma-\sigma_d)^2$ for $\sigma > \sigma_d$ and 0 otherwise, σ_d the dynamic yield stress and ξ a fluidity correlation length. Importantly the scaling of this correlation length is predicted within this model as,

$$\xi \propto \sqrt{\frac{1}{|\sigma-\sigma_d|}} \propto \dot{\gamma}^{-1/4}. \tag{1.18}$$

Also predicted from this model is a Herschel-Bulkley expression for the flow rule of the form,

$$\sigma = \sigma_d + \mathrm{A}\dot{\gamma}^n, \tag{1.19}$$

with $n = 1/2$. All these prediction have found recent confirmations in experimental results [73] as well as in various simulations [74, 71, 75, 76, 77].

In this introduction we have set the scene of the physical problem that we want to address in this thesis, namely the mechanical response of glassy materials. More specifically we will identify through the use of numerical simulations the mechanisms at the origin of the heterogeneous mechanical response observed in glasses leading to the formation of strain localization and shear bands. In the course of the thesis the following dilemma will emerge : can the plastic flow in glasses be attributed to a local origin (with some local order parameter controlling it) or is it independant on structural details and of purely dynamical nature ?

The thesis can be seen as structured around this central question in three parts. The first part is composed of this introduction 1 and of chapter 2. We introduce the subject and the previous studies (experimental, numerical and theoretical) devoted to the rheology of glasses and present the numerical method and model system that we have chosen to represent the generic features of the rheology of glassy materials. The second part contains chapter 3 and 4. There we introduce a local coarse-grained order parameter, the local elasticity tensor and more specifically the local shear modulus, and relate this parameter to the plasticity in the model glass. The third part consists of chapter 5 and 6. There we take the complementary approach and consider, independantly of the underlying structure, the dynamics of the driven systems. Finally in the conclusion we summarize our results and propose some perspectives of our work.

Chapter 2

Numerical approach

Contents

2.1 Computer experiments

Computer experiments [78, 79, 80] play a very important role in science today. In the past, physical sciences were characterized by an interplay between experiment and theory. In experiment, a system is subjected to measurements, and results, expressed in numeric form, are obtained. In theory, a model of the system is constructed, usually in the form of a set of mathematical equations. The model is then validated by its ability to describe the system behavior in a few selected cases, simple enough to allow a solution to be computed from the equations. In many cases, this implies a considerable amount of simplification in order to eliminate all the complexities invariably associated with real world problems, and make the problem solvable. In the past, theoretical models could be easily tested only in a few simple special circumstances. So, for instance, in condensed matter physics a model for intermolecular forces in a specific material could be verified in a diatomic molecule, or in a perfect infinite crystal. Even then, approximations were often required to carry out the calculation. Unfortunately, many physical problems of extreme interest (both academic and practical) fall outside the realm of these special circumstances. Among them, one could mention the physics and chemistry of defects, surfaces, clusters of atoms, organic molecules, involving a large amount of degrees of freedom; an accurate treatment of tem-

perature effects, including anharmonicities and phase transitions; disordered systems in general, where symmetry is of no help to simplify the treatment; and so on. The advent of high speed computers which started to be used in the 50s altered the picture by inserting a new element right in between experiment and theory: the *computer experiment*. In a *computer experiment*, a model is still provided by theorists, but the calculations are carried out by the machine by following a recipe (the algorithm, implemented in a suitable programming language). In this way, complexity can be introduced and more realistic systems can be investigated, opening a road towards a better understanding of real experiments. Needless to say, the development of computer experiments altered substantially the traditional relationship between theory and experiment. On one side, computer simulations increased the demand for accuracy of the models. For instance, a molecular dynamics simulation allows to evaluate the melting temperature of a material, modeled by means of a certain interaction law. This is a difficult test for the theoretical model to pass and a test which has not been available in the past. Therefore, simulation brings to life the models, disclosing critical areas and providing suggestions to improve them. On the other side, simulation can often come very close to experimental conditions, to the extent that computer results can sometimes be compared directly with experimental results. When this happens, simulation becomes an extremely powerful tool not only to understand and interpret the experiments at the microscopic level, but also to study regions which are not accessible experimentally, or which would imply very expensive experiments, such as under extremely high pressure. Last but not least, computer simulations allow in thought experiments, things which are just impossible to do in reality, but whose outcome greatly increases our understanding of phenomena to be realized.

From the precedent discussion one can imagine that since the 50s an enormous amount of research and academic publications have been produced in the field of numerical simulations, but this literature can be separated in various sub-categories associated with various numerical methods (Ab Initio, Molecular Dynamics, Monte Carlo, Brownian Dynamics, Event Driven Dynamics, Lattice gas simulation, Finite Elements, minimization algorithms...). The choice of the numerical technique used is linked to the phenomena that one wants to model. Particularly critical for the choice of the numerical method is the time scale(s) as well as the length scale(s) over which one wants to probe the physical system of interest (see figure 2.1). Our aim in this thesis is to understand the microscopical origin of the dynamical (rheology, diffusion, relaxation times...) and static (mechanical response, vibrational modes, local structure...) properties of amorphous glassy materials therefore requiring the knowledge of the atomic scale informations concerning the positions, velocities, forces in the glasses. Moreover the typical size of the phenomena of shear band formation and strain localization at stake during the mechanical deformation of glasses (shear bands involve up to or much more than a few hundred of particles) along with the time scales over which we want to study the rheology/mechanical deformation of the glass (total strains of the order of $\varepsilon \sim 400\%$) makes methods such as Molecular Dynamics, Monte Carlo simu-

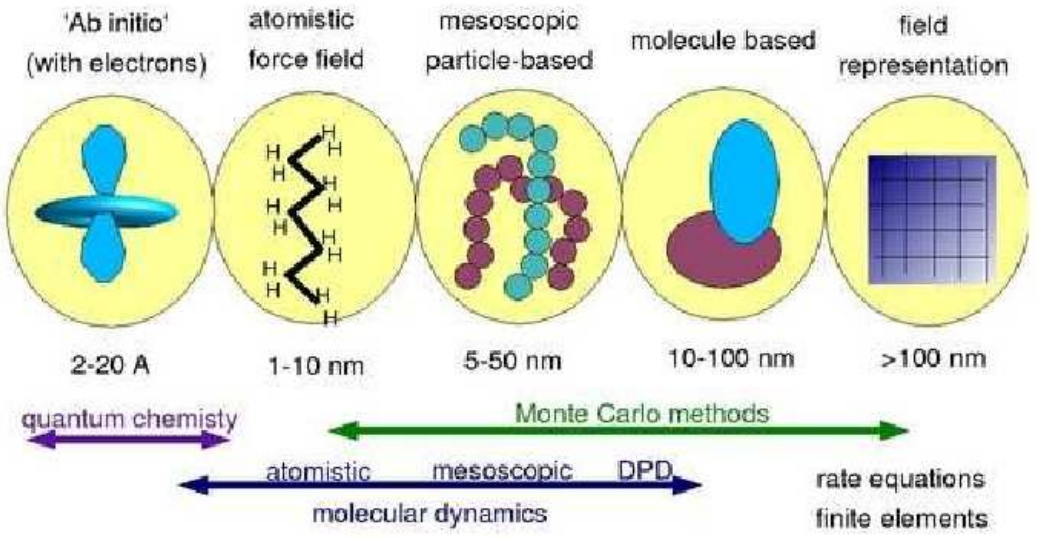

Fig. 2.1 : Schematic representation of various modeling numerical methods as a function of the length scales of interest. We will place ourselves in the mesoscopic range adapted to the use of the Molecular Dynamics technique (H. Meyer Strasbourg).

lations and Minimization algorithms the only atomic scale methods that are realistically feasible with the current computer capabilities (Ab Initio cannot reach any of these time or length scales while more mesoscopic methods do not include the atomic level description that we request). For us the Monte Carlo method is intrinsically limited by its probabilistic nature that lead to non realistic trajectories in time. As we are interested in the evolution with time (strain) of all particles we have therefore not used Monte Carlo techniques and have restricted our studies to Molecular Dynamics and Minimization methods. Within molecular Dynamics an important branch is constituted by Non-Equilibrium Molecular Dynamics (NEMD) that has been a growing field of research since the early 70s. This branch of numerical simulations is all the more important since there is at present no equivalent of the theoretical framework of equilibrium statistical physics far from equilibrium and that there is no applicable atomistic theory even for the simplest kind of non-equilibrium problems. Non-equilibrium computer simulations have therefore three useful roles to play: (1) providing the basic data through *computer experiments*, generally providing more details and greater accuracy than is available in laboratory experiments, (2) helping to identify and analyze causal mechanisms underlying the observed results of computer experiments and having analogs in laboratory experiments carried out far from equilibrium, and (3) suggesting conceptual approaches for developing necessarily approximate theoretical treatments modeling these two of experiments. These three points are representative of the spirit with which this PhD was undertaken.

2.2 Molecular Dynamics

The obvious advantage of molecular dynamics is that it offers a route to dynamical properties of the system : transport coefficients, time-dependent responses to perturbations and various correlation functions, rheological properties. Moreover it is well adapted to perform non equilibrium simulations. All simulations presented in this thesis at finite shear rates and/or temperatures to describe the rheology of the glasses (see chapter 6) and to produce the initial glass configurations through a finite temperature quenching procedure were performed with the LAMMPS (Large Scale Atomic/Molecular Massively Parallel Simulator) code (http://lammps.sandia.gov/) [81]. It is an open source, rich, flexible and fast software package, that met (modified whenever needed) all the needs of the present work.

The Molecular Dynamics technique is a method that is largely used to study classical systems with a large number of particles ($10^2 - 10^6$). The basic principle of the method is simple and consists in integrating numerically the equations of motion (EOM) of the system. This allows to follow the evolution of the system in phase space in time. Here we present only the numerical methods that we have used in this work and report the interested reader to the seminal references [79, 80] for in depth technical details.

Consider a system containing N classical particles in a rectangular simulation box of volume $V \equiv L_1 \times L_2 \times L_3$. The EOM for these N interacting classical particles are given by the Newton law:

$$\mathbf{F}_i = m_i \frac{d^2\mathbf{R}_i}{dt^2} = -\boldsymbol{\nabla}\Phi(\mathbf{R}_j) \text{ j=1,...,N} \tag{2.1}$$

where $\mathbf{R}_i$ is the position of atom i, m_i its mass, $\mathbf{F}_i$ the force on atom i and $\boldsymbol{\nabla}\Phi$ the gradient of the potential energy in $\mathbf{R}_i$ that depends on the $N-1$ other atoms j. In our simulations we will solve these EOM for interparticle potentials and forces that depend only on the relative positions of the atoms (and not for example on their velocities). In MD, the EOM are integrated numerically using various expansion of the positions and velocities. There are various algorithms that perform this integration and that are more or less CPU consuming. In any case these algorithms must conform to the principle of energy conservation at short and long times. In what follows we have used a time reversible algorithm named 'Velocity-Verlet' [80, 79] that has the advantage of presenting a small energy drift of the energy at long times. On the other hand it shows a worse energy conservation at short times relatively to more sophisticated algorithms. The algorithm follows the following integration rule:

$$\mathbf{V}_i(t) = \frac{\mathbf{R}_i(t+h) - \mathbf{R}_i(t-h)}{2h} \tag{2.2}$$

where $\mathbf{R}_i$ is the position of particle i at the time $t = nh$ (h is a time step and n an integer). From this definition, one can evaluate the position and velocity of particle i at the time $t + h$:

$$\mathbf{R}_i(t+h) = \mathbf{R}_i(t) + h\mathbf{V}_i(t) + \frac{h^2}{2m_i}\mathbf{F}_i(t) \tag{2.3}$$

$$\mathbf{V}_i(t+h) = \mathbf{V}_i(t) + h\frac{h}{2m_i}\left[\mathbf{F}_i(t+h) + \mathbf{F}_i(t)\right] \tag{2.4}$$

This algorithm is very commonly used for its great stability relatively to the discretization and numerical precision. The schematic loop that the algorithm follows goes in four steps as:

1. evaluate of the forces $\mathbf{F}_i(t)$ from the positions $\mathbf{R}_i(t)$
2. calculate the new positions $\mathbf{R}_i(t+h)$ (equation 2.3)
3. evaluate the forces $\mathbf{F}_i(t+h)$ from the positions $\mathbf{R}_i(t+h)$
4. calculate the velocities $\mathbf{V}_i(t+h)$ (equation 2.4)

These various steps are repeated during n integration steps, with n taking values up to 10^8 (for reasonable CPU time), allowing, for typical MD integration steps of about $\tau = 10^{-15}$s, to reach physical phenomena on time scales of the order of 10^{-8}s. It is important to be conscious of the fact that these short time scales are only barely reachable experimentally, for example with Raman spectroscopy techniques.

The MD conserving energy is statistically equivalent to the microcanonical ensemble NVE. Note that experimentally, it is often more practical to control the temperature T or the pressure at fixed volume V. The flexibility of the MD technique allows to extend easily the NVE formalism towards the NVT or NPT ensembles for example (we will discuss in greater detail of the various possible ensembles that MD can reproduce in section 3.3.1 of chapter 3.). In our simulations where the volume of the simulation box V and the number of particles N are kept constant we have used the control parameter T and have therefore worked within the NVT ensemble. Hence, in our simulations, the temperature T can be related to the average kinetic energy $\langle \mathrm{K} \rangle$ of the system via the equipartition of the energy. And one finds $\langle \mathrm{K} \rangle = \langle \sum_i 1/2 m_i \mathbf{v}_i^2 \rangle = \mathrm{N}_f k_\mathrm{B} \mathrm{T}/2$ where N_f stands for the number of degrees of freedom (DOF) and k_B for the Boltzmann constant. Similarly the instantaneous temperature is defined as $\mathrm{T}_{ins} \equiv 2\mathrm{K}/\mathrm{N}_f k_\mathrm{B}$, and the average of this instantaneous temperature over the entire sample must be equal to the thermodynamic temperature. Because the temperature is related to the kinetic energy, in order to control the temperature, the instantaneous velocities of the particles during the simulation run must be controlled. The first method that we used in two dimensions, consists in a direct rescaling of the particle velocities with the following ratio:

$$\left(\frac{\mathbf{v}_{new}}{\mathbf{v}_{old}}\right)^2 = \frac{\mathrm{T}}{\mathrm{T}_{ins}} \tag{2.5}$$

where $\mathbf{v}_{new}$ is the rescaled velocity and $\mathbf{v}_{old}$ is the velocity before rescaling.

The second method [82] that we used is called Nose-Hoover thermostat (we used it partly to check the validity of the results obtained from the first method). The velocity

rescaling thermostat is extremely efficient for relaxing a system to the target temperature, but once the system has reached equilibrium, it might be more important to probe a correct canonical ensemble. The extended system method was originally introduced by Nose and subsequently developed by Hoover [83]. The idea is to consider the heat bath as an integral part of the system by addition of an artificial variable s, associated with a 'mass' $\mathrm{Q} > 0$ as well as a velocity s. The magnitude of Q determines the coupling between the reservoir and the real system and so influences the temperature fluctuations. The artificial variable s plays the role of a time-scaling parameter, more precisely, the timescale in the extended system is stretched by the factor s as $\widetilde{dt} = sdt$. The atomic coordinates are identical in both systems. This leads to the following relations, $\widetilde{\mathbf{r}} = \mathbf{r}$, $\dot{\widetilde{\mathbf{r}}} = \widetilde{s}^{-1}\dot{r}$, $\widetilde{s} = s$ and $\dot{\widetilde{s}} = \widetilde{s}^{-1}\dot{s}$. The Lagrangian for the extended system is chosen to be,

$$\mathrm{L} = \sum_i \frac{m_i}{2}\widetilde{s}^2\dot{\widetilde{\mathbf{r}}}_i^2 - \mathrm{U}(\widetilde{\mathbf{r}}) + \frac{1}{2}\mathrm{Q}\dot{\widetilde{s}}^2 - gk_b\mathrm{T}_0 \ln \widetilde{s} \ . \tag{2.6}$$

The first two terms of the Lagrangian represent the kinetic energy minus the potential energy of the real system. The additional terms are the kinetic energy of $\widetilde{s}$ and the potential, which is chosen to ensure that the algorithm produces a canonical ensemble where $g = \mathrm{N}_{df}$ in real-time sampling (Nose-Hoover formalism) and $g = \mathrm{N}_{df} + 1$ (Nose formalism), with N_{df} the total number of degrees of freedom. This leads to the Nose equations of motion,

$$\ddot{\widetilde{\mathbf{r}}}_i = \frac{\widetilde{\mathbf{F}}_i}{m_i\widetilde{s}^2} - \frac{2\dot{\widetilde{s}}\dot{\widetilde{\mathbf{r}}}_i}{\widetilde{s}} \ , \tag{2.7}$$

$$\ddot{\widetilde{s}} = \frac{1}{\mathrm{Q}\widetilde{s}}\left(\sum_i m_i\widetilde{s}^2\dot{\widetilde{\mathbf{r}}}_i^2 - gk_b\mathrm{T}_0\right) \ . \tag{2.8}$$

These equation sample a microcanonical ensemble in the extended system $(\widetilde{\mathbf{r}}, \widetilde{\mathbf{p}}, \widetilde{t})$. However the energy of the real system is not constant. Accompanying the fluctuations of $\widetilde{s}$, heat transfers occur between the system and a heat bath, which regulate the system temperature. It can be shown, that the equations of motion sample a canonical ensemble in the real system. The Nose equations of motion are smooth, deterministic and time-reversible. However, because the time-evolution of the variable s is described by a second-order equation, heat may flow in and out of the system in an oscillatory fashion, leading to nearly periodic temperature fluctuations. In the LAMMPS code an optional drag keyword will damp these oscillations in an ad-hoc fashion, by altering the Nose/Hoover equations so that they no longer exactly sample the canonical ensemble. A value of 0.0 (no drag) leaves the Nose/Hoover formalism unchanged. A non-zero value adds a drag term; the larger the value specified, the greater the damping effect. Performing a short run and monitoring the temperature is the best way to determine if the drag term is working. Typically a value between 0.2 to 2.0 is sufficient to damp oscillations after a few periods.

The stretched timescale of the Nose equations is not very intuitive and the sampling of a trajectory at uneven time intervals is rather inpractical for the investigation of dynamical properties of a system. However, as shown by Nose and Hoover, the Nose equations

of motion can be reformulated in terms of real system variables. The transformation is achieved through, the following formulas, $s = \widetilde{s}$, $\dot{s} = \widetilde{s}\dot{\widetilde{s}}$, $\ddot{s} = \widetilde{s}^2\ddot{\widetilde{s}} + \widetilde{s}\dot{\widetilde{s}}^2$, $\mathbf{r} = \widetilde{\mathbf{r}}$, $\dot{\mathbf{r}} = \widetilde{s}\dot{\widetilde{\mathbf{r}}}$, $\ddot{\mathbf{r}} = \widetilde{s}^2\ddot{\widetilde{\mathbf{r}}} + s\dot{\widetilde{\mathbf{r}}}^2$ and with substituting $\gamma = \dot{s}/s$ the Lagrangian equation of motion can be rewritten as,

$$\ddot{r}_i = \frac{\mathbf{F}_i}{m_i} - \gamma \mathbf{r}_i \ , \tag{2.9}$$

$$\dot{\gamma} = \frac{-k_b \mathrm{N}_{df}}{\mathrm{Q}} \mathrm{T}(t) \left(\frac{g}{\mathrm{N}_{df}} \frac{\mathrm{T}_0}{\mathrm{T}(t)} - 1 \right) \ . \tag{2.10}$$

In both algorithms, some care must be taken in the choice of the fictious mass Q and extended-system energy E_e . On the one hand, too large values of Q (loose coupling) may cause a poor temperature control (Nose-Hoover thermostat with $\mathrm{Q} \to \infty$ is MD which generates a microcanonical ensemble). Although any finite (positive) mass is sufficient to guarantee in principle the generation of a canonical ensemble, if Q is too large, the canonical distribution will only be obtained after very long simulation times. On the other hand, too small values (tight coupling) may cause high-frequency temperature oscillations. The variable s may oscillate at a very high frequency, it will tend to be off-resonance with the characteristic frequencies of the real system, and effectively decouple from the physical degrees of freedom (slow exchange of kinetic energy). As a more intuitive choice for the coupling strength, the Nose equations of motion can be expressed as,

$$\dot{\gamma} = -\frac{1}{\tau_{\mathrm{NH}}} \left(\frac{g}{\mathrm{N}_{df}} \frac{\mathrm{T}_0}{\mathrm{T}(t)} - 1 \right) \tag{2.11}$$

with the effective relaxation time

$$\tau_{\mathrm{NH}}^2 = \frac{\mathrm{Q}}{\mathrm{N}_{df} k_b \mathrm{T}_0}. \tag{2.12}$$

2.3 Quasistatic protocols - Potential energy minimization

At first sight one can wonder how a minimization algorithm can give some insight on the evolution of a system, after all finding a minimum consists in finding a unique state, 'a minimum'. It is true that while time is not easily compatible with the use of minimization algorithms, these algorithms can if used iteratively provide efficiently the evolution of a system with respect to external parameters that are changed progressively. Moreover, it is well known in the numerical simulation community, that 'minimization is much cheaper than dynamics'. In molecular systems the basic question that minimization algorithms try to respond to is to find a minimum energy as a function of the atomic coordinates. One can further divide this problem in two categories, namely trying to find a global minimum or a local minimum. Another information that can be essential is to locate saddlepoints and this is again another minimization problem where information is needed as to the shape of the energy landscape between neighboring minima. One also differentiates between

constrained and unconstrained optimizations (another term used for minimizations). For example, if on one hand one is able to define an energy function $E(\mathbf{R}_i)$ that depends on $d \times N$ coordinates (in d dimensions) that are free to take any possible values then the optimization problem is unconstrained, if on the other hand the particle coordinates must satisfy some relation or equation, for example they must remain within a certain spatial region then one is faced with a constrained optimization problem. In practice one can avoid the constraint and include it in the form of the functional energy.

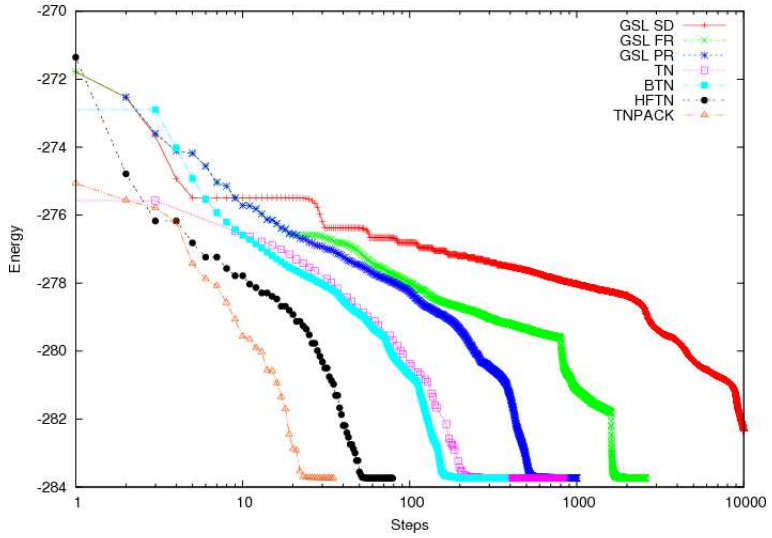

Fig. 2.2 : Evolution of the energy of a Lennard-Jones glass sample containing 100 particles during energy minimization for various algorithms. From slowest to fastest, steepest descent algorithm (GSL SD) [84], Fletcher-Reeves conjugate gradient algorithm (GSL FR) [84], Polak-Ribiere conjugate gradient algorithm (GSL PR) [84], block truncated newton (BTN) [85], truncated newton (TN) [86], hessian free truncated method (HFTN) [87], truncated newton package (TNPACK) [88].

In this work we are interested in finding a local minimum in an unconstrained optimization problem. Indeed the quasistatic protocol that we use can be summarized by the two following steps that we apply iteratively,

1. move affinely all the particles positions $\mathbf{R}_i$ of the sample under Lees-Edwards boundary conditions or move by a fixed amount the particles of the wall under rigid wall boundary conditions

2. minimize the energy function $E(\mathbf{R}_i)$ and find the corresponding state $\mathbf{R}_i$.

This type of simulation technique was first introduce by Kobayashi *et al* [89] as a way to bypass intrinsic limitations of molecular dynamics simulations to reach long time scales and therefore low shear rates. There are various algorithms that can perform this type of minimization such as the descent methods (D), steepest descent methods (SD), simplex methods (Si), conjugate gradient methods (CG), damped molecular dynamics (DMD) or Newton-type methods (N) (for a review see [90] and references therein). In practice there is

not one method that is 'the best' and the speed of the minimization depends largely on the problem at hand, for example for a perfectly quadratic potential energy the N methods will find the minimum in one step while in a complex energy landscape it will perform poorly. We found that methods that combine different aspects of these various algorithms can be more efficient. Also beyond the minimization routine employed in the minimization the structure of the minimization algorithm code can also be often an important limiting factor in the speed of the minimization. In figure 2.2, as a qualitative indication of the efficiency of various freely available algorithms to find the local minimum in a small glass sample containing about 100 particles in two dimensions, we have shown the number of steps required to reach the local minimum. We see in this figure that the methods that perform best are of the class of the truncated Newton methods (TN). Truncated Newton methods were introduced in the early 1980s [91] and have since been gaining popularity. They are based on the idea that an exact solution of the Newton equation at every step is unnecessary and can be computationally wasteful in the framework of a basic descent method. Any descent direction will suffice when the objective function is not well approximated by a convex quadratic and, as a solution to the minimization problem is approached, more effort in solution of the Newton equation may be guarranted. Their appeal to scientific applications is their ability to exploit function structure to accelerate convergence.

2.4 Examples of simulated sheared glassy materials

We present here some numerical results obtained in the literature on driven glassy materials that use one of the two methods presented in the two previous sections. We follow the same classification as in section 1.3 of the introductory chapter and present the simulated materials in decreasing stiffness order[1].

Metallic glasses. These non-crystalline materials, referred to as bulk metallic glasses (BMG) alloys, have only been successfully produced in the last twenty years. In order to understand the technologically limiting mechanism of shear localization in the form of nearly atomically thin bands called shear bands, the group of Michael Falk was one of the first to reproduce these failure modes in MD computer simulations [92] of a simple analog of a metallic glass (see figure 1.4 in the introductory chapter). Falk in line with the pioneering simulations of Kobayashi *et al* [89] and of Deng *et al* [93] used a binary Lennard-Jones model. More recent simulation have been performed to model the mechanical response of BMGs with semiempirical tight-binding potentials [94] or effective medium theory potentials [95]. It is worth noting that the strain rates that have been achieved with the current computer capacities are several orders of magnitude higher than experi-

[1] We present here succinctly a selection of numerical studies where an important part has been devoted to the the characterization of the microscopical mechanisms involved in the deformation of the glasses.

mental ones, a condition common to all the atomistic calculations dealing with mechanical deformation of solids. It follows that the numerical findings obtained are not immediately comparable to experimental results but rather allow to provide strong hints as to the mechanisms involved in the plastic flow and deformation of BMG. Quasistatic methods, based on on Lennard-Jones potentials have also been used recently to model BMGs [96].

Mineral glasses. Mineral glasses such as silica glasses (a-$Si0_2$) or amorphous silicon (a-Si) have also been tested extensively in NEMD simulations. Using an empirical potential developed by Vashishta *et al* [97], Rountree *et al* [98] have shown for example that amorphous silica develops a permanent anisotropic structure after extended shear plastic flow. Another example of NEMD on a-SiO_2 is that of Léonforte *et al* [76] where using the force field proposed by van Beest *et al* [99] (BKS potential) they investigated with MD simulations the properties of the nonaffine displacement field induced by macroscopic uniaxial deformation. They demonstrated the existence of a length scale characterizing the correlations of this field (corresponding to a volume of about 1000 atoms), and compared its structure to the one observed in a standard fragile model glass.

Demkowitz and Argon using NEMD and potential energy minimization (PEM) simulations of amorphous silicon (a-Si) [100, 101, 102] with the Stillinger-Weber potential have characterized the plastic flow of this material and related the flow properties to the existence of two distinct local environments, with specific structural properties. More recently comparing various force fields for a-Si Talati *et al* [8] have also studied the mechanical response of quasistatically sheared samples and showed that on average, the localization of elementary plastic events and the co-ordination defect sites appear to be correlated. For the Tersoff potential and the SW potential the plastic events centered on defect sites prefer 5-fold defect sites, while for the modified Stillinger-Weber potential such plastic events choose 3-fold defect sites.

Polymers. In [7] the authors examine the plastic deformation of a model polymeric glass under tension. They use a Lennard-Jones potential to model the interactions between monomers of different chains while the bonding energy between successive monomers of the same chain is taken to follow a quadratic potential. The strain is here applied through an athermal quasistatic procedure and the authors in their study relate the local elastic properties of the material to the failure modes in the material.

Soft glassy material. In an important series of papers [103, 104, 105] the authors reproduce in NEMD simulations many of the rheological properties (existence of a yield stress, hysteretic effects, shear banding...), shared by various soft glassy material such as complex systems like pastes, dense colloidal suspensions, foams... Again to model the generic characteristic of this class of materials the authors use a binary mixture of Lennard-Jones particles. Showing the versatility of the Lennard-Jones potential the authors also

map their results to the metallic glass physical situation.

Foams. Disordered foams [9] have been extensively studied through the use of numerical simulation in the last ten to fifteen years. Kawasaki's vertex model [106] was the first to incorporate dissipative dynamics in its description of two-dimensional dry foams. At low shear rates, the elastic energy of the foam shows intermittent energy drops of the type shown in figure 1.9 in the introduction. Weaire and co-workers [107] were the first to develop a model appropriate to a disordered wet foam. The model does not include dissipation and the effect of shear is studied in the quasistatic limit. The first model capable of treating wet, disordered foams at nonzero shear rate was proposed by Durian [108]. His model pictures the foam as consisting of spherical bubbles that can overlap. Two pairwise-additive interactions between neighboring bubbles are considered, a harmonic repulsive force that mimics the effect of bubble deformation and a force proportional to the velocity difference between neighboring bubbles that accounts for the viscous drag and the dissipation. This last model is a very schematic model of a foam and is very close in its simplicity to a Lennard-Jones glass model, without attractive part in the interaction potential.

This brief overview of simulations of driven glassy systems shows that a great variety of materials display common rheological and mechanical characteristics. In a first approximation many authors have used simplified models to describe the interaction between particles, one of this simplified potentials that has been extensively used in the literature is the Lennard-Jones potential. Of course by choosing to use such a simple potential we do not intend an exact matching between the properties of our model and a specific experimental system, but rather wish to focus on generic aspects of the rheology of these glassy materials. In the following section we present the Lennard-Jones potential that we choose and discuss the quenching procedure that we have used to form the model Lennard-Jones glasses studied in this thesis.

2.5 A model system : the Lennard-Jones glass

The two most commonly LJ models used in the literature are the by now standard 6-12 LJ potential introduced by Lançon (later popularized by Falk) [3] and Kob and Andersen [109],

$$\mathrm{U}_{\alpha\beta}(r) = 4\varepsilon_{\alpha\beta}\left[\left(\frac{\sigma_{\alpha\beta}}{r}\right)^{12} - \left(\frac{\sigma_{\alpha\beta}}{r}\right)^{6}\right] , \tag{2.13}$$

where the subscripts α and β denote the small (S) and large (L) particles. The two models differ only in the values attributed to the zero-energy interatomic distances $\sigma_{\alpha\beta}$ and to the bond strengths $\varepsilon_{\alpha\beta}$, with in the Lançon (Kob-Andersen) model $\sigma_{\mathrm{SS}} = 2\sin(\pi/10)$ ($\sigma_{\mathrm{SS}} = 0.88$), $\sigma_{\mathrm{LL}} = 2\sin(\pi/5)$ ($\sigma_{\mathrm{LL}} = 1$), $\sigma_{\mathrm{SL}} = 1$ ($\sigma_{\mathrm{SL}} = 0.8$), $\varepsilon_{\mathrm{SS}} = 0.5$ ($\varepsilon_{\mathrm{SS}} = 0.5$),

$\varepsilon_{\mathrm{LL}} = 0.5$ ($\varepsilon_{\mathrm{LL}} = 1$), $\varepsilon_{\mathrm{SL}} = 1$ ($\varepsilon_{\mathrm{SL}} = 1.5$), the ratio of the number of large molecules over the number of small particles being $\mathrm{N_L/N_S} = (1+\sqrt{5})/4$ ($\mathrm{N_L/N_S} = 0.25$). To lower the computational cost these potentials are truncated ans shifted at a distance $\sigma_c = 2.5\sigma_{\mathrm{SL}}$. The masses are all taken equal to 1. The choice of this bidispersity was originally justified by the will to make contact with experimental amorphous metallic glasses. Moreover the highly frustrated nature of these model glasses guaranties that the materials avoid local crystallization (especially in two dimensional systems) that would otherwise occur with monodisperse systems. Both systems have also exhibited a glass transition and the corresponding supercooled liquids around $\mathrm{T_G}$ have been extensively studied in the recent literature.

Here partly to make contact with experimental observations made on slightly polydisperse colloids [110] (see also numerical simulations [111, 112]) but also to somewhat smooth out the size distribution of the particles, we have used a shifted LJ potential [113, 114, 115, 76] for polydisperse particles. Natural LJ units are used, i.e., we set the energy parameter $\varepsilon \equiv 1$, the particle mass $m \equiv 1$, and the mean diameter $\sigma = \langle \sigma_i \rangle \equiv 1$. Note that while the particle mass is strictly monodisperse the particle diameters σ_i are homogeneously distributed between 0.8 and 1.2, corresponding to a polydispersity index $\delta\sigma/\sigma \simeq 0.12$ which is sufficient to prevent large scale crystalline order. We did not attempt to make the particles even more polydisperse fearing demixing or systematic radial variation of particle sizes in the case of disk-shaped aggregates. We have also used a cutoff distance r_c similar to the binary models along with a shifted potential at r_c. The density of the glass $\rho = 0.925$ was chosen as to obtain an initial minimal pressure [114]. In what follows all the physical quantities will be expressed in terms of the LJ units. These units are σ for the length units, ε for the energy units and m for the mass units. From these three units one can deduce the time unit $\tau = \sqrt{m\sigma^2/\varepsilon}$ and the temperature unit $\varepsilon/k_{\mathrm{B}}$. While we do not claim that our model describes quantitatively any experimental situation it is nevertheless useful to try and put some orders of magnitude on the different physical quantities that we model depending on the physical reality that we want to describe. Simulation results that are obtained in reduced units can always be translated back to real units [79]. For example translated in real units for metallic glasses one has $\varepsilon \approx 4 \times 10^{-20}$J, $\sigma \approx 5$Å, $\tau \approx 2.5 \times 10^{-12} s$ [116].

Now that we have defined the interatomic potential we can discuss in more details in the following section the computer experiments that we have performed. First we will describe the quenching procedure that we have applied to reach the glassy state of the material and second we will present the various technical issues associated with the shearing procedure that was applied on the glasses.

2.6 Simulation details

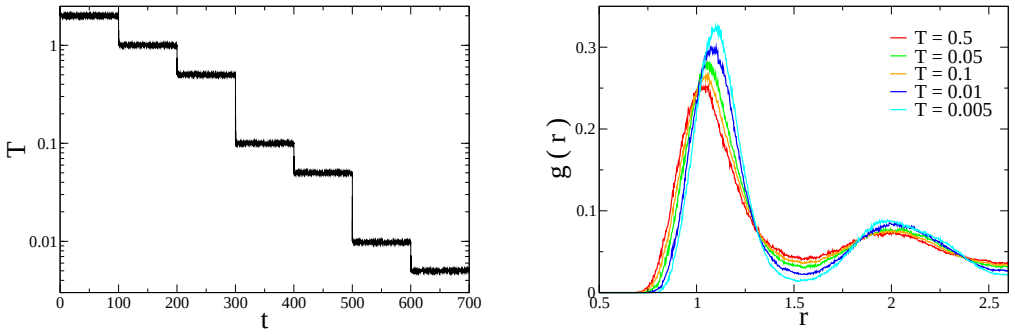

Fig. 2.3 : **Left :** Temperature evolution during the quench protocol used to produce the Lennard-Jones glass samples. Time and temperature are expressed in LJ units. **Right :** Evolution during quench of the radial distribution function.

Quenching procedure. The quench generally starts with molecular dynamics at some fixed temperature using a simple velocity rescaling thermostat. Then, for most samples analysed in this thesis, we progressively cool down the system by a succession of thermal steps at T=0.5, 0.1, 0.05, 0.01, 0.005, 0.001, 0.0005 and 0.0001 (see figure 2.3), the temperature remaining constant over a fixed time interval of 100 unit time for each temperature step. Following the initial MD sequence we quench the systems further down to its athermal limit by iterating the HFTN minimization algorithm described in section 2.3 until the configurations reach their local energy minima. We have also performed quenches at various quench rates and checked that in all case for quench rates ranging from $\dot{q} = 10^{-2}$ to $\dot{q} = \infty$ the system was indeed forming a glass, we will not present the results associated with these different glass samples in this thesis and report the discussion on the influence of the quench rate to future publication. In order to proceed to a systematic finite-size study, i.e. study the influence of the box sizes L, we have generated with this quench protocol 24 configurations for square system sizes L=25.9938, 52.9875 and 103.975, 8 configurations of size L=207.95 and one large configuration of size L=500, all at the same density $\rho = 0.925$. Figure 2.3 shows, for a sample of size L=103.975 and containing 10000 particles, the progressive evolution with temperature of the radial distribution function (RDF) of the LJ system. The RDF at the lowest temperature shown (here 0.005) is characteristic of a glass former with the presence of a broad second pic and the absence of crystalline structure (for a monodisperse LJ glasses in two dimensions the preferred crystalline structure is the hexatic order).

Boundary conditions. Two types of boundary conditions have been implemented in this thesis, either with periodic Lees-Edwards boundary conditions (LEBCs) or with two

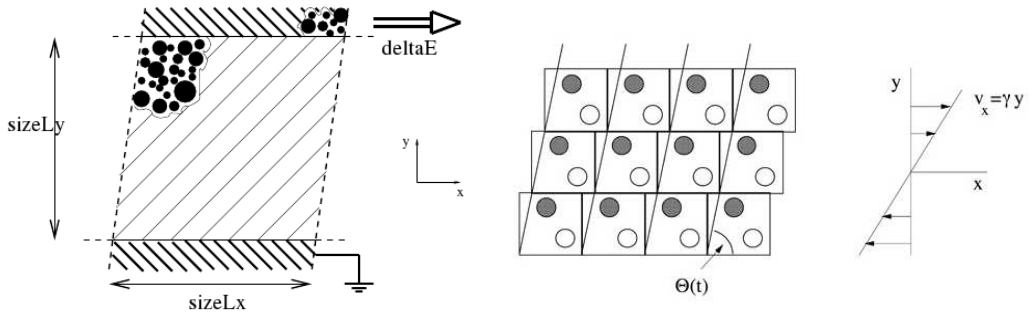

Fig. 2.4 : **Left :** Schematic representation [117] of the quasistatic shearing protocol in two dimensions and under RWBCs. The bottom and top walls contain here frozen LJ particles, while the x direction remains periodic. **Right :** Schematic representation of the LEBCs.

rigid walls extending along the x axis as is depicted in figure 2.4 (RWBCs). In the case of the RWBCs we defined the two walls of thickness b by freezing two layers of particles at y_W and $-y_W$. For the system of sizes 25.9938, 52.9875, 103.975, 207.95 the values of y_W are respectively 10, 22.5, 49 and 100, with a wall width that can be deduced by the formula $b = (L_y - 2y_W)/2$, and is therefore always larger than 2 which garanties that no particle can be lost through walls. The two types of boundary conditions have a different influence on the flow of the glasses as we will see in the next chapters. The RWBCs have a direct impact in the sense that they confine the particles within a restricted vertical area $[-y_W, +y_W]$, and particles that come near the rigid walls are made to bounce back inside this vertically limited space. This limits for example diffusion and other dynamical properties in a way that makes difficult any finite size scaling analysis. The LEBCs on the other hand allow the particles to diffuse over y distances larger than the size of the box. Nevertheless the flow of the glass must satisfy the Bravais lattice generated by the LE periodicity. In any case the periodicity, along y but also along x, affects the physical properties that occur in the glass on length scales comparable to a fraction of the simulation box, for example, as we will see in chapters 5 and 6, system spaning shear bands will 'feel' the presence of the periodic boundary conditions.

Shear protocol at $\dot{\gamma} = 0$. The technical details associated with this method are reported in great details in [114, 115, 118, 5, 117]. The quasistatic shear protocol applied to the quenched glasses is shown in figure 2.4 for the RWBCs. The protocol under RWBCs consists in applying a displacement step δu_x on all particles of the top wall, parallel to the x axis, while imposing at the particles comprising the bottom wall to remain fixed. A certain number, say n, of incremental steps is then applied on the system, while between each such increment the system is left to relax to its nearest local energy minimum by the HFTN minimization algorithm presented in section 2.3. The displacement step δu_x for each system size at y_W is chosen to generate an elementary incremental strain of $\delta\varepsilon_e =$

$\delta u_x/(2y_W) = 5.10^{-5}$. This incremental strain was shown [5] to be sufficiently small to be a reasonable approximation of the limit $\delta u_x \to 0$ in the sense that the elastic response of the material at this strain is preserved. The quasistatic protocol was also applied under LEBCs. The principle is exactly the same as in the RWBCs but this time each incremental step consists in affinely shearing the entire material (see figure 2.4) by the same elementary stain increment $\delta\varepsilon_e = 5.10^{-5}$. This quasi-static procedure so defined ensures that after a local 'bond' breaks, new bonds can form instantaneously. At the density considered here ($\rho = 0.925$) this makes it very unlikely that the material could fracture, at least under the volume preserving deformations that we consider here. A total strain ε_{tot} of about 200% was applied on the glass samples of all sizes and for both LEBCs and RWBCs.

Shear protocol at $\dot{\gamma} \neq 0$. As [2] in the quasistatic procedure one can enforce a macroscopic shear motion to the sample either by defining rigid walls and imposing a constant velocity translation say on the top wall or by deforming the simulation box at a given shear rate. The first method corresponds to RWBCs while the second to the LEBCs, both methods are implemented in LAMMPS [81]. Now turning to the thermostat method one would assume that the most realistic thermostat is one where the heat exchange occurs from the sides of the sample as would be the case with a real piece of material. As discussed in [104, 119] this type of 'realistic' heat exchange can be achieved by coupling each wall atom to its equilibrium lattice position via a harmonic spring. Then as shear is applied to the material the lattice sites are moved with a constant velocity while the corresponding atoms are allowed to move (the harmonic forces garanty that the wall atoms will follow on average the imposed velocity). With this method one can thermostat the walls independently of the bulk material. This presents the extra advantage to leave unperturbed the dynamics of the bulk particles. The temperature that establishes in the bulk results in this method from the heat exchange with the walls, which satisfies on average the equality between the work done on the system and the dissipated heat, $\sigma\dot{\gamma} = \dot{Q}$. The drawback of thermostatting the system through the heat exchange with the walls is that, depending on the shear rate and the stiffness of the harmonic spring, measured by the spring constant k_h, a temperature profile can develop across the system. Note that the smaller the harmonic spring constant, the better the heat exchange with the walls and thus the more efficient the system is thermostatted the imposed shear rate having the opposite effect. On the other hand, if k_h is too small, the fluid particles may penetrate the walls. A safe choice of k_h corresponds to the spring constant associated with the curvature of the LJ potential which is of the order $k_{LJ} \approx 60$. A slight modification of the LAMMPS code allowed us to implement such thermostatting procedure. Various tests performed with this thermostatting protocol have

[2] In order to study the finite shear rate dependence of the rheology of the glasses we have implemented MD simulations. This work has been started after the quasistatic simulations and there has not been the same amount of systematic analysis of the numerical protocol. We therefore present these finite $\dot{\gamma}$ MD results of this section and of chapter 6 as preliminary results that we will develop further in future publications.

confirmed the existence of thermal profiles with large temperatures in the center of the sample.

In order to prevent this uncontrolled temperature increases in the bulk[3], we have therefore decided to apply direct thermostatting to the inner particles at all shear rates. For this purpose, we divide the system into parallel layers of thickness $L_y/10$ and rescale once every n_T integration step the y-component of the particle velocities within the layer, so as to impose the desired transverse temperature $T_y = 0.5\langle v_y^2 \rangle$. Such a local treatment is necessary to keep a homogeneous temperature profile when flow profiles become heterogeneous. By doing so we avoid the pathological case where a plastic rearrangement having heated the material in a local region a global rescaling is lowering the temperature in regions that have not been heated (far from the event).

In order to implement a dynamical regime where the temperature effect is negligible (athermal limit), one needs to impose a sufficiently low temperature T. An estimate of this temperature can be given by the following argument confirmed by visual inspection of movies of the deforming glasses at various shear rates. Indeed the athermal limit is reached when the typical relative displacement associated with the external shear applied at shear rate $\dot{\gamma}$ is larger than the typical vibrations of the atoms in their 'cage', assumed for simplicity quadratic with an effective curvature $k_h \approx 60$. This leads to the following equality defining a threshold temperature T_c,

$$\sqrt{\frac{k_B T_c}{m\omega_0^2}} \lesssim \frac{2\pi\dot{\gamma}\sigma}{\omega_0} \ , \tag{2.14}$$

where we have introduced the characteristic pulsation $\omega_0 = \sqrt{k_h/m}$ of the harmonic 'cage'. This argument leads to a temperature $T_c \lesssim 40\dot{\gamma}^2$, namely $T_c \approx 4.10^{-3}$ at $\dot{\gamma} = 10^{-2}$ and $T_c \approx 4.10^{-7}$ at $\dot{\gamma} = 10^{-4}$. These values are in good agreement with what is observed in simulation runs where one can observe that below T_c the global shear of the material is visible while for $T > T_c$ the thermal agitation is dominating the dynamics and hides the global shear. Having realized this, the question now is to see how these low temperatures can be achieved[4] and in particular how frequently (or with what damping parameter 2.12) one needs to rescale the transverse temperature to achieve the athermal limit. In order to achieve the fastest possible cooling of the system we have applied a transverse velocity rescaling at every MD time step. For a time step of $\tau_{LJ} = 0.01$ this corresponds to a thermostatting rate of $r = 100$. In practice this amounts to impose the transverse temperature at the desired value (we have chosen an arbitrarily small $T_y = 5.10^{-8}$ in the simulations of chapter 6) but does not guaranty that the thermostatting has transfered to

[3] As we are interested in studying separately the effects of temperature and strain on the rheology of the glasses we turned to other thermostatting protocols that allow to maintain a constant and controlled temperature in the bulk.

[4] We have already seen that the shear dominated temperature regime could not be reached by a 'realistic' thermostat from the walls

the other velocity components (here v_x), as this energy transfer occurs within the velocity autocorrelation time τ_{VACF} [105]. Nevertheless this method is sufficient to maintain a zero transverse temperature.

Chapter 3

Continuum mechanics and elasticity at small scales

Contents

In this chapter we will adress two major issues: First, how can one apply everything one knows about mechanical properties of macroscopic systems at small scales ? Second, what are the mechanical properties of amorphous glassy materials ?

Indeed for many years the description of materials was only devoted to their macroscopic properties. Recently in an era of nanotechnologies and miniaturization there has been a shift of focus towards small systems. Examples are plentiful : mesoscopic solid state physics, micro and nano-elasticity and microfluidics are rapidly developing fields. In addition to the theoretical puzzles and the interesting physics exhibited by these 'small' systems the recent advances in the manufacture and control of micro to nanoscale mechanical and

electronic devices renders the need for good theoretical description and models of micro to nanoscale materials an urgent industrial need. In this chapter we will use a theoretical framework that helps one to derive expressions of the macroscopic fields of continuum mechanics in terms of microscopic quantities and to extend and test the applicability of the classical theories to smaller length scales and finer resolutions.
In parallel to this, using this framework we will study the properties of amorphous systems at small length scales, where a continuous elastic description breaks down. Indeed this is apparent when one considers their vibrational and transport properties, or the way forces propagate in these solids. Little is also known about the microscopic cause of their rigidity. The inherently disordered nature of the glassy materials we study here makes the use of the text-book theory of Lattice Dynamics developed by Born and Von Kármán to describe lattice solids inapplicable to amorphous solids for a description at all scales. The limitation of this approach comes essentially from the fact that one relies heavily in this procedure on the periodicity of the lattice as well as on some more subtle assumptions. Within the coarse-graining framework developed in this chapter we will show that linear continuum elasticity is not straightforward in small or disordered systems. As expected whilst one finds that linear continuum elasticity is valid on sufficiently large scales, we will see that as the coarse-graining is reduced deviation from the linear behavior sets in.

3.1 Microscopic approaches

3.1.1 A meaningful reference state

Our[1] intuitive concept of a solid is macroscopic. A solid has shear rigidity. It retains its shape when external forces are applied to it or rather returns to it when the external forces are removed. This can be regarded as a macroscopic definition of a solid. At a microscopic scale this rigidity pertains to the existence of a rigid reference frame/configuration $\{\mathbf{R}_1\} = \{\mathbf{R}_1, \mathbf{R}_2 ..., \mathbf{R}_i, ...\}$ where the $\mathbf{R}_i$'s correspond to the positions of the elementary units of the system, being atomic position or more mesoscopic structures depending on the type of solids considered. Interestingly it is the existence of such a well defined microscopic reference state [121] and its rigid stability [122] that differentiates between a solid and a liquid and helps to characterize the initial moments of melting. Indeed, Lindemann proposed that melting is caused by a vibrational instability in the crystal lattice when the root-mean-square displacement of the atoms reaches a critical fraction (δ_{L}) of the distance between them. Lindemann [123] originally conceived δ_{L} as applying to the interior of the crystal, but in a later version it was applied to events at the surface, where the amplitude of atomic vibrations is larger than in the interior. Born, on the other hand, proposed that a 'rigidity catastrophe' occurs - caused by a vanishing elastic shear modulus - that determines the melting temperature within the bulk crystal. In other words, the crystal

[1] The following discussion is inspired by the review on amorphous solids from Alexander [120]

no longer has sufficient rigidity to withstand melting, so this process is often referred to as 'mechanical melting'. These two distinct theories have each accumulated an extensive literature [124]. It appears that the Lindemann and Born criteria are satisfied similarly well for an amorphous material and for a crystalline solid and therefore according to these criteria one can say that an amorphous glass is just as solid as a crystal.

3.1.2 Two possible microscopic expansions

The Cauchy-Born expansion

From the preceding discussion it appears that there is no obvious obstacle at applying the Cauchy-Born expansion around disordered reference states. And indeed it comes as follows. One expands the many-particle energy $\mathrm{U}(\{\mathbf{r}\})$ in the components of the single particle deviations $\mathbf{u}_i = \mathbf{r}_i - \mathbf{R}_i$

$$\mathrm{U}(\{\mathbf{r}\}) = \mathrm{U}(\{\mathbf{R}\}) + \sum_{i=1}^{\mathrm{N}} \left[\frac{\partial \mathrm{U}}{\partial \mathbf{r}_i}\right]_{\{\mathbf{R}\}} \mathbf{u}_i + \frac{1}{2}\sum_{i,j} \left[\frac{\partial^2 \mathrm{U}}{\partial \mathbf{r}_i \partial \mathbf{r}_j}\right]_{\{\mathbf{R}\}} \mathbf{u}_i \mathbf{u}_j + \text{h.o.t.}, \tag{3.1}$$

where we use the Einstein summation convention ($\mathbf{u}_i \cdot \boldsymbol{\nabla}_i$ is a sum over all the particle positions indexed by i). For an equilibrium configuration the total force on each particles is zero ($\forall i \ \boldsymbol{\nabla}_i \mathrm{U} = \mathbf{0}$) and the linear term in u_i's in the expansion cancels. Therefore in the harmonic approximation one has simply $\delta \mathrm{U} = \frac{1}{2}\left[\mathbf{u}_j \cdot \boldsymbol{\nabla}_j\right]^2 \mathrm{U}$. It is convenient to express this expansion in matrix form, by defining the set of displacements $\mathbf{u}_1, \mathbf{u}_2, ...$ as a N-component vector $|\mathbf{u}\rangle$. Then equation 3.1 can be written in the form $\delta \mathrm{U} = -\langle \mathbf{u}|\mathrm{H}|\mathbf{u}\rangle$, where the matrix H is known as the dynamical matrix [125]. For a 2-body interaction potential (in our case it is the Lennard-Jones potential $\phi_{\mathrm{LJ}}(\mathbf{r}_{ij}) = 4\varepsilon\left[\left(\frac{\sigma_{ij}}{r_{ij}}\right)^{12} - \left(\frac{\sigma_{ij}}{r_{ij}}\right)^{6}\right]$) the total potential energy U is decomposed in a sum of two body terms as $\mathrm{U} = \frac{1}{2}\sum_{i,j} \phi_{\mathrm{LJ}}(\mathbf{r}_{ij})$ and the dynamical matrix has the following simplified tensorial expression:

$$\begin{aligned} \mathrm{H}_{i\alpha,j\beta} &= \frac{1}{2}\frac{\mathrm{T}_{ij}}{r_{ij}}\left(\delta_{\alpha\beta} - n_\alpha n_\beta\right) + \frac{1}{2}\mathrm{K}_{ij} n_\alpha n_\beta \ \text{, for } i \neq \mathrm{j}, \\ \mathrm{H}_{i\alpha,i\beta} &= -\sum_j \mathrm{M}_{i\alpha,j\beta} \ \text{, } \forall \ \mathrm{i}, \end{aligned} \tag{3.2}$$

$\mathbf{n}$ being the unit vector of the bond, $\mathrm{T}_{ij} \equiv \partial \mathrm{U}(r_{ij})/\partial r_{ij}$ the tension of the bond and $\mathrm{K}_{ij} \equiv \partial^2 \mathrm{U}(r_{ij})/\partial^2 r_{ij}$ the stiffness of the bond between two interacting particles i and j.

Once the components of the dynamical matrix are known one can numerically diagonalize it and recover the vibrational eigenstates of the material. Indeed the N eigenvectors of the dynamical matrix are the normal modes of the particle system, and its eigenvalues are the squared angular frequencies of these modes. We will come back to this approach in section 4.3 where we will discuss the importance of the low energy eigenvectors in the mechanical properties of the glass, the so called 'soft modes'.

Historically the classical work (mostly 19th century) on elasticity relied heavily on microscopic models in clarifying continuum field concepts such as stress and strain. It was generally assumed that the energy had to be a sum of two-body central force interactions (the Cauchy model). Thus the energy appeared as a function of the distances between interacting particles and microscopic expressions for the stress appeared naturally in the expansion. The expansion in terms of displacements $\mathbf{u}_i$'s that we have just presented was only introduced later for the analysis of lattice dynamics by Born and Huang [126]. If the latter expansion presents the advantage of mathematical simplicity - one expands directly as a Taylor series around a reference frame - it also lacks of a microscopic intuitive quality. This drawback is not so apparent for crystals where periodicity and symmetries allow for simple derivation of the physical quantities of interest even down to the microscopic level. In the next paragraph we will see that by generalizing the old procedure to write the mechanical energy as a function of distances we will get some simpler intuitive insight on the mechanical properties of disordered materials.

The expansion in distances

In the previous paragraph we described the internal energy U of a system consisting of N particles as a function of their positions $\mathrm{U}(\{\mathbf{r}\})$. Elementary geometrical considerations show that one can always describe the internal configuration of the solid by specifying n_{ind} independent distances in the system, where $n_{ind} = \mathrm{N} - n_{rig}$, $n_{rig} = \frac{1}{2}d(d+1)$ counts the rigid body degrees of freedom of the system as a whole and N is the total number of degrees of freedom of the N particles in d dimensions. Note that n_{ind} is always far smaller than the total number of distances between particles (pairs) in a solid $n_{tot} = \frac{1}{2}\mathrm{N}(\mathrm{N}+1)$, and that only n_{ind} distances are sufficient to determine all the others if they are independent. One can therefore reparametrize the internal energy U only as a function of these n_{ind} independent distances $\mathrm{U} \equiv \mathrm{U}(\{r\}_{ind})$. The expansion of the energy U around the internal reference configuration $\{\mathrm{R}\}_{ind}$ in term of distances $r_{ij} = \|\mathbf{r}_{ij}\| = \|\mathbf{r}_i - \mathbf{r}_j\|$ now reads[2]

$$\mathrm{U}(\{r\}) = \mathrm{U}(\{\mathrm{R}\}) + \sum_{(i,j)} \left[\frac{\partial \mathrm{U}}{\partial r_{ij}}\right]_{\{\mathrm{R}\}} \delta r_{ij} + \frac{1}{2} \sum_{(i,j),(k,l)} \left[\frac{\partial^2 \mathrm{U}}{\partial r_{ij} \cdot \partial r_{kl}}\right]_{\{\mathrm{R}\}} \delta r_{ij} \delta r_{kl} + \text{h.o.t.}, \quad (3.3)$$

[2]Here we omit the subscript 'ind' in the description of the set of distances on which the energy depends. This emphasizes that the derivation only uses the fact that the energy can be written as a function of a set of distances and this is not restricted to independent ones. In practice one has to be conscious of the existence of two different situations. First, $n_{bond} > n_{ind}$, there are redundant surplus bonds in the system in which case the expansion of the energy $\mathrm{U}(\{r\}_{bond})$ in 3.3 which is a function of all the n_{bond} bonded distances $\{r\}_{bond}$ has to be reevaluated into a new expression $\widehat{\mathrm{U}}(\{r\}_{ind})$ of the same energy but expressed in terms of the subset n_{ind} of geometrically independent distances $\{r\}_{ind}$. Secondly, $n_{bond} < n_{ind}$, the bonded distances act as constraints on the allowed configurations of the system but cannot fix unambiguously a unique geometrical configuration, such bonded networks are referred to as floppy. For a general discussion of rigidity theory in glassy systems see [127].

where

$$\delta r_{ij} = r_{ij} - \mathrm{R}_{ij}. \tag{3.4}$$

Following [120] one can evaluate δr_{ij} in terms of the relative displacements $\mathbf{u}_{ij} \equiv \mathbf{u}_i - \mathbf{u}_j$,

$$\delta r_{ij} = u''_{ij} + \left[(u^{\perp}_{ij})^2/2\mathrm{R}_{ij}\right] + \text{h.o.t.}, \tag{3.5}$$

where

$$\begin{aligned} u''_{ij} &= \mathbf{u}_{ij} \cdot \widehat{\mathbf{R}}_{ij}, \\ u^{\perp}_{ij} &= \sqrt{u^2_{ij} - {u''_{ij}}^2} \end{aligned} \tag{3.6}$$

are, respectively, the components of the relative deviation, $\mathbf{u}_{ij}$, parallel and perpendicular to the reference vector $\mathbf{R}_{ij}$ and, as usual, with the definitions, $\mathbf{R}_{ij} = \mathbf{R}_i - \mathbf{R}_j$ and $\widehat{\mathbf{R}}_{ij} = \mathbf{R}_{ij}/\mathrm{R}_{ij}$.

As stated earlier and discussed in [120] there is a number of advantages of the expansion 3.3 over 3.1. The first is that the expansion in terms of distances in the form 3.3 guarantees the translational rotational invariance symmetry as a whole and also as a local symmetry. The second is that while the role played by stresses is somehow obscured in 3.1 where stress terms do not appear explicitly when one expands directly in the $\mathbf{u}_i$'s because all linear terms must vanish in equilibrium, it appears explicitly in 3.3 - we will come back to the role played by local stresses later in this chapter. The third advantage concerns many-body interactions terms such as 3-body bending and 4-body twist interactions that are known to play an important role on the shear rigidity of solids and are therefore included in some potential interaction models in simulations (see for example the case of $a-\mathrm{S}i$ [8] or $a-\mathrm{S}i0_2$ [76]). Again these terms do not show up explicitly when one writes the harmonic expansion in terms of the components of the displacements $\mathbf{u}_i$. Finally we will see that the microscopic expansion 3.3 allows for a simple understanding of the microscopical origin of each term of the continuum limit of the energy. The passage from the microscopic expansion of the energy to the continuum limit is precisely the topic of the next section.

In most of the numerical simulation that we will present in this thesis we have chosen a Lennard-Jones interaction potential with a cutoff $\mathrm{R}_c \sim 2.5$, hence the number of bonds in 2D satisfies approximately $n_{bond} = \pi \mathrm{R}_c^2 \mathrm{N}/2 \sim 10\mathrm{N} > 2\mathrm{N} - 3 = n_{ind}$, and we should pay careful attention to the fact that the distances in the expansion 3.3 are not independent. In practice it is not simple to chose n_{ind} independent distances in which to expand the energy and we will in the rest of the thesis expand in all n_{bond} distances, doing this we implicitly assume that the expansion is to be complemented by $n_{bond} - n_{ind}$ (independent) extra constraints on the distances.

3.2 Continuum mechanics 1 : homogeneous hypothesis

3.2.1 Terms arising from the first order expansion of the energy

Linear term and first expression of the stress tensor

From 3.3 and 3.5 we see that the first order expansion of the energy in distances contributes to two terms,

$$\frac{\partial \mathrm{U}}{\partial r_{ij}}\delta r_{ij} = \mathrm{T}_{ij}u''_{ij} + \mathrm{T}_{ij}\left(\frac{u_{ij}^{\perp 2}}{2\mathrm{R}_{ij}}\right) \tag{3.7}$$

remembering that $\mathrm{T}_{ij} \equiv \partial \mathrm{U}(r_{ij})/\partial r_{ij}$ is the tension of the bond $i-j$. In the Lagrangian approach all particle coordinates are refered to the reference configuration and we associate with the discrete displacements $\mathbf{u}_i$ the continuous displacement field $\mathbf{u}(\mathbf{R})$, such that $\forall i$, $\mathbf{u}(\mathbf{R}_i) = \mathbf{u}_i$, and,

$$\mathbf{u}_{ij} \equiv \mathbf{u}_i - \mathbf{u}_j = \mathbf{u}(\mathbf{R}_i) - \mathbf{u}(\mathbf{R}_j)\ , \tag{3.8}$$

assuming that $\mathbf{u}(\mathbf{R})$ is continuous and derivable we get by Taylor expansion,

$$u_\alpha(\mathbf{R}_i) = u_\alpha(\mathbf{R}_j) + \left(\mathrm{R}_i^\beta - \mathrm{R}_j^\beta\right)\left[\frac{\partial u_\alpha}{\partial \mathrm{R}_j^\beta}\right]_{\mathbf{R}} + \text{h.o.t.} \tag{3.9}$$

Often the homogeneous assumption is made and the displacement gradient is assumed to be constant - equal to the macroscopic affine strain - over the entire sample or over the considered length scale of coarse-graining and one then has in the lowest order in gradient expansion 3.9,

$$u_{ij\alpha} \simeq u_\alpha(\mathbf{R}_i) - u_\alpha(\mathbf{R}_j) = \mathrm{R}_{ij}^\beta \cdot \partial_\beta u_\alpha\ , \tag{3.10}$$

and the component of $\mathbf{u}_{ij}$ parallel to $\mathbf{R}_{ij}$ is,

$$u''_{ij} = \mathbf{u}_{ij}\cdot\widehat{\mathbf{R}}_{ij} \simeq \frac{\mathrm{R}_{ij}^\alpha \mathrm{R}_{ij}^\beta}{\mathrm{R}_{ij}}\cdot\partial_\beta u_\alpha = \frac{\mathrm{R}_{ij}^\alpha \mathrm{R}_{ij}^\beta}{\mathrm{R}_{ij}}\cdot\frac{1}{2}\left(\partial_\beta u_\alpha + \partial_\alpha u_\beta\right) = \frac{\mathrm{R}_{ij}^\alpha \mathrm{R}_{ij}^\beta}{\mathrm{R}_{ij}}\cdot\varepsilon^{(1)}_{\alpha\beta}\ , \tag{3.11}$$

where $\boldsymbol{\varepsilon}^{(1)}_{\alpha\beta}$ is the linear part of the Green-Saint Venant nonlinear strain tensor defined as,

$$\boldsymbol{\varepsilon}_{\alpha\beta} = \frac{1}{2}\left(\partial_\alpha u_\beta + \partial_\beta u_\alpha + \partial_\alpha \mathbf{u}\cdot\partial_\beta \mathbf{u}\right) \tag{3.12}$$

Reporting this microscopic expression in the first term on the right hand side of equation 3.3 helps to write a first contribution U^1 to the total energy U as,

$$\mathrm{U}^1 = \sum_i s_i^{\alpha\beta}\cdot\varepsilon^{(1)}_{\alpha\beta}, \tag{3.13}$$

where we have defined the symmetric 'site stress' tensor defined for each particle i by[3],

$$s_i^{\alpha\beta} = \frac{1}{2}\sum_j \mathrm{T}_{ij}\frac{\mathrm{R}_{ij}^{\alpha}\mathrm{R}_{ij}^{\beta}}{\mathrm{R}_{ij}} \ . \tag{3.14}$$

One can simply see that this microscopically derived term leads in the continuum limit to a contribution to the elastic energy of the following form:

$$\mathrm{U}^1 \longrightarrow \mathrm{U}^1_{continuum} = \int \mathbf{dr}\cdot\sigma_{\alpha\beta}(\mathbf{r})\cdot\varepsilon^{(1)}_{\alpha\beta}(\mathbf{r}) \ , \tag{3.15}$$

where $\sigma_{\alpha\beta}(\mathbf{r})$ and $\varepsilon^{(1)}_{\alpha\beta}(\mathbf{r})$ are respectively the stress and linear strain at $\mathbf{r}$ in the reference configuration $\{\mathbf{R}\}$. From the preceeding arguments we see that the continuum limit involves a double expansion, first in powers of the components of the deviation field $\mathbf{u}(\mathbf{r})$ - assume that the displacements are small - and is also a gradient expansion in the derivatives of this field - assume that the field is sufficiently smooth. If the first hypothesis remains valid in the study of the mechanical response of disorder glassy materials for sufficiently small macroscopic sollicitations to the sample, we will discuss in the next section 3.3 the limit of applicability of the second hypothesis and will propose means of overcoming this limit.

Let us now pursue with the second term in the linear part of the expansion 3.3, i.e. the second term on the right hand side of 3.7.

The two effects of stresses

Born and Huang in their seminal paper (1954) define an 'equilibrium' solid as a solid with no stresses in its reference state. This definition - which means that separately and simultaneously, all binary potentials are at their minimum $\partial \mathrm{U}/\partial r_{ij} = \mathrm{T}_{ij} = 0$[4] - applies reasonably well for most crystalline solids where the effects of stresses on the bulk elastic properties are small either because stresses are inexistant in the reference state or localized around defects concentrated on small scales and therefore having mainly local effects. In amorphous materials as we will see in the next section 3.3 the 'initial stresses' [129] or 'frozen stresses' are present everywhere in the sample and one cannot simply neglect their contribution to the properties of the material. On the macroscopic scale on the other hand the importance of initial stresses has long been acknowleged for example in the physics of the vibrations of stretched springs or drumheads or in problems of elastic stability such as buckling of loaded columns [130]. In the examples above the initial stresses appear as

[3] Note that in this expression a coefficient $\frac{1}{2}$ is introduced to avoid double counting of pairs of interacting particles. Indeed this coefficient was not present in the first order expansion of 3.3 or 3.7 because there the sum was implicitly taken directly over bonds and not as a double sum running over indices i and j.

[4] One can easily verify for example that in crystals of inert gases where the binary potentials describe satisfactory the material one has a distance between nearest neighbours that corresponds within a very small error to the minimum of the binary (Lennard-Jones) potential [128] and one therefore has a bond tension that cancels everywhere ($\mathrm{T}_{ij} = 0$).

a contribution of the following form to the macroscopic expansion of the elastic energy of the materials,

$$\mathrm{U}^2_{continuum} = \int \mathbf{dr} \cdot \sigma_{\alpha\beta}(\mathbf{r}) \cdot \varepsilon^{(2)}_{\alpha\beta}(\mathbf{r}) \ , \tag{3.16}$$

where we have defined $\varepsilon^{(2)}_{\alpha\beta}$ as the nonlinear part of the Green-Saint Venant strain tensor 3.12. In this paragraph making use of the expansion of the energy in terms of distances 3.3 we will look at the microscopic origin of these stress induced contributions to the elastic energy, we will isolate two contributions and estimate their macroscopic counterpart in the continuum limit. For this purpose let us consider the second term on the right hand side of equation 3.7 and for reasons that will become clear later we propose to rewrite this term as[5],

$$\frac{u^{\perp 2}_{ij}}{2\mathrm{R}_{ij}} = \frac{\left(u^2_{ij} - u''^2_{ij}\right)}{2\mathrm{R}_{ij}} \ . \tag{3.18}$$

The continuum limit is now simple to take. Let us first take the continuum limit of u^2_{ij}. Under the assumption of affinity 3.9 one has,

$$u^2_{ij} = \mathrm{R}_{ij\alpha}\mathrm{R}_{ij\beta}\partial_\alpha u_\gamma \partial_\beta u_\gamma \ , \tag{3.19}$$

which combined with 3.18 yields in the continuum limit the contribution to the energy 3.16, This is the first effect of stress - the so called direct effect. The second effect of stress is contained in the term u''_{ij} of 3.18 and because it can be treated in the continuum limit similarly to the second order terms of the expansion in distances 3.3 we present it in the following paragraph.

3.2.2 Terms arising from the second order expansion of the energy

In the Born Huang definition of a solid - a solid with no stresses in its reference state - the first order terms of 3.3 cancels out and one is left with the second order contribution. To the order considered - quadratic in displacements - this term can be rewritten under the assumption that there are no rotations as,

$$\left[\frac{\partial^2 \mathrm{U}}{\partial r_{ij} \cdot \partial r_{kl}}\right]_{\{\mathrm{R}\}} \delta r_{ij} \delta r_{kl} \approx \left[\frac{\partial^2 \mathrm{U}}{\partial r_{ij} \cdot \partial r_{kl}}\right]_{\{\mathrm{R}\}} u''_{ij} u''_{kl} \ . \tag{3.20}$$

[5] To see the mathematical equivalence of the two expansions - in terms of distances and in terms of displacements - let us recover these two terms from the expansion in displacements 3.1. The second term in this expression can be developped as follows,

$$\begin{aligned} \frac{\partial^2 \mathrm{U}}{\partial \mathbf{r}_i \partial \mathbf{r}_j} &= \frac{\partial}{\partial \mathbf{r}_j}\left[\frac{\partial \mathrm{U}}{\partial \mathbf{r}_i}\right] = \frac{\partial}{\partial \mathbf{r}_j}\left[\sum_k \frac{\partial \mathrm{U}}{\partial \mathbf{r}_{ik}}\right] = \sum_k \sum_l \frac{\partial}{\partial \mathbf{r}_{jl}}\left[\frac{\partial \mathrm{U}}{\partial \mathbf{r}_{ik}}\right] = \sum_k \sum_l \frac{\partial}{\partial \mathbf{r}_{jl}}\left[\frac{\mathbf{r}_{ik}}{r_{ik}}\frac{\partial \mathrm{U}}{\partial r_{ik}}\right] \\ &= \sum_k \sum_l \left(\frac{\mathbf{r}_{ik}}{r_{ik}}\frac{\partial}{\partial \mathbf{r}_{jl}}\left[\frac{\partial \mathrm{U}}{\partial r_{ik}}\right] + \frac{\partial \mathrm{U}}{\partial r_{ik}} \cdot \frac{\partial}{\partial \mathbf{r}_{jl}}\left(\frac{\mathbf{r}_{ik}}{r_{ik}}\right)\right) \ , \end{aligned} \tag{3.17}$$

where one can prove - once contracted with the displacements $\mathbf{u}_i \mathbf{u}_j$ of equation 3.1 - that the first part of the sum in 3.17, contains the quadratic term of the expansion 3.3 while the second term contains the two terms of 3.18

We see here that this formalism that expands in terms of distances helps to distinguish simply three cases. For a Cauchy type potential energy $\mathrm{U} = \sum \mathrm{U}_{ij}(r_{ij})$ that contains only two-body interaction contributions, the only derivatives present in 3.20 contain only the two site indices derivatives $\frac{\partial^2 \mathrm{U}}{\partial r_{ij}^2}$. For more general potential containing three-body (bending) and four-body (twist) contributions to the total energy one would have to include also the three and four site terms, $\frac{\partial^2 \mathrm{U}}{\partial r_{ij} \partial r_{ik}}$ and $\frac{\partial^2 \mathrm{U}}{\partial r_{ij} \partial r_{kl}}$, in the following work we will mainly consider model systems where only two-body interactions are considered. In this case the Born Huang contribution to the total elastic energy is therefore[6],

$$\frac{1}{2} \sum \left[\frac{\partial^2 \mathrm{U}}{\partial r_{ij}^2} \right]_{\{\mathrm{R}\}} u_{ij}''^{\,2} \ . \tag{3.21}$$

This term is reminiscent of the second effect of the initial stresses discussed in the previous paragraph - the so called indirect effect - that contributes to the total elastic energy as (see equations 3.7 and 3.18),

$$- \sum \left[\frac{\partial \mathrm{U}}{\partial r_{ij}} \right]_{\{\mathrm{R}\}} \frac{u_{ij}''^{\,2}}{2\mathrm{R}_{ij}} \ . \tag{3.22}$$

The continuum limit of these two terms containing the component u_{ij}'' of the relative displacement parallel to the reference vector can be delt with in the same way. As already discussed in the first paragraph 3.2.1, by substituting the continuum expression for u_{ij}'' 3.11 in 3.21 and 3.22 one gets the summed contribution,

$$\mathrm{U}^3 = \sum \frac{1}{2} \left(\mathrm{K}_{ij} - \mathrm{T}_{ij}/\mathrm{R}_{ij} \right) \frac{\mathrm{R}_{ij}^{\alpha} \cdot \mathrm{R}_{ij}^{\beta} \cdot \mathrm{R}_{ij}^{\gamma} \cdot \mathrm{R}_{ij}^{\delta}}{\mathrm{R}_{ij}^2} \varepsilon_{\alpha\beta}^{(1)} \varepsilon_{\gamma\delta}^{(1)} \tag{3.23}$$

where K_{ij} can be regarded as the spring constant or the stiffness of the bond $i-j$ and T_{ij} is the tension of this bond. From equation 3.23 one can easily identify the macroscopic elastic tensor obtained in the Born approximation and valid for pair interaction potentials as,

$$\mathrm{C}_{\alpha\beta\gamma\delta}^{\mathrm{Born}} = \frac{1}{\mathrm{N}} \sum_i \mathrm{C}_{\alpha\beta\gamma\delta}^{(i)} \ , \tag{3.24}$$

where

$$\mathrm{C}_{\alpha\beta\gamma\delta}^{i} = \sum_j \left(\mathrm{K}_{ij} - \mathrm{T}_{ij}/\mathrm{R}_{ij} \right) \frac{\mathrm{R}_{ij}^{\alpha} \cdot \mathrm{R}_{ij}^{\beta} \cdot \mathrm{R}_{ij}^{\gamma} \cdot \mathrm{R}_{ij}^{\delta}}{\mathrm{R}_{ij}^2} \ . \tag{3.25}$$

The first equation 3.24 above is valid only under the homogeneity assumption. In the continuum limit this gives,

$$\mathrm{U}^3 \longrightarrow \mathrm{U}_{continuum}^3 = \int d\mathbf{r} \cdot \mathrm{D}_{\alpha\beta\gamma\delta}(\mathbf{r}) \cdot \varepsilon_{\alpha\beta}^{(1)}(\mathbf{r}) \cdot \varepsilon_{\gamma\delta}^{(1)}(\mathbf{r}) \ , \tag{3.26}$$

where by identification of equations 3.23 and 3.26 one can define a microscopic expression of the fourth order elastic tensor $\mathbf{D}$ under the assumption of homogeneous strain.

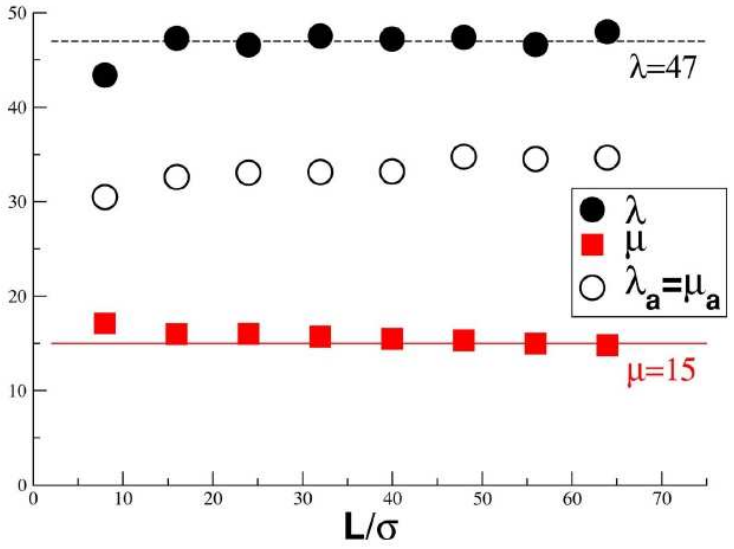

Fig. 3.1 : Lamé coefficients λ (spheres) and μ (squares) vs system size L. Full symbols correspond to the direct measurement using Hooke's law; open symbols are obtained supposing affine deformations (Born term). The effect of system size is weak. The coefficients relying on a negligible nonaffine field differ by a factor as large as 2 from the true ones. Clearly, a calculation taking into account the nonaffine character of the displacement is necessary for disordered systems. Figure taken from [118].

3.2.3 Limits of the homogeneity assumption

In the previous paragraphs we have derived continuum elasticity from the particle scale in the long-wavelength limit - we have derived microscopically expressions for the stress and elasticity tensor and recovered the classical continuum limit of the elastic energy. These derivations are correct at a local level but their generalization to larger systems relied heavily on the hypothesis of affine (homogeneous) deformation of the material, which is strickly speaking verified only for perfect lattices - i.e. with one atom per unit cell. There are therefore numerous cases where the affinity assumption is not verified. In fact only very few Bravais lattices with nearest neighbor bonds are rigid - in particular one can easily see that the shear modulus of a simple square structure has zero shear modulus whilst the calculations of the previous paragraph would produce a finite elastic modulus - and the only two-dimensional Bravais lattice which is rigid with nearest-neighbor interactions is the triangular lattice. In structural glasses the situation is similar and the inherently disordered nature of the glasses makes the continuum predictions - concerning the elasticity tensor - of the previous paragraph largely erroneous. In [118] the macroscopic Lamé coefficients λ and μ were calculated by directly applying macroscopic deformation to the glass samples - for the same two-dimensional, amorphous, Lennard-Jones system that we analyse in this thesis - using on the one hand the elasticity tensor $C^{Born}_{\alpha\beta\gamma\delta}$ expressed in 3.24 and on the other hand

[6] Let us remind here that the following sum is taken over all independent distances in the reference state.

the values obtained by explicitely applying two independent macroscopic deformations to the samples exactly as would be done experimentaly to recover the mechanical properties of a material. In figure 3.1 we see that the Born approximation in this case tends to lower the shear modulus μ, and to increase the coefficient λ. From the preceding discussion we see that the failure of the Born calculation is associated with the existence of a deviation from the affine response of the material - the so-called non-affine displacement - which stores part of the elastic deformation energy. This field is defined by substracting from the actual displacement of the atoms the displacement that would be obtained in the affine hypothesis. In the next section we will see what are the possible methods to deal with this complication. We will also discuss the second problematic of this chapter concerning the validity and the ways to extent continuum mechanics at small scales.

3.3 Continuum mechanics 2 : general case

3.3.1 Thermodynamic approach - global constants

This work is mainly concerned with athermal systems or with systems quenched at finite temperatures well below the glass transition temperature. Therefore the presentation of the thermodynamic approach originally applied by Ray [131] to the calculation in simulations of different response functions[7] such as the stress or the elastic tensor of different model materials - crystalline and amorphous - seems here a priori unapplicable. Indeed as we will see the expression of the response functions that are calculated numerically contain equilibrium fluctuation terms that in the limit of zero temperature should take an infinite time to compute. On the other hand the procedure presented in these fluctuation methods is very general - does not for example make the simplifying assumption of an affine deformation of the material - and besides its importance in the estimate of the elastic constants at finite temperature it can if taken in the zero temperature limit give us a better understanding of the role played by the non-affine field. Moreover the presentation of the thermodynamic framework is a necessary step to introduce the notations and definitions of the different quantities - stress, strain, elastic constant - presented in this chapter. In addition we will see in section 3.3.3 that the clear presentation here of the thermodynamic fluctuation method will enable us to discuss on a generalisation of the global method to the estimate of the response functions locally through the introduction of a coarse-graining technique.

The starting point of the thermodynamic description of elasticity is to acknowledge the fact that if one thinks usually that the original form of molecular dynamics generates

[7] Response function are by definition function that are associated with derivatives of the basic thermodynamic state variables like energy, pressure, entropy and include the thermodynamic state variables themselves. They have to be distinguished from (non-equilibrium) transport properties, such as the thermal conductivity, electrical conductivity, and viscosity.

the microcanonical ensemble EVN in reality most model systems are enclosed in a cell described not simply by its volume V but more generally by a $d \times d$ matrix $\mathbf{h}$ formed by the three independent vectors that constitute the simulation cell. Parrinello and Rahman were the first to allow for changes in both the size and shape of the molecular dynamics cell and allowed $\mathbf{h}$ to become a dynamical variable. Hence the Parrinello-Rahman form of molecular dynamics generates the HtN ensemble where t is the thermodynamic tension and H the enthalpy. In this framework the authors presented thereafter the fluctuation formula for the calculation of elastic constants. Later their calculation were generalized and tested on model system by Ray and coworkers in different statistical ensembles[8]. Let us first introduce some definitions that will be useful to ultimately derive the elastic constants. First the cartesian coordinates of any point $\mathbf{R}$ in the cell can be expressed as[9]

$$\mathrm{R}_\alpha = h_{\alpha\beta}\mathrm{X}_\beta \ , \tag{3.27}$$

where $\mathbf{X}$ is a rescaled vector whose components lie in $[0,1]$. Integrals over $\mathbf{R}$ can be converted into integrals over $\mathbf{X}$ by using a scaling factor $\det(\mathbf{h})$, which represents the volume of the cell, V. The metric tensor $\mathbf{G}$ is constructed from $\mathbf{h}$ as,

$$\mathbf{G} = \mathbf{h}^{\mathrm{T}} \cdot \mathbf{h} \ , \tag{3.28}$$

where $\mathbf{h}^{\mathrm{T}}$ is the transpose of $\mathbf{h}$. $\mathbf{G}$ is used in transforming dot products from the original Cartesian to rescaled coordinates, according to,

$$\mathrm{R}_\alpha \mathrm{R}'_\alpha = \mathrm{X}_\alpha \mathrm{G}_{\alpha\beta} \mathrm{X}'_\beta \ . \tag{3.29}$$

Elasticity theory describes the deformation of any configuration from a reference configuration in terms of a strain tensor. This tensor is constructed by relating the vector connecting two points in the deformed configuration to the corresponding displacement of the same points in the reference configuration. If the reference configuration of the simulation box is denoted by $\mathbf{h}_0$, the strain is given by,

$$\varepsilon = \frac{1}{2}\left[\left(\mathbf{h}_0^{\mathrm{T}}\right)^{-1}\mathbf{h}^{\mathrm{T}}\mathbf{h}\left(\mathbf{h}_0\right)^{-1} - \mathbf{1}\right] = \frac{1}{2}\left[\left(\mathbf{h}_0^{\mathrm{T}}\right)^{-1} \cdot \mathbf{G} \cdot \left(\mathbf{h}_0\right)^{-1} - \mathbf{1}\right] \ . \tag{3.30}$$

Usually the reference configuration $\mathbf{h}_0$ will be defined as a state of the system under zero applied external stress. If one starts with a cubic cell, $\mathbf{h}_0$ is the identity matrix and the relation between $\boldsymbol{\varepsilon}$ and $\mathbf{G}$ simplifies. The thermodynamic variable conjugate to this strain tensor, in the sense that the elementary work done on the system can be written in the form

$$\delta \mathrm{W} = \mathrm{V}_0 t_{\alpha\beta} d\varepsilon_{\beta\alpha} \ , \tag{3.31}$$

is the thermodynamic tension $\mathbf{t}$, also known as Piola-Kirchhoff second stress tensor. $\mathrm{V}_0 = \det(\mathbf{h}_0)$ denotes the volume of the system in the reference configuration. This thermodynamic tension tensor can be related to the more usual Cauchy stress tensor $\boldsymbol{\sigma}$ through

[8] for a single component system one can construct 8 such ensembles, namely the EVN, TVN, HPN, TPN, SVμ,TVμ, SPμ and TPμ ensembles.

[9] Here we follow the presentation made by Barrat in [132]

$$\boldsymbol{\sigma} = \mathrm{V}_0 \mathbf{h} \left(\mathbf{h}_0\right)^{-1} \mathbf{t} \left(\mathbf{h}_0^{\mathrm{T}}\right)^{-1} \mathbf{h}^{\mathrm{T}} / \mathrm{V} \ . \tag{3.32}$$

The tension is the derivative of the free energy with respect to the strain, which is calculated from the reference configuration. The Cauchy stress, on the other hand, is the derivative of the free energy with respect to an incremental strain taken with respect to the actual configuration. This Cauchy stress tensor is the one that enters momentum conservation and whose expression is given by the thermodynamic average of the usual Irving-Kirkwood formula[10] for pairwise additive potentials. While the Cauchy stress has a mechanical meaning in terms of forces within the sample, the thermodynamic tension is a purely thermodynamic quantity, and does not in general have a simple mechanical interpretation. Here we concentrate on the case of small deformation where these differences between stress tensors vanish.

Armed with this formalism, the derivation of the elastic constant can be obtained for example following [133, 134, 131, 135] in the ThN ensemble - one speaks in that case of the isothermal elastic contants - with the following expression of the free energy,

$$\exp(-\beta \mathrm{F}) = \int d\mathbf{p}^{2\mathrm{N}} d\mathbf{R}^{2\mathrm{N}} e^{-\mathrm{H}/k_{\mathrm{B}}\mathrm{T}} \ , \tag{3.33}$$

where H is the hamiltonian of the system. In the ThN ensemble the thermodynamic law can be written,

$$d\mathrm{F} = -\mathrm{S}d\mathrm{T} + \mathrm{V}_0 t_{\alpha\beta} de_{\beta\alpha} \ , \tag{3.34}$$

and one defines respectively the thermodynamic tension $\mathbf{t}$ and the isothermal elasticity tensor $\mathbf{C}$ as [136],

$$t_{\alpha\beta} = \frac{1}{\mathrm{V}_0} \frac{\partial \mathrm{F}}{\partial \varepsilon_{\alpha\beta}}\bigg|_{\mathrm{T}} \ , \tag{3.35}$$

$$\mathrm{C}_{\alpha\beta\gamma\delta} = \frac{1}{\mathrm{V}_0} \frac{\partial^2 \mathrm{F}}{\partial \varepsilon_{\alpha\beta} \partial \varepsilon_{\gamma\delta}}\bigg|_{\mathrm{T}} \ . \tag{3.36}$$

From equations 3.33 and 3.35 one easily recovers the expression of the thermodynamic stress $\mathbf{t}$,

$$\mathrm{V}_0 t_{\alpha\beta} = \left\langle \frac{\partial \mathrm{H}}{\partial \varepsilon_{\alpha\beta}}\bigg|_{\mathrm{T}} \right\rangle - \frac{\mathrm{N}}{\mathrm{V}} k_{\mathrm{B}}\mathrm{T} \frac{\partial \mathrm{V}}{\partial \varepsilon_{\alpha\beta}}\bigg|_{\mathrm{T}} = \langle t_{\alpha\beta}^{\mathrm{IK}} \rangle - \frac{\mathrm{N}}{\mathrm{V}} k_{\mathrm{B}}\mathrm{T} \frac{\partial \mathrm{V}}{\partial \varepsilon_{\alpha\beta}}\bigg|_{\mathrm{T}} \ , \tag{3.37}$$

where one can show [133, 134, 131, 135] that the term $\frac{\partial \mathrm{H}}{\partial \varepsilon_{\alpha\beta}}$ reduces to the Irving Kirkwood formula of the stress,

$$t_{\alpha\beta}^{\mathrm{IK}} = \sum_i p_{i\alpha} p_{i\beta}/m + \frac{1}{2\mathrm{V}} \sum_{i,j} \mathrm{R}_{ij\alpha} f_{ij\beta} \ . \tag{3.38}$$

A second derivative of the free energy with respect to strain yields, can be obtained in the limit of zero strain, after a slightly longer derivation (we refer the interested reader for the

[10] If we neglect the kinetic part, the Irving Kirkwood stress is equal to the site stress given in 3.14

detailed derivation to the references [134, 135]),

$$\begin{aligned} \mathrm{C}_{\alpha\beta\gamma\delta} &= \frac{\mathrm{V}_0}{k_\mathrm{B}\mathrm{T}}\left(\langle t^{\mathrm{IK}}_{\alpha\beta} t^{\mathrm{IK}}_{\gamma\delta}\rangle - \langle t^{\mathrm{IK}}_{\alpha\beta}\rangle\langle t^{\mathrm{IK}}_{\gamma\delta}\rangle\right) \\ &\quad -\frac{1}{4}\left(\langle t^{\mathrm{IK}}_{\beta\gamma}\rangle\delta_{\alpha\delta} + \langle t^{\mathrm{IK}}_{\alpha\delta}\rangle\delta_{\beta\gamma} + \langle t^{\mathrm{IK}}_{\beta\delta}\rangle\delta_{\alpha\gamma} + \langle t^{\mathrm{IK}}_{\gamma}\rangle\delta_{\beta\gamma}\right) \\ &\quad +\mathrm{C}^{Born}_{\alpha\beta\gamma\delta} + \frac{\mathrm{N}}{\mathrm{V}}k_\mathrm{B}\mathrm{T}\left(\delta_{\alpha\gamma}\delta_{\beta\delta} + \delta_{\alpha\delta}\delta_{\beta\gamma}\right) \ . \end{aligned} \tag{3.39}$$

The first term is the 'fluctuation term', the second arises from the effect of stress, the third term is referred to as the 'Born term' and is defined here as the canonical average of the expression given at zero temperature in 3.25 and the last term is sometimes called the 'kinetic term'.

In what follows we want to see how one can deal with the limiting case of an athermal system, case that we are mainly interested in. A naive approach to the calculation of the elastic properties in such systems would consist in taking the second derivative of the free energy - that coincides with the potential energy in the athermal limit - with respect to strain with the hypothesis that the response is homogeneous in the material. Such an approach is known to yield elastic constants that correspond to the Born expression 3.25 and therefore as we have already discussed in the previous section proves in fact completely incorrect for disordered systems, or even for crystals with a complex unit cell. This can be understood as follows. In the athermal limit the free energy F identifies with the potential energy $\mathrm{U}(\{\mathrm{R}_{ij}\},\boldsymbol{\varepsilon})$ - that can be expressed in the deformed configuration as a function of the set of distances $\{\mathrm{R}_{ij}\}$ and the Green Saint-Venant strain tensor $\boldsymbol{\varepsilon}$ - and can be expanded as,

$$d\mathrm{F} = d\mathrm{U} = t_{\alpha\beta}\varepsilon_{\alpha\beta} + \mathrm{C}_{\alpha\beta\gamma\delta}\varepsilon_{\alpha\beta}\varepsilon_{\gamma\delta} + h.o.t. \ . \tag{3.40}$$

The simplifying assumption of the affine deformation made in the previous section corresponds in taking the derivatives of the above potential energy $\mathrm{U}(\{\mathrm{R}_{ij}\},\boldsymbol{\varepsilon})$ with respect to strain at fixed rescaled positions $\mathbf{X}$. In a real deformation the rescaled positions $\mathbf{X}$ can also evolve with the applied strain $\varepsilon_{\alpha\beta}$ and one must derive the potential energy not at fixed positions $\mathbf{X}$ but rather keeping the force $\mathbf{f}$ on each atom equal to zero in the deformed configuration in order to remain at equilibrium during the deformation. The general expression of the elastic constants should then read in the athermal limit[11],

$$\mathrm{C}_{\alpha\beta\gamma\delta} = \left.\frac{\partial^2\mathrm{U}}{\partial\varepsilon_{\alpha\beta}\partial\varepsilon_{\gamma\delta}}\right|_{\mathbf{f}=\mathbf{0}} = \frac{\partial}{\partial\varepsilon_{\alpha\beta}}\left(\left.\frac{\partial\mathrm{U}}{\partial\varepsilon_{\gamma\delta}}\right|_{\mathbf{X}} + \left.\frac{\partial\mathrm{U}}{\partial\mathbf{X}_i}\right|_{\boldsymbol{\varepsilon}}\left.\frac{\partial\mathbf{X}_i}{\partial\varepsilon_{\gamma\delta}}\right|_{\mathbf{f}=\mathbf{0}}\right) \ , \tag{3.42}$$

[11] Here we use the following mathematical identities that apply for example given two independent variables, x and y, and a third which is a function of these two, z(x,y), then we have for any function of x and y, f(x,y), that

$$\left.\frac{\partial f}{\partial x}\right|_z = \left.\frac{\partial f}{\partial x}\right|_y + \left.\frac{\partial f}{\partial y}\right|_x\left.\frac{\partial y}{\partial x}\right|_z \ . \tag{3.41}$$

In our problem x would be the strain $\varepsilon_{\alpha\beta}$, y the rescaled positions $\mathbf{X}$, z the forces $\mathbf{f}$ that apply on the particles and f the potential. energy U.

and at equilibrium $\mathbf{f}_i = \frac{\partial \mathrm{U}}{\partial \mathbf{X}_i}\Big|_{\boldsymbol{\varepsilon}} = \mathbf{0}$ for each particle and one is left with,

$$\mathrm{C}_{\alpha\beta\gamma\delta} = \frac{\partial^2 \mathrm{U}}{\partial \varepsilon_{\alpha\beta} \partial \varepsilon_{\gamma\delta}}\Big|_{\mathbf{X}} + \frac{\partial^2 \mathrm{U}}{\partial \varepsilon_{\alpha\beta} \partial \mathbf{X}_i}\Big|_{\boldsymbol{\varepsilon}} \frac{\partial \mathbf{X}_i}{\partial \varepsilon_{\gamma\delta}}\Big|_{\mathbf{f}=\mathbf{0}} \quad . \tag{3.43}$$

Moreover by differentiating the equilibrium condition $\mathbf{f}_i = \frac{\partial \mathrm{U}}{\partial \mathbf{X}_i}\Big|_{\boldsymbol{\varepsilon}} = \mathbf{0}$ with respect to strain one obtains,

$$\frac{\partial^2 \mathrm{U}}{\partial \varepsilon_{\alpha\beta} \partial \mathbf{X}_i}\Big|_{\mathbf{X}} + \frac{\partial^2 \mathrm{U}}{\partial \mathbf{X}_i \partial \mathbf{X}_j}\Big|_{\varepsilon} \frac{\partial \mathbf{X}_j}{\partial \varepsilon_{\alpha\beta}}\Big|_{\mathbf{f}=\mathbf{0}} = \mathbf{0} \ , \tag{3.44}$$

and reinjecting the expression of $\frac{\partial \mathbf{X}_j}{\partial \varepsilon_{\alpha\beta}}\Big|_{\mathbf{f}=\mathbf{0}}$ so derived in 3.44 in 3.43 one gets,

$$\mathrm{C}_{\alpha\beta\gamma\delta} = \mathrm{C}^{Born}_{\alpha\beta\gamma\delta} - \boldsymbol{\Xi} \cdot \mathbf{H}^{-1} \cdot \boldsymbol{\Xi} \ , \tag{3.45}$$

where

$$\boldsymbol{\Xi} = \frac{\partial^2 \mathrm{U}}{\partial \varepsilon_{\alpha\beta} \partial \mathbf{X}_i}\Big|_{\boldsymbol{\varepsilon}} \ , \tag{3.46}$$

and where $\mathbf{H}$ is the Hessian matrix defined by,

$$\mathbf{H} = \frac{\partial^2 \mathrm{U}}{\partial \mathbf{X}_i \partial \mathbf{X}_j}\Big|_{\boldsymbol{\varepsilon}} \quad . \tag{3.47}$$

Note that expression 3.45 can be recovered by taking the zero temperature limit of expression 3.39 as was shown first in [134]. In practice the evaluation of the second term in 3.45 is numerically difficult as one has to diagonalize the Hessian matrix, which becomes very time consuming as the number of particles in the system increases. So generally the actual procedure to obtain zero temperature elastic constants consists in carrying out explicit macroscopic deformations on the sample - either by energy potential minimization (see section 2.3) or by low temperature molecular dynamics (section 2.2) techniques - and to recover the elastic constants by inverting the macroscopic stress-strain relations. In [118] the elastic constants of the same Lennard-Jones polydisperse as the one used in this thesis were derived with this direct method and were compared with the elastic constants that one gets under the affine assumption. As we have already seen in paragraph 3.2.3 the 'relaxation-fluctuation' term in 3.39 or 3.45 has a dramatic effect on the estimated macroscopic elastic constants shown in figure 3.1.

If this approach helps to take into acount the disorder nature of the glassy materials and the influence of the nonaffine field it was not originally designed to be applied for small system (rather the opposite - valid in the thermodynamic limit). In the next chapter we present a method to calculate microscopically derived expressions of the different continuum mechanics fields of interest, and to assess the validity of the continuum mechanics and of elasticity at small scales.

3.3.2 Literature review - local constants

It is surprising to see that despite the growing importance of nanostructures the question of the accurate description of these materials at small scales and fine resolutions is not always addressed. So in many recent publications the methods of calculation of the fields of continuum mechanics -strain, stress, elasticity tensor...- valid in the thermodynamic limit are assumed to remain so at nanometric scales without further discussion. As we will discuss in details later the extension of continuum mechanics at small scales is all the more important in that a local accurate knowledge of the continuum fields of mechanics (strain, stress, elastic constants in mechanical response of material or strain rate, stress, velocity fields, viscosity in rheology) is necessary to describe the heterogeneous rheology/mechanical response of a vast class of complex materials. Indeed these local fields are the necessary ingredients in the growing literature concerned with the developement of local constitutive laws of the dynamics in materials such as granular materials, glassy materials, complex fluids (see [17]). We present in this paragraph first some existing methods to derive the local strain, stress and elastic moduli and then we discuss in greater details a coarse-grained method developped by Goldenberg and Goldhirsch [137] and that we used extensively in our work. We discuss the advantages of the latter method over earlier derivations.

Previous derivations of the local strain

Let us first consider local possible estimates of the strain tensor. The first and most commonly used approximation concerning the local strain tensor is to adopt the assumption of affinity also refered to as mean field or Voigt [138] assumption and to assume therefore that the local strain tensor can be identified with the global applied strain. This assumption was for example made in section 3.2 and leads as we have shown to incorrect expressions of the elastic constants. To make contact with granular materials we can here mention that this assumption is also at the heart of the so-called effective medium theory that gives an estimate of the effective elastic moduli of a random packing of identical elastic hard spheres [139]. Similarly to what we discussed in section 3.2.3 for a system of polydisperse soft spheres, it was shown in [140] that if the affine assumption seems reasonably verified for an applied isotropic deformation and predicts reasonably well the bulk modulus it breaks down and gives wrong estimates of the shear modulus.

To overcome this oversimplification of the problem a necessary step is to acknowledge for the heterogeneous nature of the strain field in the material and to define an expression of the local strain tensor. There exist many different ideas to interpret the strain tensor from a microstructural point of view. Most of them belong to one of the two following approaches [141, 142].

Strains based on an equivalent continuum. In these approaches one extrapolates locally the discrete displacements to a continuous function of space. Then according to the Gauss-Ostrogradski theorem the gradient of displacements $\overline{\gamma_{\alpha\beta}}_{(\mathrm{V})}$ can be estimated for a domain

of volume V and surface S as,

$$\overline{\gamma_{\alpha\beta}}_{(\mathrm{V})} = \frac{1}{\mathrm{V}} \int_{\mathrm{V}} \frac{\partial u_\alpha}{\partial x_j} d\mathrm{V} = \frac{1}{\mathrm{V}} \int_{\mathrm{S}} u_\alpha n_\beta d\mathrm{S} \tag{3.48}$$

Using some sort of compartimentation of the sample the gradient tensor of displacement is then computed based on the microscopic particle displacements and local geometry of the sample. As for any numerical integration scheme, there is some arbitrariness on how to calculate the volume integral 3.48, different approaches differ for example in the mesh that they use and in the simplifications that they note due to geometrical properties of the arrangement of particles. One can quote the following references and their specificities, Bagi [141] uses a Delaunay mesh with geometrical simplifications in the summation over the mesh cells that allow for an estimate of the discrete version of 3.48, valid in 2D or 3D. Kruyt and Rothenburg [143] consider for the mesh only cells associated with contact pairs of particles, their algorithm is only valid in 2D. Kuhn's [144] approach is very similar to the previous derivations but uses a slightly different summation algorithm, only valid in 2D. Cambou [145] directly uses the same mesh as Kruyt and Kuhn but gives another simple estimate of the strain on each cell, this approach is valid in 2D as well as in 3D. Note that since the boundaries of the equivalent continua displacement of the Kruyt-Rothenburg strain, of the Kuhn strain and of the Cambou strain are the same, and since the continuous displacement field is defined in the same way, the meaning of these approaches is the same and hence these three strains are equal and only differ in the algorithm that is used to effectively determine the sum associated with the discrete version of 3.48[12].

Best fit strains. In this type of method the strain tensor derivation is based on finding the displacement gradient tensor that gives the smallest deviation from the characteristic displacements of the same system of volume V and surface S discussed above. The characteristic displacement can be the displacements of particle centers, the relative displacements at the contacts, etc. Depending on the kind of displacements to be approximated by an average displacement gradient, different versions of best-fit strains are gained. Considering the best fit to the displacement of the particle centers included in the sample studied, Cundall and Strack [146] gave the average strain of this assembly of particles as a simple sum over the boundary particles in 2D and 3D. Similarly Koenders [147] suggested that the incremental dispacement gradient tensor should be defined as a least squares best fit to the displacement of the boundary particles, but using the Gauss-Ostrogradski theorem he converts the surface sum into a volume sum. The best fit strain proposed by Liao et al. [148] is based on a similar line of thought, but instead of the particle displacements, its fundamental quantity is the contact deformations that can be determined from the particle displacements and rotations. Here the strain is determined as a best fit to the contact point displacements and unlike the Cundall or Koenders strain the Liao et al. strain takes into account the particle rotations. As an improvement to this method Cambou [145] proposed to consider not only the contacting but also all the neighbouring pairs of particles (in the

[12] For the explicit expressions of the strains discussed in the following paragraphs we report the interested reader to the cited references

Delaunay sense) in the fitting procedure. Finally Gullett *et al*, in a recent publication, proposed a derivation where the discrete deformation gradient emerges from a weighted least squares minimization, hence introducing a tunable length scale.

An important test of the validity of these micromechanical definitions of strains is to compare the global strain tensors according to the above micromechanical definitions with the macroscopic strain tensor determined from the displacement of boundaries of the assembly [143]. A comparative study of some of the methods described above is made in [142] for a biaxial shear of an assembly of spheres confined in a square domain confined in four straight walls. The results showed that except Liao's and Cundall's fitting procedures most microscopicaly defined strains tend to the global deformation strain if averages are calculated over the entire sample.

The methods presented above have been used in different studies interested in the accurate local description of the heterogeneous response of complex materials under external load. Other geometrical quantifiers of the anisotropy of the material locally have also been presented for example in the context of foams, where the so-called fabric tensor was studied. Recently more sophisticated local analyses were performed on different types of materials by the use of the tensorial Minkowsky functional (described in [149]), that very interestingly marked an anisotropicity phase transition in disordered sphere packs at densities corresponding to random close and random loose packing.

Let us conclude by saying that the above approaches suffer from several shortcomings. As mentionned the underlying assumption of the best fit procedures that the particle displacements are specified by an affine deformation field (even at a local level) cannot be exact for disordered configurations. Moreover these methods are inconsistent with continuum mechanics foundations in the sense that the time derivative of the strain tensor should, to linear order, be equal to the rate of strain tensor i.e., the symmetrized gradient of the velocity [150]. The best fit strains do not conform to this requirement. Finally and most importantly the above methods are not constructed to allow for a systematic coarse-graining of the microscopic strain at different length scales. A possible extension of the methods would be to coarse-grain the precedent microscopic strain expressions by a weighting function. We will see that in the coarse-graining procedure used by Goldenberg and described in details in [137] the coarse-graining is computed directly on the displacements rather than on a local microscopic strain, allowing for the method to be consistent with the first principles of continuum mechanics.

Previous derivations of the local stress

Many authors [151, 152, 153] have proposed an expression for the average stress tensor in terms of the forces acting at the contacts between particles and of the geometry of the assembly of particles. The derivation of the expression for the average stress tensor of an assembly of particles enclosed in a volume V and surface S can proceed as for the

strain in two steps. In the first step the average stress tensor is related to quantities involving forces exerted on the particles by the boundary that encloses the assembly of particles. The second step equates, by the use of Gauss's theorem 3.48, these quantities involving external forces to quantities involving internal forces. The result of the first step is a micromechanical expression for the average stress tensor $\overline{\sigma_{xy}}_{(\mathrm{V})}$ which for a region of volume V can be expressed as,

$$\overline{\sigma_{\alpha\beta}}_{(\mathrm{V})} = \frac{1}{\mathrm{V}} \int_{\mathrm{V}} \sigma_{\alpha\beta} d\mathrm{V} = \frac{1}{\mathrm{V}} \int_{\mathrm{S}} x_\alpha \sigma_{\nu\beta} n_\nu d\mathrm{S} \ , \tag{3.49}$$

where the α coordinate of a point on the surface S was simply introduced through $\sigma_{\alpha\beta} = \partial_\nu x_\alpha \sigma_{\nu\beta}$ and the volume intregral was subsequently simplified using Gauss' theorem and the equlibrium condition $\partial_\beta \sigma_{\alpha\beta} = 0$. The term $\sigma_{\nu\beta} n_\nu$ corresponds to the traction force exerted in point $\mathbf{x}$ of the surface by the exterior. The second step of the derivation allows to reformulate the expression 3.49 of the stress tensor in terms involving internal - rather than surface - forces. The later formulation of the stress of a region of volume V enclosed by a surface S corresponds to the Irving-Kirkwood 3.38 expression of the stress tensor in the limit of zero velocities and were the sum is taken over bonded particles (particles in contact in the case of granular materials) located both inside the domain. The derivation for an expression of the stress tensor at finite temperature was given in 3.3.1 by means of classical statistical mechanics and will be discussed more in details also in section 3.3.3.

Here one must understand that the expressions of the stress given above, in contrast with the strain that is a dynamical quantity - as it requires at least two configurations for its calculation -, can be obtained for any given configuration of particles if the force field is known - note however than in many experiments the force field is not known theoretically and the estimate of the stress and force fields cannot be simply deduced from the positions of the particles. In practice though to establish a (local) constitutive law of the material one needs to calculate not only the instantaneous local stress field but rather the incremental stress field. We have seen in section 3.2 how one can simply derive an expression of the incremental local stress field directly from the knowledge of the positions of the particles on the reference configuration if one assumes that the strain is homogeneous in the material. In fact there is some symmetry between strain and stress and one can also in a similar way as in 3.2 derive a simple expression of the local strain if one assumes homogeneous stress (we refer the interested reader to the treatment of Kruyt).

Again as for strain derivations we emphasize here some of the drawbacks of these methods namely, the sensitivity to the discrete nature of the boundary over which are calculated the discrete deriving from 3.48 and the fact that the stress expressions introduced above do not conform to one of the milestones of continuum mechanics i.e. conservation equation of momentum.

Previous derivations of the local moduli

As we have discussed in section 3.3.1 the estimate of the bulk constants is well established and has lead to a substancial literature, the generalization to the measure of local elastic constants is a more recent field. In simulations Kluge [154] and Alber [155] carried out such calculations of the local elastic constants in the neighbourhood of a grain boundary in model crystal systems. More recently several authors used similar generalizations of formula 3.39 to calculated the local elastic constants in composites [156, 7], in Lennard-Jones glasses [157, 158, 159] and in metallic glasses [160]. In these approaches the authors have used a subdivision of the macroscopic sample in cells (typically cubes) of different sizes and applied a modified version of 3.39 to these subdomains. Unfortunately a systematic cell size effect was not discussed by the authors. We will come back to this point in section 3.4.2 were we specifically quantify the convergence behaviour of the local elastic moduli to the macroscopic constants. Another study of local elastic constants and stresses in the highly stressed region beneath a nanoindenter was made recently by VanVliet [161] and used these local tensor to construct an elasticity based criterion that they used to predict initiation of dislocations.

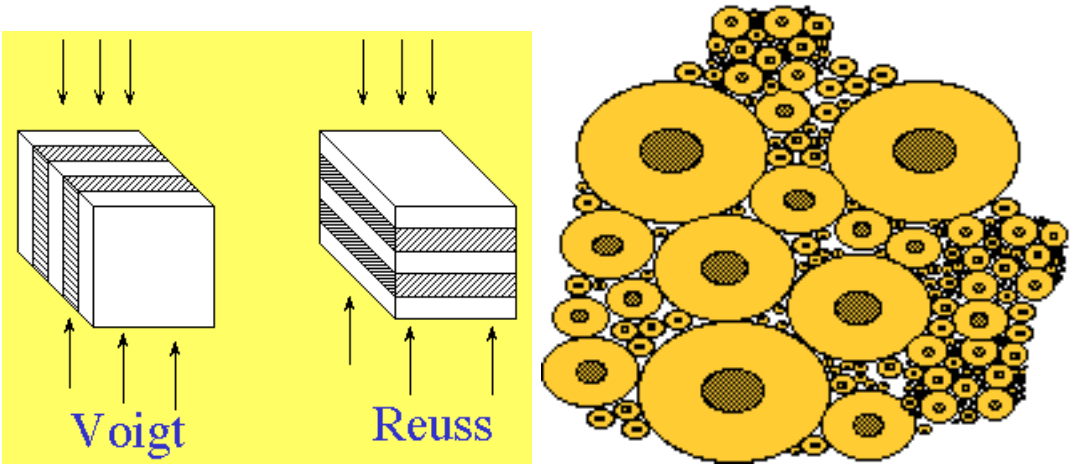

FIG. 3.2 : **Left :** For an elastic two-phase composite, the stiffness of Voigt and Reuss composites represent rigorous upper and lower bounds on the Young's modulus for a given volume fraction of one phase. The sketch illustrates the two limiting cases where the Voigt and Reuss bounds are attained. **Right :** Sketch of the coated sphere morphology with the volume filled with spheres of different size of one phase. Each sphere has a coating of a given fraction of the sphere radius. In this morphology the moduli given by the Hashin - Shtrikman formulae are exactly attainable [162].

Having characterized the heterogenous nature of the material in terms of local stress and strain fields is a first step, but to go even further one would like to deduce from this a macroscopic constitutive law, i.e. the effective elasticity tensor of the material. This ultimate goal is rather simple only for ideal crystaline structures with one atom per unit cell. There is a very large literature on this subject. We have already seen in section 3.23 how one can derive a microscopic expression of the Born elastic moduli, i.e. the elastic moduli

under the unrealistic assumption of uniform strain in the material. An expression of the same type can be obtained if one makes the assumption of uniform stress in the material. A more systematic method consists in establishing bounds on the permitable values of the elastic constants. These bounds are for an elastic, anisotropic two-phase composite material, depicted on figure 3.2, called the Voigt and Reuss bounds and are rigorously attained in this case, where the modulus for the Voigt composite is $E_c = E_1V_1 + E_2V_2$, in which E_c, E_1 and E_2 refer to the Young's modulus of the composite, phase 1 and phase 2, and V_1 and V_2 refer to the volume fraction of phase 1 and phase 2 with $V_1 + V_2 = 1$. This is an exact analytical form for this morphology (think of the analogy of springs in parallel). The modulus of the Reuss composite is $1/E_c = V_1/E_1 + V_2/E_2$ (think of the analogy of springs in series). Another simple physical model where an effective modulus can be obtained exactly is the isotropic coated-spheres model. For such isotropic composites the bounds given by Hashin and Shtrikman are exactly attainable, and are tighter than the Voigt-Reuss bounds. As shown in figure 3.2 in this composite the full volume is filled with spheres of different size of one phase; each sphere has a coating of a given fraction of the sphere radius, made of material of the second phase. Note that in this model one can derive only an exact expression of the bulk modulus and not of the shear modulus. Interestingly, Christensen and Lo [163] showed that a variant of the coated-spheres model, a 'three-phase model', does permit an exact solution of the effective shear modulus. Other exact solutions can be obtained for the effective elastic moduli of a matrix of given bulk and shear modulus containing a small concentration of ellipsoidal inclusions with different elastic properties. A review of all these approaches is given in [164, 165].

3.3.3 The coarse-grained approach - local constants

In this paragraph we detail the approach developped by Goldhirsch and Goldenberg that provides precise definitions of the fields of continuum mechanics in terms of microscopic variables in a systematic way, consistent with conservation equations of continuum mechanics, and at different coarse-graining length scales. Most of their work is essentially a coarse-grained equivalent of the derivations obtained in statistical mechanics ([166], see also, as an example of a statistical derivation, the expression of the stress tensor obtained as a thermodynamic average in the ThN ensemble in 3.3.1.). As Irving and Kirkwood in [166], Goldenberg and Goldhirsch [137] base their description of matter on the three following fields, mass density ρ, momentum density $\boldsymbol{p}$ and energy density e. The general form of the equations satisfied by these fields can be shown phenomenologically in any textbook on continuum mechanics to correspond to the three conservation equations for mass, the equation of continuity, for momentum, the equation of motion, and for energy, the equation of energy transport (we do not consider conservation of moment of momentum, electrical

charge and of magnetic flux in this work)[13]

$$\frac{\partial \rho}{\partial t} = -\frac{\partial}{\partial x_\beta}\left(\rho \mathrm{V}_\beta\right) \ , \tag{3.50}$$

$$\frac{\partial p_\alpha}{\partial t} = -\frac{\partial}{\partial x_\beta}\left(\rho \mathrm{V}_\alpha \mathrm{V}_\beta - \sigma_{\alpha\beta}\right) \ , \tag{3.51}$$

$$\frac{\partial e}{\partial t} = -\frac{\partial}{\partial x_\beta}\left(\mathrm{V}_\beta e - \mathrm{V}_\alpha \sigma_{\alpha\beta} + c_\beta\right) \ . \tag{3.52}$$

Irving and Kirkwood in their seminal paper [166] showed how these conservation equations can be obtained from first principles of classical statistical mechanics and by doing so found respectively the following expressions of mass, momentum, stress tensor and heat current densities[14] in terms of molecular variables,

$$\rho(\mathbf{r},t) = \sum_i \langle m_i \delta(\mathbf{r} - \mathbf{r}_i(t))\rangle \ , \tag{3.54}$$

$$p_\alpha(\mathbf{r},t) = \sum_i \langle m_i v_{i\alpha} \delta(\mathbf{r} - \mathbf{r}_i)\rangle \ , \tag{3.55}$$

$$\begin{aligned}
\sigma_{\alpha\beta}(\mathbf{r},t) &= -\sum_i \langle m_i \left(v_{i\alpha} - \mathrm{V}_\alpha\right)\left(v_{i\beta} - \mathrm{V}_\beta\right)\delta(\mathbf{r} - \mathbf{r}_i(t))\rangle \\
&+ \frac{1}{2}\sum\sum_{j\neq k}\langle \frac{\mathrm{R}_{jk\alpha}\mathrm{R}_{jk\beta}}{\mathrm{R}_{jk}}\mathrm{V}'(\mathrm{R}_{jk})\{1 - \frac{1}{2}\mathrm{R}_{jk\nu}\partial_{x_\nu}... \\
&+ \frac{1}{n!}\left(-\mathrm{R}_{jk\nu}\partial_{x_\nu}\right)^{n-1} + ...\}\delta(\mathbf{r} - \mathbf{r}_i(t))\rangle \ ,
\end{aligned} \tag{3.56}$$

where the first term $\sigma^{\mathrm{V}}_{\alpha\beta}(\mathbf{r},t)$ is the contribution of intermolecular forces to the stress tensor ($\boldsymbol{\sigma}^{\mathrm{V}} \cdot d\mathbf{S}$ represents the force acting across dS due to the interaction of molecules on opposite sides of dS), and is commonly refered to as 'contact stress' or 'collisional stress', while the second term $\sigma^{\mathrm{K}}_{\alpha\beta}(\mathbf{r},t)$ is a kinetic contribution usualy called 'kinetic' or 'streaming stress' ($\boldsymbol{\sigma}^{\mathrm{V}} \cdot d\mathbf{S}$, viewed from a coordinate system moving with the local velocity $\mathbf{u}$, is the momentum transferred per unit time across the area dS).

These expressions were presented in recent publications [137, 150] for athermal disordered systems such as granular materials or glasses, in a slightly modified version where

[13] Here we present the conservation equation without the effect of body forces and sources or sinks.

[14] We only present the expression for the heat current as a footnote as we will not look at thermal properties in much details in this thesis. The formula as derived in [166] is given by,

$$\begin{aligned}
&q_\alpha(\mathbf{r},t)\sum_i \langle m_i 2 \ |\mathbf{v} - \mathbf{V}|^2 \left(v_{i\alpha} - \mathrm{V}_\alpha\right)\delta(\mathbf{r} - \mathbf{r}_i(t))\rangle + u_\beta\left[\sigma^{\mathrm{V}}_{\alpha\beta} - \frac{1}{2}\sum\sum_{j\neq i}\langle \mathrm{V}(\mathrm{R}_{ij})\delta_{\alpha\beta}\delta(\mathbf{r} - \mathbf{r}_i(t))\rangle\right] \\
&+ \frac{1}{2}\sum\sum_{j\neq i}\langle\left[\mathrm{V}(\mathrm{R}_{ij})\delta_{\alpha\beta} - \frac{\mathrm{V}'(\mathrm{R}_{ij})}{\mathrm{R}_{ij}}\mathrm{R}_{ij\alpha}\mathrm{R}_{ij\beta}\{1 + ... + \frac{1}{n!}\left(-\mathrm{R}_{ji\nu}\partial_{x_\nu}\right)^{n-1} + ...\}\right] v_{i\beta}\delta(\mathbf{r} - \mathbf{r}_i(t))\rangle
\end{aligned} \tag{3.53}$$

they were used directly in real space and were assumed to remain valid for single realisations (i.e. use of the expressions 3.54, 3.55 and 3.56 without the brackets). Moreover in their treatment Goldenberg and Goldhirsch by substituting a weighting function $\phi(\mathbf{R})$ in place of the delta function in these expressions allowed for the definition of coarse-grained local fields coherent with the conservation equations 3.50, 3.51 and 3.52. Their derivation of the coarse grained local fields goes as follows. For local mass and momentum density use the definition 3.54 where $\delta((\mathbf{r}-\mathbf{r}_i(t))$ is replaced by $\phi((\mathbf{r}-\mathbf{r}_i(t))$. In the rest of this thesis we have chosen the weighting function to be a gaussian function. One can then define respectively the coarse grained mass density, momentum density and velocity fields as,

$$\rho(\mathbf{r},t) = \sum_i m_i \phi(\mathbf{r}-\mathbf{r}_i(t)) \ , \tag{3.57}$$

$$p_\alpha(\mathbf{r},t) = \sum_i m_i v_{i\alpha} \phi(\mathbf{r}-\mathbf{r}_i) \ , \tag{3.58}$$

$$\mathbf{V}(\mathbf{r},t) = \mathbf{p}(\mathbf{r},t)/\rho(\mathbf{r},t) \ . \tag{3.59}$$

Using a slightly different derivation than in [166], Goldenberg showed in [137, 150], that by reporting 3.58 in 3.51 one can express the coarse grained stress density as[15]

$$\begin{aligned} \sigma_{\alpha\beta}(\mathbf{r},t) = & - \sum_i m_i v'_{i\alpha}(\mathbf{r},t) v'_{i\beta}(\mathbf{r},t) \phi(\mathbf{r}-\mathbf{r}_i) \\ & - \frac{1}{2} \sum_{i,j} f_{ij\alpha}(t) \mathrm{R}_{ij\beta}(t) \int_0^1 ds \phi(\mathbf{r}-\mathbf{r}_i+s\mathbf{r}_{ij}) \ , \end{aligned} \tag{3.62}$$

where Goldenberg introduced the fluctuating velocity field of particle i,

$$\mathbf{v}'_i(\mathbf{r},t) = \mathbf{v}_i(t) - \mathbf{V}(\mathbf{r},t) \ . \tag{3.63}$$

Again as in 3.56 we recover the decomposition of the stress tensor in 'kinetic stress' and 'contact stress', but in the athermal limit which we are mainly interested in, the kinetic contribution vanishes. It is this expression of the stress tensor, rather than the earlier stress expressions derived in 3.3.2, that will be used in section 3.4.1 to characterize the local elastic properties of the Lennard-Jonesium.

[15] Similarly by inserting the coarse grained formulation of the energy density,

$$e(\mathbf{r},t) = \frac{1}{2} \sum_i m_i v_i^2 \phi(\mathbf{r}-\mathbf{r}_i) + \frac{1}{2} \sum_{i \neq j} \mathrm{V}(\mathrm{R}_{ij}) \phi(\mathbf{r}-\mathbf{r}_i) \ , \tag{3.60}$$

into 3.52, one can identify the coarse grained heat flux,

$$c_\beta(\mathbf{r},t) = \frac{1}{2} \sum_i v'_{i\beta} \left(m_i v_i'^2 + \mathrm{V}(\mathbf{R}_{ij}) \right) \phi(\mathbf{r}-\mathbf{r}_i) + \frac{1}{4} \sum_{ij} f_{ij\alpha} r_{ij\beta} \left(v'_{i\alpha} + v'_{j\alpha} \right) \int_0^1 ds \phi(\mathbf{r}-\mathbf{r}_i+s\mathbf{r}_{ij}) \ . \tag{3.61}$$

In a similar manner we derive the coarse grained version of the strain tensor. First by noting that the (Lagrangian) displacement field defined by $u(\mathbf{R},t) = r(\mathbf{R},t) - \mathbf{R}$ can be obtained by integration of the coarse grained velocity 3.59,

$$\mathbf{u}(\mathbf{R},t) = \int_0^t \mathbf{V}(\mathbf{R},t')dt' = \int_0^t \frac{\sum_i m_i \mathbf{v}_i(t')\phi\left[\mathbf{r}(\mathbf{R},t') - \mathbf{r}_i(t')\right]}{\sum_j m_j \phi\left[\mathbf{r}(\mathbf{R},t') - \mathbf{r}_j(t')\right]} dt' \ . \tag{3.64}$$

Goldenberg *et al* reexpressed the coarse grained displacement in two parts,

$$\begin{aligned} \mathbf{u}(\mathbf{R},t) \quad = \quad & \frac{\sum_i m_i \mathbf{u}_i(t)\phi\left[\mathbf{r} - \mathbf{r}_i(t)\right]}{\sum_j m_j \phi\left[\mathbf{r} - \mathbf{r}_j(t)\right]} + \\ & \int_0^t \frac{1}{\rho}\frac{\partial}{\partial r_\beta} \sum_i m_i v'_{i\beta}(\mathbf{r},t') u'_{i\alpha}(\mathbf{r},t')\phi\left[\mathbf{r} - \mathbf{r}_i(t')\right] dt' \ , \end{aligned} \tag{3.65}$$

where the first term in the right hand side $u^{lin}(\mathbf{r},t)$ is linear in strain while the second term is of second order in strain. So in the framework of linear elasticity we can define the linear strain field as,

$$\varepsilon^{lin}_{\alpha\beta}(\mathbf{r},t) = \frac{1}{2}\left[\frac{\partial u^{lin}_\alpha(\mathbf{r},t)}{\partial r_\beta} + \frac{\partial u^{lin}_\beta(\mathbf{r},t)}{\partial r_\alpha}\right] \ . \tag{3.66}$$

This expression of the linear strain was numerically computed by Goldenberg [150] in a simple linear chain of point masses with disorder introduced in both the Young's modulus of the spring connecting the particles and in the rest lengths of the springs. The linear strain was then compared with previous definitions of strain introduced in section 3.3.2 and to the exact numerical solution. It was found that while the best fit strain provides a poor approximation to the exact strain, the linear strain remains very close to the exact solution, making the linear strain a robust estimator local strains. Again it is expression 3.66 that will be used to derive the local elastic properties of our model Lennard-Jones glass. This will be the object of the next section, but before let us discuss briefly some limits of our approach and of some existing different routes to extend the applicability of continuum mechanics to small scales.

3.3.4 Alternative continuum formulations

In continuum mechanics the choice of the densities of the conserved entities for the description of matter is associated with the assumption that all information in a many-body system, except that pertaining to conserved entities, is averaged over in time and space. This assumption remains valid when there is a good scale separation between the 'microscopic' and the 'macroscopic' scales in the material considered and therefore breaks down when small systems or fine resolutions are considered. Therefore even the validity of the conservation equations 3.50, 3.51 and 3.52 becomes dubious when applied for small parts of the system. A trivial example that illustrates this idea is the case of two particles that interact under Newtonian gravitational law, while the total mechanical energy of the pair

is constant the mechanical energy of only one particle is not constant in time. In general when the macroscopic scale or the wavelength at which we analyse a problem is of the same order as the microscopic (in our case the interatomic distances) scale, the appropriate continuum description exhibits memory effects, i.e., it can be non-local in time and/or in space. Such nonlocal and history dependent descriptions, referred to as nonlocal (or gradient) continuum field theories, are not convenient to use as the behaviour at a material point is influenced by the state and history of all points of the body. Another approach to deal with such nonlocal continuum mechanics is to introduce new continuum fields in the problem. This type of approaches refered to as micropolar or Cosserat type models have been used for example to model the formation of shear bands of finite width in granular media. In the next section we leave aside these kind of approaches and pursue with the coarse-grained formalism valid in a local framework of continuum mechanics. We will propose arguments for the validity of this local treatment.

3.4 Local elasticity map in a model Lennard-Jones

3.4.1 Numerical procedure

Now having calculated in the previous section the stress 3.62 and strain 3.66 tensors locally we are in a position to derive the corresponding components of the local elastic tensor as in the case of a macroscopic deformation. Our approach presuposes that the definitions given of the global elastic constants remain valid at a local level. Indeed globally the elastic constants are defined as the coefficients $\mathrm{C}_{\alpha\beta\gamma\delta}$ of the second order expansion of the energy density as a function of the Green-Saint Venant strain components [167] $\varepsilon_{\alpha\beta}$,

$$\frac{\mathrm{F}-\mathrm{F}_o}{\mathrm{V}} = \mathrm{C}^o_{\alpha\beta\alpha\beta} + \frac{1}{2}\mathrm{C}_{\alpha\beta\gamma\delta}\varepsilon_{\alpha\beta}\varepsilon_{\gamma\delta} + \dots \,, \tag{3.67}$$

or as the first order expansion of the local stress components $\sigma_{\alpha\beta}$ as a function of the local linear strain [168]

$$\sigma_{\alpha\beta} = \mathrm{C}^o_{\alpha\beta} + \mathrm{C}'_{\alpha\beta\gamma\delta}\varepsilon^{lin}_{\gamma\delta} + \dots \,, \tag{3.68}$$

with

$$\sigma_{\alpha\beta} = \frac{1}{\mathrm{V}}\frac{\partial \mathrm{F}}{\partial \varepsilon^{lin}_{\alpha\beta}} \,. \tag{3.69}$$

In case of an unstressed solid, the two definitions are strictly equivalent, but in case of a solid with initial stresses ($\mathrm{C}^o \neq 0$ as in our Lennard-Jones glasses), the difference between the two components $\mathrm{C}_{\alpha\beta\gamma\delta}$ and $\mathrm{C}'_{\alpha\beta\gamma\delta}$ depends on the quenched stress components, due to the non-linear dependence of ε as a function of ε^{lin} [167]. More precisely one has the following correspondance between the two tensors,

$$\mathrm{C}'_{\alpha\beta\gamma\delta} = \mathrm{C}_{\alpha\beta\gamma\delta} - \frac{1}{2}\left(2\mathrm{C}^o_{\alpha\beta}\delta_{\gamma\delta} - \mathrm{C}^o_{\alpha\gamma}\delta_{\beta\delta} - \mathrm{C}^o_{\alpha\delta}\delta_{\beta\gamma} - \mathrm{C}^o_{\beta\delta}\delta_{\alpha\gamma} - \mathrm{C}^o_{\beta\gamma}\delta_{\alpha\delta}\right) \,. \tag{3.70}$$

In order to obtain the local elastic constants we assume that the global formulas 3.67, 3.68, 3.69 and 3.70 remain valid locally. Furthermore in our model glass system, we have checked that the contribution of the local quenched stresses can be neglected in the local version of equation 3.70 which simplifies to $C'_{\alpha\beta\gamma\delta} = C_{\alpha\beta\gamma\delta}$. One can therefore apply the same symmetry arguments as in the macroscopic case to reduce the number of independent coefficients of the elasticity tensor $C'_{\alpha\beta\gamma\delta}$. Since the linear strain is symmetric by definition, and the stress is symmetric in the absence of torques there are at most 9 constants in 2D. As discussed in [167, 168] the existence of a strain energy function from which the equations of elasticity can be derived by variational methods implies a further symmetry of the elastic tensor : $C_{\alpha\beta\gamma\delta} = C_{\gamma\delta\alpha\beta}$, reducing the number of independent thermodynamic constants to 6 in 2D. To extract the 6 independent elastic coefficients necessitates at least two independent deformation modes on our sample. Each deformation provides three linear equations for the moduli. The general stress-strain relation in terms of matrices is written as follows, using a Voigt type notation. For each coarse-graining scales W, the coarse-grained stress and strain components are measured on a grid, and are expressed respectively as the $3 * 1$ column vectors $\widehat{\mathrm{T}}$ and $\widehat{\mathrm{E}}$ and one has in 2D the relation $\widehat{\mathrm{T}} = \widehat{\mathbf{C}}\widehat{\mathrm{E}}$ that means:

$$\begin{pmatrix} \sigma_{xx} \\ \sigma_{yy} \\ \sqrt{2}\sigma_{xy} \end{pmatrix} = \begin{pmatrix} C_{xxxx} & C_{xxyy} & C_{xxxy} \\ C_{xxyy} & C_{yyyy} & C_{yyxy} \\ C_{xxxy} & C_{yyxy} & C_{xyxy} \end{pmatrix} \begin{pmatrix} \varepsilon_{xx} \\ \varepsilon_{yy} \\ \sqrt{2}\varepsilon_{xy} \end{pmatrix} \tag{3.71}$$

This expression can be compared with the expression obtained in the framework of homogeneous and isotropic linear elasticity:

$$\begin{pmatrix} \sigma_{xx} \\ \sigma_{yy} \\ \sqrt{2}\sigma_{xy} \end{pmatrix} = \begin{pmatrix} \lambda + 2\mu & \lambda & 0 \\ \lambda & \lambda + 2\mu & 0 \\ 0 & 0 & 2\mu \end{pmatrix} \begin{pmatrix} \varepsilon_{xx} \\ \varepsilon_{yy} \\ \sqrt{2}\varepsilon_{xy} \end{pmatrix} \tag{3.72}$$

where μ is the shear modulus and λ the Lamé coefficient ($(\lambda + \mu)$ is the inverse of the compressibility modulus in 2D).

The use of 2 such deformations therefore closes the system of unknowns, giving 6 equations for 6 unknowns. Nevertheless, in order to estimate the deviation from linear elasticity the numerical procedure used here consists in applying three different uniform deformation modes, two uniaxial deformations parallel to the x and y axis and a simple shear parallel to the x axis. This procedure provides 9 linear equations for the moduli. The stress components which are not used in this procedure are then calculated using these elastic moduli, and their values compared to those computed directly using equation 3.62. As a measure of the extent to which the system is described by linear elasticity at a given position and for a given value of the coarse-graining scale W we use the root mean square, Δ, of the relative differences between the stress components calculated by employing the measured moduli and the directly measured exact values (normalized by the norm of the exact values).

For each configuration we calculate also the 3 eigenvalues c_i and eigenvectors E_i for

$i = 1, 2, 3$ of the local tensor $\widehat{\mathrm{C}}$. The comparison between equations 3.71 and 3.72 would provide $c_1 = 2\mu$, $c_2 = 2\mu$ and $c_3 = 2(\lambda + \mu)$ in an homogeneous and isotropic system. We will now discuss the results obtained in our model Lennard-Jones glass, as a function of the coarse-graining scale W.

To summarize the numerical procedure goes as follows:

1. Apply the HFTN minimization algorithm to generate three macroscopic deformations, two uniaxial compressions parallel to the x and y axis and one simple shear parallel to the x axis.

2. Apply the code, with the appropriate boundary conditions for each macroscopic deformations, that calculates the local coarse grained fields either on a grid or on the particle positions.

3. Feed the three local strain and stress tensor fields corresponding to each macroscopic deformation to the code that solves the inversion problem 3.71 and provides the local elastic constants and the deviation from linear elasticity.

We have applied this numerical protocol to different samples of two dimensional model glasses. All of the samples studied were at the same density and polydispersity, different boundary conditions were tested, Lees-Edwards and fixed walls, as well as different system sizes, ranging from 625 particles up to 250000 particles always confined in square cells. In the next paragraph we discuss mainly the results obtained on the quenched glasses under the cooling protocol described in 2.6 and before any macroscopic strain is applied to the samples, i.e. in the initial pre-strained state, $\varepsilon_{macro} = 0\%$. We postpone the study of other effects on the local elasticity map of these glasses such as the effect of cooling rate, shear rate, total macroscopic strain, density, temperature to subsequent chapters of this thesis or to future publications.

3.4.2 Analysis of the local fields

The domain of validity of Hookes's law can now be measured by the W-dependence of the error function Δ. It is shown in figure 3.3. This figure shows that the error Δ goes progressively to zero, thus validating Hooke's law at large coarse-graining scales W. However, this convergence obeys a power-law $\Delta \propto \mathrm{W}^{-1.32}$ and therefore doesn't exhibit a characteristic scale above which Hooke's law would be true. Nevertheless, we can see in figure 3.3 that the error Δ is already less than 1% for $\mathrm{W} \geqslant 5$. It means that above $\mathrm{W} = 5$, the error made in computing the stress components using the elastic modulus is less than a hundredth of the actual value of the stress, that is far smaller than the contribution of quenched stresses for example. We can thus consider that the system obeys Hooke's law reasonably well on scales larger than $\mathrm{W} = 5$. Below that scale, different factors could explain the departure from Hooke's law: the first one is the coarse-graining. Below $\mathrm{W} = 5$ it has been shown in a

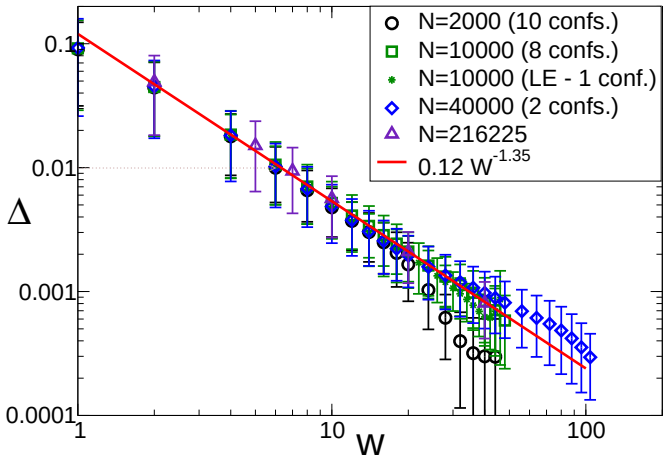

FIG. 3.3 : Deviation Δ from linear elasticity as a function of the coarse-graining parameter W. For $W \geqslant 5$ Hooke's law is satisfied locally with more than 1% accuracy.

previous paper [169] that the contribution of the coarse-graining deformation to the actual deformation is small. The contribution of the fluctuating field can not be neglected, giving rise to high values of the real strain and therefore a significant decrease of the elastic moduli. In fact, the fluctuating field is not differentiable, so that it is not possible in this case to compute quantitatively the linear strain components. It is one of the interests of the use of a coarse-graining field to deal with differentiable displacements fields. The fluctuating field appears thus as a 'noise field'. An additional strongly fluctuating term should then be taken into account for $W < 5$ in an attempt to describe accurately the mechanical behavior of the material. Another contribution to the departure from Hookes's law at small scale is due to the coupling to second and third neighbors outside the volume element. This contribution (not taken into account here since we are restricted to first order derivatives in the displacement field) could be introduced by considering the contribution of higher order derivatives of the deformation in the framework of linear but long-range elasticity [170]. This section is devoted to the measurement of elastic moduli, thus we will leave these considerations for further studies, and focus now on the computation of elastic moduli in the domain of validity, that is for $W > 5$.

Figure 3.4(a) shows the average value of each of the eigenvalues $< \overline{c_i} >$ of $\widehat{C}$ as a function of the coarse-graining scale W. The notation $\overline{c}$ stands for a spatial averaging over the sample and angular brackets stand for a statistical averaging over different configurations. The spatial averaging is obtained by computing the elastic moduli on a grid with elements of width W/2. The number of the different samples used in the statistical averaging - for each given size L - is the same as indicated in the figure 3.3. We get first the average

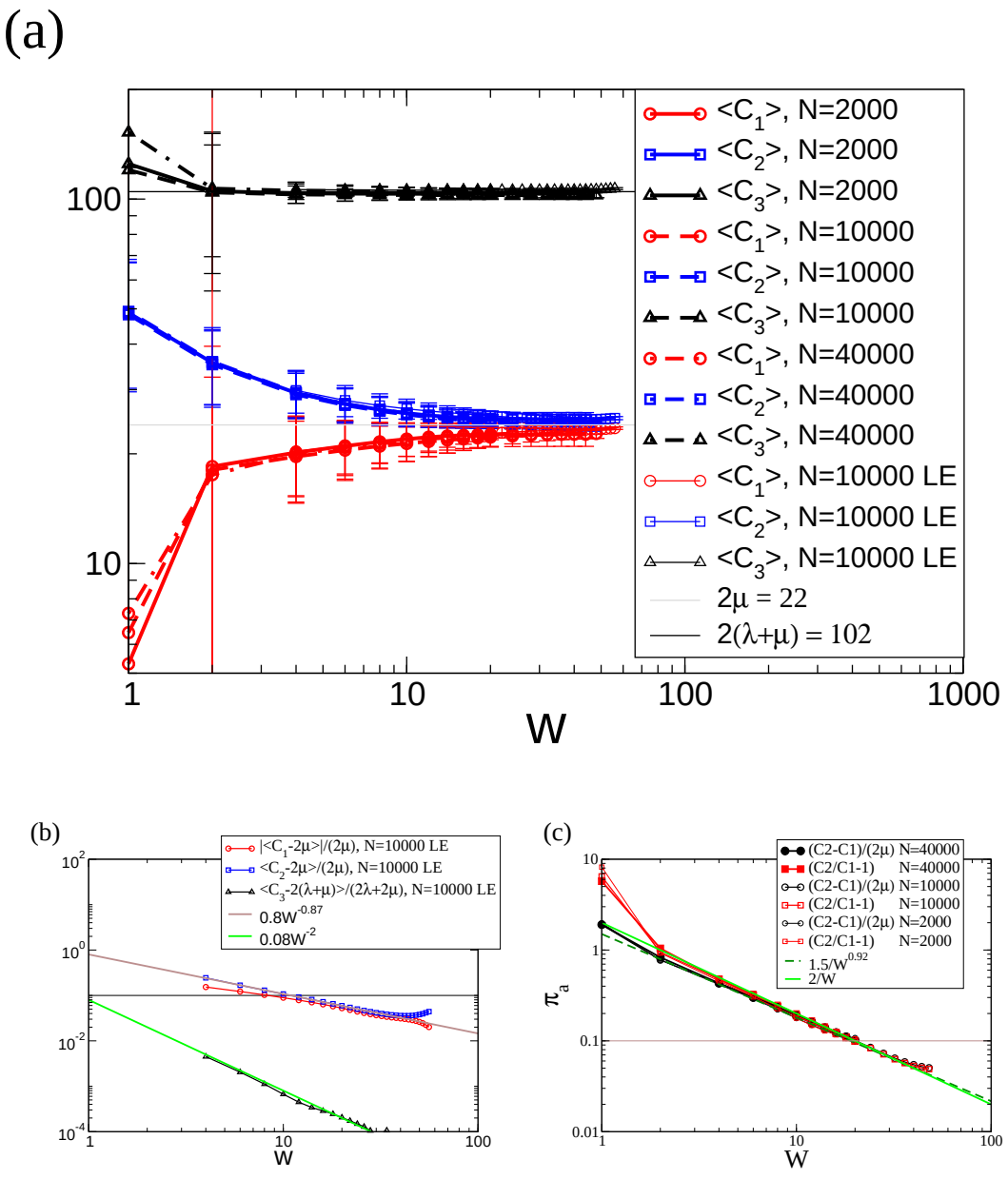

Fig. 3.4 : (a) The three eigenvalues of the elasticity tensor averaged spatially as a function of the coarse-grain length W. (b) log-log plot of the convergence of the three eigenvalues to the limit values obtained by a coarse graining on the whole system size. (c) Anisotropy parameter π_a as a function of the coarse-graining scale W.

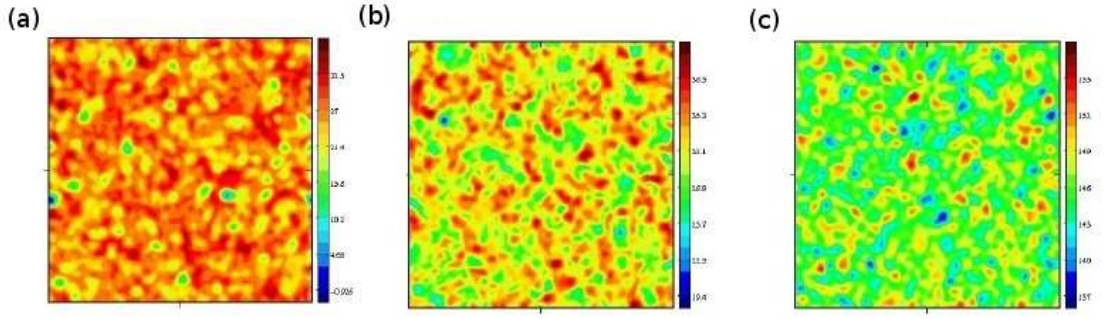

FIG. 3.5 : The three eigenvalues of the elasticity tensor for a coarse-graining length W = 10 on a square sample of size 500 × 500 containing 226225 particles, (a) C1, (b) C2, (c) C3.

value of the $(L/(W/2))^2$ values obtained on the grid, for each sample. Then we average the values obtained on the different samples. The figure 3.4(a) shows a progressive convergence for large W to the values obtained in the framework of homogeneous and isotropic linear elasticity. Indeed, for very large W, $< \overline{c_1} >$ and $< \overline{c_2} >$ go to the same value $2\mu \approx 22$ obtained also by looking at the macroscopic response of the system to various mechanical sollicitations, and $< \overline{c_3} >$ converges to twice the inverse compressibility $2(\lambda + \mu) \approx 102$ measured as well by the global response of the sample [114, 115]. The method used here to compute the elastic moduli of the system for large W appears thus to be consistent with measurements of the global response of the system.

The convergence of the average local elastic moduli to their macroscopic value is independent of the system lateral size L as long as W < 0.5L. For larger W, the boundary conditions (Lees Edwards or fixed walls) may affect the convergence and cause finite size effects. As shown in figure 3.4(b), the moduli decay approximately as $1/W^{\alpha}$ to their limit value, with $\alpha \approx 0.87$ for c_1 and c_2, and $\alpha \approx 2$ for c_3. The inverse compressibility converges thus far more quickly to its macroscopic value, than the shear moduli. The difference between the macroscopic value and the spatial average of the small scale measurements of c_i ($2\mu \approx 22$ while $< \overline{c_1}(W = 5) > \approx 18$ for example) is due to the inhomogeneous strain field. By looking at $(< C > -C_{\infty})/C_{\infty}$ (figure 3.4(b)), it appears that for W > 5, the discrepancy to the macroscopic value is already less than 1% for $< c_3 >$, while it becomes less than 10% only for W > 10, for $< c_1 >$ and $< c_2 >$. We conclude that for 5 < W < 10 the moduli are well defined, but the measured values are not compatible with homogeneous elasticity since the different moduli involved at different coarse-graining scales have different scale dependence. We did not find any solid explanation for the non-trivial power-law appearing in this convergence. It appears that the convergence of the inverse compressibility is inversely proportional to the volume W^2, and the convergence of the shear moduli closer to a surface effect $\propto W$. As a side note we speculate that in 3D samples these power law convergences should be respectively inversely proportional to $\propto W^3$ and $\propto W^2$ - i.e.

volume and surface effects. Note also that one of the shear moduli is smaller than the limiting value, while the other is larger. This difference between smooth and hard directions will now allow us to quantify the anisotropy of the local mechanical response.

The anisotropy measured at small scale can be quantified by the ratio $(< \overline{c_2} > - < \overline{c_1} >)/(2\mu)$ that goes to zero for large W. We call it the anisotropy parameter π_a. It is shown in figure 3.4(c). It can be noticed that c_1 and c_2 always obey $< \overline{c_1} > \leqslant 2\mu$ and $< \overline{c_2} > \geqslant 2\mu$, so $\pi_a \geqslant 0$. The decay of the anisotropy parameter π_a (figure 3.4(c)) obeys also a power-law $\propto 1/\mathrm{W}^{0.92}$, close to $1/\mathrm{W}$. These power-law decays prevent us to define properly a characteristic scale above which the homogeneous and isotropic behaviour is recovered. In figure 3.4(c), we see that the anisotropy parameter becomes less than 10% for $\mathrm{W} > 20$ only. It means that, below $\mathrm{W} = 20$, it is possible to find locally a well defined direction associated with a very low local shear modulus. At this scale, the anisotropy in the mechanical response cannot be neglected.

The preferred direction of strain is given locally by the analysis of the eigenvectors E_1, E_2 and E_3. Each eigenvector contains the 3 distinct elements of a 2D strain tensor whose eigendirections $\mathbf{e}_1$ and $\mathbf{e}_2$ ($\mathbf{e}_1$ and $\mathbf{e}_2$ are orthogonal) are computed. We plot on figure 3.6 the distribution of the local quantity $\mathrm{S}_i = (tr(\mathrm{E}_i))^2 / 2tr(\mathrm{E}_i^2)$, that takes the value 0 if the deformation is pure shear and 1 for pure dilatation. One observes as expected that the two deformations associated with the two lowest eigenvalues are of pure shear type while the third deformation is a pure compression.

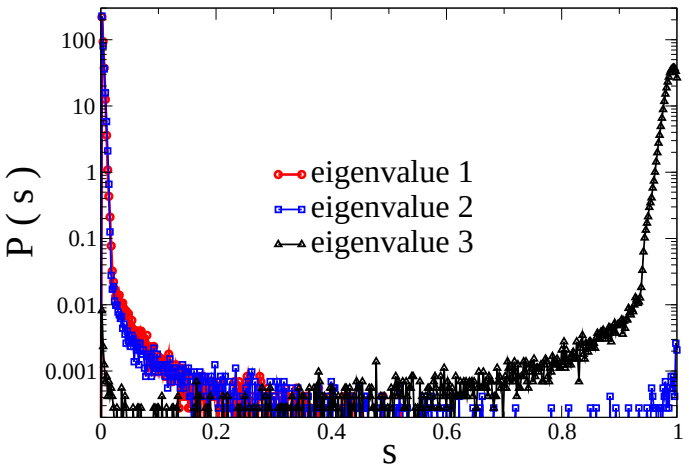

Fig. 3.6 : Distribution for each eigenvalue E_i of the local elasticity tensor of the quantity $\mathrm{S}_i = (tr(\mathrm{E}_i))^2 / 2tr(\mathrm{E}_i^2)$. The distribution is obtained over the entire plastic flow regime.

In order to explore more deeply the inhomogeneities of the elastic moduli inside the system, we will now study their distribution as a function of W, and then their spatial

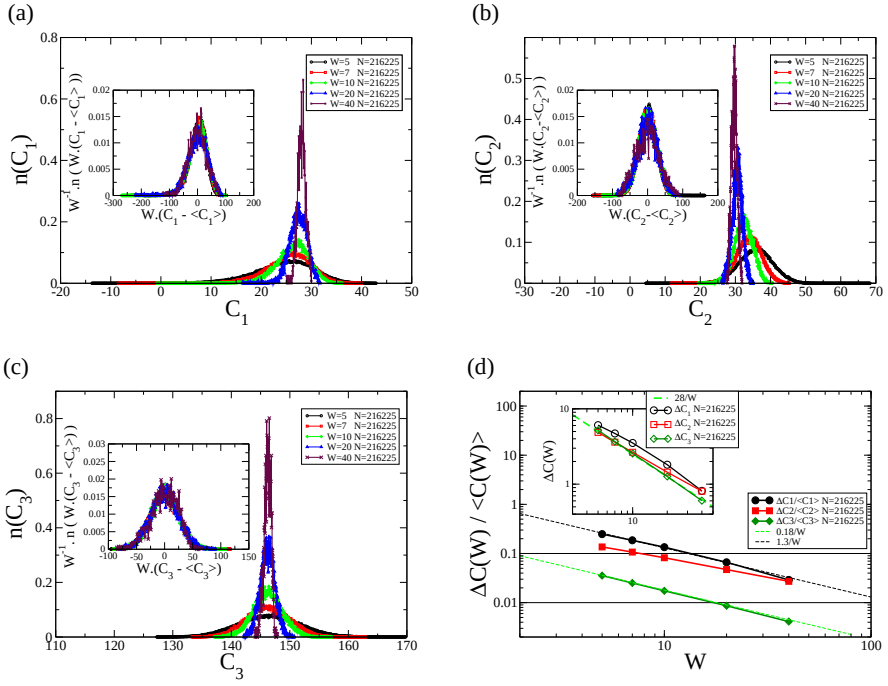

FIG. 3.7 : The figures (a), (b) and (c) show, respectively, the distributions of the three lowest eigenvalues c_1, c_2 and c_3 for different coarse-graining lengths W. The inset of each figure show the distributions rescaled by W. Figure (d) shows that the distributions get narrower as W increases to converge to the macroscopic values of the elastic constants. The variances of the distributions is plotted as a function of W. The variances normalized by the average values of the distributions are also plotted. Both curves show a power law evolution with W.

correlations. The distributions of c_1, c_2 and c_3 are shown in figure 3.7 for various W and for N = 216225. First, we can see in these distributions, that zones with negative moduli can appear if the coarse-graining scale W is sufficiently small, as already observed in [156]. It is not in contradiction with the mechanical stability of our system, since the local elastic moduli computed here are only part of the second order derivative of the total mechanical energy, due to the coarse-graining, as well as to the non trivial dependence of the non-affine local deformation as a function of the applied displacement. The rescaling of the distributions by W is also shown in the figures 3.7. It is very good for sufficiently large values of W (typically W > 10). The variance of the distribution as a function of W is shown in the inset of figure 3.7(d). It decays as 1/W and is always smaller than the corresponding average value. It is thus impossible to identify a characteristic lengthscale by the comparison of the variance and the average value of the moduli c_i.

The decay of the relative fluctuations $\Delta c / < \bar{c} > \propto 1/\mathrm{W}$ for a given W can be interpreted in the framework of a sum of uncorrelated variables with finite variance, the distribution being nearly gaussian. The apparent rescaling of the distribution thus corresponds to a sum of spatially uncorrelated variables. Note that, while this ratio is very small for c_3 for every value of W ($\Delta c_3/c_3 < 0.01$ for $\mathrm{W} \geqslant 5$), it is much larger for c_1 ($\Delta c_1/c_1 > 10\%$ while $\mathrm{W} \leqslant 15$ for N = 216225). We can thus conclude that the inhomogeneity is far more pronounced in the shear modulus c_1 than in the compressibility c_3. The inhomogeneity of c_1-modulus is even far from been negligible while $\mathrm{W} \leqslant 15$.

By comparing this result with the result obtained for the isotropy, we can conclude that at a scale W > 20 the system becomes reasonably isotropic and homogeneous. Below this scale, it is homogeneous but not yet isotropic for 15 < W < 20. All these results are summarized in Table 3.1. Of course, these values must be nuanced by the fact that the criteria used are a little arbitrary and simply related with a comparison of orders of magnitude. No characteristic lengthscale can be clearly identified since all the quantities checked here have a power-law dependence with the scaling length W.

The distribution of the elastic moduli has been checked along the full deformation process. We can thus compare the distribution of moduli during elastic deformation and during plastic flow. We can also compare these distributions before and after a plastic rearrangement occurred in the system. The plastic rearrangements are identified here as in [5, 6] by the decrease of the total stress as a function of the applied strain. We see in figure 3.8 that the distribution is progressively displaced to smaller values of the shear modulus, before it reaches a plastic plateau, but remains globally unchanged during all the plastic flow. During the plastic flow, the difference between the distributions appears on extremal values. Before a plastic rearrangement occurs, the smallest value of c_1 (open circle in figure 3.8) is generally smaller than after the event occurred (full circle). The distribution of the smallest value of this elastic modulus is shown in the inset of figure 3.8

W	0	5	10	15	20
Hooke's law	NO	YES	YES	YES	YES
Homogeneity					
$\frac{\langle\bar{c}\rangle-2\mu}{2\mu}<10\%$	NO	NO	YES	YES	YES
$\frac{\Delta c}{\langle\bar{c}\rangle}<10\%$	NO	NO	NO	YES	YES
Isotropy					
$\frac{c_2-c_1}{2\mu}<10\%$	NO	NO	NO	NO	YES

Table 3.1: Analysis at different coarse-graining length scales W.

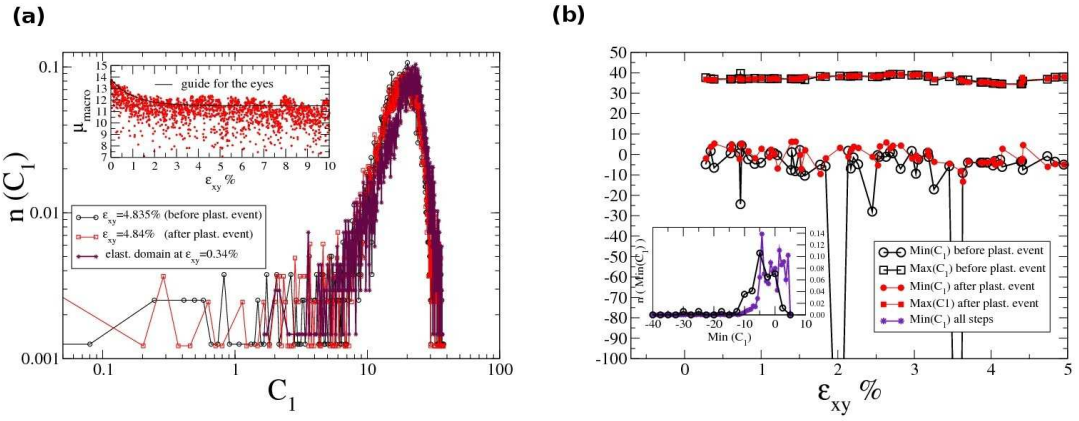

Fig. 3.8 : (a) Distributions of the local shear modulus c_1 averaged over the elastic regime and for two configurations in the plastic regime, just before and just after a rearrangement. **Inset**: Evolution with the macroscopic strain of the instantaneous macroscopic shear modulus defined as $\Delta\sigma_{xy,macro} = \mu_{macro}\Delta\varepsilon_{xy,macro}$. (b) Evolution with the strain of the maximal and minimal values of c_1. **Inset**: Distribution of the maximal and minimal values of the local elastic modulus c_1 over the entire plastic regime for all configurations, and for configurations just before the occurence of a plastic event.

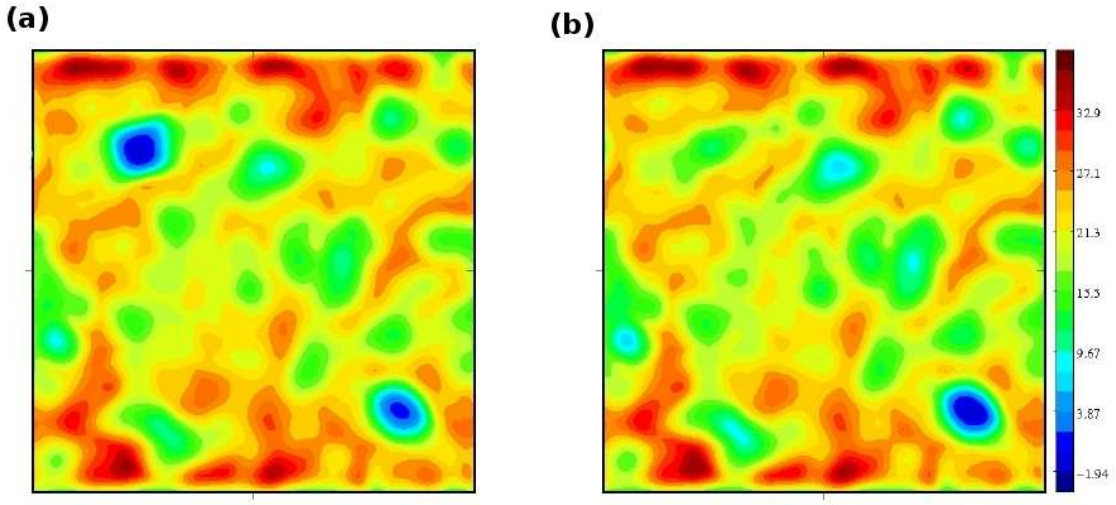

FIG. 3.9 : Map of the local shear modulus for a coarse-grained length W = 5 in the linear portion of the stress-strain mechanical response of the glass. (a) $\varepsilon_{xy} = 0.27108\%$ just before a plastic event and (b) $\varepsilon_{xy} = 0.2761\%$ just after the plastic event.

for the full deformation process. It confirms that the smallest values are smaller before a plastic rearrangement than after[16]. We will come back to this observation in section 4.2.4.

Finally, it can be interesting to analyse in details the spatial correlations of the moduli in our systems. The spatial correlations of the lowest modulus c_1 are shown in figure 3.10 for various W and N = 216225. The spatial correlations go to zero at large distances. It shows spatial oscillations with very small amplitude, that are visible while W $<$ 10, but that disappear for W $\geqslant$ 10. The distance between successive maxima is about a few tens interatomic distances, but seems to be size-dependent. Unfortunately, our data are not sufficiently precise to allow us to characterize this size-dependence. For $r < 3$W only, the spatial correlations are controlled by the W-dependence of the coarse-graining function (see figure 3.10(b)). It can be fitted by a gaussian $\propto \exp(-(r/\mathrm{W})^2/1.7)$. We can thus conclude that the spatial correlations are dominated by the W-dependence of the coarse-graining function at small distances, but displays oscillations at larger scales. The domain for which these oscillations are visible (W $<$ 10) corresponds to the domain in which the heterogeneity in the distribution of the moduli is noticeable. All these results show that a coarse-graining at scales W $>>$ 10 will loose informations (on the heterogeneities, on the spatial correlations, even on the local anisotropy.). In the rest of this thesis we will thus use only the value W = 5 for the coarse-graining scale.

[16] This observation is also confirmed by a plot of the local elastic constant before and after a plastic event as shown in figure 3.9.

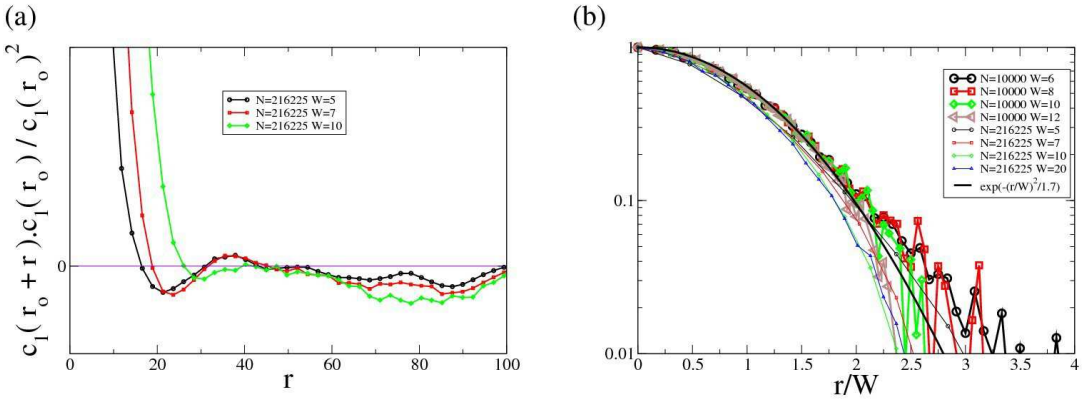

FIG. 3.10 : (a) Spatial correlation function of the local shear modulus c_1: $\langle(c_1(0)-\overline{c_1})(c_1(r)-\overline{c_1})\rangle$. (b) Scaling of the function with the coarse-graining length W for small values of r.

Chapter 4

Link between structure and dynamics

Contents

In the previous chapter we presented a method that extends the domain of applicability of continuum mechanics and linear elasticity down to a length of about five interatomic distances. With this method we introduced microscopically derived expressions of the various fields of continuum mechanics and we discussed in detail on a method to calculate a coarse-grained local elasticity tensor. In this chapter we take the lowest eigenvalue c_1 of this local elastic tensor, i.e. an effective local shear modulus, as the relevant local coarse-grained order parameter to relate the structural disorder of the glass to its observed heterogeneous mechanical response. We will show that in contrast to other local structural indicators previously analysed the local shear modulus presents an important degree of correlation with the heterogeneous dynamics in the sheared glasses. Moreover the use of the coarse-grained technique introduced in the previous chapter will anable us to estimate the length scale at which this correlation is maximal.

Our approach is reminiscent of similar studies attempting to relate structure and dynamics in static supercooled liquids. As illustrated[1] in various numerical [172, 16, 173, 174, 175, 176, 177] and experimental studies (for excellent reviews on models and experiments

[1] Here we refer to the review made by Berthier in the introduction of [171]

we refer the reader to [178]), over (essentially) the last two decades, supercooled liquids near the glass transition show peculiar dynamical features that have been associated to spatially heterogeneous dynamical relaxation. Yet, their structure, as measured by two-point correlation functions, appears homogeneous and unspectacular. There are various theoretical pictures that try to incorporate connections between static and dynamic properties and it is tempting (and maybe fruitful) to try and test some of the ideas developed in the framework of supercooled liquids to achieve a better understanding of the structure/dynamics relation in the related problem of driven glasses. Let us mention some of these approaches. In a picture based on dynamical facilitation [179, 180] one postulates the existence of mobile and immobile regions, with the implicit assumption that these regions have a structural origin. Frustration-based theories [181] infer dynamical behavior by assuming the existence of domains with a preferred local order. Alternatively, one can attempt to connect static and dynamical properties through the configurational entropy [182, 183] through two-point density correlations [184], through elastic properties [185, 186], or through the idea of a rough energy landscape [187, 188].

4.1 Previous attempts. Literature review

It is an almost impossible task to try and summarize the ensemble of references that are dealing with the question of a structural signature of the dynamics of glassy materials. In fact what arouses the curiosity is the apparent paradox with glassy materials that can be formulated as follows, how can a system with the apparent structure of a liquid behave so differently than the liquid ? It is to answer this crucial question that so many papers have been devoted to try and extract some hidden structural order parameter in glassy materials. Here we present some (the list is by no means exhaustive) of these local order parameters that have been considered in glasses. Most of the discussion below concerns results obtained through the extensive use of numerical simulations, as experimentally it remains difficult to measure local quantities and even more to correlate local structural and local dynamical information.

4.1.1 Geometrical local order parameters

Local volume. One of the simplest ideas originally proposed (see [189] for a review) is that, for a particle or a cluster of particles to rearrange, a certain amount of free volume is needed (see figure 4.1). In liquids or supercooled liquids thermal fluctuations are at the origin of such a local density decrease. More precisely [189], suppose that the region of rearranging molecules is approximately spherical and that the radius must increase by Δr before a flow event has a fair chance of taking place. Then, by assuming that the surrounding material behaves (on the time scale of a rearrangement) as an isotropic elastic

medium, with elastic constants G_∞ and K_∞, one can calculate the reversible work W necessary to create the required local expansion. The radial displacement of the surrounding material being of pure shear type the work is independent of the bulk modulus K_∞ and one finds $W \propto G_\infty V_c$, where the constant of proportionality is a characteristic volume. This type of reasoning is at the heart of the elastic models and was originally proposed to explain the non-Arrhenius temperature dependence of viscosity in supercooled liquids, $\eta = \eta_0 \left[\frac{\Delta F(T)}{k_B T}\right]$. Nevertheless there is no proof that the rearrangements occurring in glassy materials necessarily go through a dilated transition state. Moreover the assumption of compact spherical rearranging topologies is not guaranteed, and more complex shapes (including fractal) could be envisaged, for example in supercooled liquids rearrangements have been shown to occur in the form of cooperative string like structures [16]. Note that as we will see in figure 4.18 in the sheared polydisperse Lennard-Jones glass analyzed in this thesis the local volume before, during and after a plastic rearrangement doesn't display any change, contrasting with the above arguments.

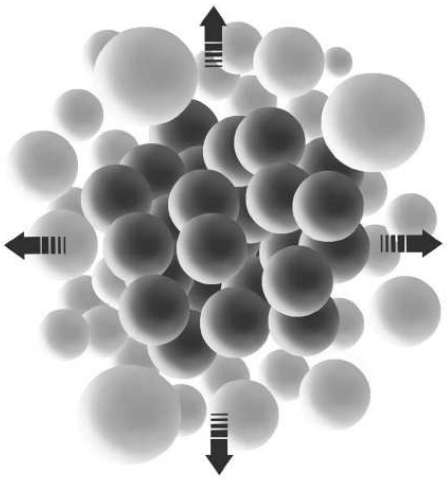

Fig. 4.1 : A molecular rearrangement with the dark spheres showing molecules before the flow event. A flow event takes place if the region volume briefly expands sufficiently due to a thermal fluctuation. According to statistical mechanics the probability of this happening is the reversible work done on the surrounding fixed structure to bring about the same expansion [189].

First neighbors and Voronoi tessellation. In the previous paragraph we assumed that the local density was given by the average number of particle centers within a certain volume. Usually in order to associate a local volume to each particles one makes use of the Voronoi tessellation. The Voronoi cell associated to an atom i being the set of all points closer to i than to any other atom j of the sample. In addition to the volume or surface that can be associated to each particle with this tessellation, one can also count the number of direct neighbors by counting the number of faces or edges of the individual cells. Within this formalism it becomes possible to identify defects (less neighbors than average) and to

try to correlate this local structural information with the dynamics in the studied material. Recently this formalism was applied to characterize the dynamics of aging or driven model binary Lennard-Jones glasses [190, 191] and of amorphous silicon [101, 8]. In model binary glasses the density of such defects allowed Procaccia to extract a growing length scale at the approach of the glass transition temperature associated with the disappearance of liquid like defects (defined by the authors as the cells where a small particle is surrounded by seven particles or a large particle by five particles). The classification of the different types of local environments also allowed the authors to derive a 'statistical description' of the thermal properties of the bidisperse glass in terms of these elementary units [192]. Yet no direct link was observed between such structural defects and the location of plastic rearrangements in the binary Lennard-Jones glass. Figure 4.1 illustrates a similar finding by superimposing the plastic irreversible displacement field during a single plastic event in our quasistatically sheared polydisperse glass with a map of the voronoi defects just prior to the rearrangement. The situation seems different in a model amorphous silicon glass (in contrast to simple Lennard-Jones glasses a-Si is a directionally bonded material where the diamond-like tetrahedral structure is favored) where some degree of correlation between the coordination defects and localization of plastic events has been observed [8]. Interestingly in a-Si a structural signature of plastic rearrangements in the material can be found also at highest order neighbors.

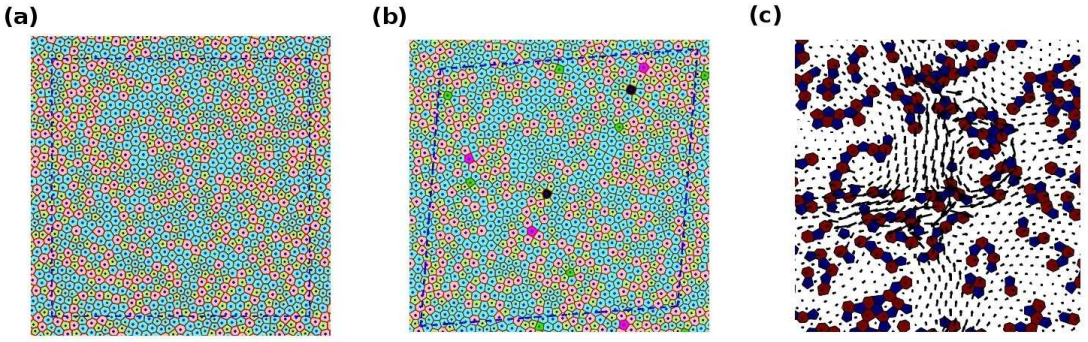

Fig. 4.2 : (a) The Voronoi polygon construction in the glassy state at T = 0.1 with the following colorcode. Small particles in pentagons (heptagons) are light green (dark green) and large particles in pentagons (heptagons) are violet (pink). Note the total absence of liquid-like defects. (b) A strained configuration after the linear elastic response is lost, $\delta = 3 \times 10^3$. Note the reappearance of liquid-like defects with the shear [190].(c) Displacement field during a single plastic event superimposed with voronoi defects. In brown (heptagons) and in blue (pentagons). No apparent connection between the location of the rearrangement and the voronoi defects

Second neighbors and preferred geometries. The mechanical response of a-Si has been recently extensively studied and represents similar features as what is observed in Lennard-Jones systems, namely the occurrence of localized plastic events that through an

auto-catalytic process form micro shear bands. Yet, in contrast with Lennard-Jones glasses, the favored tetrahedral nature of the silicon crystal is also present at a local level in a-Si and to describe the local structure of a-Si it is necessary in addition to nearest-neighbor distances to also provide additional information such as the nearest neighbor bond angles. Figure 4.3 shows the two typical silicon atoms arrangement along with the corresponding radial distribution function (RDF). Demkowicz and Argon [101] argued that transitions between these two states occur during plastic events and by comparing the RDF of the atoms in the region where plastic deformation occurs with the bulk RDF they show that an 'instability-producing bond' is created in the transitional state (figure 4.3 (b)). In their study they also show that the atoms can be classified, according to their average nearest neighbor bond angles μ (figure 4.3 (c)), as liquid-like or solid-like.

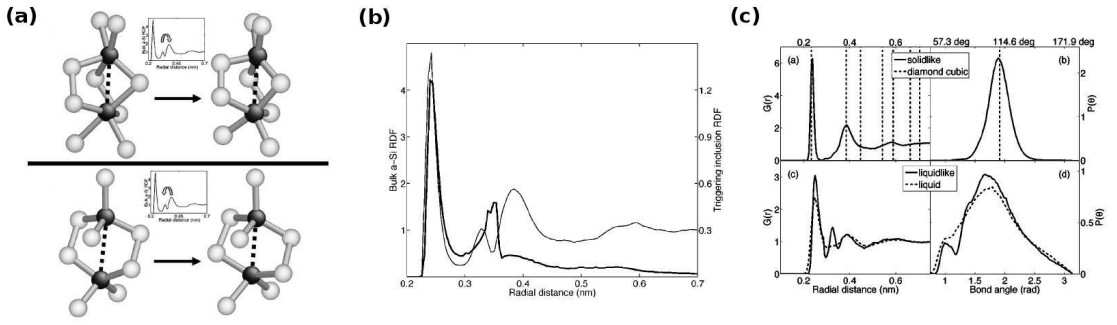

Fig. 4.3 : (a) Atomic configuration changes associated with nearest neighborhoods of bonds that undergo a transition across the IPB length are shown. Dark atoms correspond to endpoints of bonds that undergo this transition. On the top, the bond undergoing the transition elongates beyond the IPB length while on the bottom figure it contracts below the IPB length. (b) The radial distribution function (RDF) compiled from interatomic distances among atoms comprising triggering clusters (thick line) is compared to a typical RDF for bulk a-Si in a state of steady flow (thin line). (c) Comparison of the RDF and angle distribution function (ADF) of the two distinct atomic environments of a-Si with the RDF and ADF of diamond cubic c-Si and molten Si allow these environments to be identified as 'solid-like' and 'liquid-like' [101].

In two dimensional monodisperse Lennard-Jones systems the local crystalline preferred structure is the hexagonal structure where each atom is surrounded by six nearest neighbors. As for a-Si one can try and track locally the preferred structure with the help of the hexatic order parameter [193] that projects neighbors of each particle on the spherical harmonics and that takes the value 1 if perfectly crystalline and 0 if perfectly disordered. Such analysis have been preformed recently on monodisperse, bidisperse and polydisperse Lennard-Jones systems. In the case of monodisperse glasses [194, 195] this local order analysis allowed the authors to quantitatively discuss the phenomenon of shear induced crystallization with the nucleation of crystallites or 'solid-like clusters' as depicted on figure 4.4. The largest cluster size in the sample grows with shear, as shown in figure 4.4, to reach a limiting value of about 170 solid like particles, and the dynamics is subsequently

dominated by the adjustment of these created clusters to the global shear. Hamanaka and Onuki [196] used the same local order parameter to characterize the heterogeneous dynamics of binary mixtures for different size dispersities and compositions. As expected the displacements were shown to concentrate in the grain boundaries of the polycrystal (figure 4.4), this behavior is enhanced for low polydispersity and/or low concentration of large particles, in other words as the system becomes more monodisperse. Finally a similar analysis was applied by Kawasaki *et al.* [197] to the case of polydisperse glass formers in their supercooled state. By time averaging the hexatic local order parameter over the relaxation time of the glass τ_α they find that one can still observe clusters of high order that they coin 'medium-range crystalline order' (MRC0) (figure 4.4) and that these ordered regions of particles are less mobile than less ordered regions, suggesting that MRCO may be the origin of dynamic heterogeneity in a supercooled liquid. The two examples presented above, a-Si and Lennard-Jones glasses, illustrate that depending on the system under study the favored geometrical topologies vary. Of course these local topologies are selected on energetic grounds.

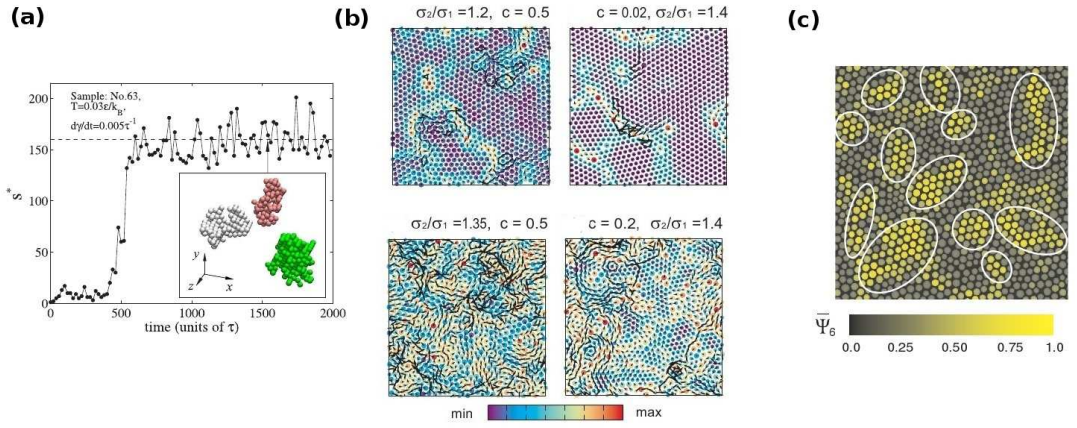

Fig. 4.4 : (a) Main: size of the largest cluster versus time in a sheared monodisperse Lennard-Jones glass. Broken line corresponds to the value 160. The study sample is still the same as for the previous figures. Inset: Three largest clusters at the moment indicated by arrow. The sizes of the clusters are N1 = 177, N2 = 130 and N3 = 126 particles. [195] (b) Disorder variable D (opposite of hexatic order parameter) at $T = 0.2\varepsilon/k_B$ and $\phi = 0.9$ for a bidisperse Lennard-Jones glass. The arrows represent the particle displacement over a time of the order of the relaxation time of the different glasses τ_α [196]. (c) Snapshot of a polydisperse colloidal system of $\phi = 0.631$ for polysidpersity $\Delta = 9\%$ [197].

4.1.2 Mechanical local order parameters

Global yield stress criteria. To understand when a complex fluid or solid glassy material will yield necessitates in theory a detailed understanding of the microstructure of

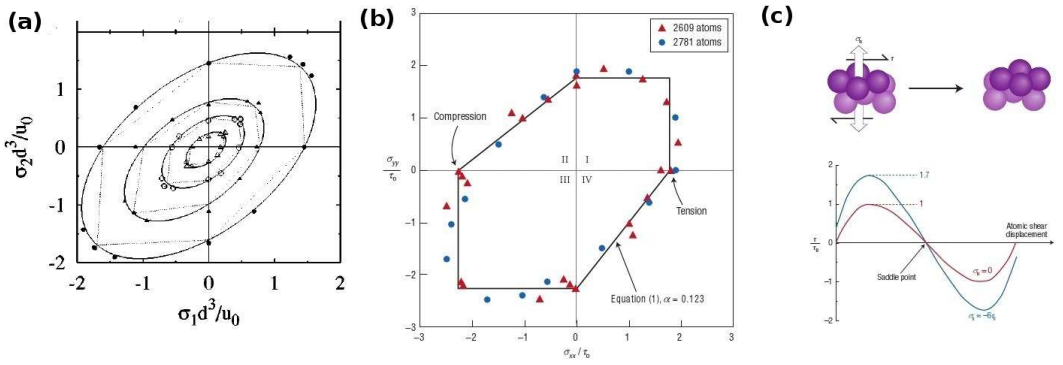

Fig. 4.5 : (a) Yield points for biaxial stress states obtained on a model polymer system [198]. The ellipses represent the pressure modified Von-Mises yield surface and the dashed lines show the pressure modified Tresca yield surface. (b) Yield surface of a model metallic glass. Normalized principle stresses σ_{xx} and σ_{yy} at yield ($\sigma_{zz} = 0$) extracted from computational multiaxial mechanical tests. Data for two different amorphous structures are shown, composed of 2609 and 2781 atoms, respectively. The solid line is the Mohr-Coulomb yield criterion, plotted with the value of $\alpha = 0.123$ obtained from the elementary shear transformation zone analysis of figure (c). (c) On the top figure is represented a representation of the elementary three dimensional shear transformation zone used in [199]. The four upper (darker) atoms move as a unit with respect to the five lower atoms, and a trajectory with constant normal-stress σ_n is determined in the shear direction. In the bottom figure the applied shear stress τ necessary to maintain a given atomic shear displacement, normalized by the maximum value of τ at $\sigma_n = 0, \tau_0$. The beginning and end of the curve correspond to the starting and ending structures seen in the top figure. The maximum value of τ necessary to complete the shear displacement of the top figure increases with an applied compressive stress.

a material and of the mechanisms available to the microstructure to deform and absorb energy. In practice, ignoring the microstructural deformation mechanisms, macroscopic continuum phenomenological yield criteria have been devised to predict yielding behavior in materials. Naturally the stress tensor (along with the strain tensor) that appears in any mechanical experiment (figure 4.5) is used in the existing yield criteria. Note that the definition of a unique yield criterion does not appear straightforward and many possible choices are usually considered, departure from linear mechanical response, maximum of the stress-strain response or stationary plateau value of the macroscopic stress. Experimentally moreover it appears difficult to extract 'the' yield stress for a given material and different experimental protocols give often different results. Nevertheless several criteria based on the stress tensor have produced robust results and over the past three centuries, a number of yield criteria have been formulated that predict whether a combination of stresses on a solid will produce irreversible deformation[2]. The yield criteria are expressed in terms either of the principal stresses or in terms of the stress (or deviatoric stress) invariants (for a review see [200]). As the global yield criteria have also been tested at a local level we present here briefly their definition. The Tresca criterion assumes that yield will occur when the maximum shear stress $\tau_{\mathrm{T}} = \frac{1}{2}\left|\sigma_i - \sigma_j\right|_{max}$ (here σ_i are the principal stresses) is equal to some yield stress, while in the Von-Mises definition yield is related to the octahedral or deviatoric stress $\tau_{\mathrm{VM}} = \frac{1}{3}\left[(\sigma_1-\sigma_2)^2 + (\sigma_2-\sigma_3)^2 + (\sigma_3-\sigma_1)^2\right]^{1/2}$. In these two criteria the yield is assumed to be pressure independent which is rather well verified for different metals. In contrast in polymers glasses [198] and metallic glasses [199] pressure modified versions of these criteria also referred to as Mohr-Coulomb criteria are more suitable. Hence while in the original Von-Mises criterion $\tau^y_{\mathrm{VM}} = \tau_0$, the pressure modified version includes a linear pressure dependence in the value of the octahedral shear stress $\tau^y_{\mathrm{VM}} = \tau_0 + \alpha p$. Similarly the pressure modified Tresca criterion reads $\tau^y_{\mathrm{T}} = \frac{3}{\sqrt{2}}(\tau_0 + \alpha p)$. This pressure modifications are motivated by an analogy to friction, where the shear stress is linearly related to normal pressure, rather than to an energy argument like that used to motivate the original Von-Mises criterion.

Looking for local stress criteria. These type of global yield criteria have been extrapolated to hold at the local level in different phenomenological theories of the rheology of glassy materials (see section 1.4.2) but also in different numerical studies [201, 202, 203, 67] to relate local rearrangements with a local version of the above stress criteria. In [6][3] we have attempted to address the question of the existence of such local plasticity criterion in the polydisperse Lennard-Jones system of this thesis. In this work, in order to relate the position of the center of the plastic rearrangements to local stress criteria, we have compared the distribution of the stress components obtained for the whole system, and the value of the same stress component on the particle in the center of the plastic event, one

[2] The stress based criteria can be re-expressed in terms of the strain tensor with the use of the constitutive relation of the materials relating the stress and strain tensors.

[3] Here we reproduce almost exactly the section 5 of this paper.

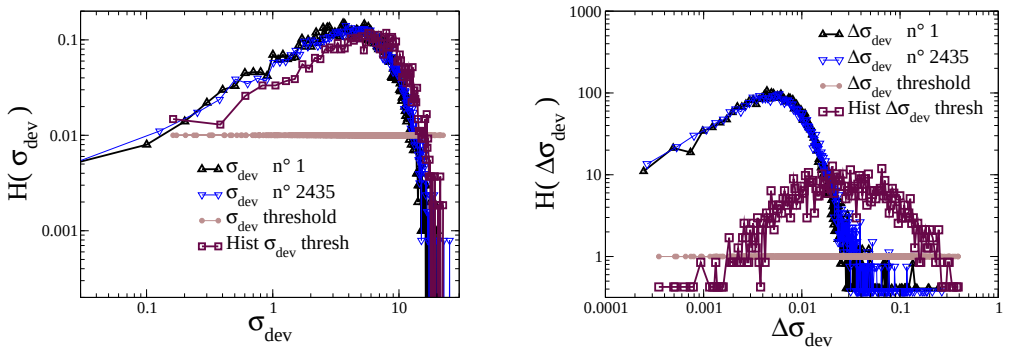

FIG. 4.6 : (a) Distribution of the deviatoric stress in a configuration of 10 000 particles for 2 different strains in the beginning and in the end of the plastic flow plateau (triangles). Comparison with the distribution of the deviatoric stress in the center of the future quadrupole just before the quadrupolar event takes place (squares), computed on the 2500 plastic events of the plastic flow regime. The 3 curves are very similar. (b) Same as in (a), but for the *incremental* deviatoric stress. In this case, the distribution obtained on the center of the quadrupoles indicates a more pronounced correspondence with the highest incremental stresses inside the sample.

step before it takes place. The result for the deviatoric stress $\sigma_{dev} \equiv \sigma_1 - \sigma_2$ is shown in figure 4.6(a). The distribution of the deviatoric stress in the whole sample is stationary: it is the same in the beginning (for example one step before the first plastic event) and in the end (e.g. one step before the last measured plastic event) of the plastic flow. It is remarkable to see in this figure, that the distribution of the deviatoric stress restricted to the center of the quadrupoles (one step before each plastic event) computed for all the plastic events is very close to the previously discussed stationary distribution obtained over the whole sample, and not only in the center of the quadrupoles. The position of the center of the quadrupoles appears to be unrelated with any threshold value in the local stress components. The saturation of the macroscopic stress, and the associated well defined yield stress σ_Y in these systems can thus be related only to the alternation of increase and decrease of stress and to its intermittent behavior, rather than to any identified local stress threshold. The existence of an apparent macroscopic yield stress is not related to a local yield stress. Note that criteria based on Tresca or Mohr-Coulomb criterion, involving the most probable relation between deviatoric stress and pressure have also been tested in our numerical systems. It shows a general tendency for the pressure to be affinely related to the deviatoric stress in the plastic flow regime. However, this tendency is shared by all the particles in the system, and not only by the particles at the center of the quadrupoles. It thus appears, like in the case of the deviatoric stresses, that a global Mohr-Coulomb criterion, or equivalently -for 2D systems- a Tresca criterion, is valid in the plastic flow regime, but is does not provide a locally selective criterion for plasticity. Figure 4.6 shows the same distributions as for the deviatoric stress, but for the incremental deviatoric stresses: it means $\sigma_{dev}(n+1) - \sigma_{dev}(n)$. In this case, quenched stresses are not taken into account,

and a large incremental stress is generally the signature of a large local deformation. The distribution of incremental stresses is also stationary. The distribution restricted to the center of the quadrupoles is displaced to larger increases in the deviatoric stresses. This point has also been mentioned by Robbins *et al.* [55] and underlines the role played by incremental stresses in the dissipative dynamics of the systems, in comparison with total stresses that are more or less unchanged. It suggests that the incremental stress $\Delta\sigma$ can be a more important parameter for plastic purposes than the stress σ itself. However, its distribution is very broad, and a criterion based only on the incremental stresses is not very selective: it does not even exclude the possibility for the center of the quadrupole to take place where the increase of the deviatoric stress is not maximum but minimum.

Elastic Criterion. Let us now make connection with the derivation of continuum mechanics from microscopic consideration that we have introduced in section 3.1 to introduce a local elasticity based criterion used recently to predict the nucleation of defects in crystalline materials [161, 204]. In their approach Van Vliet *et al.*, assuming as in the entire section 3.1 homogeneous deformation of a 'representative volume element' (RVE), use locally the free energy expansion in terms of the incremental displacement $u(\mathbf{x})$, combining the expressions 3.16 and 3.26 to obtain,

$$\Delta \mathrm{F} = \frac{1}{2} \int_{\mathrm{V}(\mathbf{r})} d\mathbf{r} \mathrm{D}_{\alpha\beta\gamma\delta}(\mathbf{r}) u_{\alpha,\beta}(\mathbf{r}) u_{\gamma,\delta}(\mathbf{r}) \ , \tag{4.1}$$

where $\mathrm{D}_{\alpha\beta\gamma\delta} = \mathrm{C}_{\alpha\beta\gamma\delta} + \sigma_{\alpha\beta}\delta_{\gamma\delta}$, with $\mathrm{C}_{\alpha\beta\gamma\delta}$ the local Born elasticity tensor of 3.24 and $\sigma_{\gamma\delta}$ the local Cauchy stress of equations 3.14 and 3.15. Representing the displacement by a plane wave perturbation, $u_\alpha(\mathbf{r}) = w_\alpha e^{i\mathbf{k}\cdot\mathbf{r}}$ allow them to obtain the simple stability condition for the RVE,

$$\Lambda(\mathbf{w}, \mathbf{k}) \equiv (\mathrm{C}_{\alpha\beta\gamma\delta} w_\alpha w_\gamma + \sigma_{\beta\delta}) k_{\beta\delta} > 0 \ . \tag{4.2}$$

As discussed in [161, 204] the sign of Λ reflects the concavity of F. If there exists a pair of $\mathbf{w}$, $\mathbf{k}$ such that Λ is negative, then homogeneity of this RVE cannot be maintained and defect singularities will form internally. In other words, the elastic stability of the RVE can be determined by minimizing Λ with respect to the polarization vector $\mathbf{w}$ and the wave vector $\mathbf{k}$; the minimum value of Λ, Λ_{min}, therefore provides a measure of the microstiffness locally, with instability predicted at the position where Λ_{min} vanishes. As already discussed in section 3.2.3, the main approximation of this approach is in the assumption of homogeneous elasticity that allows to derive average microscopic expressions of the local Born elastic and stress tensor used in 4.2. In the case studied here this homogeneity assumption can be assumed to hold sufficiently far from any already existing defects in the crystal but would break down for the perfectly disordered glassy material. Nevertheless this approach gives an intuition of the idea that we followed in the previous chapter where we derived a local elastic criterion to quantify the softness of the material at a local level. In the rest of this chapter in the spirit of Van Vliet *et al.* we will use this local instability criterion to relate it to the dynamics of the glass and predict plastic activity.

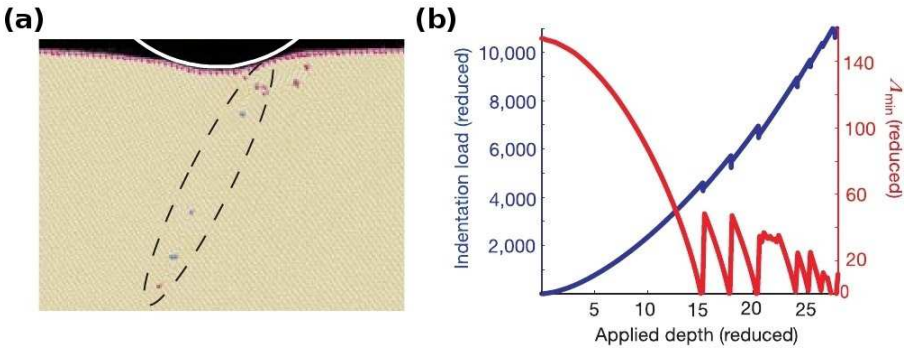

FIG. 4.7 : (a) MD simulation after several dipole nucleation events illustrating the formation of a shear band (dashed lines) after the dissociation of dislocation pairs to the free surface and crystalline interior. (b) Applied displacement load response (blue) of MD simulated bubble raft, showing correlation of load drops with a sequence of observed homogeneous dislocation dipole nucleation events. The elastic instability criterion Λ_{min} (red) tends to zero for the first several nucleation events. All nucleation events occur subsurface [161, 204].

4.2 The local shear modulus

4.2.1 Heuristic arguments

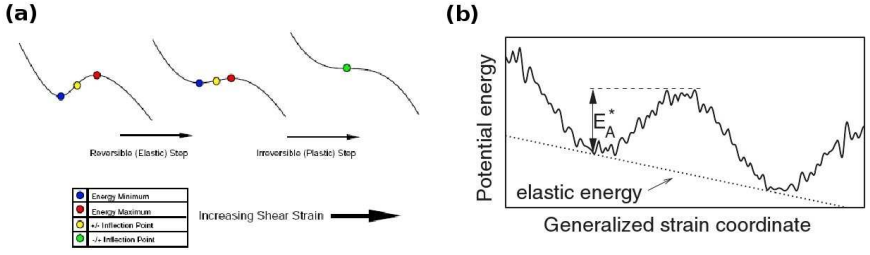

FIG. 4.8 : (a) A schematic representation of deformation induced changes of a local minimum in the potential energy landscape [205]. (b) Schematic illustration of the potential energy landscape of an individual STZ under applied shear stress. External shear strain or stress tilts the potential energy landscape and reduces the activation energy E_A^* of plastic shear events [206].

A common general idea is that the deformation in glassy systems will take place in 'weak' zones, somehow characterized by abnormally low elastic constants and increased mobility. This picture of the glass as composed of a patchwork of 'rigid' relatively strongly bonded (but amorphous) domains separated by 'soft' regions has long been postulated [120] and is at the heart of many theoretical models of the glass transition [208]. Moreover within this framework it appears tempting to relate the dynamical heterogeneities observed in glassy materials near and below the glass transition temperature to the spatially inhomogeneous elastic constant network. Experimental evidence of the heterogeneous glass

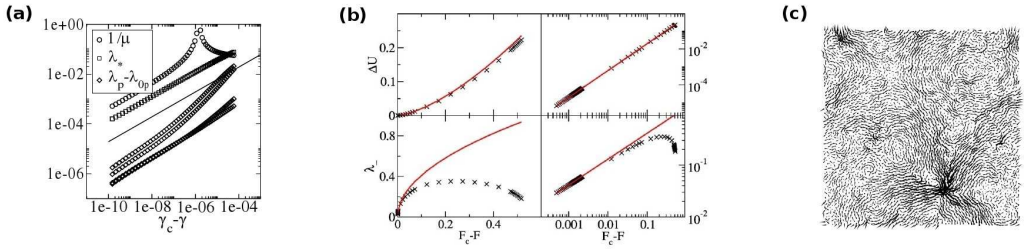

FIG. 4.9 : (a) In log-log scale (as a guide to the eye, the thick black line is $\sqrt{\gamma_c - \gamma}$), $1/\mu$ (circles), lowest eigenvalue of the Hessian (squares), next several eigenvalues minus their terminal values (diamonds) [205]. (b) Top, ΔU, and bottom, $\lambda_- = \frac{\partial^2 \mathrm{U}}{\partial x^2}|_{x_-}$, for the protein model of [207], as functions of $\mathrm{F}_c - \mathrm{F}$ where F is the external force and F_c is the critical force at which the minimum and barrier collide. (c) Nonaffine elastic displacement at a distance $\gamma - \gamma_c$ from the catastrophe [205].

structure is shown in [209] and models [210, 211] including fluctuating elastic moduli have been introduced in the last two decades to describe some acoustical (boson peak [212]) and thermal (specific heat anomalies [213, 214, 215]) properties of glasses. Let us give some heuristic arguments illustrating why the local shear modulus might be a good local order parameter to describe the mechanical response of glassy materials. In the case of crystalline materials the great symmetry of the lattices reduces the possible deformation patterns under mechanical load and for a global shear the simplest reasonable assumption is that a cooperative shearing will occur in the crystal with one plane of atoms sliding on top of another. Rather than being cooperative this sliding mechanism occurs progressively with the propagation of linear defects (dislocations)[4]. Glassy systems can be seen in a sense as a polycrystal with grain sizes of the order of the interparticle distance. They are therefore completely disordered and one needs to create a new paradigm to describe their plastic deformation. The general picture introduced for crystals that deformation must occur through successive transitions between energy minima must remain valid even for glassy materials and is in fact at the origin of the theoretical models introduced in section 1.4 of the introduction, such as the Soft Glassy Rheology model. The difficulty with glasses is to identify the typical energy barriers and topological rearrangements of particles associated with these transitions. The most general approach is to consider an energy landscape picture [216, 206, 217] of the glass in which the energy is a function of the $d \times \mathrm{N}$ degrees of freedom plus the external control parameter (e.g. strain or stress). In this picture as

[4] To propagate a defect necessitates to overcome an energetic barrier (Peierl potential) but this energy barrier is much lower than the barrier associated to the cooperative slide of a crystal plane. From this potential energy analysis one can derive the corresponding critical stress σ_{PN} (Peierl-Nabarro) required to achieve the defect propagation. In reality the plastic deformation of crystals is further complicated by mechanisms such as for example the interaction of dislocation with each other or with grain boundaries in polycrystals

the control parameter is varied, any minimum in the landscape will flatten out in some direction (the soft mode of the glass) as the minimum collides with a first order saddle point (figure 4.8 (a), [205]). This type of externally induced topological change is known as fold catastrophe and induce universal scalings of particular features of the potential energy landscape in the vicinity of the catastrophe. Written in the reaction coordinate x (i.e. the eigendirection of the soft mode) the potential energy can be simply expressed to lowest order in a Taylor expansion as $\mathrm{U} = -x^3 - \mathrm{B}x\delta$, where x is the projection of the system's coordinates onto the zero curvature direction (the soft mode) and δ is the control distance of the control parameter from the singularity. A simple functional analysis of the above function shows the following scalings for respectively the distance between minima in reaction coordinate, $\Delta x \propto \sqrt{\delta}$, the local curvatures in both minima, $\frac{\partial^2 \mathrm{U}}{\partial x^2}|_{x_{+/-}} \propto \sqrt{\delta}$, and finally the energy barrier, $\Delta \mathrm{U} \propto \delta^{3/2}$. And indeed these scalings were observed in simulations of Lennard-Jones glasses as shown in figure 4.9(a) [207] or in a model protein figure 4.9(b) [207]. Moreover as illustrated in figure 4.9(c) [207], in these athermal glassy Lennard-Jones models the topological change associated with the catastrophe was shown to be a localized quadrupolar displacement of particles (typically a few tens) also called shear transformation zones. More recently Mayr [206] on the model glass, Cu-Ti, and Delogu [218] on a model Ni-Zr showed that soft modes with similar spatial extent were preferentially activated. The above $\delta^{3/2}$ barrier scaling argument also lead Johnson and Samwer [219] to predict a $\mathrm{T}^{2/3}$ dependence in the yield stress of metallic glasses. The existence of this strain (or stress) induced softening mechanism combined with the observation of the localized nature of the topological rearrangements lead us to calculate the local elasticity modulus at different coarse-graining length scales as detailed in the previous chapter. By doing so we reduce the high number of degrees of freedom associated with each coarse-grained region to its local strain components. This approach is complementary to the detailed analysis of the soft modes of the glass and we will discuss in section 4.3 on how the two approaches compare.

4.2.2 Structural relaxation

In chapter 3 we have shown how the system could be decomposed into regions of different elastic stiffness. We now discuss how this elastic heterogeneity is related with the 'dynamics' of the system undergoing quasistatic, plastic shear deformation. To this end, we obtained the local elastic parameter c_1 for configurations of the sheared system separated by an incremental strain of $\Delta\varepsilon \simeq 5.10^{-5}$, during a set of intervals each within a total strain of $\sim 10\%$ in protocol one, under rigid boundary conditions and $\sim 6\%$ in protocol two, under Lees Edwards boundary conditions. The coarse-graining scale $\mathrm{W} = 5$ was chosen in all the subsequent analysis as the limit of applicability of linear elasticity. We recall that at this scale, $< \overline{c_1} > (\mathrm{W} = 5) \approx 18$.

One can first quantify the global relaxation time (strain) associated with the field c_1 by calculating the spatially averaged two point correlation function $\mathcal{C}(\Delta\varepsilon) = \langle \overline{c_1(\mathbf{r}, \varepsilon + \Delta\varepsilon) c_1(\mathbf{r}, \varepsilon)} \rangle$

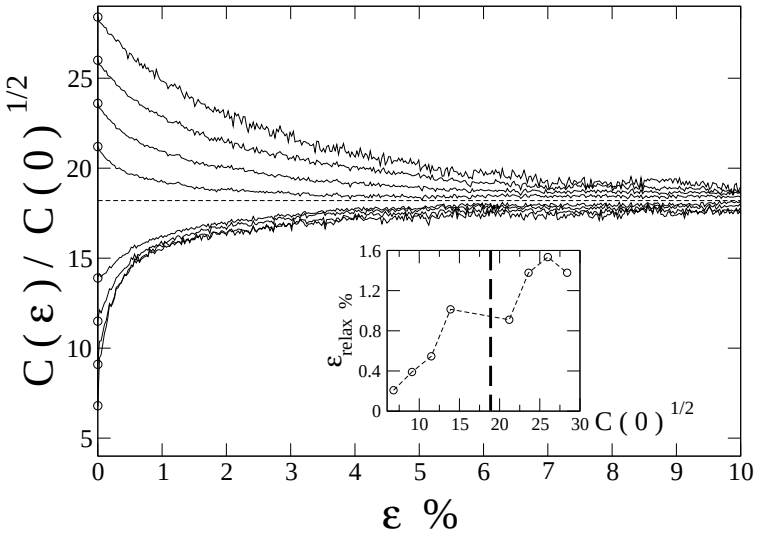

FIG. 4.10 : Autocorrelation function $C(\Delta\varepsilon) = \langle\overline{c_1(\mathbf{r},\varepsilon+\Delta\varepsilon)c_1(\mathbf{r},\varepsilon)}\rangle$ of the order parameter conditionned by the value of $c_1(\mathbf{r},\varepsilon)$ at the origin. The curves correspond from bottom to top to increasing values of $c_1(\mathbf{r},\varepsilon)$ at the origin taken in the ranges [5-7,5],[7.5,10],[10,12.5],12.5,15],[20-22.5],[22.5,25],[25,27.5],and [27.5,30] as marked by the circles. The dashed line corresponds to $\overline{c_1}$. Inset: the typical relaxation strain ε_{relax} associated with each rigidity $c_1 \sim C(0)^{1/2}$ defined as the strain for which the rescaled autocorrelation function has decayed by half.

where the notation $\overline{A}$ stands for a spatial average over the sample and angular brackets stand for a statistical average over the strain origins ε. In order to relate the relaxation strain to the local rigidity of the material we also calculate the two-point autocorrelation function of the shear modulus conditioned by its initial value. For each sampled rigidity c_1 we plot the rescaled autocorrelation function $\mathcal{C}(\Delta\varepsilon)/\mathcal{C}(0)^{1/2}$. In figure 4.10 we see that the functions $\mathcal{C}(\Delta\varepsilon)/\mathcal{C}(0)^{1/2}$ tends in the limit of large strains to the limiting value $\langle\overline{c_1}\rangle$, independently of the initial value of the shear modulus c_1. Therefore in the stationary plastic flow regime the local shear modulus $c_1(\mathbf{r},\varepsilon+\Delta\varepsilon)$ becomes uncorrelated for sufficiently large strains $\Delta\varepsilon$ from its value at the origin $c_1(\mathbf{r},\varepsilon)$, showing that in this model glass the local elasticity map does not phase separate into permanently rigid and soft regions but rather evolves dynamically under shear. In the inset of figure 4.10 we associate with each sampled rigidity c_1 a relaxation strain $\varepsilon_{relax}(c_1)$ defined as the strain for which the rescaled autocorrelation function has decayed by half. We see that $\varepsilon_{relax}(c_1)$ is a monotonic increasing function of the local rigidity parameter, that saturates for $\mathcal{C}(0)^{1/2} > \langle\overline{c_1}\rangle$. We see also that softer regions ($\mathcal{C}(0)^{1/2} < \langle\overline{c_1}\rangle$) relax more quickly than rigid ones.

To our knowledge this result represents one of the first numerical evidence of a clear relation between a structural order parameter and the dynamics in a glassy system. The measurement of the local elasticity map presents the advantage to be independent of the

specificity of the glass under study, requiring only the measure of a local stress and strain. This result confirms the description introduced in section 3.4.2 of the material as a composite material made of 'soft' fast relaxing zones (for $c_1 \leqslant \overline{c_1}$) and of 'rigid' stable zones (for $c_1 \geqslant \overline{c_1}$). As seen in figure 4.10 the strain associated with the rigid 'scaffolding' of the material is found to be of the order of $\varepsilon_{relax} \simeq 1.5\%$. This value is similar to the strain necessary to enter the fully plastic regime $\varepsilon_{plastic} \simeq 2\%$. As suggested in figure 4.11 where the relative number of soft zones evolves in parallel with the total shear stress and reaches a maximum percentage ($\approx 60\%$) before a large plastic event, one can also see this typical strain as the necessary strain required to achieve percolation through the material of soft zones, i.e. when the material's rigid scaffolding is no longer connected [2].

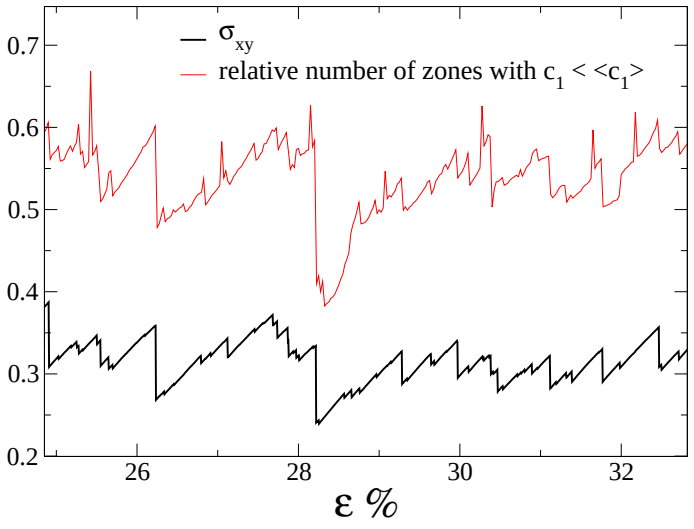

Fig. 4.11 : Evolution of the total shear stress (thick line) and the relative number of soft zones (relative number of points $\mathbf{r}$ where $c_1(\mathbf{r}) < \overline{c_1}$) as a function of the applied shear strain, in th plastic flow regime.

This relaxation strain of the order of 1.5% can be compared with the typical strain separating two irreversible rearrangements [5] in the sample $\Delta\varepsilon_{event} \sim 0.1\%$. An estimate of the number of plastic rearrangements required to renew the rigid 'scaffolding' of the material can therefore be given as $\varepsilon_{relax}/\Delta\varepsilon_{event} \simeq 15$, hence typically 15 events for a sample containing 10000 particles. Figure 4.13 shows the evolution of the rigid scaffolding over a total strain of $\simeq 0.9\%$.

4.2.3 Relation between the local elasticity map, the local mobility and the long time dynamical heterogeneity

We have characterized the dynamics of the underlying structure in terms of the shear rigidity order parameter. We want now to see how this structure is coupled to the displacement field in the sheared material.

In order to describe the relation between the local elasticity of the material and its dynamics, one can try to quantify the connection between the local domains presenting small local modulus and an increased mobility of the particles in these domains. A vast literature has grown in the last five years on the connection between static structural properties and dynamical heterogeneities in glass formers. While different approaches have partially failed to support such a link between local structure (such as local free volume, local inherent state potential energy, defects, Voronoi tessellation, local stress or strain...) and dynamics, Harrowell et al. [220] have recently shown that the spatially heterogeneous 'local Debye-Waller (DW) factor' (defined as the mean-squared vibration amplitude of a molecule over a time of approximately 10 periods of oscillation of this molecule) in a two-dimensional glass forming mixture could be mapped perfectly on the locally measured dynamical propensity that relates to the long term dynamical heterogeneities in the material. Berthier *et al.* [171] pursued this discussion showing how the influence of structure on dynamics is much stronger on large length scales than on shorter ones, and that the choice of the coarse-graining scale in the structure-dynamics problem is crucial. Here we make connection with this literature and claim that the local order parameter c_1 is a good candidate to establish a relation between structure and dynamics. One can understand this assertion by the fact that c_1 and the DW factor contain a similar physical information in probing the local stiffness of the material. Of course in a quasistatic deformation one can not simply measure a local DW factor on short time scales and the order parameter c_1 is a good measure of the stiffness of a region. Following Cooper and Harrowell in [220] we define a quasistatic analogue of the dynamic propensity as $\langle[\mathbf{r}_i(\varepsilon) - \mathbf{r}_i(0)]^2\rangle$ where $\mathbf{r}_i(\varepsilon) - \mathbf{r}_i(0)$ is the displacement without the affine contribution due the macroscopic strain ε. Unlike the original definition of the dynamical propensity in [220] the average is taken here over all the particles in a given range of the order parameter c_1 and not over an iso-configurational ensemble of N-particle trajectories. Figure 4.12 shows that the order parameter c_1 is indeed related to the long term propensity and that soft regions ($c_1 \leqslant \overline{c_1}$) present an increased non-affine mobility in comparison with more rigid regions of the material ($c_1 \geqslant \overline{c_1}$).

The relation between mobility (plasticity) and low shear modulus is illustrated in figure 4.14 by looking at how the spatial distribution of these two quantities are mapping onto each other. In this figure, the cumulative non-affine displacement field (that is essentially irreversible) appears to nucleate from the initial reference state near the soft zones of the material and to grow in a cooperative manner up to the point where the material fails macroscopically forming a vertical shear band across the sample. In figure 4.15 we distinguish between mobile and immobile particles, and between soft and rigid zones. The

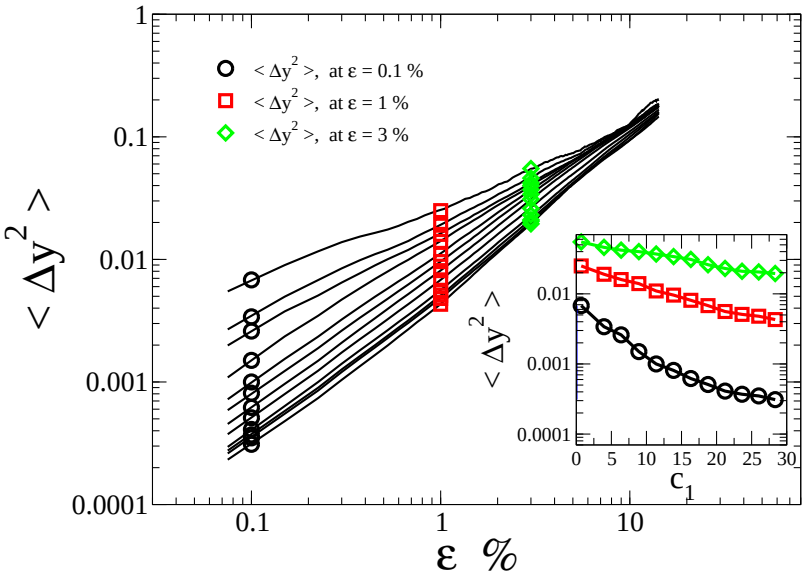

FIG. 4.12 : Mean-square displacement $\langle \Delta y^2 \rangle$ for different values of the original local shear modulus c_1. From top to bottom the curves correspond to c_1 taken in the ranges [0-2.5],[2.5,5],[5-7.5],[7.5,10],[10,12.5],12.5,15],[20-22.5],[22.5,25],[25,27.5],and [27.5,30]. Inset: $\langle \Delta y^2 \rangle$ is shown as a function of c_1 for different relaxation strains.

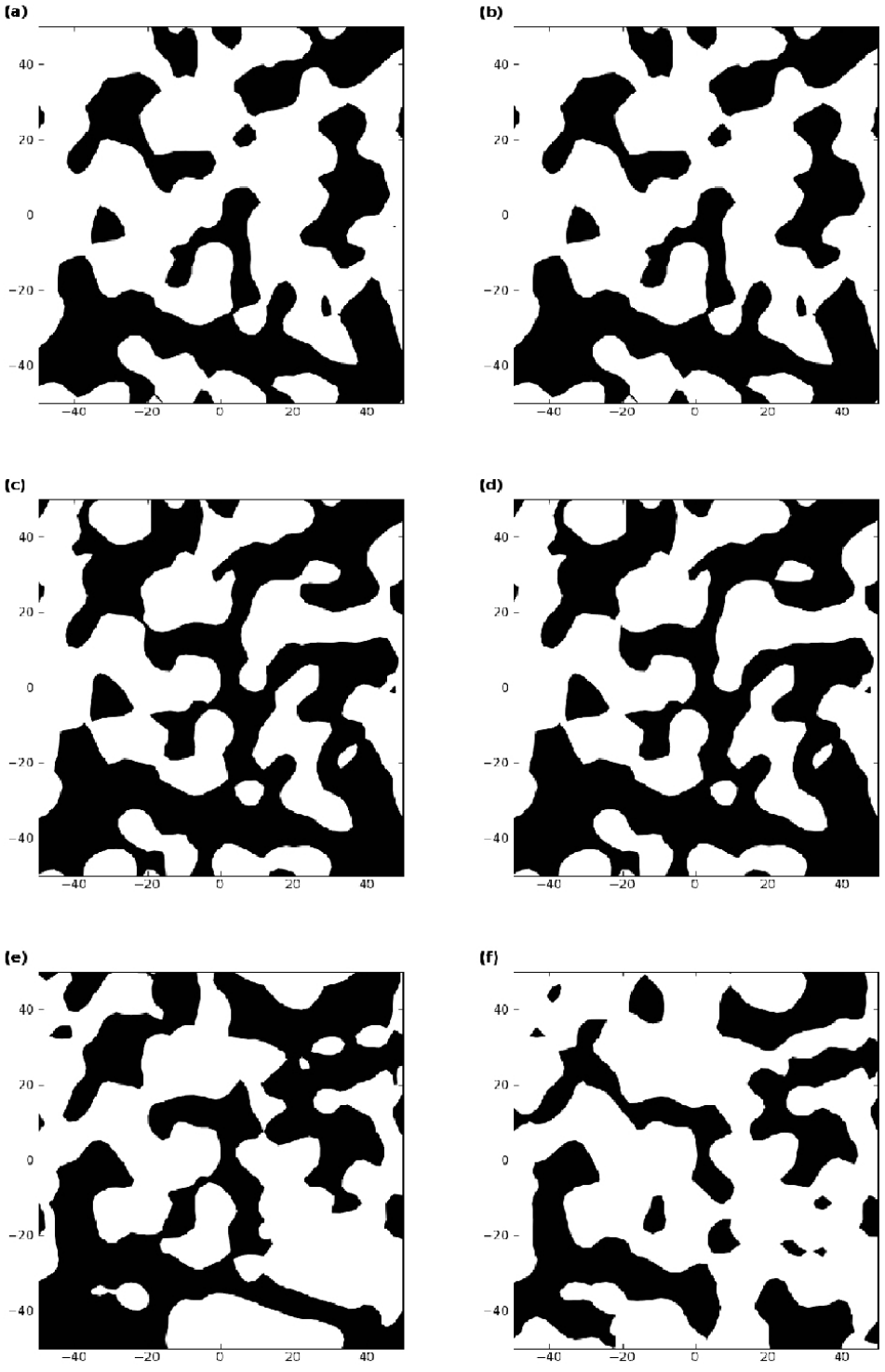

Fig. 4.13 : Shear modulus divided in rigid ($c_1 \geqslant \overline{c_1}$, black) and soft zones ($c_1 \leqslant \overline{c_1}$, white) for different macroscopic strains. Figures (a) to (f) correspond to a macroscopic strain of (a)2.5%, (b)2.55%, (c)2.65%,(d)2.7%,(e)3.25% and (f)3.4%.

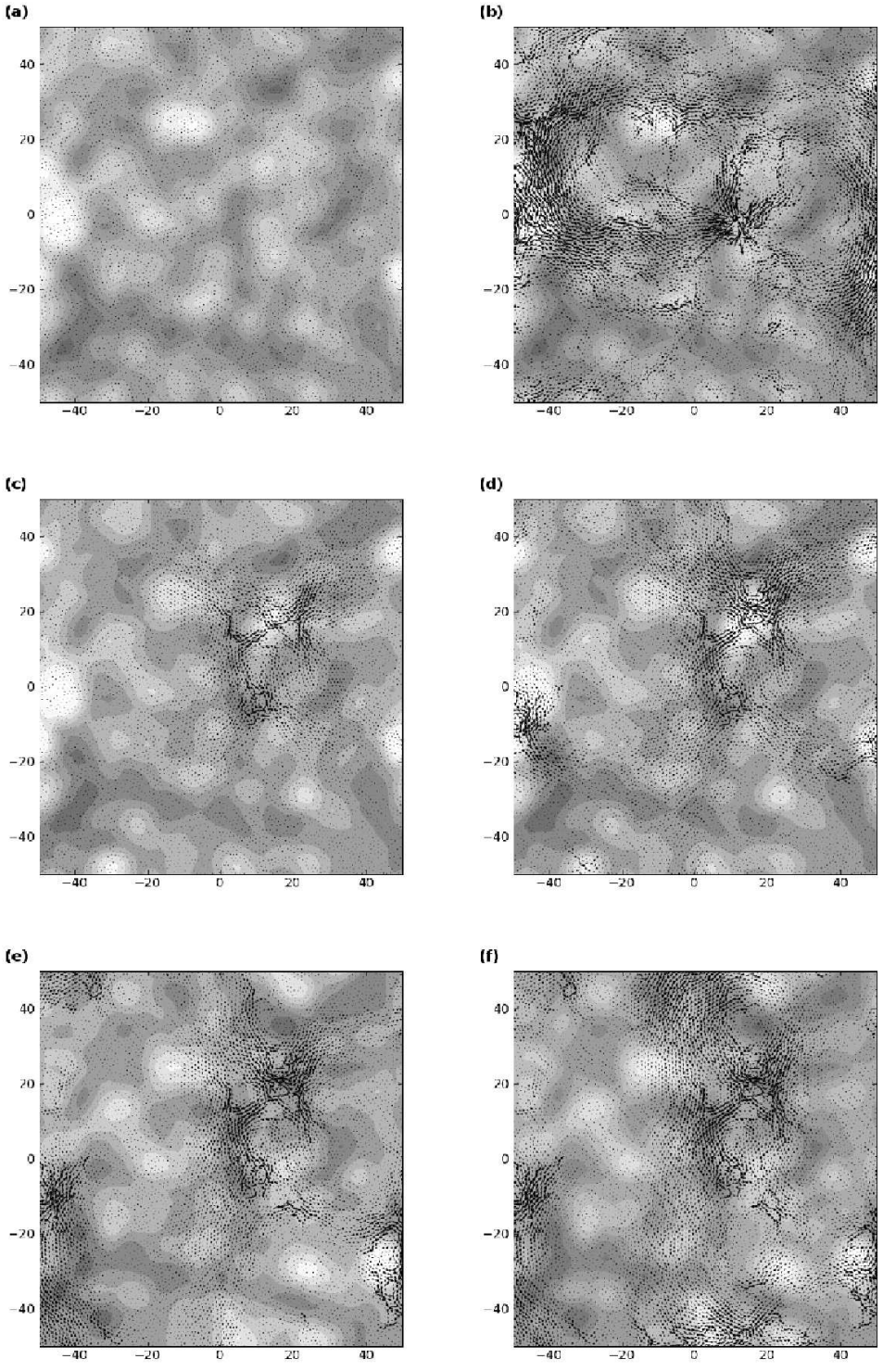

Fig. 4.14 : We represent the local map of the shear modulus at the same macroscopic strain values as in figure 13. These values correspond to the onset of plastic rearrangement of the material. These maps are superimposed with the non-affine displacement accumulated from figure (a). Figures (a) to (f) correspond to a macroscopic strain of (a)2.5%, (b)2.55%, (c)2.65%,(d)2.7%,(e)3.25% and (f)3.4%. Note that the non-affine field is multiplied by a factor 300 on figure (b) to illustrate the very strong correlation of the elastic non-affine field with the elasticity map for small incremental strain intervals (here 0.05%).

mobile and frozen particles are identified somehow artificially by the amplitude of the transverse nonaffine displacement: $\Delta y \geqslant 0.02$ for a total strain of 1% and $\Delta y \leqslant 0.02$ respectively. The soft zones are identified by $c_1 \leqslant \overline{c_1}$ and the rigid zones by $c_1 \geqslant \overline{c_1}$. In figure 4.15, we plot the distribution of shear modulus associated with each group of particles (mobile and frozen) and the distribution of nonaffine displacements for the rigid and soft portion of the sample. Figure 4.15 confirms the visual impression of figure 4.14 that most of the displacement is concentrated in the soft regions of the material and conversely that mobile particles are located in soft zones.

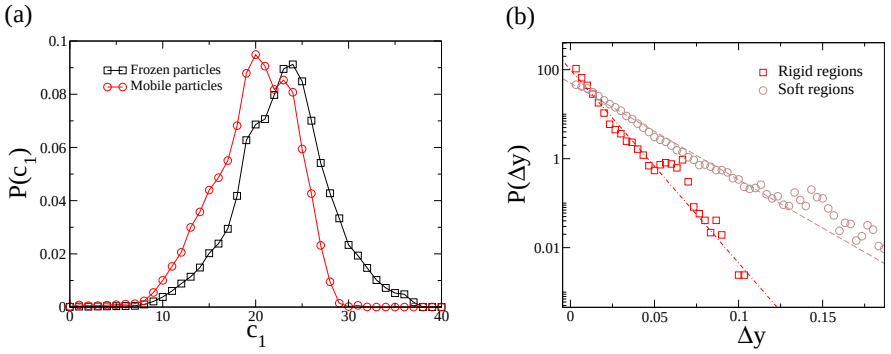

Fig. 4.15 : (a) Distribution of the local shear modulus for mobile and immobile particles. (b) Distribution of the nonaffine field during a total strain of 1% for rigid and soft regions.

We showed that most of the displacement occurs in soft zones. As seen in figure 4.14 the dynamics in the sheared glass is not trivial with regions that concentrate most of the non-affine displacement field and others that remain quiescent. The appearance of bursts of mobility seems therefore strongly dictated by the underlying heterogeneous elastic structure of the material and one cannot understand cooperative dynamics in the glass without considering this underlying structure. Anticipating on the next two chapters[5] we would like now to address the question of the degree of cooperativity of this mobility field in the material and its relation with the local elasticity map. In the literature the dynamical heterogeneity of aging [221] or sheared [222, 6, 223] glassy systems is commonly quantified by a four-point correlation function defined as:

$$\chi_4(\mathbf{k},\varepsilon) = \frac{1}{\mathrm{N}}\left[\langle \mathrm{F}_s(\mathbf{k},\varepsilon)^2\rangle - \langle \mathrm{F}_s(\mathbf{k},\varepsilon)\rangle^2\right] \tag{4.3}$$

where $\mathrm{F}_s(\mathbf{k},\varepsilon)$ is the self intermediate scattering function defined by:

$$\mathrm{F}_s(\mathbf{k},\varepsilon) = \sum_i cos\left(\mathbf{k}.(\mathbf{r}_i(\varepsilon) - \mathbf{r}_i(0))\right). \tag{4.4}$$

[5] For the definition of the two and four point correlation functions see equations 5.3.2 and 5.3.2 in chapter 5

It is important to note here that the symmetry of the mechanical deformation introduces an anisotropy in k-space in the relaxation of the self intermediate scattering function (SISF) $\mathrm{F}_s(\mathbf{k},\varepsilon)$. Typically one has at the first peak (k_P) of the static structure factor a relaxation strain of $\mathrm{F}_s(k_x = k_\mathrm{P},\varepsilon)$ of about 0.2% while for $\mathrm{F}_s(k_y = k_\mathrm{P},\varepsilon)$ the relaxation strain is of about 1%. This difference can be attributed to the formation of shear bands in our model glass, preferentially along the x axis, therefore increasing the mobility along this axis. These results seem in contradiction with recently reported similar studies in a model binary supercooled liquid, where an isotropic relaxation is reported for $\mathrm{F}_s(\mathbf{k},\varepsilon)$. It would be interesting to clarify, if these discrepancies could be attributed to the thermal agitation present in [223] and absent in our athermal simulations. Also in figure 4.16(a) in order to relate mobility and structure we calculate the SISF for different region of the material according to their rigidity. One sees in the inset of figure 4.16(a) that the relaxation strain associated with each SISF grows linearly with the local shear modulus below the average shear modulus ($c_1 \leqslant \overline{c_1} \approx 18$) and then reaches a plateau at a value of about $\varepsilon_{relax} \sim 0.85\%$. Again this provides a clear evidence of the connection between the structural order parameter c_1 and the dynamical response of the material. It cuts the sample into soft ($c_1 \leqslant \overline{c_1}$) and rigid ($c_1 > \overline{c_1}$) zones.

In figure 4.16(b) we see in $\chi_4(k_y = k_\mathrm{P},t)$ that the number of particles evolving in a cooperative way grows linearly with strain from zero to ~ 500 particles for LE boundary conditions and to ~ 100 for rigid boundary conditions. It is indeed system size dependent and evolves as $\mathrm{N}.f(\xi/\mathrm{L})$, as shown in [224, 225, 226]. We will come back in more details to this point in chapter 6.

The maximum cooperativity is achieved at a strain of $\varepsilon \sim 2\%$ in the LE case as well as in the rigid walls case. Theoretical predictions concerning the four-point correlation function are reported in [221] where the authors focus their studies on static supercooled liquids near the glass transition temperature. Whether or not one can identify the dynamical correlation length scale to the typical spatial extent of the soft zones of the material remains unclear from this analysis and requires further studies. We note that the typical strain at which the cooperativity $\chi_4(k_y = k_\mathrm{P},t)$ is maximal ($\varepsilon_{max} \sim 2\%$) does not correspond exactly to the structural α-relaxation strain $\varepsilon_\alpha < 1\%$ defined as $\mathrm{F}_s(k_y = k_\mathrm{P},\varepsilon_\alpha) = 1/e$ calculated for the same wave vector, but the order of magnitude is actually the same for the systems studied here.

4.2.4 Predicting plastic activity

To understand the dynamics in the soft phase and more generally the rheology (or mechanical response) of the material one would like to understand what first triggers the nucleation source points (local plastic events) at some specific locations and second how these local rearrangements interact in a cooperative manner.

In the previous section we have analyzed the coupling between the elasticity map and

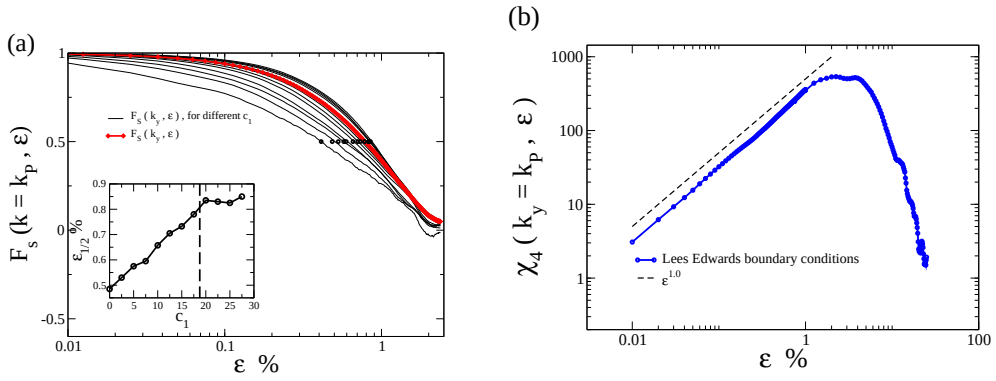

FIG. 4.16 : (a) Intermediate scattering function (SISF) $F_s(\mathbf{k},\varepsilon)$ plotted for $\mathbf{k}= k_y = k_P$ (diamonds) and for regions of different softness c_1 (thin lines, from bottom to top the rigidity c_1 is increased). Inset in (a): the relaxation strain is shown as a function of the softness at the origin. (b) 4 point correlation function represented for Lees-Edwards boundary conditions (circles). For small strain increments the linear behavior is highlighted (dotted line).

the nonaffine field in the material and claimed that, for sufficiently large strain, the nonaffine field (for exemple shown in figure 4.14) is essentially irreversible (plastic). We checked this assertion by comparing for each particle in the system the total nonaffine displacement and the purely irreversible displacement. The irreversible displacement field is defined as the residual displacement field resulting when after each macroscopic elementary strain increment $\delta\varepsilon \sim 5.10^{-5}$ the 'virtual' reverse shear $-\delta\varepsilon$ is applied on the system. For a purely reversible deformation this field should cancel exactly, but here one observes that, for most incremental deformation steps, a non-vanishing residual irreversible displacement field is present. With this numerical protocol we can extract for each particle i of the system the purely irreversible displacement $\mathbf{\Delta r^i_{irrev}}$ from the total nonaffine displacement $\mathbf{\Delta r^i_{na}}$. Hence for each particle i the total nonaffine displacement over a macroscopic strain $\Delta\varepsilon = \sum_n \delta\varepsilon_n$ can be decomposed into $\mathbf{\Delta r^i_{na}}(\Delta\varepsilon) = \sum_n \mathbf{\Delta r^i_{irrev}}(\delta\varepsilon_n) + \sum_n \mathbf{\Delta r^i_{rev}}(\delta\varepsilon_n)$. The relative error $\|\mathbf{\Delta r^i_{na}}(\Delta\varepsilon) - \mathbf{\Delta r^i_{irrev}}(\Delta\varepsilon)\|/\|\mathbf{\Delta r^i_{na}}(\Delta\varepsilon)\|$ averaged over all particle is obtained and being less than 5% confirms our assumption that the nonaffine displacement is dominated by an irreversible plastic contribution. Based on this observation we describe here the link between plasticity in the material and the local elasticity map. To obtain this information we study here the dynamics of the local rigidity c_1 calculated on each particle over a strain range of 10%.

Figure 4.17 illustrates the evolution of the coarse-grained modulus c_1 on a particle that experiences plastic activity (i.e. that rearranges over the strain range). We have superimposed the quantity D_{BF} - BF standing for best fit - defined in [3], which evaluates the degree of local deviation from affinity. This parameter was found to very accurately distinguish between plastic like zone ($D_{BF} \sim 1$) and normal elastic zones ($D_{BF} < 10^{-4}$). Figure 4.18(a) shows the average behavior of the same quantity c_1, averaged for all plastic

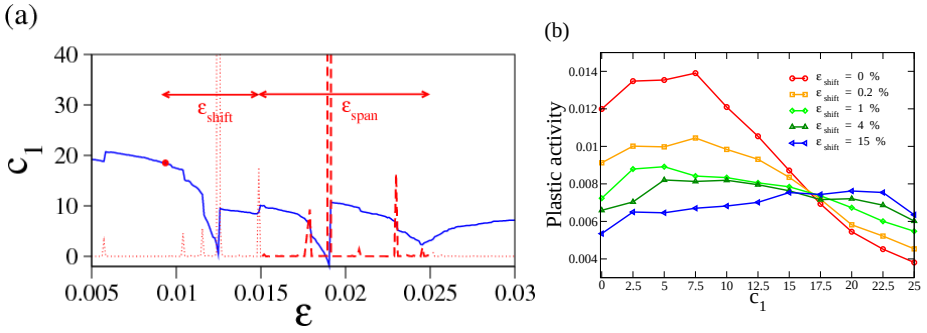

FIG. 4.17 : (a): Evolution of c_1 of a particle in a plastic zone. The dotted line represents the parameter D_{BF} that marks the local deviation from affinity. ε_{shift} and ε_{span} are defined for the point marked in red. (b): cumulative plastic activity for $\varepsilon_{span} \sim 0.5\%$ and for different values of ε_{shift}.

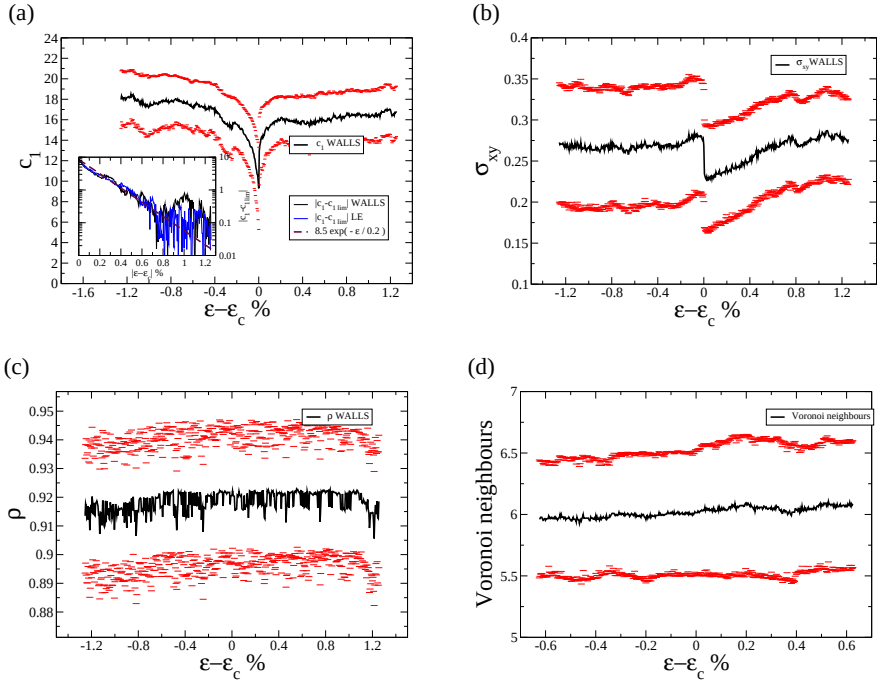

FIG. 4.18 : Evolution of different fields around a plastic event and averaged over all plastic events. (a) local shear modulus, (b) local shear stress, (c) local density and (d) number of Voronoi neighbors.

events. The result which is typical of the dynamics of c_1 shows that before a plastic event occurs on the site the modulus c_1 decreases over a typical strain interval of about 0.2% to become zero or even negative at the plastic irreversible event, where the non-affine displacement becomes important ($D_{BF} \sim 1$). Then the local structure is relaxed and the local modulus gets a higher value ($c_1 \sim 18$ after the event). Note that this value $c_1 \sim 18$ is smaller than the macroscopic value for 2μ but corresponds to the average value $\overline{c}_1$ of the shear modulus at the scale $W = 5$ of description. Just before a plastic event, the local shear modulus is very low $c_1 << \overline{c_1}$. The average decrease of c_1 before a plastic event is fitted approximately by an exponential decay to its limit value. We have no explanation for the moment for this exponential fit. It shows a characteristic strain $\sim 0.2\%$.

It is interesting to compare in our system this order parameter with other possible predictors of plasticity introduced in the literature. These parameters are the local stress [201, 68, 67], the local deformation strain [57, 227], the local free volume [3, 228, 229], coordinance defects [8, 191] as well as other local criteria derived from macroscopic mechanics such as Tresca local yield criterion or a local Mohr-Coulomb [198, 199]. In figure 4.18 we have summarized the evolution of some of these fields measured locally in our model glass at the sites that undergo plastic rearrangement before, during and after the relaxation takes place. The curves are averaged over all plastic events over the strain studied (≈ 1000 events). It shows that the density and the inverse compressibility are not affected by the plastic event. The shear stress is affected since it decreases suddenly after the plastic event occurred; but before the plastic event, the variation of shear stress is very small, and on a very small strain-range. Thus the conclusion appearing from the above analysis is that the local shear modulus c_1 is the best criterion in our Lennard-Jones glasses, to identify zones that are about to rearrange.

In order to identify the effect of a very low initial local shear modulus $c_1 << \overline{c_1}$ on the plastic activity over a larger strain span, we have calculated the shifted plastic activity $A(i, \varepsilon_{macro}; \varepsilon_{shift}, \varepsilon_{span})$ measured at each site i and every step in the macroscopic strain ε_{macro} and defined as the integral over a strain range ε_{span} of typically a few % of the local quantity D_{BF} starting from a shifted value of the macroscopic strain $\varepsilon_{macro} + \varepsilon_{shift}$ from the actual macroscopic total strain ε_{macro} where c_1 is measured. Note that ε_{shift} and ε_{span} are adjustable parameters.

In figure 4.17 we illustrate the meaning of this two parameters. ε_{span} is the range over which the plastic activity is recorded, in the limiting case of $\varepsilon_{span} \to \infty$ one should obtain the average activity of the glass former. ε_{shift} allows to subtract a systematic bias associated with the conditional probability to have an increased plastic activity for low initial values of c_1. In figure 4.17 we also plot the correlation between the average activity and c_1 for different ε_{span}. The plastic activity is a number that counts the number of significant plastic events. It is incremented by 1, as soon as $D_{BF} > 0.2$. It appears that the probability to encounter a plastic event is larger for originally soft regions ($c_1 <$

$\overline{c_1}$). Moreover, the predictive character of the structural softness of the material on the subsequent plastic activity of the glass former holds even for relatively large strain $\varepsilon_{shift} \sim 4\%$.

4.3 Relation with soft modes

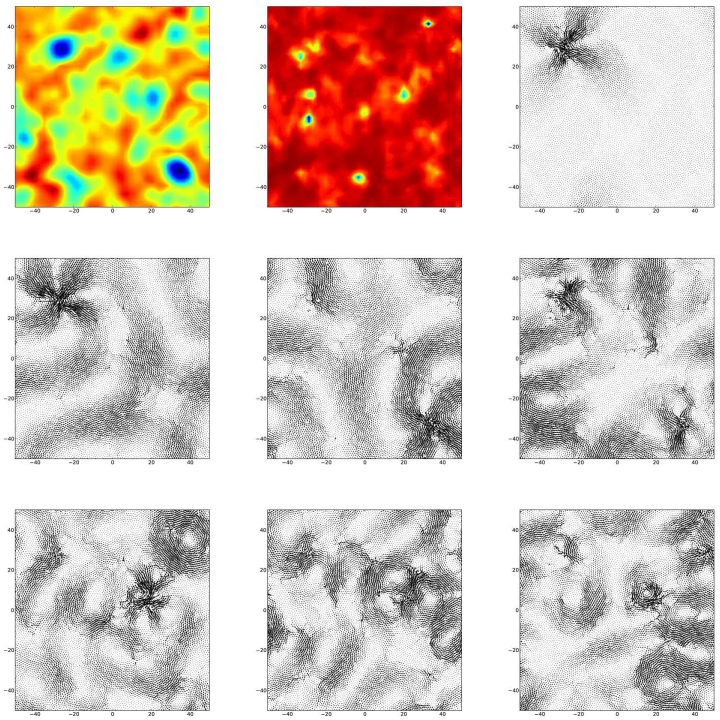

Fig. 4.19 : Analysis of the elasticity map and soft modes of a configuration at a macroscopic strain $\varepsilon = 0.2725\%$ just prior to a localized quadrupolar rearrangement. From top to bottom and from left to right : Local elasticity map of the shear modulus C1 for a coarse-graining W = 5, map of the average participation fraction $|\mathbf{e}_\omega(\mathbf{x})|^2$ over the 30 lowest eigenmodes, actual non-affine displacement during the plastic rearrangement between $\varepsilon = 0.2725\%$ and $\varepsilon = 0.275\%$, first six eigenmodes with a participation ratio below 0.4 (see figure 4.23), i.e. the eigenmodes 10, 11, 26, 28, 29 and 34.

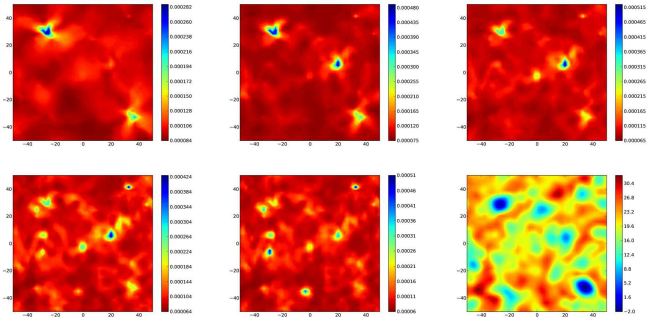

Fig. 4.20 : Map of the average participation fraction on the same configuration as in figure 4.19 for the 10, 30, 50, 75 and 100 lowest eigenmodes. Comparison with the local elasticity map of figure 4.19.

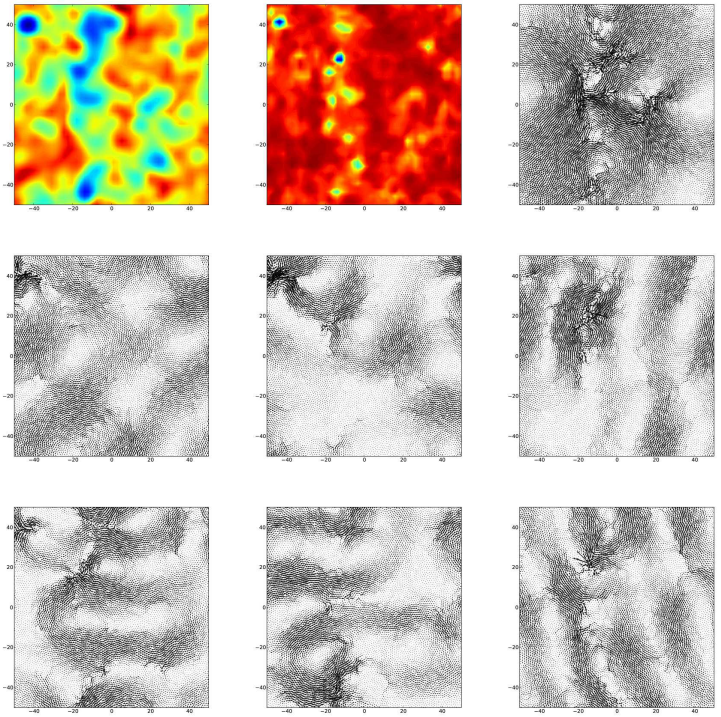

Fig. 4.21 : Analysis of the elasticity map and soft modes of a configuration at a macroscopic strain $\varepsilon = 5.8625\%$ just prior to a large shear band. From top to bottom and from left to right : Local elasticity map of the shear modulus C1 for a coarse-graining W = 5, map of the average participation fraction $|\mathbf{e}_\omega(\mathbf{x})|^2$ over the 30 lowest eigenmodes, actual non-affine displacement during the plastic rearrangement between $\varepsilon = 5.8625\%$ and $\varepsilon = 5.875\%$, first six eigenmodes with a participation ratio below 0.4 (see figure 4.23), i.e. the eigenmodes 9, 10, 11, 12, 15 and 16.

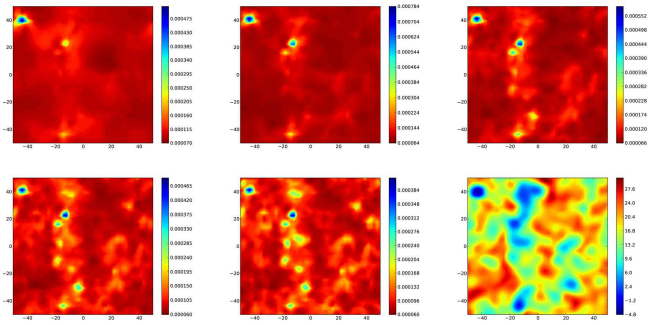

Fig. 4.22 : Map of the average participation fraction on the same configuration as in figure 4.21 for the 10, 30, 50, 75 and 100 lowest eigenmodes. Comparison with the local elasticity map of figure 4.21.

From what we have discussed so far in this chapter it appears that while on the one hand some local criteria at the atomic level, such as voronoi volume, neighbors, defects, energy, site stress, Born elastic constant, do not contain much information as to the tendency for increased local motion or plasticity, local criteria on a mesoscopical coarse-grained scale, such as the local shear modulus, on the other hand seem to correlate rather well with increased local mobility. This observation was also made by Berthier *et al.* in [171] where it was shown that the influence of structure on dynamics is much stronger on large length scales than on shorter ones, and that the choice of the coarse-graining scale in the structure-dynamics problem is crucial. This can be simply understood by looking at the onset of a plastic rearrangement in the sheared glass. Indeed if in this critical configuration one tries to displace a single particle while keeping all the others fixed then the particle will appear to be in a stable energy state. This is obviously in contradiction with the fact that at the critical point the system is in an instable state and is about to rearrange along a soft direction of cooperative motion of many particles (a soft mode). In theory therefore to obtain the most accurate correlation between structure and motion one needs to identify the soft modes of the material by diagonalizing the Hessian matrix of the entire system. Of course the possibility that a cluster of particles at some mesoscopic length scale dominates the instability mechanisms at the onset of plasticity is a possibility. In fact, Mayr [206] showed in simulations of metallic glasses that such a length scale exists in the sense that the activation energy of such clusters of particles appears to reach a minimum at some specific length scale of about 10 interatomic distances. Along these lines we want here to compare the local coarse grained shear modulus with the soft modes of the sheared glass and check that the two quantities contain similar information. The possibility to relate the structure and the dynamics at some mesoscopic scale is a prerequisite for many mesoscopic models of the rheology of glassy materials and is therefore an important conceptual question. Analysis of soft modes have been already performed in the literature of sheared glassy materials [205, 114] and supercooled liquids [186], exhibiting deviations from the plane wave eigenmodes - that would be expected in the crystalline materials - in the form of localized modes. In the previous two pages we present a detailed comparative study of the local coarse-grained approach with the soft mode analysis of two configurations of the sheared polydisperse glass at the onset of a plastic rearrangement. In figures 4.19 and 4.20 the configuration is chosen in the linear portion of the stress-strain mechanical response and the rearrangement is a localized quadrupole. In figures 4.21 and 4.22 the configuration is in the plastic regime and the plastic event is this time a large shear band that divides the sample vertically.

In both figure 4.19 and 4.21 the bottom two last rows show the first six localized eigenvectors of the glass configurations. To select the localized eigenvectors one calculates the participation ratio of each eigenmode [117] defined by,

$$\mathrm{P}(\omega) = \left[\mathrm{N} \sum_{i=1}^{\mathrm{N}} \left(\mathbf{e}_{\omega}^{i} \cdot \mathbf{e}_{\omega}^{i} \right)^2 \right]^{-1} , \tag{4.5}$$

where ω stands for the pulsation of the mode and $\mathbf{e}_\omega^i$ for the displacement of particle i of eigenmode ω, with the following normalization of the eigenmodes $\sum_{i=1}^{\mathrm{N}} \left(\mathbf{e}_\omega^i \cdot \mathbf{e}_\omega^i\right) = 1$. $\mathrm{P}(\omega)$ takes simple values in the following cases, for a completely delocalized mode where all particles move together $\mathrm{P}(\omega) = 1$ (see eigenmodes 1 and 2 in figure 4.23), for a mode localized on a single particle $\mathrm{P}(\omega) = 1/\mathrm{N}$ and for a plane wave $\mathrm{P}(\omega) = 2/3$. In figure 4.23 we have represented the participation ratios of the lowest 100 modes of the two glass configurations. This plot anabled us to extract the six lowest most localized eigenmodes ($\mathrm{P}(\omega) < 0.4$) and to show them in figures 4.20 and 4.22.

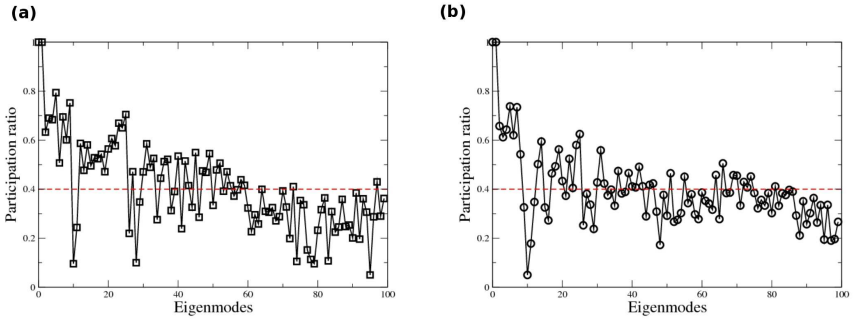

Fig. 4.23 : Participation ratio of the 100 lowest eigenmodes of (a) the configuration of figure 4.19 at $\varepsilon = 0.2725\%$, (b) the configuration of figure 4.21 at $\varepsilon = 5.8625\%$. The dashed lines at $\mathrm{P}(\omega) = 0.4$ are arbitrarily chosen to determine a localization criterion.

These are compared with the actual non-affine deformation that occurs in the plastic event (first row third column in figure 4.19 and 4.21) and illustrate the already observed fact [205] that plastic rearrangement in sheared glasses are dominated by these soft modes. More specifically one sees that while the total displacement field is undifferentiable from the softest mode at the onset of plasticity for localized quadrupolar rearrangements [205, 6], this identification becomes impossible for shear bands. Indeed as discussed by Lemaitre in the later case the shear band is the results of a cascade mechanism triggered by an initial localized soft mode whose signature is lost at the end of the irreversible process. Recently Widmer-Cooper *et al.* [186] have calculated the normal modes of the local energy minimum configuration, the so-called inherent state, of supercooled liquids and have showed in the spirit of what is observed in sheared glasses that irreversible reorganization originates from localized soft modes. To quantify this assertion they have compared the displacement of the 30 lowest frequency modes for each configuration with the subsequent irreversible structural reorganization in the supercooled liquid. Here we have reproduced this analysis for the glass by plotting on a grid the average participation fraction $p_i = \left|\mathbf{e}_\omega^i\right|^2$ over the first 100 eigenmodes and the second images of the first row of figure 4.19 and 4.21 illustrate the results for the two samples studied. As can be expected the blue zones on these figures correspond to an above average participation fraction and are related to the location of the localized soft modes of figure 4.23. Quite remarkably one sees that these maps correlate very well with the local elasticity maps of the local shear modulus C_1. This observation can

be taken as a confirmation of the existence of a typical length scale over which it 'makes sense' to define mesoscopic local quantities such as the local shear modulus. Another point that this quantitative study clarifies is the question of the prediction of a plastic event, more specifically can one predict if the system is going to relax by a local rearrangement or is the relaxation going to trigger an avalanche and form a shear band. Of course between the two extreme cases of the localized quadrupole or of a shear band that traverses the sample all avalanche sizes are possible for the plastic rearrangements[6] where we will relate the typical size of a plastic avalanche to external control parameters such as the temperature and shear rate. Nevertheless by looking at the local elasticity map and the average participation fraction prior to the formation of the vertical shear band of figure 4.21 it is tempting to relate the existence of this large cascade to the fact that the soft regions seem to percolate, in this case vertically along the shear band, through the sample. Yet more work needs to be done to make this point quantitative and we leave it here for further studies.

To summarize we can see that, while the soft modes were shown to correlate well with the dynamics in the supercooled liquid, in this chapter we showed how the local elasticity map relates also to the dynamics in the sheared glass. By making the connection between the two structural analysis we therefore expect the local elasticity map analysis to be relevant for the characterization of the supercooled state. The existence of such a mesoscopic tunable local order parameter is of great importance in order to understand the interplay between this underlying structure and the complex dynamics of driven glasses or of supercooled liquids. We hope that the above analysis of the local softness and rigidity of glassy disordered materials shed some new light and will open new perspectives in the understanding of the complex spatiotemporal dynamics of these systems. The study of this heterogeneous response of glassy materials is the topic of the next chapters.

[6] We will come back to this point in chapter 6

Chapter 5

Dynamical heterogeneity of a sheared glass ($\dot{\gamma} = 0$ and $\mathrm{T} = 0$)

Contents

When subjected to slow driving many systems exhibit an intermittent response with the appearance of discrete and impulsive events spanning a broad range of sizes. Such a scale-invariant behavior is generally observed in driven nonlinear, dynamical systems and examples of such crackling signals are ubiquitous in nature (for a review see [230]) with among other examples earthquake magnitudes (quantified by the famous Gutenberg and Richter law), biological extinctions, fluids invading porous materials and other problems involving invading fronts, the dynamics of superconductors and superfluids, sound emitted during martensitic phase transitions or plastic deformation of crystals, fluctuations in the stock market, the barkhausen noise emitted along the hysterisis loop in ferromagnets or

ferroelectrics, the serrated stress-strain curve (Portevin-Le Chaterlier effect) which some materials exhibit as they undergo plastic deformation...

As illustrated by Bak [231] despite their great variety these out of equilibrium phenomena usually share three common features, namely, power law distributions of the events sizes, temporal fourier transform spectra proportional to a power α (usually $0 < \alpha < 2$) of the inverse frequency and fractal geometry of the dynamical structures involved in the events. To explain such universal scaling behaviors Bak *et al* introduced (in one of the most ever cited paper [232]) the concept of self-organized criticality. According to this theory, driven dissipative dynamical systems spontaneously reach a critical state that is characterized by the three characteristics signaling scale invariance.

Turning now to glassy materials, it was shown that various such systems (granular media [233, 234], foams [10, 235], emulsions [53, 234], micelles [236], metallic glasses [237]...) exhibit an intermittent stress-strain mechanical response. The slowly driven (quasistatic) regime of some of these systems was shown to be compatible with self-organized criticality displaying all the three aforementioned characteristics, with broad power law distributions and fractal dynamical structures (see the review for the case of foam simulations in [9]). On the other hand power law distribution of structural rearrangements size can also result from simple continuum elasticity considerations. Moreover a detailed analysis of the intermittent stress-strain curves has shown that the finite size of the systems, the applied shear rates and the temperature considered alter the distribution of the rearrangement sizes, energy drops, stress drops and strain interval between rearrangements.

In this chapter we study the complex spatio-temporal mechanical response by a careful analysis of the intermittent response and velocity profiles of the sheared material. We relate these observations to the spatial structure of the plastic rearrangements. And propose a simple model of the stress evolution in the glass in terms of uncorrelated local plastic rearrangements.

5.1 Observations of the heterogeneous response

5.1.1 Intermittent stress-strain curve

Intermittent response of sheared glasses. In order to understand the origin of these characteristic exponential cutoffs, we present here a detailed analysis of the distributions of stress drops, energy drops and strain intervals between plastic events during quasistatic shear - under both Lees-Edwards and rigid walls boundary conditions - of different two dimensional polydisperse Lennard-Jones glass samples of different sizes. Figure 5.1 illustrates the typical responses of the glasses under Lees-Edwards boundary conditions for three square samples of length 25, 50 and 100 LJU. We show the (averaged) macroscopic shear stress and energy per particle as a function of the total strain applied to the system.

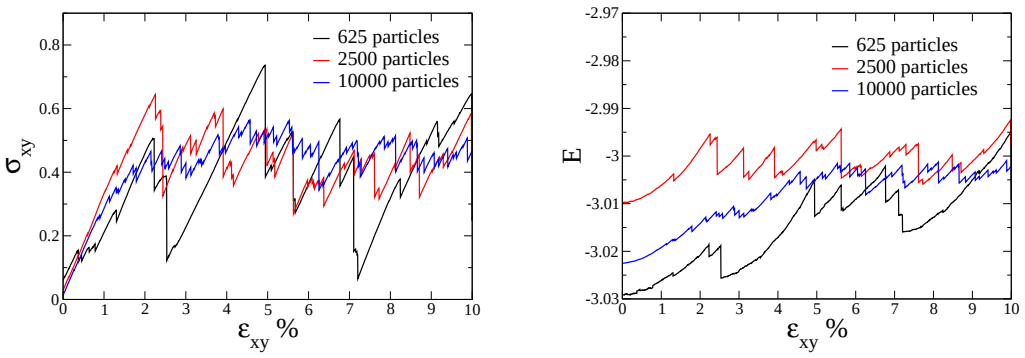

Fig. 5.1 : **Left :** Stress-strain response of three two-dimensional polydisperse Lennard-Jones glass under Lees-Edwards boundary conditions. Each curve corresponds to a different square cell of size 25, 50 and 100 particle diameters. **Right :** Energy-strain mechanical response of the same samples. Here the total energy is divided by the total number of particles to produce the average energy per particle.

Both the global shear stress and energy have an intermittent behavior, with an alternance of small and large jumps, giving rise to negative slopes that are the signature of dissipative events.

Experimental studies on disordered materials (foams, granulars), far below the glass transition temperature [12, 14, 238, 239, 9, 240, 13, 10, 11], associate the dissipative events observed in figure 5.1 to the existence of a collective behavior of localized rearrangements leading to a strongly heterogeneous mechanical response as shown in the existence of shear bands in the macroscopic plasticity of such systems. Along these experimental evidences, in the last five to ten years, extensive numerical simulations of quasistatically sheared model glassy systems have confirmed this picture of a cascade mechanism but have also generated heated debates first as to the validity of the potential energy minimization (PEM) method (see section 2.3) to represent the physical reality of slowly driven systems and second as to the localized nature of the elementary rearranging plastic events associated to the macroscopic stress and energy releases of figure 5.1. In the next chapter we will resolve the first controversy by showing how finite shear rate simulations in the limit of (very) low shear rates do indeed converge towards the quasistatic response obtained with the PEM method. In this section dwelling on our previous findings [5] but also on the recent work of Maloney and Lemaître [205] and of Lerner and Procaccia [241] (this last paper appeared during the completion of this thesis) we try to resolve the second controversy. In fact the direct observation of snapshots (or movies) of the displacement field inside the sheared polydispersed glasses provides the striking realization that structural irreversible rearrangements happen on different length scales. The two extreme occurrences being the localized quadrupolar event depicted in figure 5.2 (the so-called T1 event in foams) and the system spanning shear bands of figure 5.2. Interestingly these two limiting cases

help also to intuitively understand the scaling of the average stress drops with system size [205, 5, 241]. Indeed if one assumes that the amplitudes of the relaxation events are system size independent and that each elementary strain step of figure 5.1 is small enough as to single out an irreducible plastic unit[1] then one easily finds that for a localized quadrupole the average stress drop of the entire sample scales with the volume V of the samples while for system spanning shear bands the average stress drop scales with the size L of the systems.

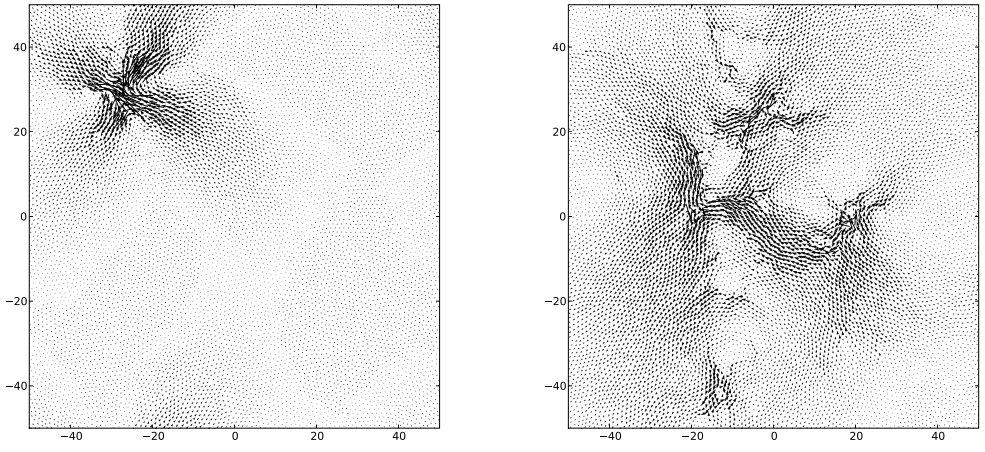

FIG. 5.2 : **Left :** Displacement field during a local rearrangement. **Right :** Displacement field ($\times 20$) associated with a more complex spatial structural rearrangement involving many vortices.

A precise analysis of the probability density functions (PDFs) of the stress, energy and strain increments can therefore inform us on the spatial organization of the plastic events. One therefore expects the average stress drops $\langle \Delta\sigma \rangle$ to scale as $\langle \Delta\sigma \rangle \propto N^{0.5}$ for localized events and $\langle \Delta\sigma \rangle \propto N^{1}$ for linear shear bands while for more complex geometries (fractal) or for an intermediate case one can expect an intermediate power exponent α verifying $\langle \Delta\sigma \rangle \propto N^{\alpha}$. Furthermore (following Maloney *et al* [205]) one can now derive the average energy drop scaling with system size. Indeed on average the energy released in the sudden drops in the stress-strain response of 5.1 in the plastic flow is exactly equal to the work done to elastically load the glass (in the elastic reversible branches of figure 5.1) and the equality reads [241] $\sigma_Y \langle \Delta\varepsilon \rangle V = \sigma_Y \frac{\langle \Delta\sigma \rangle}{\mu} V = \langle \Delta U \rangle$, where σ_Y is the average stress in the plastic regime or yield stress. The energy scaling follows immediately from this equality and one has $\langle \Delta U \rangle \propto N^{\beta}$ with $\alpha - \beta = 1$. The first equality of the last equation also allows to relate the average strain intervals between plastic jumps $\langle \Delta\varepsilon \rangle$ to the average stress jumps $\langle \Delta\sigma \rangle$, their proportionality guarantying that they follow the same scaling with system size $\langle \Delta\varepsilon \rangle \propto N^{\alpha}$. These results were discussed in detail in two-dimensional model glass

[1] If the elementary strain step is too large one can indeed observe simultaneously two localized events that would have been separated under a smaller strain step. This would yield a wrong estimate of the typical elementary stress relaxation and affect the distributions of figure 5.3.

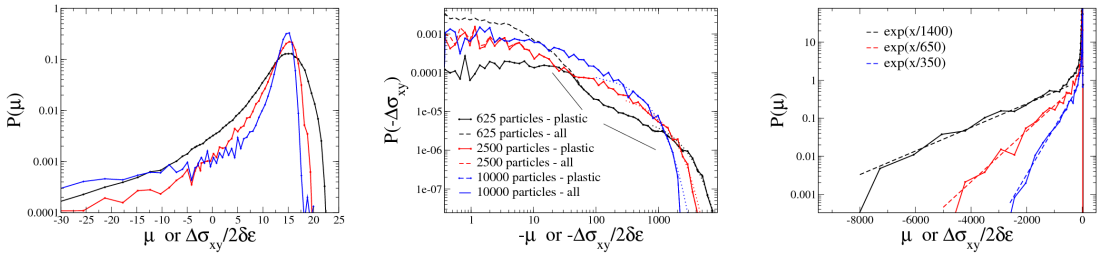

Fig. 5.3 : The three figures highlight different portions of the same distributions of stress increments (or equivalently the effective shear modulus) for the three sizes 25, 50 and 100 ULJ and the boundary conditions of figure 5.1. **Left :** Portion of the distribution dominated by the elastic response of the material. The position of the peak of the distribution corresponds to the macroscopic shear modulus of the model glasses.**Middle :** Log-log representation of the PDFs highlighting the intermediate values of stress drops. The black lines are guide for the eyes and are the power laws $\propto \mu^{-2}$ and $\propto \mu^{-0.8}$. The large dotted lines only visible for 625 and 2500 particles are the PDFs calculated over all the strain increments while the continuous lines are calculated over only plastic strain increments (see text). Finally the small dotted lines correspond to the exponential fits of the large stress drops. **Right :** Log-lin representation highlighting the large stress drops values of the PDFs and rescaled so that all exponential fits cross at the same point of coordinates (0,1).

systems [205] and [241] but also three-dimensional realistic simulations of metallic glasses [237]. While Maloney *et al* found scaling exponents $\alpha \sim 0.5$ and $\beta \sim -0.5$ consistent with lines of slip that extend along the length of the system, Lerner *et al* ($\alpha \sim 0.37$ and $\beta \sim -0.63$) and Bailey *et al* ($\alpha \sim 0.7$ and $\beta \sim -0.3$) in 3D found intermediate values that they attribute to a fractal geometry of the avalanches somewhere between localized and string like in two dimensions and between string like and planar in three dimensions. Here we reproduce these results on our polydisperse Lennard-Jones system. To do so we generated 24 square samples of size (Lx,Ly)=(25,25), 8 (50,50) and 8 (100,100). We then proceeded to a 400% quasistatic shear of these samples under both Lees-Edwards and rigid walls boundary conditions and for an elementary strain step of $\Delta\gamma_e = 10^{-4}$. We checked that this value of the elementary strain step was sufficient to resolve the elastic peak (figure 5.3 left) and that the PDFs (figure 5.3) were unaffected for a strain increment ten times smaller $\Delta\gamma_e = 10^{-5}$. In the calculation of the PDFs of figure 5.3 and figure 5.4 we have ignored the plastic events that occur in the transient regime ($\varepsilon \lesssim 2\%$). The PDFs of these transient events were calculated separately and were shown to be much smaller jumps in the noisy plateau region. The average energy loss (that can be obtained as the average stress jump times the elementary imposed deformation) is thus by at least one order of magnitude larger in the plateau than in the previous part. This suggests rather different types of microscopic response in the two different regions. The dynamics being dominated in the transient regime by small localized quadrupolar rearrangements (l.h.s. of figure 5.2) while extended shear bands become more frequent (r.h.s of figure 5.2)

in the plastic regime. Figure 5.3 highlights the three different regimes of values of the stress increments. On the left one sees that the distribution of these incremental stresses is peaked around the value given by the elastic response with an elastic shear modulus $\mu \sim 11.7$ and shows around this value softer, as well as more rigid, steps typically with a gaussian distribution. If one looks on the softer side the probability of finding large stress drops is accentuated and the middle figure 5.3 illustrates in log-log representation this intermediate regime corresponding to averagely large stress drops $-1000 < \Delta\sigma/2\delta\varepsilon < -1$. The crossover between a Gaussian distribution and the exponential cutoff for larger values gives the impression of an intermediate power law regime (see black segments for power laws $\propto \mu^{-2}$ and $\propto \mu^{-0.8}$ as a guide to the eyes. Note that on this figure we have separated the contributions from purely plastic strain increments (solid lines) from the total contribution from all strain intervals (dashed lines). Here a plastic strain increment was defined as a strain increment where the maximum displacement transversely to the direction of shear was more that 1% of the diameter of a particle. Finaly the figure on the right 5.3 illustrates the large stress drop exponential cutoffs. In figure 5.4 we proceed to the rescaling of the raw PDFs (insets) of the stress jumps, energy jumps and elastic strain intervals. We find in good agreement with Maloney *et al* that the curves scale with system size with the scalings $\langle\Delta\sigma\rangle \propto \frac{1}{L}$,$\langle\Delta E\rangle \propto \frac{1}{L}$ and $\langle\Delta\gamma\rangle \propto \frac{1}{L}$ corresponding to the power exponents $\alpha = 0.5$ and $\beta = -0.5$. This finding seems to corroborate the picture of the glass rearranging in the plastic flowing regime predominantly through the formation of slip lines (figure 5.2 r.h.s.). Yet this assertion needs to be nuanced as the scaling is valid on the exponential cutoffs of the PDFs and doesn't work as well for the 'power law' intermediate range of values. In fact we have checked on the samples containing 625 particles that about 25% of the plastic events (solid lines in figure 5.3) take values of instantaneous shear modulus μ larger than 1000 (or equivalently stress drop $\Delta\sigma$ larger than 0.1) i.e. in the exponential cutoff regime. Moreover these plastic events contribute for about 50% of the stress release in the plastic flow. Therefore from this analysis and contrary to what is suggested in [241] one cannot simply rule out a possible contribution of localized events to the dynamics of the glass, as about 50% of the energy dissipated is not shown to be associated to system spanning shear bands. In fact this is confirmed by a simple analysis of the structural rearrangements during plastic flow confirming qualitatively this picture of 25% of large system spanning events.

Let us at this point discuss also on the dependance of the stress fluctuations on the length scales at which we observe the systems. In the above arguments we have studied the average macroscopic stress fluctuations and we would like now to show how these findings are modified if one calculates rather than the PDFs of the macroscopic fields $\Delta\sigma$, ΔU the PDFs of their coarse grained counterparts $\Delta\sigma^W$, ΔU^W, where W is the length scale over which the local stress and energy increments are averaged. In contrast to the chapter 3 and 4 here we have calculated these coarse grained stresses by using a simple averaging of the usual Irving-Kirkwood stress formulation (see 3.38) over cells of diameter $d = L/n$ with n ranging from 3 to 26. This procedure was repeated for every configurations at regular strain

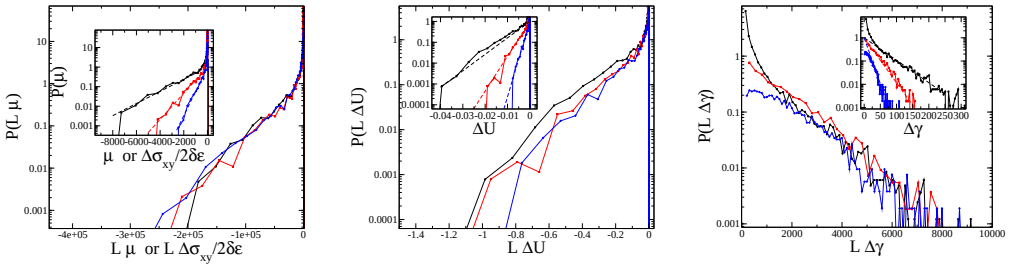

Fig. 5.4 : Raw PDFs in the insets and rescaled PDF in the main panels. **Left :** Stress drops. **Middle :** Energy drops. **Right :** Strain increments.

intervals of $\Delta\varepsilon = 5.10^{-4}$ of a sheared glass of size 104×104 containing 10000 particles for a total strain $5\% < \varepsilon < 10\%$. The PDFs is represented in log-log representation in figure 5.5 and illustrates the progressive transition from an approximately even PDF when calculated at the atomic level (green curve) to the asymmetric macroscopic PDF (black curve), with the exponential cutoff for large stress increments progressively pushed to lower and lower values as the coarse graining increases. Also on this figure the power law regime only barely visible in the macroscopic PDF (figure 5.3) is strongly enhanced (extending over almost three decades) when one calculates the PDF at the atomic level, the dashed line shows that this power law is roughly $\propto \Delta\sigma^{-1.7}$.

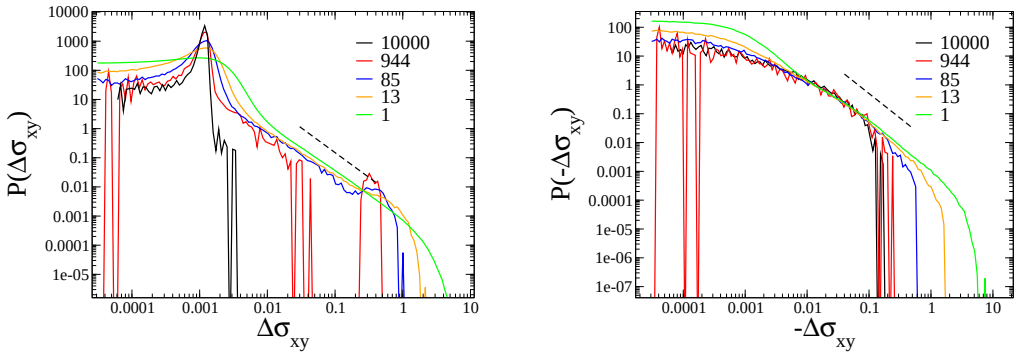

Fig. 5.5 : Log-log representation of the PDF of the stress drops where the stress are calculated over cells of different diameters ranging from the total sample of size 104×104 (macroscopic stress) to the site stress (stress calculated on a single particle) and going through cells of diameter $d = 104/3$, $104/10$ and $104/26$. The averages are calculated in the plastic flow for a total strain $5\% < \varepsilon < 10\%$. **Left :** Positive stress jumps. **Right :** Negative stress jumps. The dashed line represent a guide to the eyes for a power law $\propto \Delta\sigma_{xy}^{-1.7}$.

5.1.2 Fluctuating velocity profiles

The intermittent mechanical response observed in the previous paragraph is the macroscopic manifestation of strongly heterogeneous underlying deformation processes as illus-

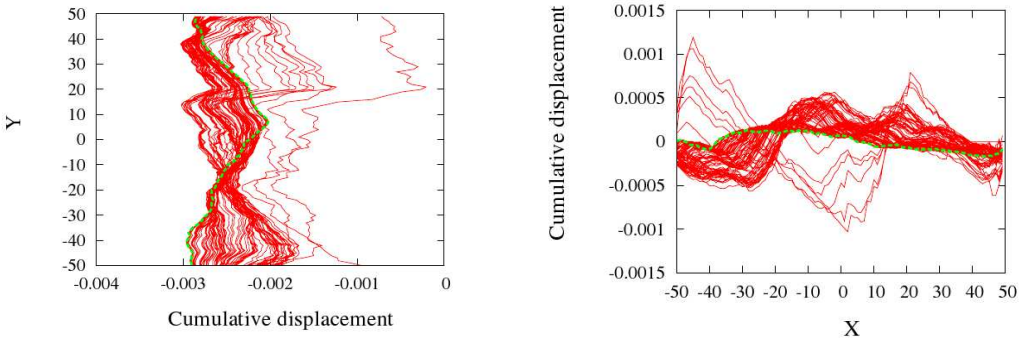

FIG. 5.6 : Velocity profiles. **Left :** Along the x direction, **right :** along the y direction.

trated in figure 5.2. One way to quantify the size of the rearranging regions is to compute the participation ratio τ for the non-affine displacement field associated with the event τ defined as,

$$\tau \equiv \frac{1}{\mathrm{N}} \cdot \frac{(\sum_i u_{n.a.}(i)^2)^2}{\sum_i u_{n.a.}(i)^4} \ , \tag{5.1}$$

where $u_{n.a.}(i)$ is the non-affine displacement of the particle i, that is the displacement after its usual affine shear component (corresponding to a uniform shear strain) has been removed. For rearrrangements involving the entire system $\tau \sim 1$ while for local quadrupolar events $\tau \to 0$. In order to get a schematic idea of the typical relaxation processes of the sheared glass it is interesting to study in details the displacement (and stress fields) induced by the two limiting rearrangements, namely the local quadrupole and shear band. For local plastic rearrangements one can identify the center of the plastic rearrangement by selecting the particle undergoing the largest non-affine displacement. This particle is at the center of a redistribution of shear stresses with an apparent symmetry characteristic of a quadrupole (or dipole of displacement field). As shown in [205, 5, 242] by moving in a coordinate system (ρ, θ) and projecting the corresponding radial and azimuthal part of the displacement field onto circular harmonics $e^{i.n.\theta}$ one gets the well-known (1/r)-dependence of the radial projection, along with $cos(2\theta)$ angular dependance. These events also conform rather well to the theoretical prediction of Eshelby for the stress redistribution associated to a plastic inclusion in an elastic homogeneous, linear and isotropic medium [243, 67] $\Delta\sigma_{xy} \propto \frac{cos(4\theta)}{r^2}$. As can be seen in figure 5.2 the local plastic events are alined with the directions of compression and extension of the macroscopic strain tensor. Due to its geometry the effect of such a plastic quadrupolar rearrangement is therefore expected to appear as a slip in the velocity profiles equivalently along the x and y axis. Under rigid walls boundary conditions at $y = \pm \mathrm{H}/2$, were H is the width of the sample, the extent of the vertical displacement will be limited, while as shown in figure 5.2 this is not the case for periodic Lees-Edwards boundary conditions. System spanning shear bands that are associated to a slip of one portion of the sample on the other along the x and y directions are on the other hand more sensitive to the boundary conditions. Indeed for rigid walls

the possibility of vertical system spanning shear bands is removed and shear bands will only form along the x axis resulting in an anisotropicity between the two directions. Under Lees-Edwards boundary conditions the vertical constraint is less stringent but the vertical shear bands must conform to the Bravais lattice imposed by the periodicity. As can be seen in figure 5.2 a vertical shear band has formed that seems to accomodate the Lees-Edwards boundary conditions by taking a complex not strictly linear form with some sort of kink near the top part of the sample. As illustrated in figures 5.6 the total contribution of all the plastic rearrangements leads to a slow convergence of the velocity profiles[2] towards the affine linear limit with strong fluctuations. Here we have calculated the cumulative non-affine displacement along the x and y direction of a 100×100 sample under Lee-Edwards BC and for a macroscopic strain ranging from 2.5% to 25% by strain steps of 0.25%. Each velocity profile is normalized by the total applied strain and represents therefore the average non-affine displacement per unit strain step $\delta\varepsilon = 0.0025\%$. It is quite stricking that the convergence on average to the linear profiles is not achieved even after 22.5% deformation of the sample. It is also interesting to note here that fluctuations in velocity profiles along the y axis converge faster to the linear profile than along the x axis, confirming the prediction that horizontal shear bands are favoured with respect to vertical shear bands in the case of Lees-Edwards BC[3]. After 22.5% deformation one sees indeed in figures 5.6 that the typical fluctuations along the x axis ($\Delta u_x \sim 10^{-4}$) are about ten times larger than along the y axis ($\Delta u_x \sim 10^{-5}$). Note that this anisotropy is consistent with the anisotropy observed in the faster relaxation of the self intermediate scattering function along the x direction and discussed in 4.2.3.

To make contact with the recent observations of shear banding in various experimental and numerical works as discussed in the introduction we detail here the spatio-temporal occurrence of the plastic rearrangements[4]. As shown in figure 5.7 for sufficiently large plastic events it is easy to identify the center line of such an elementary reorganization, because the displacements of the particles are so high that they lead to an inversion of the instantaneous 'velocity field' in the direction of the sollicitation, above and below the elementary shear bands. Besides the largest displacement inside the sample (located at the edge of a shear band) can reach more than 100 times the displacement imposed at the wall, i.e. it is close to one particle size in our case. Here in line with many experimental observation on foams [244, 245, 246, 238] we see in figure 5.7 that these elementary shear bands can take place anywhere in the sample, and not only at the boundaries, as observed experimentally elsewhere also on foams [10], leading once averaged over a sufficiently long strain interval to a linear velocity profile. We have checked on samples of different sizes and under Lees-Edwards and rigid BCs that the distribution of the distances between the centers of successive shear bands (figure 5.7) is exponential, with a characteristic length

[2] Here the simulation beeing quasistatic the notion of time is replaced by the macroscopic applied strain. Similarly by 'velocity field' we mean the displacement within a given strain interval

[3] Of course under rigid walls one cannot calculate a velocity profile along the y axis

[4] The following discussion is extracted from the paper [5]

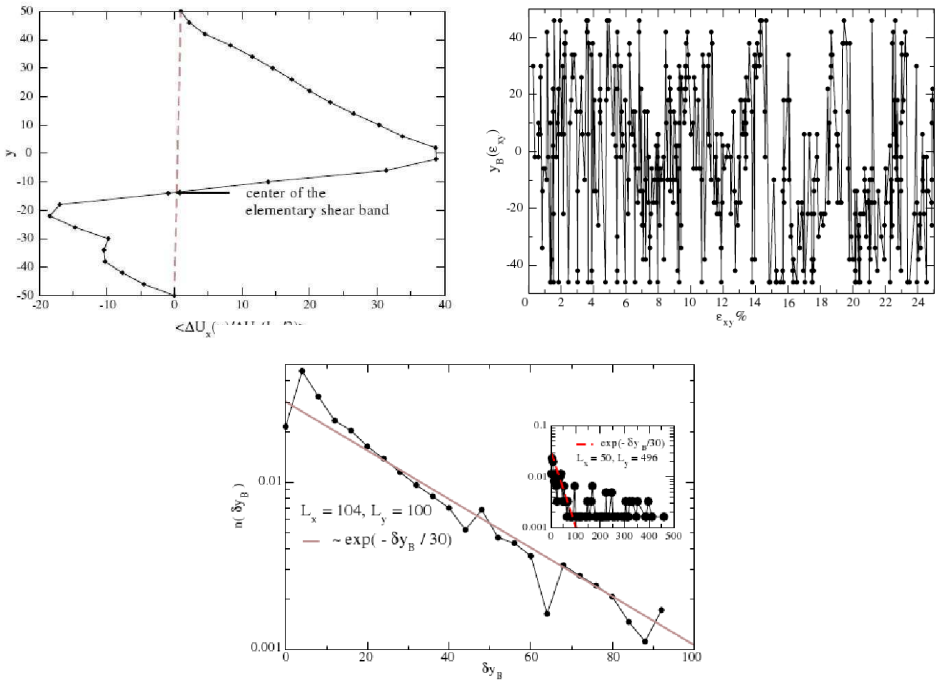

FIG. 5.7 : **Top left :** Averaged horizontal displacement associated to a single but large event. The y-position, where the non-affine displacement field is equal to zero, allows to determine the center of the elementary shear band. Distances are expressed in units of the average particle diameter a. **Top right :** Position y_B of the centers of elementary shear bands (determined as described previously), here for the 5000 first steps. No localization appears, even for very large deformation (170%, not shown here). **Bottom :** Distribution of the distances δy_B between successive elementary shear bands for $L_x = 104$, $L_y = 100$. The characteristic distance of the exponential fit is $\xi \sim 30a$. Inset: same distribution for the largest system size $L_y = 496$. The characteristic distance is the same, ξ.

$\xi_B \sim 30a$, independent on the system size, that corresponds to the size ξ of the rotational structures that have been identified in the elastic response of the system. The characteristic distance between successive elementary shear bands in our system is thus equal to the width of the elementary shear band itself. From these results one can tentatively propose a picture in which the rearranging zones propagate essentially in a random-walk manner with a step size of approximately $30a$, confined by the two boundaries. The distribution of distances covered by the upper wall between successive occurrence of elementary shear bands (figure 5.3) is also exponential, with a characteristic length l_c, that does not depend significantly on the system size ($l_c \sim 0.13a$ in our case). We can find an explanation for the order of magnitude of this length l_c, by dividing it by the radius $\xi/2$ of a vortex. If we assume that the deformation is localized within a 'weak' region of thickness $\xi/2$, and that the system outside this shear band is essentially unstrained, the characteristic distance l_c covered by the wall between successive occurrence of elementary shear bands corresponds to a deformation of $2l_c/\xi \simeq 1\%$ within the weak region. This order of magnitude is approximately equal to the elastic threshold ε_{xy} for the strain within the elementary shear band. The elementary shear bands can thus be seen as weak locations where all the deformation concentrates, giving rise -from a given local strain threshold- to a large plastic event that relaxes all the accumulated elastic energy. The next shear band event is spatially strongly correlated, within a distance ξ. Within this picture, we can simply describe the construction of the plastic flow 'velocity' profile as a diffusive process. For a sample with transverse size L_y, the number of bands that are created by a total strain ε is $\varepsilon L_y/l_c = (\varepsilon L_y)/(\varepsilon^p_{xy}\xi)$. If the bands are created in a spatially correlated manner, with a typical distance ξ, this will result in an effective diffusion coefficient for these plastic events of the form $D_{eff} = \xi^2 \times (L_y/\varepsilon_{xy}\xi)$ (here the strain plays the role of time). The shear will diffuse through the sample over a 'time' scale $L_y\varepsilon_{xy}/\xi$. For a sample of width $L_y \sim 100a$ and with $\xi \simeq 30a$ the corresponding strain is small, and the boundaries will almost immediately limit shear band diffusion. The shear profile then is created by essentially independent rearrangements. An essentially homogeneous profile will be obtained when the rearrangement density becomes of the order of the inverse of the particle size, i.e. $\varepsilon \sim \varepsilon^p_{xy}\xi/a$. In a larger sample, on the other hand, this picture suggests that the time (or strain) scale for establishing a homogeneous profile may be very large, in fact proportional to system size, which could explain the commonly observed tendency towards shear localization in such systems. In the next section, we explore the effect of the two kinds of dissipative events described here (quadrupolar events and elementary shear band), on the local dynamics of the particles.

Let us summarize the results obtained in this section on the one hand from the analysis of the macroscopical mechanical response of the glasses and on the other hand from the study of the velocity profiles of the sheared materials.

- First the scaling of the stress drops of large events with system size has shown that the relaxation and energy dissipation in quasistatically sheared glasses occurs through

nonlocal system spanning and approximately linear avalanches in the system that contribute to about half the dissipation but also through other more localized plastic rearrangements that do not verify the scaling with system size and contribute to the other half of the dissipated energy.

- Second we showed that the successive plastic rearrangements also present some spatial correlation over the typical length scale ξ, but that this cooperative (diffuse) behavior of the plastic rearrangements is somehow limited by finite size effect making an analysis in term of spatialy random occurances of plastic events valid beyond a short characteristic strain scale of about 1%. This is consistant with observation of linear average velocity profiles in simulations on small systems while velocity profiles obtained experimentaly on large systems often display persistant shear banding.

In the next section we propose to rationalize these observation by proposing as a first approximation a simple description of the sheared glass as composed essentialy of uncorrelated localized quadrupolar rearrangements. We confront the results of this simple model to the simulations allowing to clarify the relative contribution of localized quadrupolar events vs extended plastic rearranging units (shear bands) to the mechanical response of quasistatically sheared glasses. We conclude this section by discussing the successes and limitations of this approach.

5.2 Minimal model : sum of quadrupoles

5.2.1 Numerical results assuming uncorrelated localized quadrupolar events.

In order to test if the stress drop PDFs presented in the previous section can be reproduced by a simple model with local uncorrelated quadrupoles we generate $N_e = 10^5$ plastic quadrupolar events, with a stress field perturbation $\Delta\sigma_{xy}(A) = \frac{A cos(4\theta)}{r^2}$ as seen in figure 5.8, discretized on a square grid of size L. In addition the amplitudes A of the quadrupoles are drawn from the three following distributions, respectively an exponential PDF $P_E(A)$, a normal PDF $P_N(A)$ and a Pareto PDF $P_P(A)$ defined as,

$$P_E(A) = \frac{1}{\sigma_A} \exp\left(\frac{-A}{\sigma_A}\right) , \tag{5.2}$$

$$P_N(A) = \frac{1}{\sqrt{2\pi\sigma_A}} \exp\left(\frac{-A^2}{2\sigma_A^2}\right) , \tag{5.3}$$

$$P_P(A) = c\frac{d^c}{(d+A)^{c+1}} . \tag{5.4}$$

We then calculate the distribution of stress increments $P(\Delta\sigma^W)$ averaged over cells of various lengths W over the entire square sample and for periodic boundary conditions.

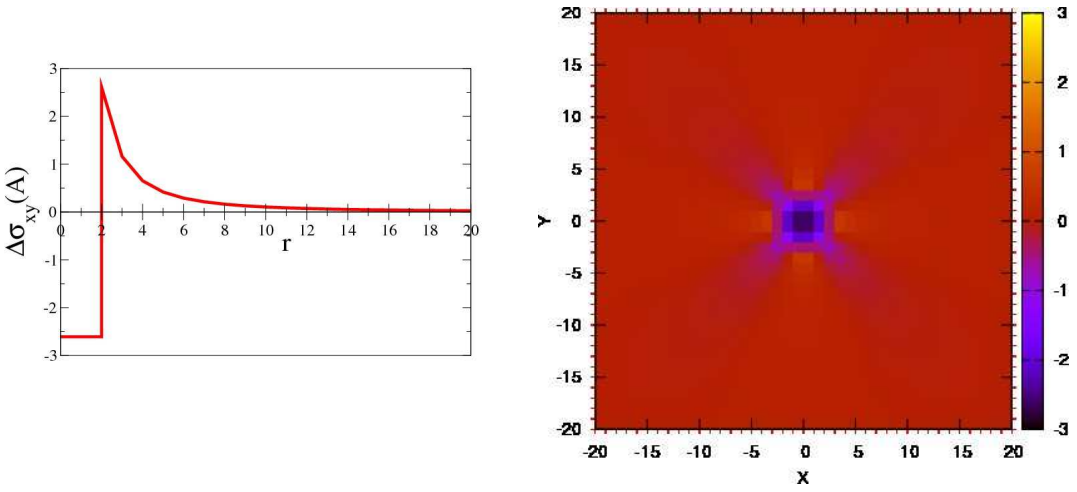

Fig. 5.8 : Typical quadrupole used in the numerical calculations, of amplitude A (here A ~ 0.25) diameter of the core $d = 4$. **Left :** values of the stress drop along a line crossing the core of the quadrupole. **Right :** discretized values of the spatial stress redistribution.

This simple numerical calculation allowed us to directly test the influence on the PDFs of the size of the system, the coarse-graining over which are calculated the local stress increments $\Delta\sigma^{W}$ (see figure 5.5) and the choice of the distribution of amplitudes A of the quadrupoles and to compare these predictions with the simulations obtained on the realistic glass. On the first couple of figures 5.9, which is the analogous of figure 5.5 for the numerical model, we see that the features of 5.5 are qualitatively retrieved. First as is the case in the real glass the local PDF initially symmetric for small values of W becomes more and more asymmetric as W tends to the size of the sample. The exponential cutoff is retrieved for large values of the stress drops (or increments) and is maintained for all coarse-graining scales for negative values of the stresses while shifted to lower and lower values again in accord with figure 5.5. Finally and unexpectedly the power law decay of the PDF in the intermediate regime of stress values ($P(\Delta\sigma) \propto \Delta\sigma_{xy}^{-1.8}$ represented by the dashed line) is in good agreement with the value obtained on the real glass ($P(\Delta\sigma) \propto \Delta\sigma_{xy}^{-1.7}$). The next couple of figures represent the PDF calculated when the amplitude of the random events rather than chosen from the exponential PDF $P_E(A)$ are drawn from the Pareto $P_P(A)$ and normal $P_N(A)$ laws. Interestingly we see that as expected (see next section) it is indeed this distribution of the amplitude of the nucleus of the quadrupolar event that dictates the large stress increments cutoffs along with the cutoff in the distribution of the macroscopic stress drops. With these qualitative observations in mind we now proceed in the next section to the analytical resolution of this model of uncorrelated local plastic events.

5.2.2 Analytical calculation of the model.

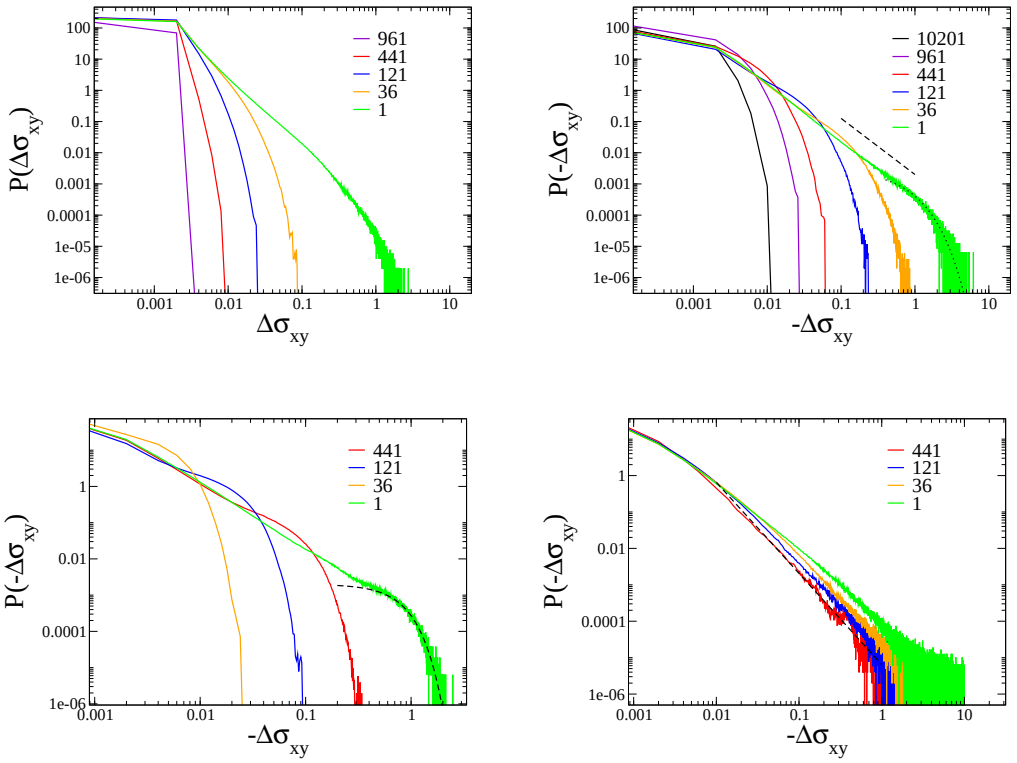

Fig. 5.9 : Log-log representation of the PDF of the stress drops where the stress are calculated over square cells of different sizes L ranging from the total sample of size 104×104 (macroscopic stress) to the site stress (stress calculated on a single mesh of the grid) and going through cells of sizes L = 6, 11, 21 and 31. The averages are calculated for a total number $N_e = 10^5$ of simulated quadrupolar events . **Top left :** Positive stress jumps for an exponential distribution $P_E(A)$ of the amplitude A of the plastic events. **Top right :** Negative stress jumps for $P_E(A)$. The dashed line represent a guide to the eyes for a power law $\propto \Delta\sigma_{xy}^{-1.8}$. The dotted lines correspond to an exponential fit $\propto \exp(-\Delta\sigma_{xy}/0.5)$.**Bottom left :** Negative stress jumps for $P_N(A)$. The dashed lines marks the limiting Gaussian behavior of the PDF $\propto \exp(-\Delta\sigma_{xy}^2/(2 \cdot 0.5^2)$. **Bottom right :** Negative stress jumps for $P_P(A)$. The dashed lines marks the limiting power law behavior of the PDF $\propto \Delta\sigma_{xy}^{-2.5}$.

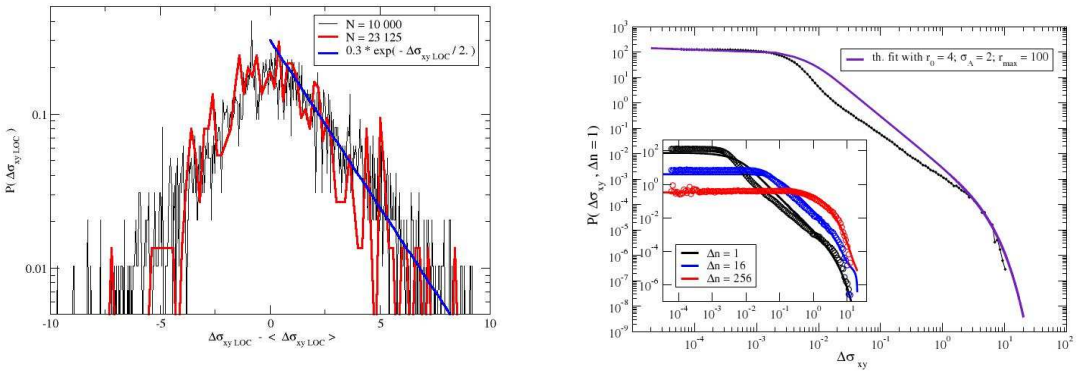

Fig. 5.10 : **Left :** Distribution of shear stress releases in the center of the quadrupoles, during a plastic event. The fit is exponential with a characteristic $\Delta\sigma = 2$.**Right :** Comparison of the distribution $P(\Delta\sigma_{xy}, \Delta n = 1)$ with the theoretical fit discussed in the text. The parameters of the fit are indicated in the legend box. Inset: evolution of the distribution with Δn. The symbols are the numerical results. The lines are obtained by a simple convolution of the theoretical curve obtained for $\Delta n = 1$. It assumes no temporal correlation between successive events.

Analytical calculation without the angular dependence. In the following[5], we take the quadrupolar isolated event as the elementary building block to explain the plastic deformation of the material, and we propose a simple model that describes the plastic deformation (as shown in the redistribution of stresses) as a sum of uncorrelated quadrupoles of random amplitude A.

We first identify the distribution P(A) in our system. As shown by Picard et al. [247], a quadrupolar event involves in 2D a long-range redistribution of stresses, due to a local pure shear. The corresponding stress change is of the form.

$$\Delta\sigma_{xy}(r,\theta) \equiv \left\{ \begin{array}{c} \mathrm{A}\frac{r_0^2}{r^2} \quad , \text{ if } r_0 \leqslant r \leqslant r_{max} \\ \mathrm{A} \quad , \text{ if } 0 \leqslant r \leqslant r_0 \end{array} \right\} \tag{5.5}$$

where r_0 and r_{max} are respectively the typical size of the quadrupole and the size of the system, A is the amplitude of the quadrupoles, and $\Delta\sigma_{xy}$ denotes the incremental shear stress. We have neglected in this expression the quadrupolar angular dependence of the stress field and only considered its $\frac{1}{r^2}$ spatial decay [6] The distribution of P(A) is measured in our data (see figure 5.10). It corresponds to the incremental stress at the center of the quadrupole, that is at the place where the displacement is maximum. The best fit is exponential, with $\mathrm{P(A)} = \frac{1}{2\sigma_\mathrm{A}} \cdot \exp(-\frac{|\mathrm{A}|}{\sigma_\mathrm{A}})$ and $\sigma_\mathrm{A} = 2$ appears to be the characteristic amplitude of the quadrupolar event. It is independent of the system size, unlike the

[5] This part is extracted from our paper [6].

[6] The angular dependence mainly contributes by a scaling factor, and affect the weight of small $\Delta\sigma$ in a logarithmic way in the final result. We derive this result in 5.2.2 and proceed here with the simpler approach that yields qualitatively correct results.

distribution of macroscopic stress release that is $\propto 1/\mathrm{L}$ (figure 5.4), and appears in figure 5.10 symmetric. In reality we expect this symmetry to arise due to the fact that it is in practice difficult to select in a real simulation the core of a quadrupolar event, and if the particle that has the greatest displacement is slightly on the edge of the nucleus $r \simeq r_0$ of the plastic event we expect indeed an apparent symmetrical distribution P(A).

Using the exponential distribution P(A) shown above, we can now reproduce the distribution $\mathrm{P}(\Delta\sigma = s, \Delta n = 1)$ of the incremental shear stress $\Delta\sigma_{xy}$ averaged over the whole system. Neglecting the angular dependence of $\Delta\sigma_{xy}$ as in equation 5.5, we show that, for a given amplitude A, there is a simple bijective relation between the shear stress $\Delta\sigma_{xy}$ and the radial coordinate r. We can thus write $\mathrm{P_A}(\Delta\sigma_{xy})d\Delta\sigma_{xy} = \mathrm{P}(r)dr$, with $\mathrm{P}(r)dr = 2\pi r/\mathrm{V}dr$. Using Eq.5.5, we get

$$\mathrm{P_A}(\Delta\sigma_{xy}) = \frac{\pi \mathrm{A} r_0^2}{\mathrm{V}\Delta\sigma^2} \tag{5.6}$$

with

$$|\mathrm{A}|\frac{r_0^2}{r_{max}^2} \leqslant |\Delta\sigma_{xy}| \leqslant |\mathrm{A}| \tag{5.7}$$

In the following, we will consider only the case $\mathrm{A} > 0$, the opposite case giving the symmetric distribution corresponding to $\Delta\sigma_{xy} < 0$. Assuming that the successive events contribute independently to the total distribution $\mathrm{P}_{th}(\Delta\sigma_{xy})$ (an assumption justified by the fact that this distribution is averaged over the time origins), the average probability of having an incremental stress $\Delta\sigma_{xy}$ inside the system is thus obtained by summing over all quadrupolar events

$$\mathrm{P}_{th}(\Delta\sigma_{xy}) = c\int_{\Delta\sigma_{xy}}^{\Delta\sigma_{xy}\frac{r_{max}^2}{r_0}} \mathrm{P_A}(\Delta\sigma_{xy})\mathrm{P}(\mathrm{A})d\mathrm{A} \tag{5.8}$$

with an additional normalization factor c due to the limited range of allowed amplitudes. This gives

$$\begin{aligned}\mathrm{P}_{th}(\Delta\sigma_{xy}) = c\frac{\pi r_0^2}{2\mathrm{V}}\frac{1}{\Delta\sigma_{xy}^2}((\sigma_\mathrm{A} + \Delta\sigma_{xy})exp(-\Delta\sigma_{xy}/\sigma_\mathrm{A}) \\ -(\sigma_\mathrm{A} + \sigma_{xy}\frac{r_{max}^2}{r_0^2})exp(-\Delta\sigma_{xy}.r_{max}^2/(\sigma_\mathrm{A}.r_0^2)))\end{aligned} \tag{5.9}$$

We show here that the upper exponential cut-off is proportional to $\exp(-\Delta\sigma_{xy}/\sigma_\mathrm{A})$ and that the low $\Delta\sigma$ behavior[7] is dominated by finite size scaling proportional to $\exp(-\Delta\sigma_{xy}.r_{max}^2/(\sigma_\mathrm{A}.r_0^2))$. We have plotted this function in figure 5.10, and compared it with the result obtained numerically. We find a good agreement with the numerical result, for $\sigma_\mathrm{A} = 2$, $r_{max} = \mathrm{L} = 100$ and $r_0 = 4$. The parameter r_0 is the unique free parameter of the fit since r_{max} scales like the system size and the fitted value for σ_A corresponds to the value obtained in the measured distribution of P(A) (see figure 5.10), thus confirming our simple model. The small value obtained for r_0 shows that the plastic quadrupolar events are localized.

[7] with a logarithmic divergence if the angular dependence is taken into account see 5.2.2.

We can now compare the distribution $\mathrm{P}(\Delta\sigma_{xy}, \Delta n)$ with the theoretical distribution obtained by a simple convolution of the expression 5.9. The theoretical distribution for $\mathrm{P}_{th}(\Delta\sigma_{xy}, \Delta n)$ is obtained by the inverse Fourier Transform $\mathrm{TF}^{-1}(\widetilde{\mathrm{P}_{th}}^{\Delta n}(\Delta\widetilde{\sigma}_{xy}))$ of the Fourier transform of the theoretical distribution P_{th} obtained for $\Delta n = 1$. This convolution assumes the absence of temporal correlations between successive evolutions of $\Delta\sigma_{xy}$, as will be shown in section 5.4.2 is true. We see in figure 5.10, that both numerical and theoretical curves are in very good agreement for a large range of Δn, and that the agreement is even better for large Δn where plastic events are the main contribution to the distribution. This figure thus supports strongly our model, even for large Δn.

Analytical calculation with the angular dependance. The angular dependence mainly contributes by a scaling factor, and affects the weight of small $\Delta\sigma$ in a logarithmic way in the final result. Here we derive this result. When considering the angular dependance of the stress perturbation one needs to replace the expression of $\Delta\sigma_{xy}$ in equation 5.5 (here we omit the tensorial indexes xy) by $\Delta\sigma = \Delta\sigma^{\mathrm{A}}_{max} \cdot c$, where $\Delta\sigma^{\mathrm{A}}_{max} = \mathrm{A}\left(\frac{r_0}{r}\right)^2$ (as in 5.5) and $c = \cos(4\theta)$. Along similar lines of reasoning as what is presented in equation 5.6 one can introduce $\mathrm{P}_2(c) = \frac{1}{\pi}\frac{1}{\sqrt{1-c^2}}$ and $\mathrm{P}_1^{(\mathrm{A})}(\Delta\sigma_{max}) = \frac{1}{\alpha^2-1}\frac{\mathrm{A}}{\Delta\sigma^2_{max}}$ ($\alpha = r_{max}/r_0$), which satisfy,

$$\mathrm{P}^{(\mathrm{A})}(\Delta\sigma) = \int_{-1}^{1} \mathrm{P}_2(c)\mathrm{P}_1^{(\mathrm{A})}\left(\frac{\Delta\sigma}{c}\right)\frac{dc}{c} \ . \tag{5.10}$$

For $\Delta\sigma > 0$ (the derivation is identical for $\Delta\sigma < 0$) one can now average over $\mathrm{P}(\mathrm{A})$ yielding,

$$\mathrm{P}(\Delta\sigma) = \int_0^1 \frac{dc}{\pi}\frac{c}{\sqrt{1-c^2}}\frac{1}{\alpha^2-1}\frac{1}{d}\int_{\frac{\Delta\sigma}{c}}^{\alpha^2\frac{\Delta\sigma}{c}} d\mathrm{A}\mathrm{A}\exp\left(\frac{-\mathrm{A}}{\sigma_{\mathrm{A}}}\right) \ . \tag{5.11}$$

This expression can then be rewritten, after some simple algebra, in the following simplified form,

$$\mathrm{P}(\Delta\sigma) = \frac{1}{d\pi}\frac{1}{\alpha^2-1}\frac{d}{\Delta\sigma}\left[f\left(\frac{\Delta\sigma}{d}\right) - f\left(\frac{\alpha^2\Delta\sigma}{d}\right)\right] \ , \tag{5.12}$$

where,

$$x \cdot f(x) = \int_0^1 \frac{dc}{\sqrt{1-c^2}}\exp\left(\frac{-x}{c}\right)\left[x + \frac{1}{c}\right] \ . \tag{5.13}$$

After a rather cumbersome algebra one obtains the following expansion of the function $\mathrm{I}(x) = x \cdot f(x)$,

$$\mathrm{I}(x) = 1 + \frac{x^2}{2}\log(x) - (1 + 2\log(2) + 2c)\frac{x^2}{4} + o(x^3) \ . \tag{5.14}$$

Reporting this expression in 5.11 and after simplification gives in the limit $\Delta\sigma \to 0$,

$$\mathrm{P}(\Delta\sigma) \sim -\frac{\alpha^2+1}{d\pi}\log(\frac{\Delta\sigma}{d}) \ . \tag{5.15}$$

This calculation concludes our approach of the dynamics of the sheared glass in terms of local quadrupolar uncorrelated events. We have shown that while this simple approximation seems to reproduce qualitatively rather well the local dynamics it is inherently limited

in describing nonlocal correlation in space as well as in time. In the following section we focus on these aspects of the spatio-temporal dynamics and in particular on the notion of dynamical heterogeneity.

5.3 Statistical tools to analyse the heterogeneous flow

5.3.1 Static correlation functions

Equilibrium [8] probability densities and distribution functions allow for an efficient description of the microscopic structure of the system and provide a quantitative measure of the correlations between the positions of different particles. It is also remarkable that these distribution functions are generally sufficient to allow for the calculation of most equilibrium properties of the system. The 2-particle distribution function is defined as,

$$g(\overrightarrow{r_1}, \overrightarrow{r_2}) = \frac{P_N^2(\overrightarrow{r_1}, \overrightarrow{r_2})}{P_N^1(\overrightarrow{r_1}) P_N^1(\overrightarrow{r_2})} = V^2 P_N^2(\overrightarrow{r_1}, \overrightarrow{r_2}) \ , \tag{5.16}$$

where $P_N^n(\overrightarrow{r_1}, ..., \overrightarrow{r_n})$ is the n-body probability density and N is the number of particles. Note that the second equality is valid in the case of an homogeneous system where spatial translation invariance is satisfied, one can then write to simplify $g(\overrightarrow{r_1}, \overrightarrow{r_2}) = g(\overrightarrow{r_2} - \overrightarrow{r_1})$.

This distribution function can be simply related to the density fluctuations autocorrelation function,

$$H(\overrightarrow{r}, \overrightarrow{r'}) = \frac{1}{N} \langle \{\rho(\overrightarrow{r'}) - <\rho(\overrightarrow{r'})>\} \{\rho(\overrightarrow{r'} + \overrightarrow{r}) - <\rho(\overrightarrow{r'} + \overrightarrow{r})>\} \rangle \ , \tag{5.17}$$

where particle density at the position $\overrightarrow{r}$ is $\rho(\overrightarrow{r}) = \sum_{i=1}^{N} \delta(\overrightarrow{r} - \overrightarrow{r_i})$. For an homogeneous system we can integrate $H(\overrightarrow{r}, \overrightarrow{r'})$ over $\overrightarrow{r'}$ to obtain a function independent of the origin $\overrightarrow{r'}$ related to $g(\overrightarrow{r})$ by:

$$H(\overrightarrow{r}) = \frac{1}{N} \sum_{i}^{N} \sum_{j \neq i}^{N} < \delta(\overrightarrow{r} + \overrightarrow{r_i} - \overrightarrow{r_j}) > + \delta(\overrightarrow{r}) - \rho = \rho g(\overrightarrow{r}) + \delta(\overrightarrow{r}) - \rho \ . \tag{5.18}$$

In figure 5.11 we have shown the radial distribution function $g(r)$ at zero temperature. This function describes the spatial organization locally around each atom of the simulation box, considering the atoms as equivalent. This function informs us on the molecular order, and we therefore see in contrast with a crystal, that there is no apparent long range order as after a few interatomic distances the particles organize independently. In figure 5.11 we can also see that $g(r)$ does not depend significantly on the temperature around the glass transition temperature where the dynamical properties of the supercooled liquid change abruptly (divergence of the relaxation times of the autocorrelation functions). Therefore

[8] This paragraph is based on the book 'Theory of simple liquids' by Hansen and McDonald [248]

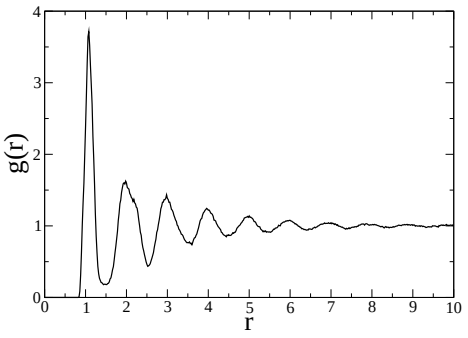

FIG. 5.11 : Radial distribution function calculated on a 104×104 sample with Lees Edwards boundary conditions.

the static correlation functions presented here does not allow us to distinguish a liquid from a glass. To gain additional information into the relation between structure and dynamics one needs to consider more complex correlation functions where time appears explicitly.

5.3.2 2-point correlation functions.

Two-times correlation functions[9]**.** The correlation function of two dynamical variables [248] $\mathrm{A}(t) \equiv \mathrm{A}[\overrightarrow{r}^{\mathrm{N}}(t), \overrightarrow{p}^{\mathrm{N}}(t)]$ and $\mathrm{B}(t) \equiv \mathrm{B}[\overrightarrow{r}^{\mathrm{N}}(t), \overrightarrow{p}^{\mathrm{N}}(t)]$ writes $\mathrm{C_{BA}}(t,s) =< \mathrm{B}(t+s)\mathrm{A}(s) >$ where the average $<>$ is defined either as an ensemble average as:

$$< \mathrm{B}(t+s)\mathrm{A}(s) >= \int \mathrm{B}[\overrightarrow{r}^{\mathrm{N}}(t+s), \overrightarrow{p}^{\mathrm{N}}(t+s)]\mathrm{A}[\overrightarrow{r}^{\mathrm{N}}(s), \overrightarrow{p}^{\mathrm{N}}(s)] f_0^{\mathrm{N}}[\overrightarrow{r}^{\mathrm{N}}(s), \overrightarrow{p}^{\mathrm{N}}(s)] d\overrightarrow{r}^{\mathrm{N}}(s) d\overrightarrow{p}^{\mathrm{N}}(s) \ , \tag{5.19}$$

where $f_0^{\mathrm{N}}[\overrightarrow{r}^{\mathrm{N}}(s), \overrightarrow{p}^{\mathrm{N}}(s)]$ is the equilibrium density probability (this definition of the averaging is difficult to implement in practice for the case of glasses where the equilibrium state is not known), either as a sliding average:

$$< \mathrm{B}(t+s)\mathrm{A}(s) >= \lim_{\tau \to \infty} \frac{1}{\tau} \int_0^{\tau} \mathrm{B}(t+s+t')\mathrm{A}(s+t')dt' \ . \tag{5.20}$$

In the time translation invariant case $\mathrm{C_{BA}}(t,s)$ is independent of the choice of s, and the correlation function is called stationary with respect to s. In our simulation the calculation of $\mathrm{C_{BA}}$ at a given time t is obtained by averaging the product $\mathrm{B}(t+s)\mathrm{A}(s)$ over a great number of origins s. In this section we have mainly looked at the observables $\rho(\overrightarrow{r}, t)$ and $\rho_\sigma(\overrightarrow{r}, t) = \sigma_{xy}(\overrightarrow{r}, t)$. Also of interest is the spatially average two-times autocorrelation function of these densities:

$$\mathrm{C}(dt, t) = \overline{\langle \rho(\overrightarrow{r}, t+dt)\rho(\overrightarrow{r}, t) \rangle} = \mathrm{C}(dt) \ , \tag{5.21}$$

[9] In our quasistatic simulations time does not appear explicitly and one must replace in everything that follows time by the number of deformation steps or strain.

where the last equality assumes time translation invariance and where $\overline{A}$ represents a spatial averaging.

In the actual algorithms we have access to the site shear stress $\sigma_{xy,i}(t)$[10](we write in the following $\sigma_i(t)$ to simplify the notation) that applies on each particle i of the system and the discrete version of equation 5.22 is[11]:

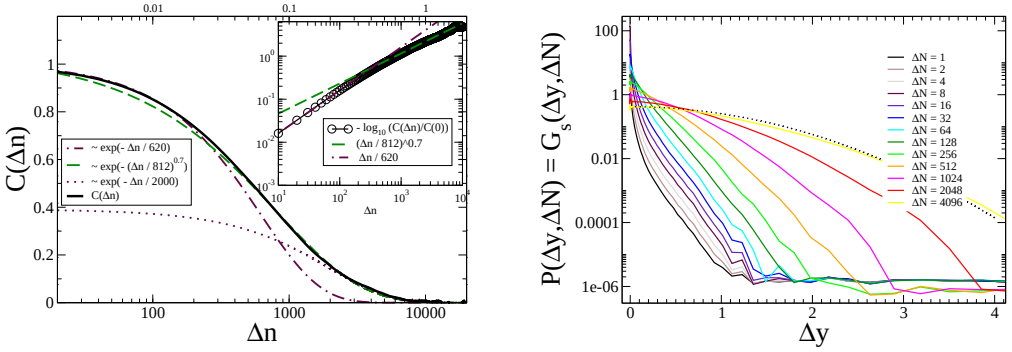

FIG. 5.12 : **Left :** Autocorrelation function of the shear stress computed on each particle and averaged over the whole sample, as a function of time (applied shear strain). The nature of the fits is indicated in the legend box. Inset : Logarithm of the autocorrelation function of the shear stress, in log-log scale, in order to determine the exponent of the corresponding stretched exponential. **Right :** Probability distribution function $P(\Delta y, \Delta N)$ or equivalently van Hove function $G_s(\Delta y, \Delta N)$ of the transverse displacement Δy for $\Delta N = 1, 2, 4, 8, 16, 32, 64....$ The log-lin scale illustrates the deviation from the Fickian behavior and the exponential tail of the distributions. The dotted line is a Gaussian fit for large ΔN where the Fickian behavior is recovered.

$$C(dt) = \frac{1}{N}\langle \sum_{i=1}^{N}\sum_{j=1}^{N} \rho_i(0)\rho_j(t)\delta(\overrightarrow{r_i}(0) - \overrightarrow{r_j}(t))\rangle \ , \tag{5.22}$$

where $\rho_j(t) = 1$ when one calculates the particle density autocorrelation function and $\rho_j(t) = \sigma_j(t)$ for the stress autocorrelation function. In general it is the Fourier transform $F(\overrightarrow{k}, t) = \frac{1}{N}\langle\rho(\overrightarrow{k}, t)\rho(-\overrightarrow{k}, 0)\rangle$ of the autocorrelation function 5.22 that is computed. This function is called intermediate scattering function and in figure 5.12 we report it for both the density and stress autocorrelation functions. More precisely we plot the self part of this function defined here as,

$$F_s(\overrightarrow{k}, t) = \frac{1}{N}\sum_i \rho_i(0)\rho_i(t)\cos\left[\overrightarrow{k}\cdot(\overrightarrow{r_i}(t) - \overrightarrow{r_i}(0))\right] \tag{5.23}$$

We have calculated these autocorrelation function for time origins t in the plastic flowing regime (i.e. for strains $\varepsilon > 1\%$). We have checked that time translational invariance is verified in this regime and in figure 5.12 we represent $C(dt)$ normalized to 1 for $t = 0$

[10]With the site stress tensor defined in 3.14 [120].

[11]Note that this expression corresponds to the Van Hove function defined in 5.25 and taken at $\overrightarrow{r} = \overrightarrow{0}$

both for displacements and stress tensors. These results compare well with what is usually observed in glassy materials [249]. One can see on both curves a first zone (for short times) where the autocorrelation function decreases slowly [12] and the function decays exponentially to zero only for much longer times of the order of N = 2000. This plateau regime is usually referred to as β relaxation. One can understand this regime intuitively in terms of a caging effect for the particles by their surrounding atoms and therefore slowing down the decay of the correlation function. It is interesting to note that while for long times one usually observe in aging glassy materials a Kohlrausch-Williams-Watts stretched-exponential decay of the autocorrelation function $C(t) = A\exp(-(t/\tau)^{\beta})$ with $\beta \leqslant 1$, here the presence an external drive of the system seems to cause a purely exponential relaxation at long times.

Temporal generalization of the correlation function $H(\overrightarrow{r}, \overrightarrow{r'})$. $H(\overrightarrow{r}, \overrightarrow{r'})$ can be generalized by constructing the two-time density correlation function $G(\overrightarrow{r}, \overrightarrow{r'}, t)$ as:

$$G(\overrightarrow{r}, \overrightarrow{r'}, t) = \frac{1}{N} < \rho(\overrightarrow{r'} + \overrightarrow{r}, t)\rho(\overrightarrow{r'}, 0) > \quad . \tag{5.24}$$

Expanding the density formulations and by integrating over $\overrightarrow{r'}$ (homogeneity hypothesis) one obtains the time and space pair correlation function called van Hove function [248]:

$$G(\overrightarrow{r}, t) = \frac{1}{N}\langle \sum_{i=1}^{N}\sum_{j=1}^{N} \delta(\overrightarrow{r} + \overrightarrow{r_i}(0) - \overrightarrow{r_j}(t))\rangle = \frac{\langle \rho(\overrightarrow{r}, t)\rho(\overrightarrow{0}, 0)\rangle}{\rho} \quad . \tag{5.25}$$

The van Hove function can be separated in two contributions:

$$G(\overrightarrow{r}, t) = G_s(\overrightarrow{r}, t) + G_d(\overrightarrow{r}, t) \tag{5.26}$$

where

$$G_s(\overrightarrow{r}, t) = \frac{1}{N}\langle \sum_{i=1}^{N} \delta(\overrightarrow{r} + \overrightarrow{r_i}(0) - \overrightarrow{r_i}(t))\rangle. \tag{5.27}$$

$G(\overrightarrow{r}, t)d\overrightarrow{r}$ corresponds to the probability to find the particle i at $\overrightarrow{r}$ within $d\overrightarrow{r}$ knowing that particle j was at the origin $\overrightarrow{r} = 0$ at time $t = 0$. $G_s(\overrightarrow{r}, t)d\overrightarrow{r}$ is the probability that an atom has moved of $\overrightarrow{r}$ within $d\overrightarrow{r}$ during a time t [248].

Nevertheless the van Hove function does not inform on the homogeneous or heterogeneous character of the dynamic. To get this information one must introduce correlation functions that characterize the fluctuations of the dynamics between two distant points of the system. We are going to introduce this type of function in the next section. We will see that in this framework the van Hove function plays the role of a dynamical order parameter

[12] In liquids this decrease is much faster and the correlation function does not display a plateau.

and that the study of the fluctuations of this order parameter quantify the heterogeneity of the dynamics.

5.3.3 4-point correlation functions.

The old idea that the abrupt slowing down of the dynamics of supercooled liquids is linked to the growth of a characteristic dynamic cooperativity length scale, has been confirmed in the last ten years in experiments, simulations and simple microscopic models [221]. The dynamic appears highly non trivial and while in some regions the movement of the particles is disordered, in others it appears collaborative. The mobility varies between the different regions and one speaks of dynamical heterogeneity (remember that the structure is roughly the same everywhere). In the recent years, the quest for a dynamical cooperativity length associated with the slowing down of the dynamics of supercooled liquids [221, 250, 251] has led to the development of new statistical tools to characterize such dynamical heterogeneities. Similarly to these dynamical heterogeneities in aging glassy materials it emerged in a recent study [5] that the motion of the particules in our system under shear is highly non-trivial. It shows a background of heterogeneous motion even in the elastic regime at very low temperature; for larger applied strains, in the plastic regime, it shows zones of very high mobility located in the vicinity of elementary shear bands and of localized quadrupolar events, and similarly zones of low mobility far from these irreversible events (the local displacement field can vary by many orders of magnitudes). This type of behavior in the mechanical response of glasses, even at zero temperature, can be seen as some kind of dynamical heterogeneity (while the dynamics here is overdamped) and it is of great interest to quantify a cooperativity degree or a cooperative length scale. To do so, Toninelli et al. [221] have proposed to look at the so-called χ_4 four point correlation function. An other possible observable is the cooperativity number introduced by Doliwa and Heuer [250], that estimates the spatial fluctuations of the two-point correlation function introduced previously. We present here these two (closely related) observables that have appeared in the last ten years in the literature and that have been shown to be good candidates to achieve this task.

Cooperativity number. First let us present the cooperativity number N_{coop} introduced in [250] and defined by:

$$N_X^{coop} \equiv \frac{Var[\Sigma X_i]}{\Sigma Var[X_i]} = \frac{\langle \{\sum_i X_i - \langle \sum_i X_i \rangle\}^2 \rangle}{\sum_i \{\langle X_i^2 \rangle - \langle X_i \rangle^2\}}, \tag{5.28}$$

where $Xi(t) = (\sigma_i(t+t') - \overline{\sigma_i(t+t')})(\sigma_i(t) - \overline{\sigma_i(t)})$ is a dynamical quantity associated to each particle. With this definition one obtains for a simple uncorrelated movement ($\langle X_i X_j \rangle = 0$) $N_{coop} = 1$, while on the contrary for a totally correlated movement of the particles ($X_i = X_j$) one gets $N_{coop} = N$. Intermediately for L independent groups each

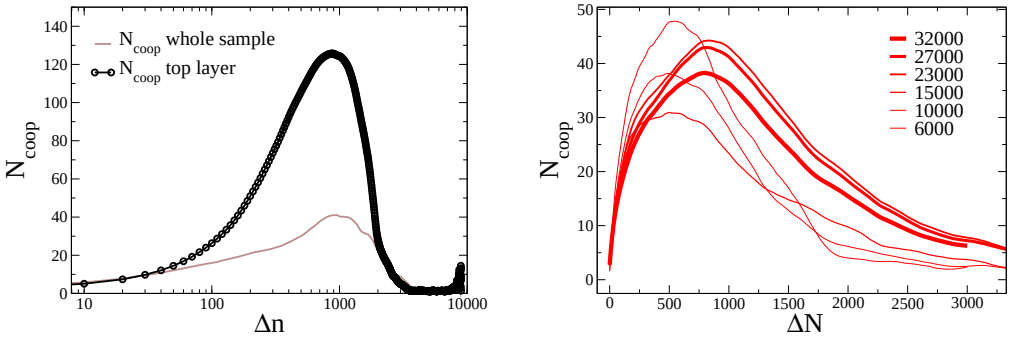

FIG. 5.13 : **Left :** Cooperativity number of the local shear stress at the borders, in comparison with cooperativity number in the center of the sample. **Right :** Cooperativity number obtained over different strain intervals. Increasing thickness of the curves reflects increasing averaging strain interval.

composed of M identical variables X_i and of zero mean ($N = L$) the cooperativity number reads

$$N_{coop} = 1 + \frac{\sum_{i \neq j} \langle X_i X_j \rangle}{\sum \langle X_i^2 \rangle} = 1 + \frac{1}{\sum \langle X_i^2 \rangle} \sum_{i=1}^{N} \sum_{j=1}^{M-1} \langle X_i^2 \rangle = M. \tag{5.29}$$

The use of the term '4-point' correlation function mentionned in the title of this section does not seem here adapted to this cooperativity number. In fact we will see in the next paragraph that $N_{coop}(t)$ is closely related to the quantity $\chi_4(t)$ called 4-point correlation function that explicitely uses four points in its definition [252]. It is important to realize that N_{coop} is a time dependent function ($N_{coop}(t)$), obtained in formula 5.29 as an average over the time origins t'. In figure 5.13 we have represented $N_{coop}(t)$, for the glass containing 10000 particles under rigid walls boundary conditions, and obtained through averaging over 32000 time origins (this corresponds to the total plastic flow regime) and for particles located at a distance d sufficiently far from the boundaries ($d > 20$). Indeed, as can be seen in figure 5.13, when the particles close to the walls are considered the resulting cooperativity number is strongly affected, and the two bands close to the walls present a behavior markedly different from the central band. This illustrates the fact that the system with walls is not completely homogeneous and that the movement of the particles within a few interatomic distances from the walls are strongly influenced by the walls. This explains the large cooperativity number near the walls ($N_{coop} \sim 200$) as all the particles move roughly as a unit in these regions. Far from the boundaries the cooperativity number is smaller, of the order of 35 to 45, corresponding to groups of 6×6 or 7×7 particles that move in a collaborative manner. The computation of N_{coop} is very CPU expensive as one configuration of the glass only provides one value of the random variable $\sum_i X_i$ of which we compute the variance. In figure 5.13 we show N_{coop} for different strain intervals and

it appears that the stationary regime is not reached even after 160% deformation (32000 steps of $\delta\varepsilon = 5 \cdot 10^{-5}$). Note finally that the use of the cooperative number does not take into account any convective aspect of the movement, the positions of the particles do not appear explicitly in expression 5.40, this contrasts with the observable χ_4 that we introduce now.

The observable $\chi_4(t)$. The dynamical susceptibility or four-point correlation function $\chi_4^p(t)$ is defined as:

$$\chi_4^p(t) = \frac{1}{N} \int d\vec{r_1} d\vec{r_2} d\vec{r_3} d\vec{r_4} G_4(\vec{r_1}, \vec{r_2}, \vec{r_3}, \vec{r_4}, t) \ , \tag{5.30}$$

where

$$\begin{aligned} G_4(\vec{r_1}, \vec{r_2}, \vec{r_3}, \vec{r_4}, t) &= \langle \rho(\vec{r_1}, 0)\rho(\vec{r_2}, t)\delta(\vec{r_1} - \vec{r_2})\rho(\vec{r_3}, 0)\rho(\vec{r_4}, t)\delta(\vec{r_3} - \vec{r_4})\rangle \\ &- \langle \rho(\vec{r_1}, 0)\rho(\vec{r_2}, t)\delta(\vec{r_1} - \vec{r_2})\rangle \langle \rho(\vec{r_3}, 0)\rho(\vec{r_4}, t)\delta(\vec{r_3} - \vec{r_4})\rangle, \end{aligned} \tag{5.31}$$

and where $\rho(\vec{r}, t)$ represents (the fluctuations of) the density of a quantity (in our case the stress density $\rho(\vec{r}, t) = \sum_i \sigma_i(t)\delta(\vec{r} - \overrightarrow{r_i(t)})$ or simply the particle density $\rho(\vec{r}, t) = \sum_i \delta(\vec{r} - \overrightarrow{r_i(t)})$).

From a theoretical point of view [252] this quantity can be understood as the fluctuations of a time dependant order parameter. Indeed one has,

$$\chi_4^p(t) = \frac{1}{N}[\langle Q_p^2(t)\rangle - \langle Q_p(t)\rangle^2] \ , \tag{5.32}$$

where

$$Q_p(t) = \int d\vec{r_1} d\vec{r_2} \rho(\vec{r_1}, 0)\rho(\vec{r_2}, t)\delta(\vec{r_1} - \vec{r_2}) \tag{5.33}$$

$$= \sum_{i=1}^{N} \sum_{j=1}^{N} \delta(\overrightarrow{r_i(0)} - \overrightarrow{r_j(t)}) \text{ if } \rho(\vec{r}, t) \text{ is the particle density,} \tag{5.34}$$

$$= \sum_{i=1}^{N} \sum_{j=1}^{N} \sigma_i(0)\sigma_j(t)\delta(\overrightarrow{r_i(0)} - \overrightarrow{r_j(t)}) \text{ if } \rho(\vec{r}, t) \text{ is the stress density.} \tag{5.35}$$

Referring to section 5.3.2 we see that this parameter is directly related to the van Hove function 5.25 with $\langle Q_p(t)\rangle = NG(\vec{0}, t)$. From this we deduce (in the case where $\rho(\vec{r}, t)$ is the particle density) that this order parameter measures the number of particles 'that are overlapping' for two configurations separated by a time interval t. The dynamical susceptibility allows therefore to quantify the fluctuations of the order parameter $Q_p(t)$. In other words we see that $G_4(\vec{r_1}, \vec{r_2}, \vec{r_3}, \vec{r_4}, t)$ plays the same role as a standard two point correlation function for an order parameter such as the magnetization in the case of a ferro-para phase transition, but that here the order parameter is itself a two-time quantity $Q(t', t'+t)$ (its value is the autocorrelation function of the density $\langle \rho(\vec{r_1}, 0)\rho(\vec{r_1}, t)\rangle$). Intuitively, if

at point $\overrightarrow{0}$ an event occurs (typically a quadrupolar event) that leads to the correlation of the stress or density over a time scale t, the 4-point correlation function measures the probability that a similar event has occurred at point $\overrightarrow{r}$ during the same time interval. Note that this order parameter is numerically ill defined (sum of dirac functions) and that we have modified it in our algorithms by $Q(t)$ that is obtained from $Q_p(t)$ where $\delta(\overrightarrow{r_1}-\overrightarrow{r_2})$ (in equation 5.33) is replaced by $W_a(\overrightarrow{r_1}-\overrightarrow{r_2})$ with the following possible choices for the coarse-graining function W_a:

$$W_a(\overrightarrow{r}) = \exp(i\overrightarrow{k}.\overrightarrow{r}) \tag{5.36}$$

$$= \exp(\frac{-\|\overrightarrow{r}\|}{2a^2}) \ . \tag{5.37}$$

As was done for the van Hove function (see equation 5.26) we distinguish in $Q(t)$ two parts $Q_s(t)$ et $Q_d(t)$ that write (here for stresses):

$$Q_s(t) = \sum_i^N \sigma_i(0)\sigma_i(t)W_a(\overrightarrow{r_i(0)}-\overrightarrow{r_j(t)}) \tag{5.38}$$

$$Q_d(t) = \sum_i^N \sum_{j\neq i}^N \sigma_i(0)\sigma_j(t)W_a(\overrightarrow{r_i(0)}-\overrightarrow{r_j(t)}) \ . \tag{5.39}$$

This leads automatically to three contributions in the 4-points correlation function $\chi_4(t) = \chi_{ss}(t) + \chi_{sd}(t) + \chi_{dd}(t)$. As was pointed out by Lacevic in supercooled liquids, the contribution $\chi_{ss}(t)$ [13] dominates when one does the calculation [252]. In most results presented in this thesis we calculate this self-self part of the four point correlation functions.

Here we can make contact with the cooperativity number $N_{coop}(t)$ defined in the previous paragraph as,

$$N_X^{coop} \equiv \frac{Var[\Sigma X_i]}{\Sigma Var[X_i]} = \frac{\langle\{\sum_i X_i - \langle\sum_i X_i\rangle\}^2\rangle}{\sum_i\{\langle X_i^2\rangle - \langle X_i\rangle^2\}} \ , \tag{5.40}$$

where $Xi(t) = (\sigma_i(t+t') - \sigma_{moyen}(t+t'))(\sigma_i(t) - \sigma_{moyen}(t))$ is a dynamical quantity associated to each particle. We see therefore that this observable N_{coop} is very closely related to χ_{ss} that measures the fluctuations of the macroscopic dynamical quantity $Q_s = \sum w_i$ where as seen above $w_i = \sigma_i(0)\sigma_i(t)W_a(\overrightarrow{r_i(0)}-\overrightarrow{r_i(t)})$.

Let us conclude by saying that this section was meant as a theoretical introduction on the 4-point correlation functions and that most results based on this parameter will be shown in the next chapter.

[13] its expression is $\chi_{ss}(t) = \sum_i\sum_j\{\langle\sigma_i(0)\sigma_i(t)\sigma_j(0)\sigma_j(t)W_a(\overrightarrow{r_i(0)}-\overrightarrow{r_i(t)})W_a(\overrightarrow{r_j(0)}-\overrightarrow{r_j(t)})\rangle$
$-\langle\sum_i\sigma_i(0)\sigma_i(t)W_a(\overrightarrow{r_i(0)}-\overrightarrow{r_i(t)})\rangle\langle\sum_j\sigma_j(0)\sigma_j(t)W_a(\overrightarrow{r_j(0)}-\overrightarrow{r_j(t)})\rangle$

5.4 Local statistical analysis

We are now going to change terminology and speak of stochastic processes [253, 254], of probability distributions, of increments (independent or not), of random variables, but in reality we are going to speak of exactly the same thing. Indeed the correlation functions introduced in the precedent section are directly linked to the PDFs that we are going to discuss now. For example, the self part of the van Hove function $G_s(\overrightarrow{r}, t)$ introduced in equation 5.27 is the probability that a particle of the system (in other words a realization of the stochastic process considered : for example here the particle displacement in time.) moves during a time t of $\overrightarrow{r}$. In the isotropic case one has exactly $G_s(\overrightarrow{r}, t) = G_s(r, t) = P(r, t)$ where $P(r, t)$ is the probability that a particle moves of r during t.

This kind of approach, based on the detailed analysis of the PDFs, will allow us to characterize the local evolution of particles (or of the stress) with time. It is particularly interesting to see how the dynamical heterogeneity observed and quantified in the previous sections is transposed at the local particle level. The use of numerical simulation, quasistatic simulation or molecular dynamics (see chapter 6), enables this by tracking the position and fields (stress, energy...) at an atomic level and for successive time intervals. In this section we will compute the PDFs of the position and atomic stress increments and we will see how the analysis of these PDFs informs on the microscopical processes that occur in the system. Also as we have seen with the theoretical models presented in chapter 1, the resolution of the Fokker-Planck type equations introduced in these models enables to obtain the PDFs $P(\sigma, t)$ (or $P(\sigma)$ in the stationary case) of each model. The analysis of the PDFs numerically allows for a direct comparison with the theoretical predictions of these models, such as the yield stress models or the Soft Glassy Rheology model.

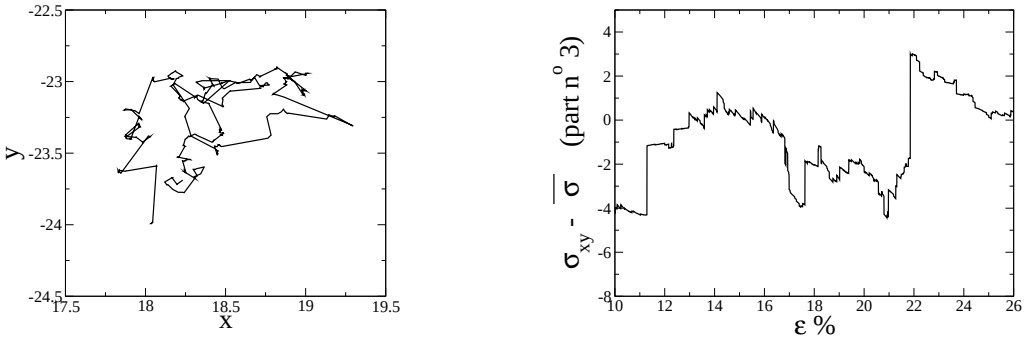

Fig. 5.14 : **Left :** Trajectory (non-affine part) of a single particle for a cumulative shear strain of 15%. The cell dimension is in this case L = 104 and the mean radius of the particles is $a = 1$. **Right :** Evolution of the shear stress on a given particle in the center of the sample, as a function of the applied shear strain. For each value the average over the sample has been subtracted.

5.4.1 Trajectory of an individual particle

In figure 5.14 [14] we show the trajectory of a particle during a total shear deformation of $\varepsilon = 25\%$. Here only the non-affine part of the displacement is reproduced (the affine component is subtracted). Our aim here is to characterize this movement [5]. It is a general result that a self similar random process with stationary increments (SSSI self similar stationary increments) is entirely characterized by the distribution of the size of its elementary increments and by the correlations that exist between each elementary increments. In addition if the variance of the sizes of the increments is not finite, the process can be of the Brownian motion or fractional Brownian motion type. For example in the most famous example of the Brownian motion one can described the process either in a probabilistic way using a Fokker-Plack differential equation (the diffusion equation):

$$\frac{\partial \mathrm{P}(x_0|x,t)}{\partial t} = \mathrm{D}\frac{\partial^2 \mathrm{P}(x_0|x,t)}{\partial x^2} \ , \tag{5.41}$$

the corresponding Markov process is defined in this case by,

$$\mathrm{P}(x_1,t_1|x_2,t_2) = \frac{1}{\sqrt{4\pi \mathrm{D}(t_2-t_1)}} \exp(-\frac{(x_2-x1)^2}{4\mathrm{D}(t_2-t_1)}) \ , \tag{5.42}$$

either by an evolution equation. For the Brownian motion the evolution equation is the Langevin equation;

$$\frac{dx(t)}{dt} = f(t) \ , \tag{5.43}$$

where $f(t)$ is a Gaussian process (hence completely defined by its covariance) of covariance $\langle f(t_1)f(t_2)\rangle = \Gamma\delta(t_1-t_2)$, and average $\langle f\rangle(t) = 0$.

One can show that the two processes so defined are identical (as two Gaussian processes with the same covariance ought to be). One therefore sees with this simple example the power of the double description Langevin equation/Fokker-Plack equation. For the random walk motion of a particle in a disordered material, as is the case here, we will see that the diffusive properties are very different from the Brownian motion.

In figure 5.15 we show the distributions $\mathrm{P}(\Delta y, \Delta \mathrm{N})$ and $\Delta y \mathrm{P}(\Delta y, \Delta \mathrm{N})$ where $\Delta \mathrm{N}$ is the number of deformation steps (each step correspond to an elementary strain of $\delta\varepsilon \sim 0.01\%$). $\mathrm{P}(\Delta y, \Delta \mathrm{N})$ can be seen as a quasi-static equivalent of the van Hove distribution correlation function, which is a standard tool to characterize diffusion in glasses and supercooled liquids. As can be seen these distributions differ from the simple Gaussian propagators of simple diffusion. Yet for sufficiently large $\Delta \mathrm{N} \to \infty$ a Gaussian distribution is recovered, or more precisely we show that the non-Gaussian parameter $\langle \Delta y^4\rangle/3\langle \Delta y^2\rangle^2 - 1$ goes to zero when $\Delta \mathrm{N}$ is increased. This is in agreement with the central limit theorem (indeed $\Delta y(\Delta \mathrm{N} = 16384)$ can be seen as a sum of 16384 random variables $\Delta y(\Delta \mathrm{N} = 1)$ of finite variance and assumed independent). We observe also, not shown in figure 5.15, that the distribution is symmetric, of zero average and of finite variance. The study of the

[14] This section is based on the section 5 of the article [5]

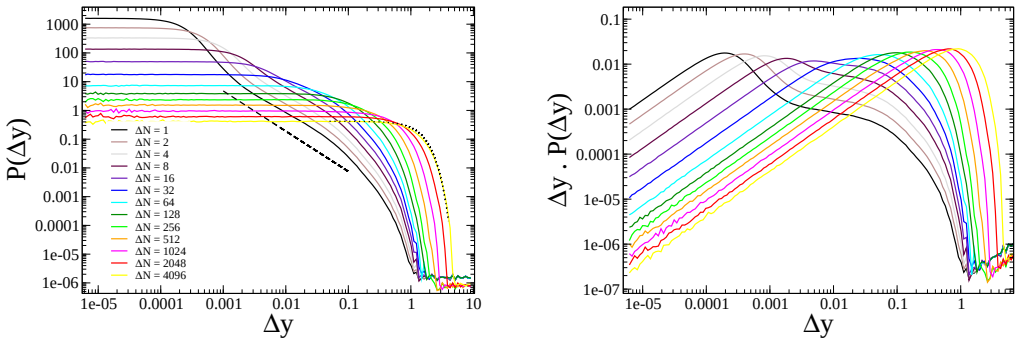

Fig. 5.15 : **Left :** Distribution $P(\Delta y, \Delta N)$ of distances Δy after ΔN steps of incremental strain imposed a t the top rigid wall. Each step $\Delta N = 1$ corresponds to a elementary strain of $\delta\varepsilon = 0.005\%$. The dashed line correspond to the power law $P(\Delta y) \propto \Delta y^{-1.4}$. The dotted line correspond to a Gaussian fit. **Right :** Same distributions but multiplied by the distance Δy itself. These function correspond to the van Hove functions. The position of the peak appearing at large ΔN evolves in a diffuse manner.

correlations between increments will be done in the next section. In figure 5.15, where $P(\Delta y, 1)$ is plotted in a log-log scale, we see that the PDF, for a given ΔN, starts with a plateau, followed by a power law decrease ended by an exponential cutoff for large Δy. In fact, the beginning and the end of this power law behavior are not self-similar (i.e. they cannot be rescaled in a form $f(\Delta y/\Delta N^{\beta})$ and for small ΔN, the long-distance contribution evolves less rapidly with ΔN than the short-distance part. This is also why the amplitude of the initial plateau, $P(0, \Delta N)$, shows two different behaviors as a function of ΔN, (see figure 5.15: a rapid decrease at small ΔN, followed by a slower decrease for larger ΔN after the power law decay has disappeared. This behavior is also shown in figure 5.15 (right) where the function $\Delta y P(\Delta y, \Delta N)$ is plotted as a function of Δy. In this representation, the values of Δy that contribute the most to the average displacement appear as peaks. It is clear that two main peaks are present. The first one corresponds to very small displacements, and its position evolves as ΔN^1. The second one, which corresponds to the actual diffusive process, appears at distances of order $\sigma = 1$, and its position increases as $\Delta N^{0.5}$. As the deformation is increased, the intensity shifts progressively from the first peak to the second one. This result supports the idea of two different relaxation mechanisms in amorphous glasses, even at zero temperature [255, 256, 257, 258]. As was recently pointed out by Lemaître and Caroli in [227] the physical significance of the two peaks is quite clear. Indeed following [227] if we plot the distribution $P_{plastic}(\Delta y)$ only of the plastic increments Δy (we consider Δy to be a plastic increment if there has been a drop of the macroscopic stress during the corresponding strain interval ΔN), we see that it accounts for most of the second peak of $\Delta y P(\Delta y, \Delta N)$, conversely the elastic distribution $P_{elastic}(\Delta y)$ accounts for most of the first peak. Note that this distinction between plastic and elastic events permits also to account for the amplitude of the second peak, that is

doubling in size when ΔN is doubling as expected for a random occurrence of plastic events in the material (see discussion in [227]). Also as explained by Lemaître this description allows to elucidate the collapse of $P_{elastic}$ on a single master curve when plotted against $\Delta y/\Delta$. Therefore as reported in [227] the shape of the distribution $P(\Delta y, \Delta N)$ can be decomposed in three parts corresponding to different physical behaviors:

- a nearly Gaussian center resulting from small-scale non-affine displacements accumulated along purely elastic segments, during which the particles are essentially convected,
- quasi-exponential tails for intermediate strain scales when the trajectory of the particles becomes dominated by the plastic jumps associated to quadrupolar events or shear bands in the system,
- a Gaussian shape associated to a diffusive regime for very large strains.

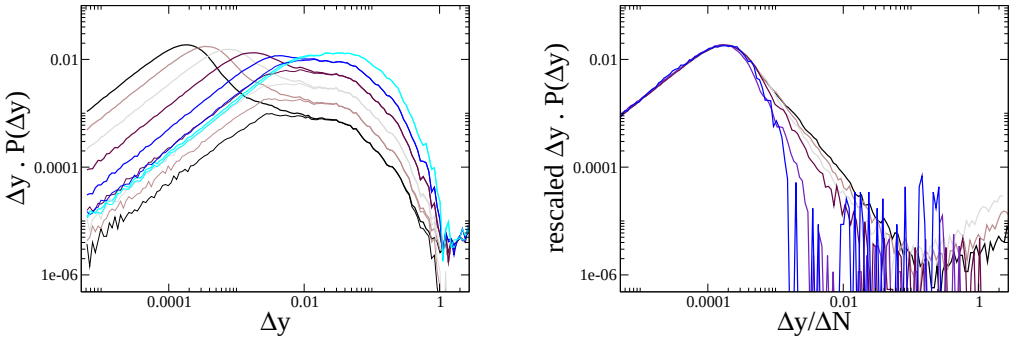

Fig. 5.16 : **Left :** Total distribution $\Delta y \cdot P(\Delta y, \Delta N)$ (thick lines) and plastic contribution $\Delta y \cdot P_{plastic}(\Delta y, \Delta N)$ (thin lines). Plastic intervals are considered when at least one macroscopic relaxation of the total stress has occured during ΔN. **Right :** Elastic contribution $P_{elastic}(\Delta y, \Delta N) = P(\Delta y, \Delta N) - P_{plastic}(\Delta y, \Delta N)$ of the distribution of transverse displacements vs $\Delta y/\Delta$N, for $\Delta N = 1, 2, 4, 8, 16, 32$ and 64. The function is normalized vertically at the maximum.

This non-Gaussian behavior at small imposed strain has already been observed in other amorphous systems like foams [257], or granular materials [258, 259]. In these systems however, the corresponding exponents, as measured in [259] for example, can be different. The exponent characterizing the hyper-diffusive motion of the particles dragged by the vortex motion in the linear regime seems thus to be material dependent, while the non-Gaussian character of the motion could be a characteristic of the small-strain deformation at zero temperature, in disordered systems. The study presented of the van Hove functions is also in line with previous observation of non Fickian trajectories in various glassy materials (see for a review [260]). The deviation from the Gaussian behavior is related to the heterogeneity of the dynamics in these glassy materials and reflects the coexistence in the

sample of mobile and frozen particles. This picture is coherent with our findings of chapter 4 where we ascribed the enhanced mobility to the elastically softer zones of the material, while particles in more rigid zones were shown to have very low mobility. This type of dynamics was recently described through the use of continuous time random walk (CTRW) [260] descriptions and reproduced the exponential decay of the tails of the distributions $P(\Delta y, \Delta N) = G_s(\Delta y, \Delta N)$ shown in figure 5.12. Finally, we have seen here that, even at zero temperature, the disorder inherent to amorphous systems is sufficient to create, under sufficiently large external sollicitations with a marked dissipative behavior (i.e. in the plastic flow regime), a diffusive motion for the individual particles. Further investigation of this diffusion process and other non-equilibrium transport processes - e.g. mobility under an external force - could allow us to explore the idea of effective temperature in these systems [258, 261].

5.4.2 Evolution of the local stress

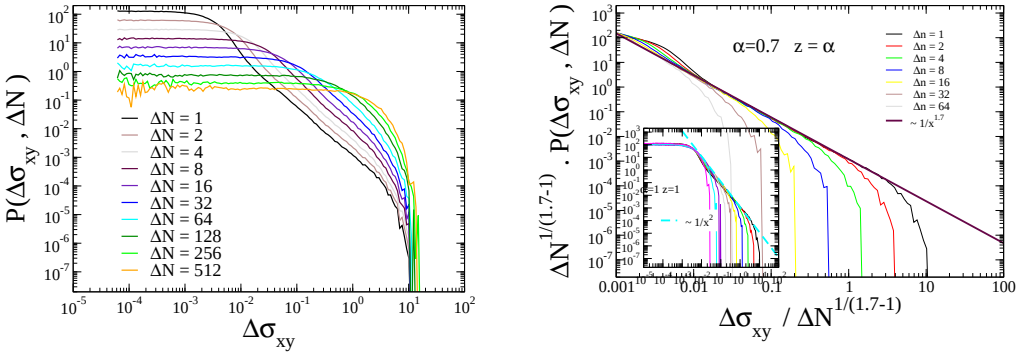

Fig. 5.17 : **Left :** Distribution $P(\Delta\sigma_{xy}, \Delta n)$ of the variation of local shear stress $\Delta\sigma_{xy}$ for different strain intervals Δn. The distribution has been obtained by averaging over the whole sample, and for different time origins. **Right :** Scaling of $P(\Delta\sigma_{xy}, \Delta N) \propto \phi(\Delta\sigma_{xy}/\Delta N^{1/z})$ with $z = \alpha$ and $\alpha = 0.7$. The scaling is very good in the intermediate range of the distribution, and for small $\Delta N < 64$ where the exponential cut-off does not play a role. Inset: the same with $\alpha = 1 = z$. This exponent corresponds also to the one discussed in the text.

To characterize the evolution of the local shear stress depicted in figure 5.14 we will examine now the full histogram of stress changes in the same manner as we did for the transverse displacements Δy. The [15] results are shown here for the shear stress component, but we have checked that all the following results are also valid for other components (pressure and deviatoric stress). In figure 5.14 we show the typical evolution of the shear stress component on a given particle up to a total strain of 25%. Here also the variations of stresses are larger than expected if they would be Brownian. In order to analyze this evolution, we have plotted in figure 5.17 the distribution $P(\Delta\sigma_{xy}, \Delta N)$ of the shear stress

[15] This part is extracted from the section 3 of our paper [6].

increments

$$\begin{aligned}\Delta\sigma_{xy}(\Delta\mathrm{N},\mathrm{N}) \equiv \quad & (\quad \sigma_{xy}(\mathrm{N}+\Delta\mathrm{N}) - \overline{\sigma}_{xy}(\mathrm{N}+\Delta\mathrm{N})) \\ & - \quad (\sigma_{xy}(\mathrm{N}) - \overline{\sigma}_{xy}(\mathrm{N}))\end{aligned} \tag{5.44}$$

for various numbers $\Delta\mathrm{N}$ of incremental shear steps ($\Delta\mathrm{N} = 1, 2, 4, 8, 16...$), averaged over the origins N and over the entire system. The distributions $\mathrm{P}(\Delta\sigma_{xy}, \Delta\mathrm{N})$ are all symmetric, with zero mean. For $\Delta n \to \infty$ one recovers a Gaussian distribution, which is consistent with the central limit theorem. However, at small imposed strains, these distributions are not Gaussian as would be the case for a Brownian evolution. A finer analysis of the distribution of the elementary increments $\mathrm{P}(\Delta\sigma_{xy}, \Delta\mathrm{N} = 1)$ in figure 5.17 shows three zones. At small incremental stress jumps $\Delta\sigma_{xy}$, we can see a plateau of approximately constant probability, whose width evolves inversely proportional to the volume V of the sample, followed by an apparent power-law decay, in a zone of approximately three decades for $100/\mathrm{V} \leqslant \Delta\sigma_{xy} \leqslant 10$ where $\mathrm{P}(\Delta\sigma_{xy}, \Delta\mathrm{N} = 1) \propto 1/\Delta\sigma_{xy}^{\alpha+1}$, and concluded by an exponential cut-off (characteristic shear stress $\Delta\sigma_{xy} \approx 1.4$). This upper cut-off allows for a finite variance of the local stress evolution. In the absence of any temporal correlations, the entire process can thus be described by the central limit theorem, with a scale invariant distribution on a finite interval. In this intermediate stress range, the probability density function $\mathrm{P}(\Delta\sigma_{xy}, \Delta n)$ is well reproduced by the scale invariant relation

$$\begin{aligned}\mathrm{P}(\Delta\sigma_{xy}, \Delta\mathrm{N}) &= \Delta\mathrm{N}^{-\mathrm{H}} f\left(\frac{|\Delta\sigma_{xy}|}{\Delta\mathrm{N}^{\mathrm{H}}}\right) \\ \textit{or} & \\ \mathrm{P}(\Delta\sigma_{xy}, \Delta\varepsilon) &= \Delta\varepsilon^{-\mathrm{H}} f\left(\frac{|\Delta\sigma_{xy}|}{\Delta\varepsilon^{\mathrm{H}}}\right)\end{aligned} \tag{5.45}$$

with

$$f(u) \propto \left\{ \begin{array}{cc} u^0 & , \text{for } u \ll 1 \\ u^{-\alpha-1} & , \text{for } 1 \ll u \ll cste.\Delta n^{-\mathrm{H}} \end{array} \right\} \tag{5.46}$$

In the intermediate stress range, the process can thus be considered as self-similar. Figure 5.17 illustrates this scaling with a good superposition of the distributions for $\alpha = 0.7$ and $\mathrm{H} \simeq \frac{1}{\alpha}$ (only for not too large $\Delta\mathrm{N}$ since for very large $\Delta\mathrm{N}$ the upper cut-off discussed before contributes significantly to the resulting distribution). The exponent α describes the algebraic (slow) asymptotic decay of the distribution of the incremental jumps $\mathrm{P}(\Delta\sigma = s, \Delta\mathrm{N} = 1) \propto s^{-\alpha-1}$ (as shown in figure 5.17). The exponent H is related to the evolution of the stress jumps as a function of the applied shear strain $\Delta\mathrm{N}$. It characterizes the $\Delta\mathrm{N}$ dependence of the crossover between a regime of approximately uniform probability (for $|\Delta\sigma| \ll \Delta\mathrm{N}^{\mathrm{H}}$) and the power law regime (for $|\Delta\sigma| \gg \Delta\mathrm{N}^{\mathrm{H}}$). The coefficient H also accounts for possible temporal statistical correlation between jumps. As stated in Taqqu *et al.* [253] the only non degenerate $\alpha - stable$ self similar processes with stationary increments that verify $\mathrm{H} = \frac{1}{\alpha}$ and where $0 < \alpha < 1$ are the $\alpha - stable$ Lévy motions. As described above, the evolution of the shear stress is thus of Lévy flight type, but only in the intermediate stress (and applied strain) range. The Lévy flight evolution implies by

definition, first that there is no temporal correlation between local stress jumps during the shear of the sample, second that the variance of elementary changes is infinite (as long as the exponential cut-off is neglected)[16]. These results can be compared with the study of the pdf $P(\Delta y, \Delta N = 1)$ of the positional jumps in the transverse direction, that showed in contrary that these jumps were correlated in time for small imposed deformation [5]. According to the above, a plausible equation that would describe the evolution within a Lévy flight process for the stress component σ, averaged over the whole system, is

$$\frac{d(\sigma(i,\varepsilon) - \overline{\sigma}(\varepsilon))}{d\varepsilon} = \eta(i,\varepsilon) \tag{5.47}$$

where $\eta(i,\varepsilon)$ is a stochastic process whose spatial average $\overline{\eta}(\varepsilon)$ is the process that is entirely characterized above (i.e. by the distribution of the elementary increment and by the absence of correlation between successive increments), and ε is the *external* imposed shear strain. For small imposed shear strain, it can be mentioned that such an equation with a noise corresponding to a Lévy motion cannot be reinterpreted in terms of the usual Fokker-Planck equation as the moments of the shear stress σ are non vanishing for all orders. However, for large strain intervals $\Delta\varepsilon$, the stochastic process becomes Gaussian, due to the existence of the upper cut-off in the distribution of $\overline{\eta}$. As we have seen in section 5.2 many of the generic features of this distribution of shear stress were accounted for by the simple model considering uncorrelated quadrupoles.

[16] In the case of Brownian motion the properties stated above on the pdf and on the process are verified (self similarity, $\alpha - stable$ process, stationary increments) but with a finite variance ($\alpha > 2$) allowing to a unique value $H = 1/2$.

Chapter 6

Rheological characteristics (influence of $\dot{\gamma} \neq 0$ and $\mathrm{T} \neq 0$)

Contents

The influence of temperature on the growth of a cooperative length scale has been investigated thoroughly for the past ten years in supercooled liquids near their glass transition temperature [221]. Similarly the influence of packing fraction on cooperativity has been studied extensively for systems near their jamming transition point [262]. One can safely say that the same amount of analysis has not been devoted to the analysis of a growing cooperativity length with lowering shear rate in driven glassy materials. In this chapter we present some preliminary results where we introduce through the use of molecular dynamics simulations the influence of finite shear rates.

6.1 Rheology of the glass

Rheological and mechanical characteristics. We do not reproduce here the details of the simulation procedures that we use in this chapter as they were presented already in details in chapter 2. Here we present the results obtained on the same two dimensional polydisperse glasses presented in chapter 5 at finite shear rates by the use of molecular dynamics and at temperatures that are well below the glass transition temperature. The thermostat transverse temperature as discussed in chapter 2 is $\mathrm{T}_y = 5{\cdot}10^{-8}$. An equivalent amount of runs were produced under two boundary condition protocols, namely rigid walls boundary conditions (simplified notation RWBCs) at $y = +/-\mathrm{H}/2$, were H is the height of

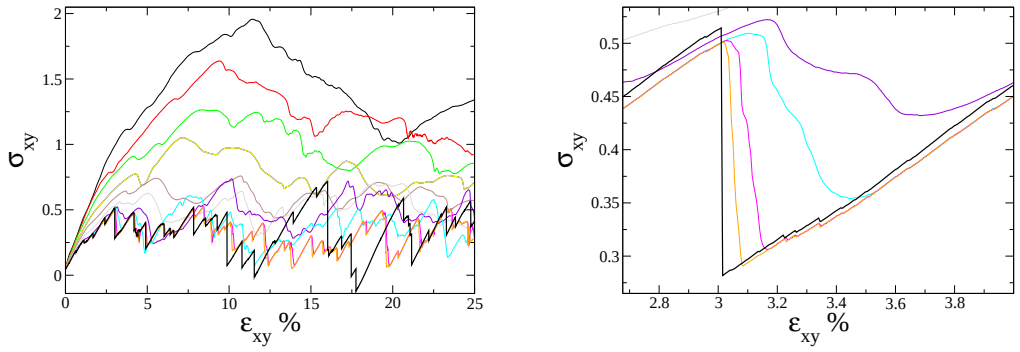

FIG. 6.1 : **Left :** stress strain mechanical response of a glass sample containing 625 particles sheared under RWBCs at shear rates ranging from $\dot{\gamma} = 10^{-2}$ to $\dot{\gamma} = 10^{-5}$ (thin colored lines from top to bottom, $\dot{\gamma} = 10^{-2}$ (black), $\dot{\gamma} = 5 \cdot 10^{-3}$ (red), $\dot{\gamma} = 2.5 \cdot 10^{-3}$ (green), $\dot{\gamma} = 10^{-3}$ (dark green), $\dot{\gamma} = 5 \cdot 10^{-4}$ (brown), $\dot{\gamma} = 2.5 \cdot 10^{-4}$ (gray), $\dot{\gamma} = 10^{-4}$ (violet), $\dot{\gamma} = 5 \cdot 10^{-5}$ (cyan), $\dot{\gamma} = 2.5 \cdot 10^{-5}$ (magenta) and $\dot{\gamma} = 10^{-5}$ (orange)). The thick black line corresponds to the quasistatic shear protocol. **Right :** Zoom in a portion of the total mechanical response, illustrating the typical relaxation time associated to a plastic rearrangement in the glass signaled in the quasistatic protocol by an abrupt stress drop.

the sample, and Lees-Edwards boundary conditions (noted LEBCs). The same quenched samples as in chapter 2 are analyzed here, namely 24 samples of (625 particles, Lx=25.9938, Ly=25.9938), 8 (2500,51.9875,51.9875) and 8 (10000,103.975,103.975) all corresponding to a density ρ of $\rho = 0.925$. We have sheared at finite shear rates in this chapter also 1 larger sample (40000,206.950,206.950) that was not sheared with the quasi-static protocol. For each simulation, we collect data over four strain units ($\varepsilon = 4$) and store all the positions of the particles at a regular strain interval of $\delta\varepsilon = 10^{-3}$[1]. For the details of the different thermostats and various parameters involved in these runs we refer again the reader to chapter 2. In figure 6.1 we have reported the mechanical response of the smallest sample for RWBCs. We observe the characteristic flow behavior associated with glassy materials with a convergence of the response to the quasistatic limit as the shear rate is progressively reduced and a global non linear flow curve of the Herschel-Bulkley type : $\tau = \tau_Y + c_1\dot{\gamma}^\beta$, where τ_Y is the yield stress, and where one can define the viscous stress $\tau_V = \tau - \tau_Y$. In figure 6.2 we draw these flow curves for both boundary conditions and for all system sizes. The stress-strainrate curves of figure 6.2 are obtained by averaging the macroscopic stress values of the sheared glass obtained in figures 6.1 for strains larger than $\varepsilon = 25\%$, i.e. deep in the plastic flowing regime once the stationary flowing regime is established. Indeed we have checked that a linear velocity profile is established in the different samples for typical strains of the order of $\varepsilon \sim 2.5\%$.

[1]Significant simulation runs and analysis were also produced in three dimensions but are not reported here for time considerations and coherence of the presentation and will make the object of future publication.

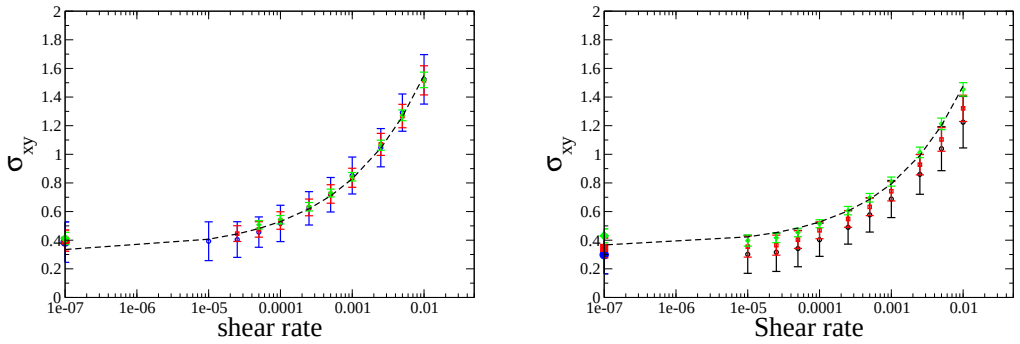

Fig. 6.2 : Flow curves associated with the different system sizes. Small open symbols correspond to finite shear rate values ranging from 10^{-5} to 10^{-2}. The larger solid points on the vertical axis correspond to the quasistatic protocol $\dot{\gamma} = 0$. **Left :** Shear under LEBCs with fit parameter to the Herschel-Bulkley rheological law, $\tau_Y \simeq 0.32$, $c_1 = 7.2$ and $\beta = 0.38$. **Right :** Shear under RWBCs, with the dashed line representing a Herschel-Bulkley fit $\tau = \tau_Y + c_1\dot{\gamma}^\beta$, with $\tau_Y \simeq 0.36$, $c_1 = 7.4$ and $\beta = 0.4$.

Convergence to the quasistatic limit. Importantly the results presented above bridge the gap between the two types of approaches used in the literature, quasistatic energy minimization protocols and finite shear rates molecular dynamics methods and resolve the controversy relative to the validity of the quasistatic protocols. Indeed as is evident from the mechanical response shown in figures 6.1 the quasistatic stress-strain curve appears as the limiting curve of the finite shear rates procedures. The superposition of the quasistatic response with the $\dot{\gamma} = 10^{-5}$ shear rate response is in fact almost perfect in the early parts of the curves before small differences are amplified irremediably. One sees for example on the right hand side of figure 6.1 how even very small relaxations at around $\varepsilon \sim 3.2-3.4\%$ in the quasistatic response (black thick line) are also visible in the lowest shear rate curves (yellow and magenta). Note that these small features of the mechanical response of the glass would not be visible if the temperature was higher and therefore inducing a noisier stress signal. The good convergence to the quasistatic protocol is also apparent in figures 6.2 where one can indeed observe that the values of the lowest finite shear rates are in good agreement with the $\dot{\gamma} = 0$ shear rate method (under both boundary conditions $\sigma_{xy}(\dot{\gamma} < 10^{-5}) \sim 0.4$), again confirming the physical relevance of the quasistatic method.

Decomposing the plastic events in elementary units. In an important series of papers [4, 205] it was recently shown by Lemaître and Maloney that the relaxation in mechanically driven glasses occurs through the formation of cascades of quadrupolar elementary units (see also chapter 5). In the quasistatic protocol to decompose the cascade in its subunits one needs to study in detail the evolution of the positions of the particles during the minimization procedure, with the inherent limitation of the minimization algorithms that one can not associate a time scale to the successive elementary rearranging

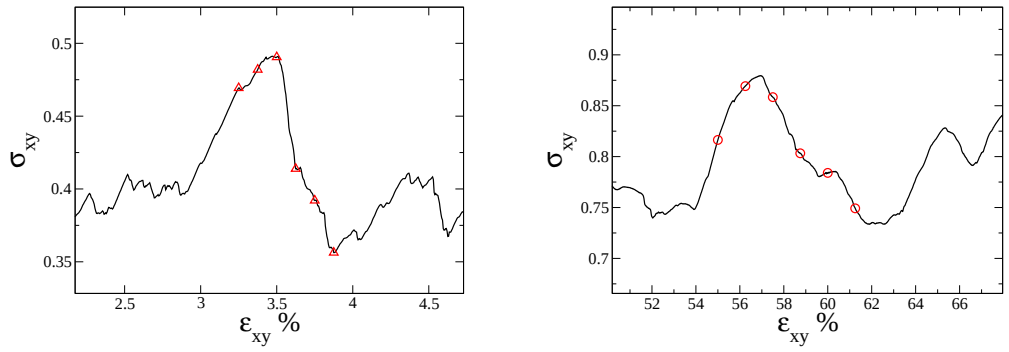

FIG. 6.3 : Portion of the mechanical stress-strain response of a Lennard-Jones glass containing 10000 particles and sheared under LEBCs for two shear-rates. **Left :** $\dot{\gamma} = 10^{-5}$. **Right :** $\dot{\gamma} = 10^{-3}$.

units. This limitation is automatically overcome in the molecular dynamics simulation where time appears explicitly in the algorithm and where one can follow the evolution of the cascade in time. As is apparent at finite shear rates in figures 6.1 the plastic relaxation is not instantaneous during a stress drop and this typical lifetime of the plastic events is transposed in the stress-strain mechanical response in these downward portions with the slopes that increase with increasing strain rate. To understand intuitively the mechanisms involved in the mechanical response of the sheared glasses and the different time scales that are relevant it is highly instructive to visualize movies of the instantaneous non-affine displacement field during the deformation. We attached, in the supplementary information part of this thesis, such material, where we have generated two movies at finite shear rates $\dot{\gamma} = 10^{-3}$ and $\dot{\gamma} = 10^{-5}$ for a sample containing 10000 particles and at regular time intervals $\delta t = 1$LJU in the plastic flow regime and during a plastic relaxation event. The two panels of figures 6.4 and 6.5 show snapshots of these movies taken at regularly spaced strain intervals corresponding to the red symbols on figure 6.3. As can be seen in this last figure, for the slowest strain rate $\dot{\gamma} = 10^{-5}$ the strain interval between snapshots is $\delta\varepsilon = 2.5 \times 10^{-3}$ (red triangles) and for the fastest strain rate $\dot{\gamma} = 10^{-3}$ it is $\delta\varepsilon = 1.25 \times 10^{-2}$ (red circles). When looking at the two panels one must bare in mind that while in the slowly sheared case the total strain applied between the first figure and the last is less than 1% in the fast case it is more than 5%. Also the non-affine displacement field represented on each snapshots correspond to the displacement during a time interval of $\delta t = 1$LJU and therefore the associated strain is $\delta\gamma = \dot{\gamma} \times \delta t$ is one hundred times larger for the fast shear than for the slow shear. If one assumes that the density of weak triggering zones of plasticity is homogeneously distributed through the sample with a shear rate independent density per unit strain Ω then one expects also to see 100 times more such nuclei of plasticity in the fast case. This explains the visual impression that there exists a higher density of local plastic displacements (black arrows) on panel 6.5 than on panel 6.4 where only a few local plastic rearrangements are observed. Another difference between the slowly

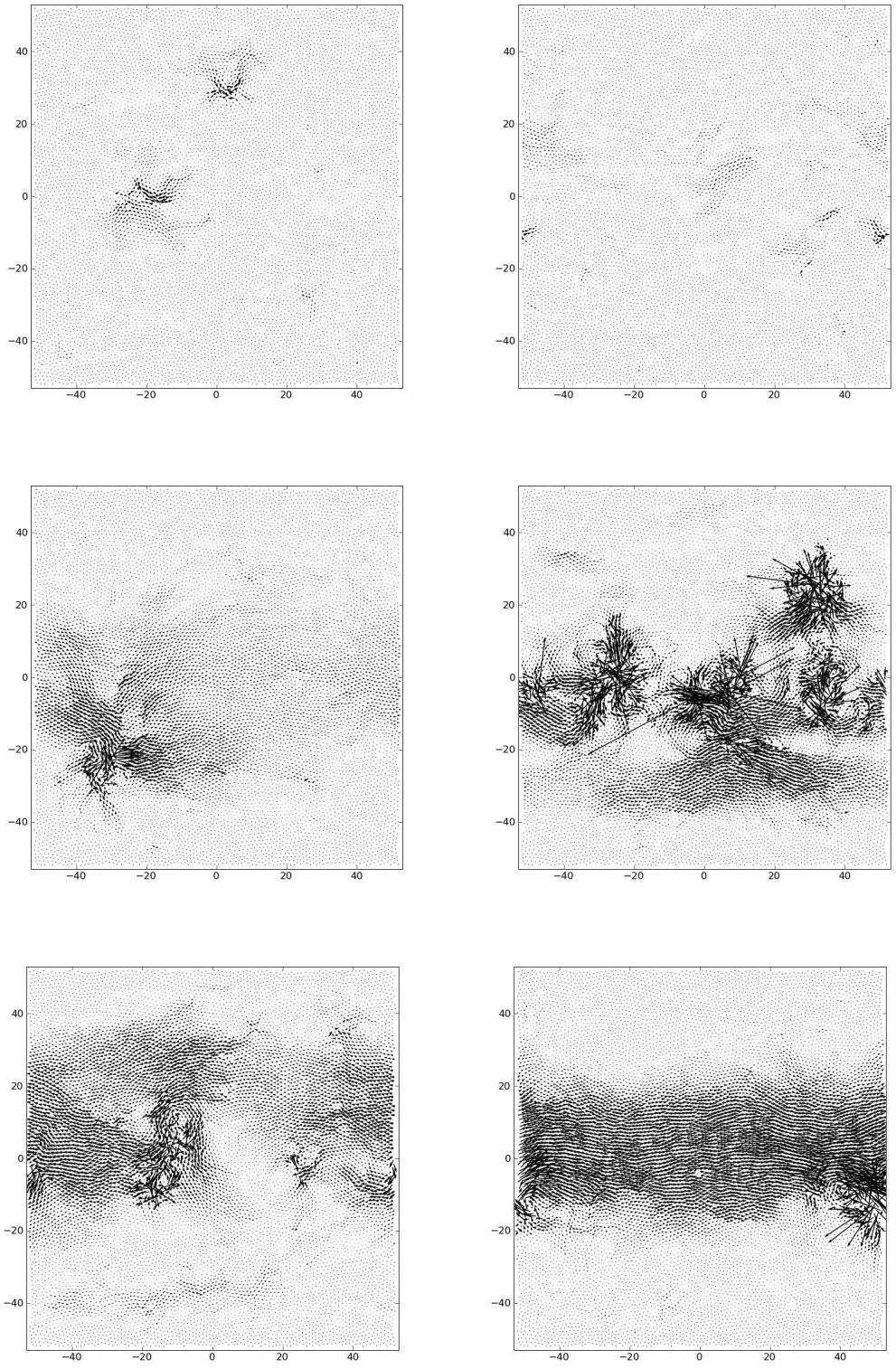

Fig. 6.4 : Snapshots of the instantaneous displacement field during 1 LJU and corresponding to the triangular symbols of figure 6.3. The shear-rate is here $\dot{\gamma} = 10^{-5}$.

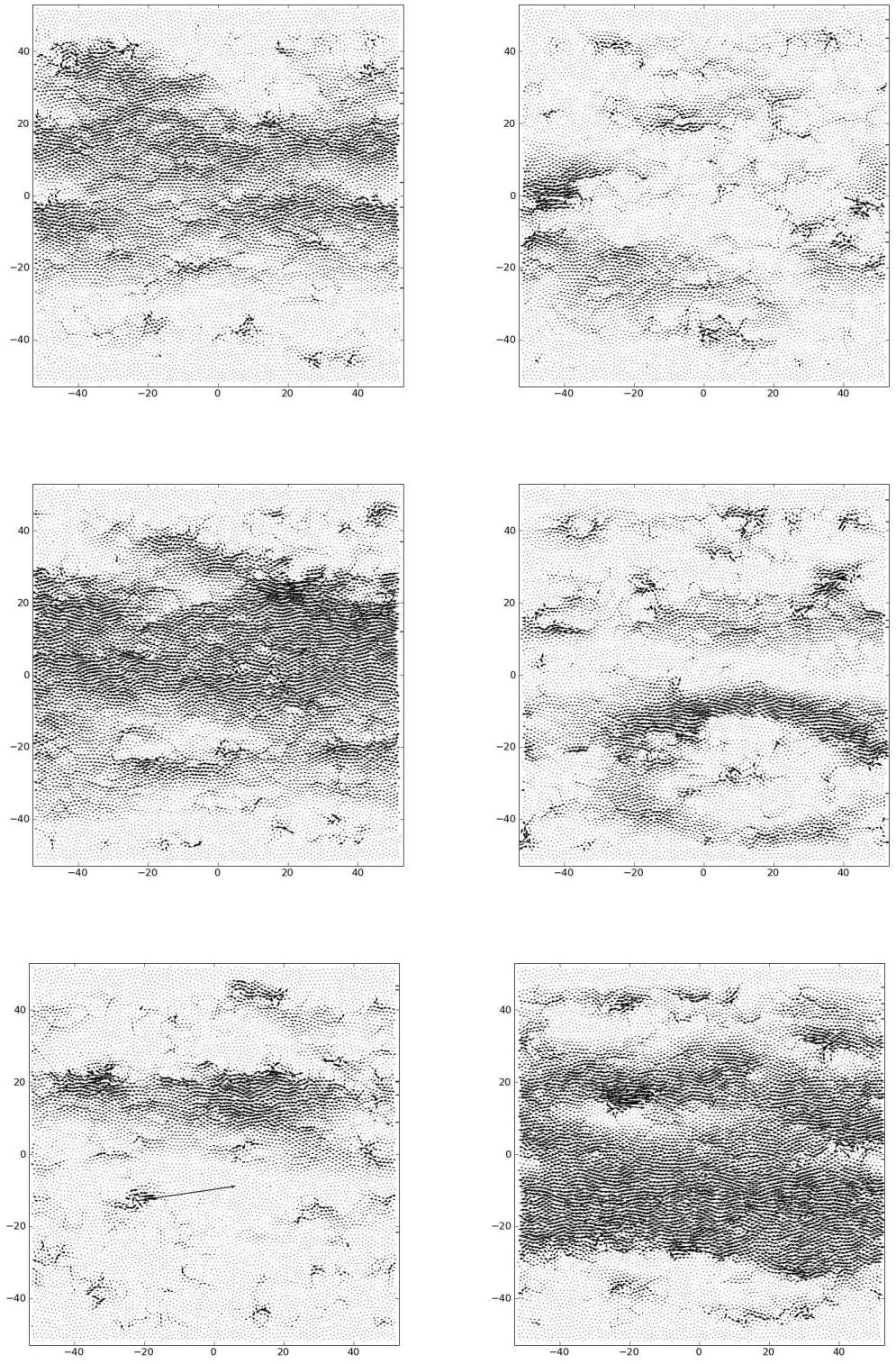

Fig. 6.5 : Snapshots of the instantaneous displacement field during 1 LJU and corresponding to the circular symbols of figure 6.3. The shear-rate is here $\dot{\gamma} = 10^{-3}$.

and fast driven regimes is that while in the fast case the nuclei do not seem to merge or percolate or evolve in a correlated manner in the slowly driven case the local quadrupoles[2] show a cooperative and correlated avalanche dynamics. This is particularly visible on the fourth panel of 6.4 where one can see about 5 such elementary plastic units forming a L-shape with four events horizontally aligned. Interestingly the typical distance between quadrupoles on this figure is about $\xi \sim 20$LJU which is reminiscent of the length scale that emerged for example in the autocorrelation function of the non-affine field in recent studies of similar Lennard-Jones glasses [118]. These findings are in line with observations of similar weak zones that grow and trigger the flip of neighbouring zones as depicted in fig. 1 of [224] confirming the validity of the picture of the dynamics of slowly driven glassy materials as dominated by the accumulation and cascading of plastic events. Beyond this general mechanism a careful study of the spatio-temporal signal associated to the slow drive ($\dot{\gamma} = 10^{-5}$) shows different time scales τ associated with an entire zoology of typical sequences of plastic events. First one observes short lived local quadrupoles, typically visible only during one snapshot $\tau_e < 1$LJU, and that do not trigger a cascade. Some local rearrangements seem to be locked and to survive for longer time intervals of the order of $\tau_e \sim 10 - 100$LJU. In general this type of rearrangement triggers in its vicinity (vertically or horizontally) subsequent similar events. Sometimes as is the case on the forth snapshot of figure 6.4 this cascade leads to the formation of a system spanning shear band. Finally one can associate also a timescale to the global relaxation process of figure 6.3 which is here for the slow shear rate $\tau_c = \gamma_c/\dot{\gamma} \sim 1000$ LJU (γ_c corresponds here to the duration of the relaxation event, i.e. the total strain associated to each downward slopes in the stress-strain response) and for the fastest shear rate $\tau_c \sim 100$ LJU. Note that these values of the typical duration of an entire relaxation process are in line with the values that one can compute from figure 6.1. In this figure one also sees that for low enough shear rates $\dot{\gamma} < 10^{-4}$ there is an intrinsic lifetime associated to a plastic rearrangement process which is proven by the fact that the slope of the stress curves in proportional to the shear rate. For shear rates larger than $\dot{\gamma} \sim 10^{-4}$ the relaxation strain becomes larger than the typical strain between relaxation events and therefore one can see this value of the shear rate as a mark of a transition to a different type of rheology also characterized by a important increase of the average yield stress as can be seen from figure 6.2. It is very striking that the avalanche like behavior seems to be somehow screened when the shear-rate is increased. This result has been reported also elsewhere in atomic scale simulation [224] but also in mesoscopic yield stress models [71] and [263]. Only rarely studied in driven glassy material the growth of a cooperativity length scale near the glass transition is well known in the supercooled liquids literature (see for example [264]) or in simple lattice gas models [265] and have been interpreted in the framework of facilitated dynamics (for a review see [266]). Of course the shear that one applies on glassy systems breaks the symmetry of

[2] Here we use as in the previous chapter the term quadrupole in reference to the stress redistribution associated to these local plastic events but here the term dipole is more adapted when one looks at the displacement field of these elementary rearrangements.

supercooled liquids (this is apparent for example in the existence of preferred orientations for the local quadrupoles and for the system spanning shear bands along the neutral axis of the external applied strain. In supercooled liquids the directions of the rearrangements are isotropic) but nevertheless it appears tempting to find, in line with supercooled liquids, a mapping between the dynamics of the sheared glass and a simpler facilitated model. The detailed description of the elementary rearranging processes that we propose here should help to devise reasonable ingredients for these models. A first approach in this direction was proposed by Picard *et al* [71] (see chapter 1 section 1.4.2 for a brief description of the ingredients of the model) and we will briefly compare our results to this model at the end of this chapter. To conclude with the description of the panels 6.4 and 6.5 let us mention that these plastic rearrangements independently of the shear rate emit a transverse sound wave propagating at a typical transverse sound speed characteristic of the Lennard-Jones glass ($c_s \sim \sqrt{\mu/\rho} \sim 3-4$ LJU) and appear in general as dark regions on the snapshots of panel 6.4 and 6.5. This allows to introduce a new timescale $\tau_s = L/c_s \sim 10$ LJU, i.e. comparable to the life time τ_e of the elementary plastic rearrangements for a system of size $L = 50$. To quantitatively characterize the spatio-temporal dynamics of the driven glasses we first compute various two-time observables (mean-square displacement, van Hove function, intermediate scattering function...) which informs on the typical relaxation times and their link with the external shear rate, we then proceed to a general description of the dynamical heterogeneity of the driven systems and prove the existence of a diverging dynamical cooperative length scale as the sheared rate $\dot{\gamma}$ tends to zero. We also provide pictorial evidence of these dynamical structures for different shear rates. Finally we discuss our results in light of recent advances and compare our observations to a phenomenological mesoscopic yield stress model.

6.2 Motion of particles

Two time correlation functions. As was already pointed out in chapter 5 the study of two time correlation function,[3] besides its direct importance to quantify the characteristic relaxation times, allows also to make comparisons with simple models of the rheology (for example it allowed us to assert the validity of a simple description of the rheology in terms of local quadrupolar rearrangements). In what follows, to examine the dynamics of the local density and the associated relaxation times, we compute therefore, on an equal foot, the self intermediate scattering function $F_s(\mathbf{k}, t)$ (already seen in section 5.3.2 of the previous chapter),

$$F_s(\mathbf{k}, t) = \frac{1}{N} \sum_i \cos\left[\mathbf{k} \cdot (\Delta \mathbf{r}_i(t))\right] \ , \tag{6.1}$$

[3] In chapter 5 time was replaced by strain.

and the self correlation function (as in [262] and similarly to equation 5.38 in chapter 6) $\mathrm{Q}_s(a,t)$ defined by,

$$\mathrm{Q}_s(a,t) = \frac{1}{\mathrm{N}} \sum_i \exp(-\frac{\Delta \mathbf{r}_i(t)^2}{2a^2}) \ , \tag{6.2}$$

where $\Delta \mathbf{r}_i(t) = \mathbf{r}_i(t'+t) - \mathbf{r}_i(t')$ is the displacement vector. In what follows it is the spatial and time average of these two function that we compute and in general in what follows we replace the displacement vector $\Delta \mathbf{r}_i(t)$ by its non-affine contribution $\Delta \mathbf{r}_i^{na}(t)$ (or even simply by the transverse displacement) defined rigorously by,

$$\Delta \mathbf{r}_i^{na}(t) = \mathbf{r}_i(t'+t) - \dot{\gamma} \int_t^{t'+t} dt'' y_i(t'') \mathbf{e}_x - \mathbf{r}_i(t) \ , \tag{6.3}$$

for a shear in the x direction. In practice we find that within a good degree of accuracy $\Delta \mathbf{r}_i^{na}(t) = \mathbf{r}_i(t'+t) - \dot{\gamma} y_i(t') \mathbf{e}_x - \mathbf{r}_i(t)$ and we use this expression. Figure 6.6 represent the function Q_s both in function of time and strain. After a slow decrease at small times/strains the function Q_s exhibits a power law decay as a function of strain ε, $\mathrm{Q}_s(a,\varepsilon) \propto \varepsilon^{-\beta}$ with $\beta \gtrsim 0.5$ signaling shear induced structural relaxation. This power law decay is in contrast with the more 'classic' self intermediate scattering function that exhibits (not shown here) a compressed exponential decay $\mathrm{F}_s(k_y,\varepsilon) \propto \exp(-(\varepsilon/\varepsilon_c)^{\beta})$, with $\beta \gtrsim 1.0$. Note also that the $\mathrm{Q}_s(a,\varepsilon) \propto \varepsilon^{-\beta}$ decay is compatible with a Gaussian distribution function of the transverse displacements $\mathrm{P}(\Delta y,\varepsilon)$ and with a diffusive transverse mean square displacement $\langle \Delta y^2 \rangle$. As shown in figure 6.6 the convergence to the quasistatic curve is verified when Q_s is plotted against strain for values of the shear rate $\dot{\gamma} \lesssim 10^{-4}$.

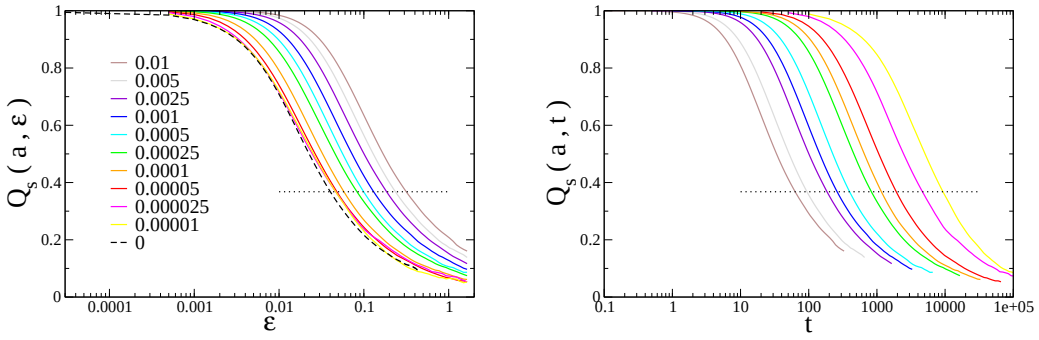

Fig. 6.6 : **Left** : 2-point correlation function $\mathrm{Q}_s(a,\varepsilon) = \sum_i \exp(-\frac{(y_i(\varepsilon)-y_i(0))^2}{2a^2})$ against strain ε for a system with LEBC. Thin lines (color on pdf version) : from top to bottom shear rate values are 0.01,0.005,0.0025,0.001,0.0005,0.00025,0.0001,0.00005 and 0.000025. Dashed line : $\mathrm{Q}_s(a,\varepsilon)$ vs ε for quasistatic shear. Doted line corresponds to the value 1/e for which we calculate the 1/e-relaxation strains and times. **Right**: $\mathrm{Q}_s(a,t)$ against time t. In both figures the parameter a is chosen equal to 0.1.

In figure 6.7 we have reported the relaxation times $t_{1/e}$ - the points of intersection of the dotted line with the colored curves in figure 6.6 verifying $\mathrm{Q}_s(a,t_{1/e}) = 1/e$ - for different

shear rates and different system sizes. Of course the relaxation strains and relaxation times are related through the simple relation $\varepsilon_{1/e} = t_{1/e} * \dot{\gamma}$ and we therefore only report the relaxation times for simplicity. In [267, 14] similar analysis were reported in experiments respectively on foams and colloids. Looking at the relaxation time dependence on shear rate in these studies they found scalings of the form $t_{1/e} \propto \dot{\gamma}^{-\nu}$ with $\nu \simeq 0.66$ in [267] and $\nu \simeq 0.8$ in [14]. Similarly in extensive numerical studies [105, 116] of sheared Lennard-Jones glassy materials the authors have computed these relaxation times without explicitly writing to our knowledge the functional form of the dependence of the relaxation time on shear rate.

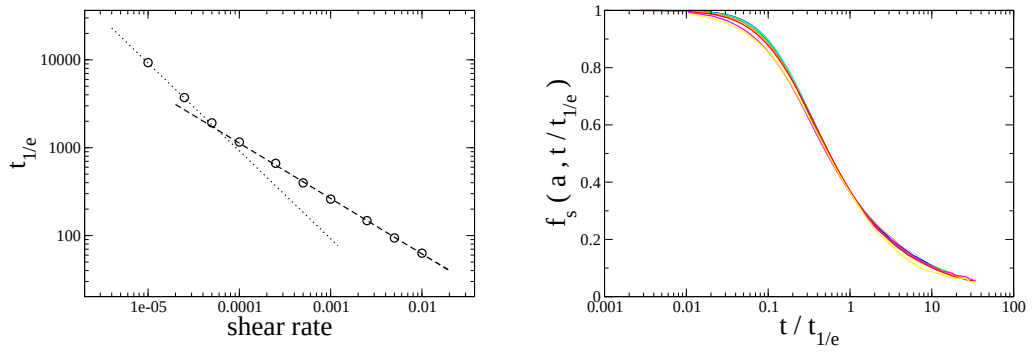

FIG. 6.7 : **Left** : Relaxation time $t_{1/e}$ vs shear rate $\dot{\gamma}$ for the system of figure 6.6. Dotted line $t_{1/e} \propto \dot{\gamma}^{-1}$, dashed line $t_{1/e} \propto \dot{\gamma}^{-0.63}$. **Right**: Rescaled self correlation function $Q_s(a,t)$ of figure 6.6 when time is rescaled by the structural relaxation time $t_{1/e}$. All curves superimpose rather well on a master curve $f_s(a, t/t_{1/e})$.

Here as shown in figure 6.7 we find two regimes : for high shear rates, $\dot{\gamma} \gtrsim 10^{-4}$, the structural relaxation time of the sheared glass scales with the global shear rate as $t_{1/e} \propto \dot{\gamma}^{-\nu}$ with $\nu \simeq 0.63$, while for lower shear rates,$\dot{\gamma} \lesssim 10^{-4}$, the relaxation functions $Q_s(a,\varepsilon)$ reach a quasistatic limit strain limit $\varepsilon_{1/e} \sim 0.04$ and therefore the associated relaxation times scale as $t_{1/e} \propto \dot{\gamma}^{-\mu}$ with $\mu \simeq 1$. The crossover between the quasistatic and shear rate dominated regimes is size dependent with the transition shear rate $\dot{\gamma}_c$ being lowered as the size of the system is increased (not shown here). Our data confirm the theoretically predicted 'time-shear superposition principle' [268, 269] : when time is scaled by $t_{1/e}$ the relaxation follows a master curve $f_s(a, t/t_{1/e})$ as shown in figure 6.7. It is tempting to try and relate as in [105, 267, 14] the scaling exponent ν of the structural relaxation time to the scaling exponent β that appears in the Herschel-Bulkley type macroscopic rheological flow curve of the material where $\sigma - \sigma_Y \propto \dot{\gamma}^{\beta}$ (see figure 6.2). Taking, as is often assumed and verified numerically [116], the structural relaxation time $t_{1/e}$ as proportional to viscosity provides an expression of an effective stress $\sigma_{eff} = \mu t_{1/e} \dot{\gamma}$, where μ is the macroscopic shear modulus. Surprisingly reporting the scaling of the relaxation time $t_{1/e}$ in this expression we see that for high enough shear rates $\dot{\gamma} \gtrsim 10^{-4}$ the effective stress scales with shear rate

as $\sigma_{eff} \propto \dot{\gamma}^{1-\nu}$. This is in good agreement with the global mechanical response of the material and one finds a posteriori that the two coefficients β and ν are compatible with the hypothesis made above and one has indeed to a good approximation $\beta = 1 - \nu$ for high shear rates. This relation breaks down for lower shear rates in a regime where shear banding becomes the dominant relaxation mechanism, as can be seen for example in the panels 6.4 and 6.5 corresponding respectively to the shear rates $\dot{\gamma} = 10^{-5}$ and $\dot{\gamma} = 10^{-3}$.

Mean square displacement (MSD). Usually to quantify the dynamics at a particle level one also calculates the MSD. In our two dimensional simulations the diffusion along the x and y directions are not equivalent. Indeed while the diffusion in the shear direction (in our case the x axis) is enhanced by the shear, the diffusion in the transverse shear-gradient direction (y axis) is unaffected. Here we therefore present the MSD $\langle \Delta y(t)^2 \rangle$ in the transverse direction. Of course in the presence of rigid boundary conditions the diffusion along the y axis is limited by the presence of walls and one must be cautious to compute the average MSD sufficiently far away from the boundaries. Figure 6.8 shows the typical transverse MSD for a system containing 625 particles under RWBCs and averaged over a total cumulative strain of 200% for each of 24 glass samples. Moreover in order to avoid boundary effects the average is computed over one third of the sample in the central region. Larger samples as well as LEBCs yield similar results and we have not reproduced these here for clarity. From figures 6.8 we see that the MSD exhibits a transition from ballistic motion at short times ($\langle \Delta y^2 \rangle \propto t^2$) to diffusive motion ($\langle \Delta y^2 \rangle \propto t^1$) for larger times. For high shear rate values ($\dot{\gamma} \gtrsim 10^{-4}$ one can rescale the entire MSD curves on a master curve $g(t/t_{\mathrm{MSD}})$, while for smaller shear rates the scaling doesn't hold for small times. The times t_{MSD} are defined here as the intersection of the MSD curves with a 'Lindemann' like criterion defined at $\langle \Delta y^2 \rangle = 0.14$ as in [267]. The time t_{MSD} is a nonlinear function of shear rate and follows the same trend as $t_{1/e}$ defined earlier (see figure 6.6), but with a slightly different exponent $t_{\mathrm{MSD}} \propto \dot{\gamma}^{-\nu_2}$, with $\nu_2 \sim 0.5$ (see doted line in the inset of figure 6.8).

Diffusion coefficient. The scaling of the MSD curves at different shear rates allows to identify the dependence of the transverse diffusion coefficient, defined by $\langle \Delta y^2 \rangle = 2\mathrm{D}_y t$, with shear rate $\dot{\gamma}$, $\mathrm{D}_y \propto 1/t_{\mathrm{MSD}} \propto \dot{\gamma}^{\nu_2}$. In order to allow comparison with diffusion in quasistatically sheared glasses we follow Lemaître [270] and compute the quantity $\mathrm{D}_{eff}(\Delta\gamma) = \langle \Delta y^2 \rangle / 2\Delta\gamma$ which is related to the usual transverse diffusion coefficient through $\mathrm{D}_{eff} = \mathrm{D}_y \dot{\gamma}$. In figure 6.9 we plot the effective diffusion coefficient $\mathrm{D}_{eff}(\Delta\gamma)$ for the various system sizes and for various finite shear rates as well as under a quasistatic protocol. For all system sizes and shear rates we see that $\mathrm{D}_{eff}(\Delta\gamma)$ increases from a finite initial value (that increases with decreasing shear rate) to an asymptotic value for large strain. The transient strain interval appears not strongly shear rate or size dependent and is of the order of $\varepsilon_{transient} = 0.25$. The dependence of the asymptotic values of D_{eff} (we will call this asymptote D from now on) on shear rate is shown in figure 6.9 and displays

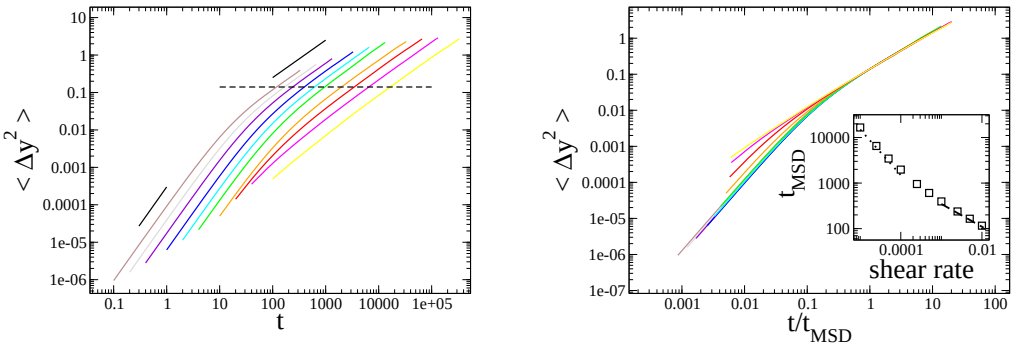

FIG. 6.8 : **Left** : Transverse mean square displacement (MSD) $\langle \Delta y^2 \rangle$ versus time for different shear rates $\dot{\gamma}$ (same color code as in previous figures). The dashed line marks the arbitrarily chosen distance criterion a verifying $a^2 = 0.14$ corresponding to a 'Lindemann' criterion for the transverse MSD of the particles. The intersection of this line with the colored curves marks the times t_{MSD}. The two thick black lines correspond to the power laws t^2 and t^1, i.e. respectively to the ballistic and diffusive regime.**Right**: same figure where time is rescaled by the times t_{MSD}. These plots are obtained in configurations with RWBCs and the average are computed in a central region of the samples therefore avoiding direct influence of the walls.

for high shear rates ($\dot{\gamma} \gtrsim 10^{-4}$), as expected from the relation $\mathrm{D}eff = \mathrm{D}_y\dot{\gamma}$, the scaling $\mathrm{D} \propto \dot{\gamma}^{\nu_2}$ ($\nu_2 \sim 0.5$). For low shear rates ($\dot{\gamma} \lesssim 10^{-4}$) on the other hand the effective diffusion coefficient saturates to a shear rate independent value that depends on system size as shown in figure 6.9.

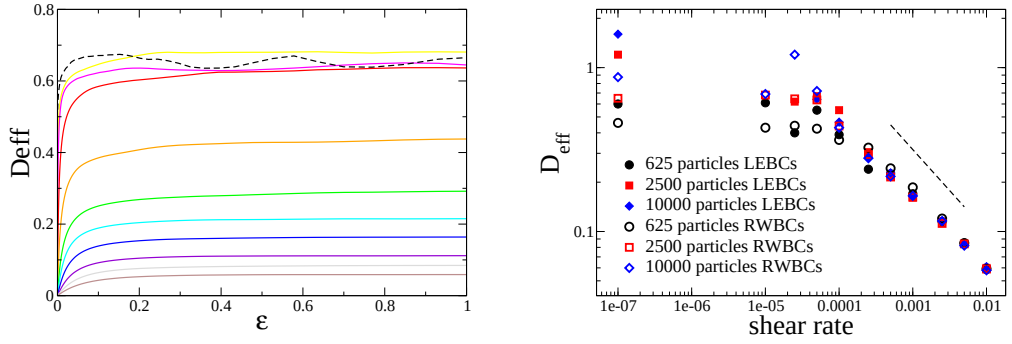

FIG. 6.9 : **Left** : Effective diffusion coefficients defined as $\mathrm{D}_{eff}(\Delta\gamma) = \langle \Delta y^2 \rangle / 2\Delta\gamma$ for different shear rates ranging from bottom to top from $\dot{\gamma} = 10^{-5}$ to 10^{-5} (same color code as previous figures) and for the quasistatic shear protocol (black dashed line). D_{eff} is computed here for samples containing 2500 particles under RWBCs. The spatial averaging is performed sufficiently far from the rigid walls to avoid boundary effects. **Right**: The asymptotic values D_{eff} are plotted for various shear rates, system sizes and boundary conditions. The dashed line marks the power law $\mathrm{D}_{eff} \propto \dot{\gamma}^{-0.5}$ as a guide to the eyes.

Lemaître [224] finds the following two limiting scaling behaviors of the effective diffusion coefficient D_{eff}. First in the high shear rate limit one gets uncorrelated localized plastic events and

$$D_{eff} \propto \ln(L) \tag{6.4}$$

whilst at low shear rates Lemaître predicts a linear scaling

$$D_{eff} \propto L. \tag{6.5}$$

This linear scaling was also obtained numerically in [271]. In this article the linear scaling of D_{eff} is recovered by the authors with a simple argument if one assumes that the mechanical response of the material is dominated by uncorrelated system spanning slip lines. One then simply has $D_{eff} = \langle \Delta r^2 / \Delta\gamma^2 \rangle \approx (\Delta\gamma/(a/L))\, a^2/12$, where a is the slip amplitude, $\Delta\gamma$ is the applied strain increment and $a^2/12$ is the average mean square displacement associated to an individual slip line and accumulated during a strain of $\sim a/L$. Note that a is assumed to be size independent.

The difference between Maloney's and Lemaître's approach is in the fact that while the latter assumes the elementary constituents of the response to be the avalanches observed in deformed glassy materials the former believes that one must take into account the entire system spanning slip lines that are formed by a cluster of avalanches as elementary constituents of the rheology.

Due to the large fluctuations of the effective diffusion our results (figure 6.9) do not allow us to resolve clearly these questions. Therefore while we cannot rule out the three main observations made by Lemaître we cannot either confirm them. First pertaining to the system size dependence of D at low shear rates we indeed observe that D grows with system size but our number of box sizes and the uncertainty for each measure of D stops us from descriminating between a $D_{eff} \propto \ln(L)$ or a $D_{eff} \propto L$ scaling. Second, at higher shear rates, with a simple argument based on the long range elastic propagator of the local quadrupoles Lemaître predicts $D_{eff} \propto \ln(L)$. This seems in contrast with our findings where D_{eff} at high shear rates seems system size independent (see figure 6.9 and compare with figure 5 in [224]). Finally due to the very long simulation time required to produce runs for shear rates below[4] $\dot{\gamma} \simeq 10^{-5}$ we cannot extract clearly the system size dependence of the critical shear rate $\dot{\gamma}_c$ separating the system size dominated regime from the shear rate dominated regime. In line with previous numerical studies (for example [224, 272, 105]) this change of behavior for the three system sizes presented here is located in the range $10^{-5} \lesssim \dot{\gamma} \lesssim 10^{-4}$. While these results convincingly illustrate the influence of shear rate on the atomic motion in a sheared glass they also call for extended simulation runs. In the next section we focus on what is thought to be associated with this change of behavior

[4] As discussed in chapter 2 a run at $\dot{\gamma} = 10^{-5}$ for a system of size L = 100 takes of the order of a few days for 400% strain.

namely the existence of a growing dynamical heterogeneity length scale as the shear-rate is reduced.

6.3 Dynamical heterogeneity

As illustrated in the introductory section of this chapter the dynamical heterogeneity is quantified in supercooled liquids near the glass transition and more recently in jammed systems near the jamming point by the so-called four-point correlation function. Here we propose to extend these approaches to the case of sheared glasses where instead of T, the temperature, in the case of supercooled liquids or ϕ, the volume fraction, in granular materials we consider here $\dot{\gamma}$ as the new control parameter. The analytical framework allowing to quantify the dynamical heterogeneity remains nevertheless identical and we therefore use these tools in our present analysis, in particular our analysis parallels the experimental study by Lechenault *et al* in [262] on the critical scalings and heterogeneous dynamics near the jamming/rigidity transition of a granular material.

As already discussed in section 5.3.3 of chapter 5 the dynamical cooperativity is quantified as the fluctuations of a two-point correlation function. Here we choose as a two point correlation function the transverse part self correlation function (as in equation 6.2) that we express here rather than in function of time in terms of the strain interval ε as,

$$Q_s(a,\varepsilon) = \frac{1}{N}\sum_i \exp(-\frac{\Delta y_i(\varepsilon)^2}{2a^2}) \ , \tag{6.6}$$

where a is a characteristic length scale over which the dynamics is probed. In figure 6.10 we represent the dependence of the spatial (index i for each particle) and temporal/strain (index ε) average $Q(a,\varepsilon) = \langle Q_s(a,\varepsilon)\rangle_{i,\varepsilon}$ as a function of both the parameter a and the strain interval ε, or rather $\gamma = \varepsilon/2$. The function is here plotted for a shear rate of $\dot{\gamma} = 10^{-4}$ and for a sample containing 2500 particles under RWBCs. $Q(a,\varepsilon)$ takes values in the range [0,1], with $Q \sim 1$ typically when the transverse motion is small relatively to a, $\Delta y \ll a$, and $Q \sim 0$ in the opposite situation when $\Delta y \gg a$. Following [262], we superimpose in figure 6.10 on the colormap of Q the root of the transverse MSD, $\delta(\gamma,\dot{\gamma}) = \sqrt{\Delta y^2}(\gamma)$. Interestingly, as for granular materials around the jamming volume fraction we see that the MSD follows very well the decay of $Q(a,\varepsilon)$ and that here also the function $Q(a,\varepsilon)$ can be rescaled for all shear rates as $Q(a,\varepsilon) = Q'(\delta(\varepsilon,\dot{\gamma})/a)$ showing that the MSD defines the only microscopical relevant distance for a given strain and shear rate.

Turning now to the fluctuations of the self correlation function $Q_s(a,\varepsilon)$ 6.6 we define the four-point correlation function $\chi_4(a,\varepsilon)$ as (see also chapter 5),

$$\chi_4(a,\varepsilon) = N\left[\langle Q_s(a,\varepsilon)^2\rangle_{i,\varepsilon} - \langle Q_s(a,\varepsilon)\rangle^2_{i,\varepsilon}\right] \ . \tag{6.7}$$

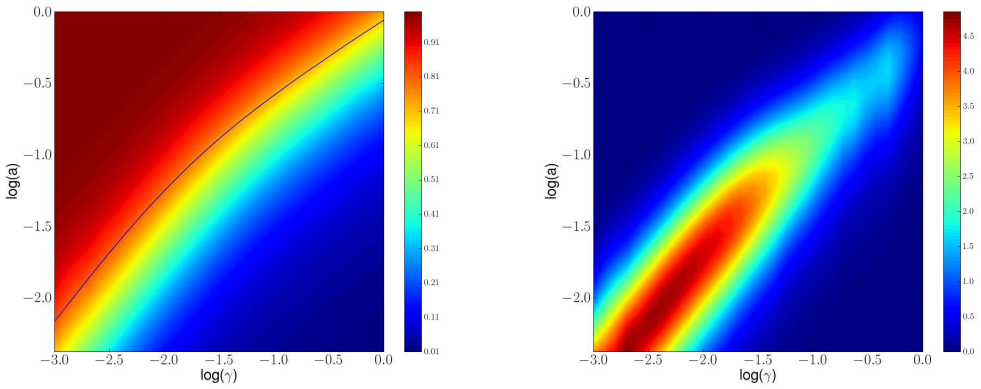

Fig. 6.10 : Dynamical correlation functions computed over the particles of a sample containing 2500 particles and sheared at $\dot{\gamma} = 10^{-4}$ under RWBCs for a total strain $\varepsilon_{tot} = 200\%$. **Left** : Correlation function $Q_s(a, \gamma)$ as a function of the probing length a and the strain γ in a log-log colormap. **Right**: Four-point correlation function $\chi_4(a, \gamma)$ in a log-log colormap.

Again we remind the reader that $\chi_4(a, \varepsilon)$ gives an estimate of the number of particles that move cooperatively when the sample is subjected to global strain ε. We produce an example of this function for a shear rate of $\dot{\gamma} = 10^{-4}$ in figure 6.10 where we see that at this shear rate the maximum cooperativity is of the order of 5 particles. Again in line with [262] we obtain the same scaling with the mean square displacement of the four-point correlation function $\chi_4(a, \varepsilon)$ that can be rescaled as $\chi_4(a, \varepsilon) = h(\dot{\gamma}, \varepsilon)\chi_4'(\delta(\varepsilon, \dot{\gamma})/a)$ where the amplitude $h(\dot{\gamma}, \varepsilon)$ depends both on shear rate and strain interval. From this figure we cannot determine if there is a point (log(a),log(ε)) with finite values in this map corresponding to an absolute maximum of the function $\chi_4(a, \varepsilon)$ as is observed by Lechenault *et al.* [262] or if the maximum is pushed at non-finite values.

We now turn to the influence of the shear rate on the dynamical cooperativity in the driven glasses. Figure 6.11 shows for different shear rates the build up of cooperativity in a glass sample containing 2500 particles. The curves start from a low value of $\chi_4(a, \varepsilon)$ at low strain go through a maximum $\chi_4^{max}(\dot{\gamma})$ at a corresponding strain $\varepsilon_{\chi_4}^{max}(\dot{\gamma})$ ($t_{\chi_4}^{max} = \varepsilon_{\chi_4}^{max}/\dot{\gamma}$) and decay to zero for larger strains. Here the log-log representations allows to see that the growth with strain is of the form $\chi_4(\varepsilon) \propto \varepsilon^4$ for high shear rate values while towards the quasistatic limit the behavior changes toward a $\chi_4(\varepsilon) \propto \varepsilon^1$ growth. Note that the ε^4 behavior is consistent with a ballistic regime while ε^1 is consistent with a regime dominated by collectively rearranging regions (see [221]). The curves of figure 6.11 allow us to extract the dependence of the time scale $t_{\chi_4}^{max}$ with shear rate $\dot{\gamma}$ and we display this in the inset of figure 6.11. We find a scaling of the form $t_{\chi_4}^{max} \propto \dot{\gamma}^{-\nu_3}$ with $\nu_3 \sim 0.65$, hence very close to the coefficient $\nu_1 \sim 0.63$ observed for the relaxation time $t_{1/e}$ associated to the correlation functions Q_s. This time dependence differs on the other hand slightly from the time t_{MSD} extracted from the Lindemann criterion on the transverse mean square displacement $\nu_2 \sim 0.5$ (see figure 6.8).

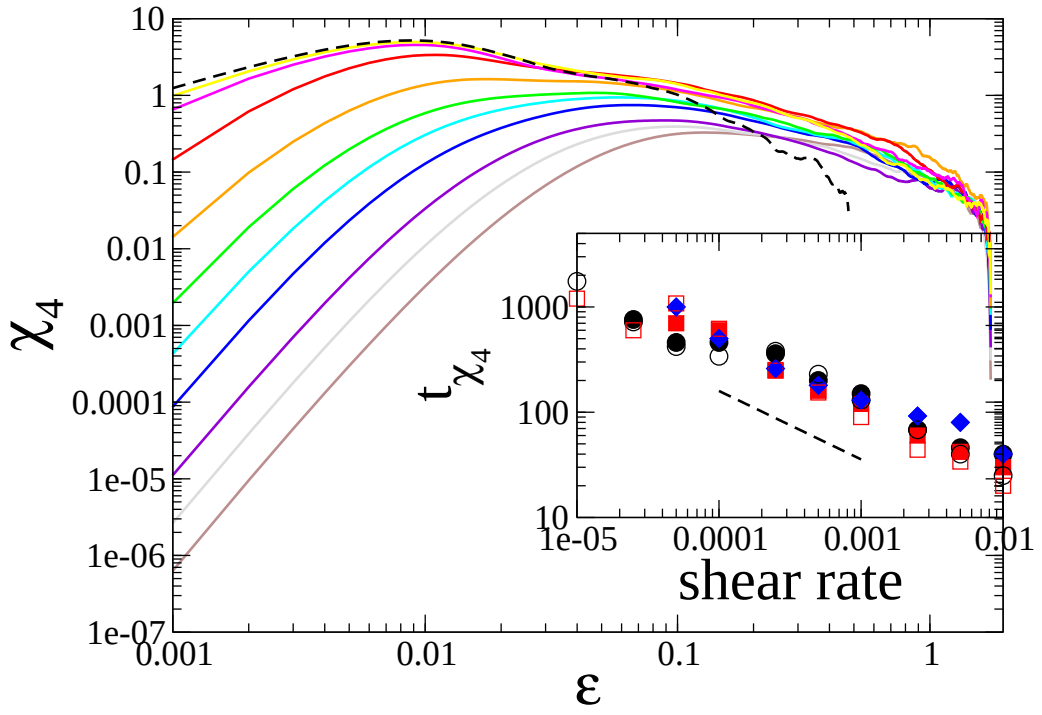

Fig. 6.11 : Four-point correlation function as a function of strain ε for different shear rates (same color code as previous figures) computed on samples containing 2500 particles and sheared under RWBCs. The averaging is done over 15 samples over a total strain of $\varepsilon = 200\%$ on each configuration. **Insert :** Shear rate dependence of the time $t_{\chi_4}^{max}$ associated to the peak of χ_4. The different symbols correspond to different system sizes and boundary conditions, see figure 6.8 for the legend. The dashed line corresponds to the power law $\dot{\gamma}^{-0.5}$ and is shown as a guide to the eyes.

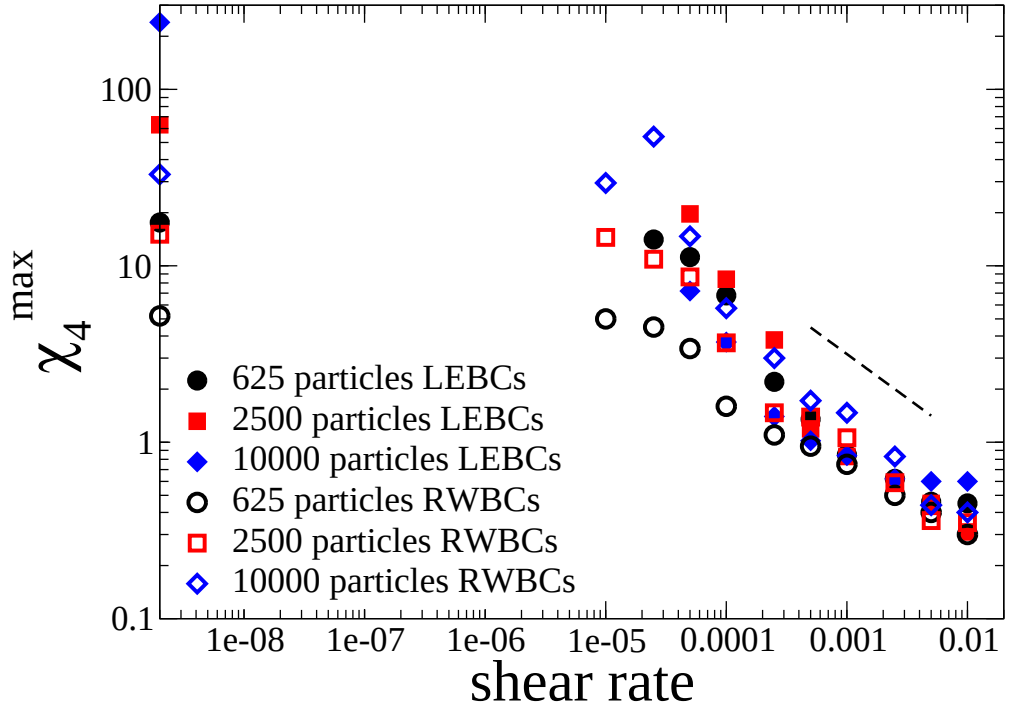

Fig. 6.12 : maximum values χ_4^{max} of the four-point correlation function as a function of shear rate $\dot{\gamma}$ for various system sizes and boundary conditions. The dashed line shows the power law $\propto \dot{\gamma}^{-\mu}$, with $\mu = 0.6$.

Again it is satisfactory to observe, in figure 6.11, the convergence of the $\chi_4(a, \varepsilon)$ associated to the finite shear rate deformation runs towards the quasistatic data as the two sets of simulations are produced from completely independent codes and procedures. For the system size analyzed in this figure (L=50) we see that the number of particles moving in a cooperative manner is of the order of $\chi_4^{max} \sim 18$ in the quasistatic regime. In figure 6.12 we have collected all the values of χ_4^{max} for the various system sizes, boundary conditions and shear rates that we have analyzed. The result shows strikingly the growth of cooperative length scale with decreasing shear rate for all system sizes. This plot illustrates again (as was the case for the flow curve or for the diffusion properties) two regimes, namely a high shear rate regime (above a critical shear rate $\dot{\gamma} \gtrsim \dot{\gamma}_c$) where χ_4^{max} grows with decreasing $\dot{\gamma}$ and a plateau regime where χ_4^{max} saturates to a system size limited value. While the data are still quite scattered they allow to extract a typical scaling coefficient μ for the dependence of χ_4^{max} on $\dot{\gamma}$ as $\chi_4^{max} \propto \dot{\gamma}^{-\mu}$, with $\mu \sim 0.4 - 0.6$. The dependence of χ_4^{max} on system size in the quasistatic regime is too noisy to be quantified precisely at the present stage of our study. It is obvious nevertheless that the dynamical cooperativity χ_4^{max} grows in the quasistatic regime with system size in a way that indicates finite size effects. We will come back to the scaling exponent μ in the last section of this chapter and relate our findings with previous observations. But let us try first to visualize the spatial structures associated to this build up of a growing dynamical heterogeneity length scale as $\dot{\gamma} \to 0$.

Dynamical heterogeneity - spatio-temporal structures. There are two aspects that we would like to illustrate here. First how does the dynamical heterogeneity build up during the strain of a glassy material, in other words when one looks at spatial maps of $Q_s^i = \exp\left(-\frac{\Delta y_i(\varepsilon)^2}{2a^2}\right)$ for increasing values of ε. Second how the dynamical heterogeneity is affected by the value of the imposed shear rate, in other words when one plots spatial maps of Q_s^i at $\varepsilon_{chi_4}^{max}$ but for different shear rates. The next two panels of 6.13 and 6.14 illustrate respectively the spatial fluctuations of $\exp\left(-\frac{\Delta y_i(\varepsilon)^2}{2a^2}\right)$ and $\exp\left(-\frac{\Delta r_i(\varepsilon)^2}{2a^2}\right)$ for various strain intervals, while the panel 6.15 illustrates the fluctuations of $\exp\left(-\frac{\Delta y_i(\varepsilon)^2}{2a^2}\right)$ at the peak of the four-point correlation function χ_4 for different shear rates. Comparing figure 6.13 and figure 6.14 confirms the already observed fact that the relaxation of the Q_s^i to zero is faster in the x direction that in the y direction. This anisotropy is here enhanced by the presence of walls but would be visible also under LEBCs. It is striking to see in figure 6.15 the growth of a cooperativity length scale as the shear rate is decreased from 10^{-3} to 10^{-5}. Indeed one sees that the response of the glass to the external shear rates becomes more and more heterogeneous as the shear rate is lowered and that at $\dot{\gamma} = 10^{-5}$, for example, the typical size of the clusters of particles that have moved more than $a = 0.1$ (the white particles) seems to reach an important fraction of system size. Note that in all these maps the clusters seem to form anisotropic structures elongated along the y axis. We attribute this anisotropy to the formation of vortices.

Let us finally conclude this chapter by giving a simple physical argument that helps

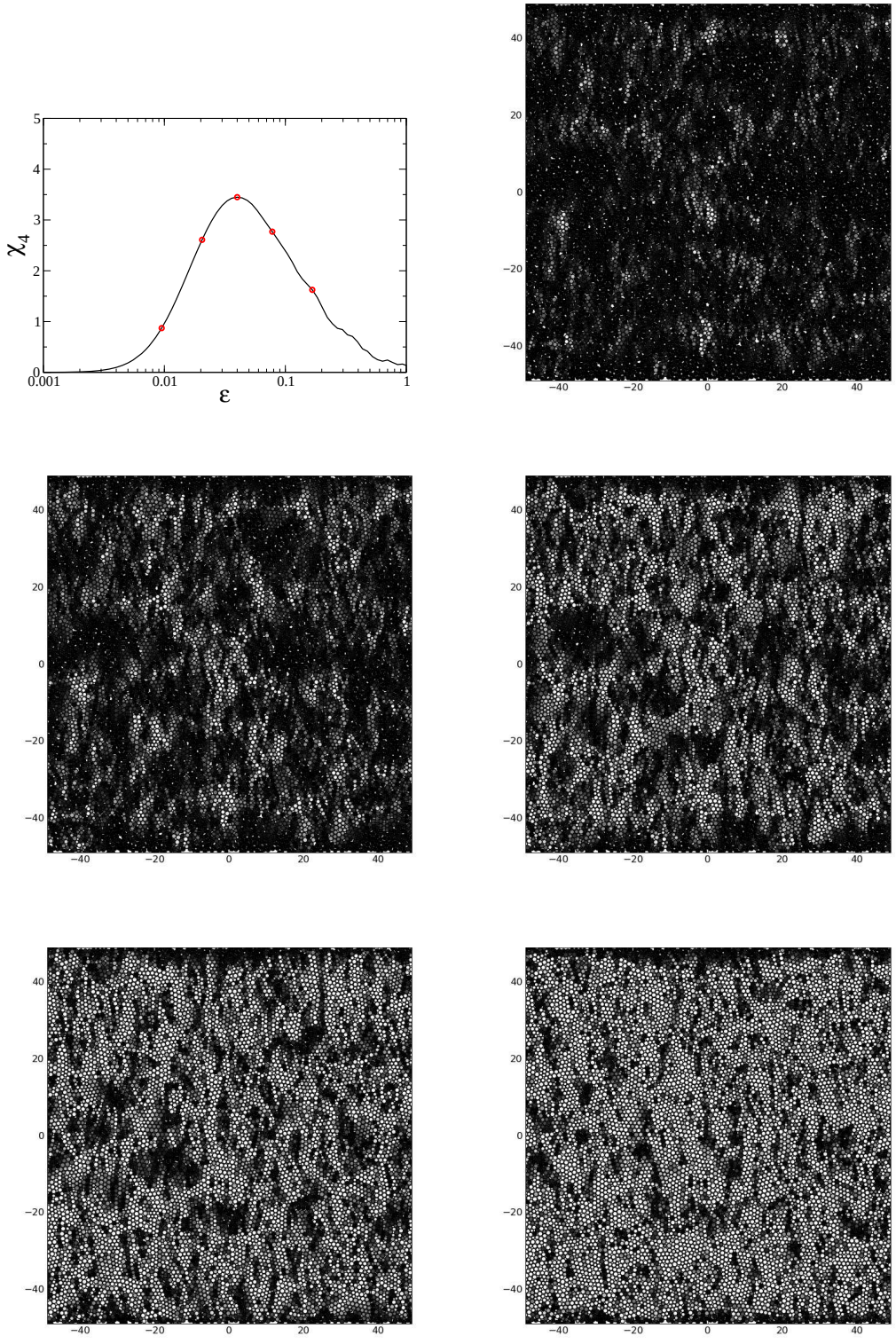

Fig. 6.13 : **Top left corner :** $\chi_4(\varepsilon)$. The red marks correspond to the strain intervals at which the five spatial maps of the self correlation function $Q_s^i(\varepsilon) = \exp\left(\frac{\Delta y_i(\varepsilon)^2}{2a^2}\right)$ are computed. From top to bottom and from left to right, $\varepsilon = 10^{-2}$,$\varepsilon = 2 \cdot 10^{-2}$,$\varepsilon = 4 \cdot 10^{-2}$,$\varepsilon = 8 \cdot 10^{-2}$,$\varepsilon = 16 \cdot 10^{-2}$. All figures are obtained on a sample containing 10000 particles under RWBCs and at a shear rate of $\dot{\gamma} = 5 \cdot 10^{-4}$.

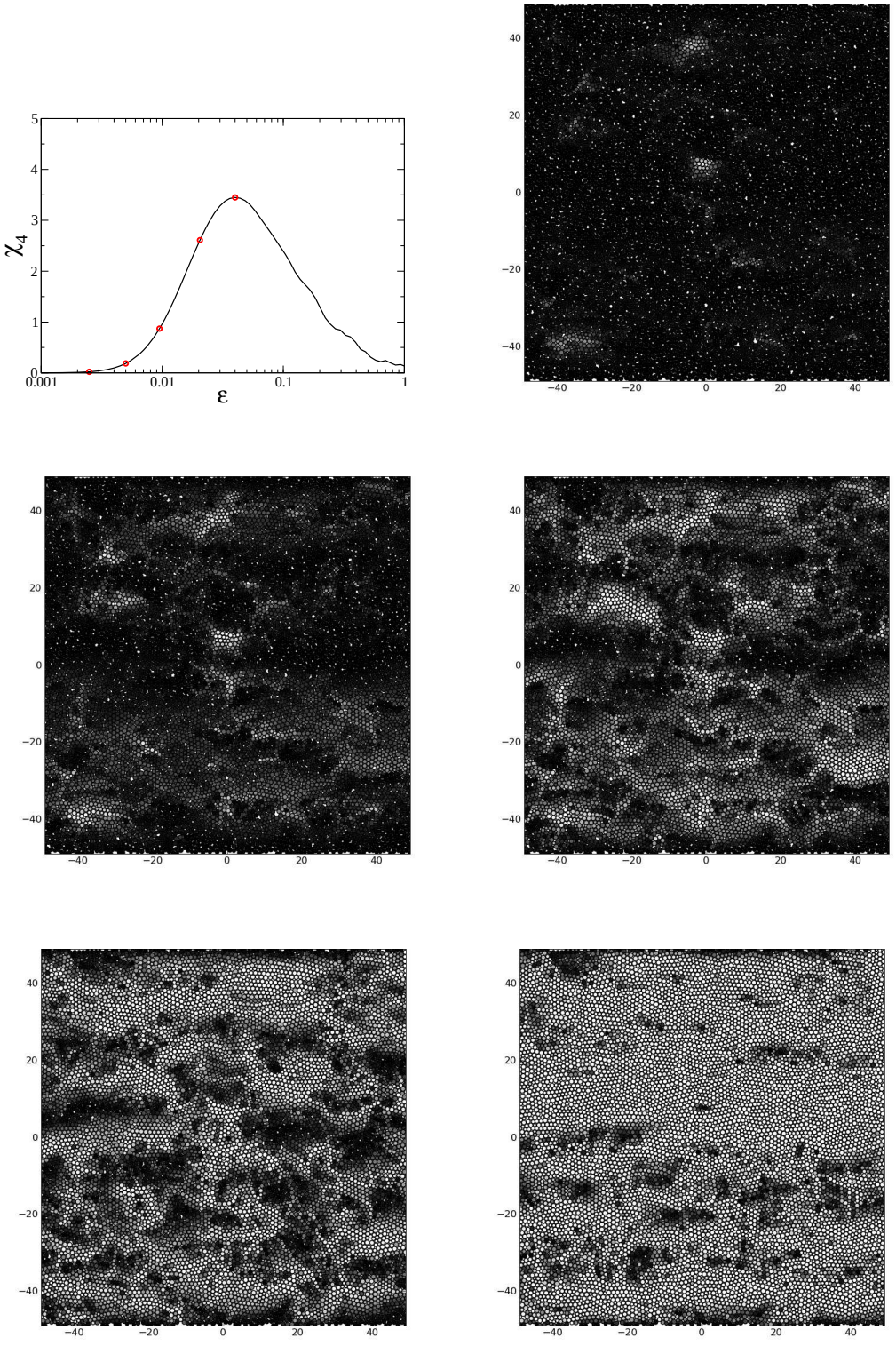

FIG. 6.14 : **Top left corner :** $\chi_4(\varepsilon)$. The red marks correspond to the strain intervals at which the five spatial maps of the self correlation function $Q_s^i(\varepsilon) = \exp\left(\frac{\Delta r_i(\varepsilon)^2}{2a^2}\right)$ are computed. From top to bottom and from left to right, $\varepsilon = 2.5 \cdot 10^{-3}$,$\varepsilon = 2.5 \cdot 10^{-3}$,$\varepsilon = 5 \cdot 10^{-3}$,$\varepsilon = 10^{-2}$,$\varepsilon = 2 \cdot 10^{-2}$. All figures are obtained on a sample containing 10000 particles under RWBCs and at a shear rate of $\dot{\gamma} = 5 \cdot 10^{-4}$.

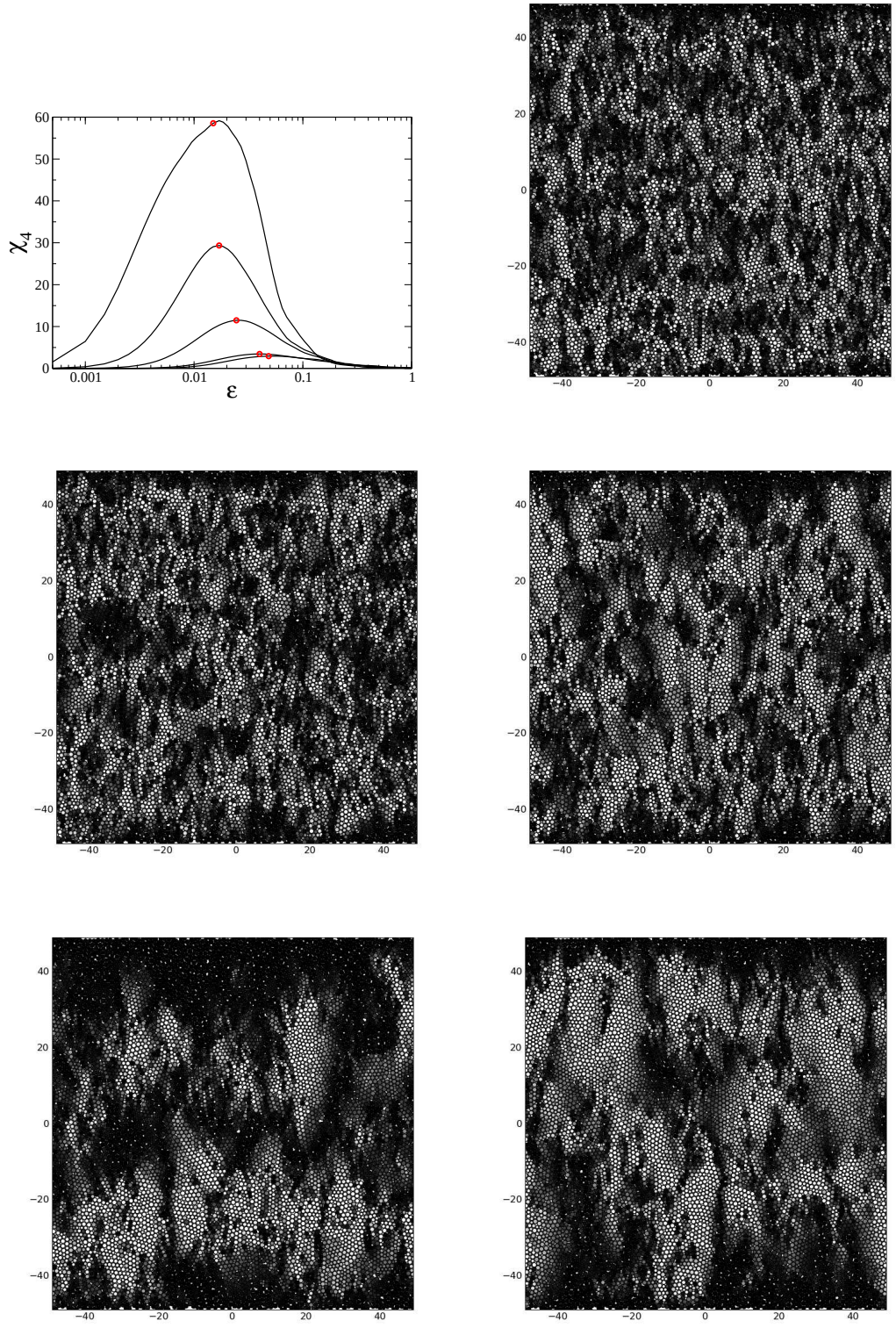

Fig. 6.15 : **Top left corner :** $\chi_4(\varepsilon)$. The red marks correspond to the strain intervals at which the five spatial maps of the self correlation function $Q_s^i(\varepsilon) = \exp\left(\frac{\Delta y_i(\varepsilon)^2}{2a^2}\right)$ are computed. From top to bottom and from left to right, $\dot{\gamma} = 10^{-3}$,$\dot{\gamma} = 5 \cdot 10^{-4}$,$\dot{\gamma} = 10^{-4}$,$\dot{\gamma} = 5 \cdot 10^{-5}$,$\dot{\gamma} = 10^{-5}$. All figures are obtained on a sample containing 10000 particles and for RWBCs.

to understand the scaling of this cooperative length scale with shear rate. The argument goes as follows. Assume that the regions that are prone to fail plastically (we call them the triggering points) under shear are homogeneously distributed in the glass and that the density per unit strain ρ_{te} (te stands for triggering events) of these points is a constant that is independent of strain rate. Then during a time interval t there are $\dot{\gamma} \times t \times \rho_{te}$ triggering points that are excited and one can define the average distance l_{te} between these points to be $l_{te} = (\rho_{te}\dot{\gamma}t)^{-1/d}$, where d is the dimension. These points by definition are triggering a quadrupolar event that as we have discussed in the previous section can induce further plastic rearrangements in its vicinity. More specifically a plastic rearrangement induces a quadrupolar redistribution of the stress in its surrounding and one expects an increased probability of having a new plastic event where the stress is increased, i.e. along the vertical and horizontal axis. The simplest hypothesis concerning the propagation of the events is that it occurs through a diffusive process[5]. One can then define a new length scale $l_D = \sqrt{Dt}$, where D is the diffusion coefficient. Now to extract a characteristic length scale we identify these two length scales, $l_{te} = l_D$ which yields a characteristic time t_c,

$$t_c = \rho^{\frac{-1}{d/2+1}} D^{\frac{-1}{1+2/d}} \dot{\gamma}^{\frac{-1}{d/2+1}} \ , \tag{6.8}$$

and a corresponding length scale scaling as,

$$l_c = \rho^{\frac{-1}{d+2}} D^{\frac{1}{d+2}} \dot{\gamma}^{\frac{-1}{d+2}} \ . \tag{6.9}$$

In two dimensions this corresponds to the scalings $t_c \propto \dot{\gamma}^{-1/2}$ and $l_c \propto \dot{\gamma}^{-1/4}$ while in three dimensions one expects $t_c \propto \dot{\gamma}^{-2/5}$ and $l_c \propto \dot{\gamma}^{-1/5}$. These results argue rather well with the observations made earlier on the relaxation time scale and on the growth of a cooperativity length scale. We argue that this length should correspond to the maximum extent of the plastic cascade and therefore to the maximum cooperativity length. Indeed when l_D becomes of the order of the distance between triggering events l_{te} each plastic cascade starts to 'feel' the presence of the neighboring cascades and its progression is perturbed. Finally we see that the exponent $-1/4$ is in good agreement with what is observed numerically in figure 6.12 and also with the predictions of the KEP model introduced in section 1.4.2 of the introduction 1.

[5]One can make the model more quantitative by mapping it to the problem of diffusion on a grid and try. One can estimate the diffusion coefficient from atomic considerations as $D \sim \xi^2/\tau$, where ξ is the optimal distance between successive plastic rearrangements and τ is the duration of plastic event. From figure 6.4 one can estimate ξ to be of the order of $\xi \sim 20 - 30\sigma$ and one can identify τ with the duration of a plastic event $\tau \sim \tau_e \sim 10 - 100$. This gives $1 \lesssim D \lesssim 100$

Chapter 7

Conclusions and perspectives

Conclusions. To identify and explain the mechanisms involved in the spatially heterogeneous response of glassy materials to an external drive we have presented in this thesis our results in three parts. In the first part, including the introduction 1 and chapter 2, we presented the existing literature concerning the mechanical response of glasses. As we have seen this consists of experimental, numerical and theoretical work on various materials ranging from metallic glasses, mineral glasses, polymeric glasses to complex fluids, foams and granular media. In fact this class of systems can even be extended to geophysical processes such as earthquakes or sea ice rheology and the question of the mechanical response of glasses can be generalized to the slightly broader question of the response of any complex system to an external drive. In chapter 2 we presented the two numerical techniques, Molecular Dynamics and quasistatic energy minimization protocol, at the heart of our work. Following a brief summary of earlier numerical simulations of sheared glassy materials we introduced and justified our choice of a polydisperse Lennard-Jones two-dimensional model glass. Because of its disordered glassy nature this system was shown to account for many of the generic properties shared by 'real' glasses and can be thought of as a good prototype model to work on.

The second part of the manuscript contains chapter 3 and 4 and can be seen as an attempt to find a local structural signature of the plastic heterogeneous response of the Lennard-Jones glass. This part was an extension of a previous work started in the group 'Théorie and Modélisation' at the Laboratoire de Physique de la Matière Condensée et Nanostructures (LPMCN) in order to test the limit of applicability of continuum mechanics at distances of the order of a few interparticle sizes. Our input has consisted in applying a novel method developed by Goldhirsh and Goldenberg to compute microscopically derived coarse-grained expressions of the local fields of continuum mechanics and in particular of the local elasticity tensor. In chapter 3, after reminding the theory of continuum mechanics and linear elasticity, we introduced the method of Goldhirsh and Goldenberg. Using this method we computed the local elasticity tensor and quantified the deviation from linear elasticity (local Hooke's law) at different coarse-graining scales. From the results a clear

picture emerged of an amorphous material with strongly spatially heterogeneous elastic moduli that simultaneously satisfies Hooke's law at scales larger than a characteristic length scale of the order of five interatomic distances. At this scale, the glass appears as a composite material composed of a rigid scaffolding and of soft zones. In chapter 4 we used this local elastic order parameter to relate structure and dynamics in sheared glasses. Only recently calculated in non-homogeneous materials, the local elastic structure plays a crucial role in the elastoplastic response of the amorphous material. We showed that for a small macroscopic shear strain, the structures associated with the non-affine displacement field appear directly related to the spatial structure of the elastic moduli. Moreover, for a larger macroscopic shear strain we showed that zones of low shear modulus concentrate most of the strain in the form of plastic rearrangements. The spatio-temporal evolution of this local elasticity map and its connection with long term dynamical heterogeneity as well as with the plasticity in the material was quantified. The possibility to use this local parameter as a predictor of subsequent local plastic activity was also discussed. We concluded this part by comparing this local elasticity maps with a soft modes analysis and showed that the two approaches contain very similar information.

In the third part, comprising chapter 5 and 6 we turned to the study of the heterogeneous response and dynamical heterogeneity that builds up in the sheared glasses. In chapter 5 we focused on the quasistatic and athermal limit and presented first the two main macroscopic signatures of the heterogeneous response, namely an intermittent stress-strain response and a fluctuating velocity profile. We showed that in the quasistatic athermal regime the spatially heterogeneous plastic flow is composed of dynamical building blocks of various sizes, ranging from local quadrupolar plastic events to system spanning shear bands. We proposed a simple analytical description of the heterogeneous stress evolution in the sample as a sum of uncorrelated localized quadrupolar plastic events. We then turned to the atomistic response of the model glass and to the precise analysis of the motion and stress evolution of the individual particles. To this aim we introduced various statistical tools such as the four-point correlation function and the cooperativity number. In chapter 6 we generalized our study of the heterogeneous dynamics to the finite shear-rate ($\dot{\gamma} \neq 0$) and temperature case ($T \neq 0$). In practice we chose an effectively athermal limit ($T \sim 0$) and focused on the influence of shear rate on the rheology of the glass. In line with previous works we found that the model Lennard-Jones glass follows the rheological behavior of a yield stress fluid with a Hershel-Bulkley response of the form, $\sigma = \sigma_Y + c_1\dot{\gamma}^{\beta}$. The global mechanical response obtained through the use of Molecular Dynamics was shown to converge in the limit $\dot{\gamma} \to 0$ to the quasistatic limit obtained with the energy minimization protocol. The detailed analysis of the plastic deformation at different shear rates showed that the glass follows different flow regimes. At sufficiently low shear rates the mechanical response reaches a shear-rate independent regime that exhibits all the characteristics of the quasistatic response (finite size effects, cascades of plastic rearrangements, yield stress...). At intermediate shear rates the rheological properties are determined by the externally applied shear-rate and the response deviates from the quasistatic limit. Finally at higher

shear rates the system reaches a shear-rate independent homogeneous regime. The existence of these three regimes was also confirmed by the detailed analysis of the atomic motion. The computation of the four-point correlation function showed that the transition from the shear-rate dominated to the quasistatic regime was accompanied by the growth of a dynamical cooperativity length scale ξ that was shown to diverge with shear rate as $\xi \propto \dot{\gamma}^{-\nu}$, with $\nu \sim 0.2 - 0.3$. This scaling was compared with the prediction of a simple model that assumes the diffusive propagation of plastic events (analogous to the 'fluidity' in the KEP model).

Perspectives. We believe that the work achieved in this thesis offers some challenging directions of future research. First the coarse-grained method presented in chapter 3 is adapted to the computation of elastic moduli (and more generally of any field of continuum mechanics) at different length scales and for all sorts of materials. A direct extension of our work would be to apply this method on some realistic model materials. An interesting question would then be to find if this measurement can be related with a more local and simpler structural property of the samples studied. In the case of model silicon systems, where local tetrahedral order due to the covalent bound is important, it has been shown that plastic activity is related with the occurrence of local coordination defects and unusual atomic environment. It is not the case in Lennard-Jones glasses. It would be very interesting to see if a criterion based on the lowest local elastic shear modulus would be also valid in other systems, independent on the local directionality of bounds. The relation between plastic activity and elastic structure discussed in chapter 4 opens new possibilities in the theoretical and experimental study of the deformation of glasses. From a theoretical point of view, the detailed study of the dynamical evolution of local elastic moduli should allow construction of a model as we have already done for the local stress components, including a criterion for local plastic rearrangement. From an experimental point of view, this study shows that the resolution for the measurement of a local elastic modulus should be less than ten interatomic distances, in order to include a description of the relevant scales of elastic heterogeneities. New experimental methods have been proposed recently in order to evaluate the deformation at the nanometer scale. This study should encourage continuation in this way.

Concerning the rheology of the glasses the results of chapter 5 and 6 call for many complementary studies. In particular the influence of finite shear rate and temperature was only introduced in this thesis and a precise study of the influence of these two external parameters on the rheology of the glassy materials is essential. These systems were shown to develop a diverging cooperativity length scale with lowering shear rate and one can ask how this dynamical length scale affects the flow of confined glassy systems. Preliminary results concerning the effect of temperature have shown surprising effects associated with the presence of a small but finite temperature and many further simulation runs at various temperatures and shear rates are needed to apprehend the rheology of the glasses. Similarly our results on a two dimensional system call for a generalization to the three dimensional

case. Our results have also confirmed at the atomic level many of the predictions of the mesoscopic extremal elasto-plastic models and quantitative comparison would require an extended amount of simulated material, larger system sizes and lower shear rates. Finally our work is a first step towards a better understanding of the elementary building blocks needed to construct a mesoscopic description of the rheology of glassy materials along with innovative constitutive laws. Another possible extension of this work would be to map the rheology of the structural glasses obtained through the use of atomic scale simulations to a kinetically constrained model, the collaborative nature of the dynamical building blocks presented in chapter 5 and 6 seems indeed to validate this type of approach.

Bibliography

[1] T. Rehren et E. B. Pusch : Late bronze age glass production at qantir-piramesses, egypt. *Science*, 308:1756, 2005.

[2] Y. Shi et M. L. Falk : Strain localization and percolation of stable structure in amorphous solids. *Phys. Rev. Lett.*, 95:095502, 2005.

[3] M. L. Falk et J. S. Langer : Dynamics of viscoplastic deformation in amorphous solids. *Phys. Rev. E*, 57(6):7192–7205, Jun 1998.

[4] C. Maloney et A. Lemaître : Subextensive scaling in the athermal, quasistatic limit of amorphous matter in plastic shear flow. *Phys. Rev. Lett.*, 93(1):016001, Jul 2004.

[5] A. Tanguy, F. Leonforte et J. L. Barrat : Plastic response of a 2d lennard-jones amorphous solid: Detailed analysis of the local rearrangements at very slow strain rate. *The European Physical Journal E - Soft Matter*, 20:355–364, 2006.

[6] M. Tsamados, M. Tanguy, F. Léonforte et J.-L. Barrat : On the study of local-stress rearrangements during quasi-static plastic shear of a model glass: Do local-stress components contain enough information? *The European Physical Journal E - Soft Matter*, 26:283–293, 2008.

[7] G. J. Papakonstantopoulos, R. A. Riggleman, J.-L. Barrat et J. J. de Pablo : Molecular plasticity of polymeric glasses in the elastic regime. *Phys. Rev. E*, 77:041502, 2008.

[8] M. Talati, T. Albaret et A. Tanguy : Atomistic simulations of elastic and plastic properties in amorphous silicon. *Europhys. Lett.*, 86:66005, 2009.

[9] S. Tewari, D. Schiemann, D. J. Durian, C. M. Knobler, S. A. Langer et A. J. Liu : Statistics of shear-induced rearrangements in a two-dimensional model foam. *Phys. Rev. E*, 60(4):4385–4396, Oct 1999.

[10] G. Debrégeas, H. Tabuteau et J.-M di Meglio : Deformation and flow of a two-dimensional foam under continuous shear. *Phys. Rev. Lett.*, 87(17):178305, Oct 2001.

[11] A. Kabla et G. Debrégeas : Local stress relaxation and shear banding in a dry foam under shear. *Phys. Rev. Lett.*, 90(25):258303, Jun 2003.

[12] M. Dennin : Statistics of bubble rearrangements in a slowly sheared two-dimensional foam. *Physical Review E (Statistical, Nonlinear, and Soft Matter Physics)*, 70(4): 041406, 2004.

[13] E. Kolb, J. Cviklinski, J. Lanuza, P. Claudin et E. Clement : Reorganization of a dense granular assembly: The unjamming response function. *Physical Review E (Statistical, Nonlinear, and Soft Matter Physics)*, 69(3):031306, 2004.

[14] R. Besseling, Eric R. Weeks, A. B. Schofield et W. C. K. Poon : Three-dimensional imaging of colloidal glasses under steady shear. *Physical Review Letters*, 99(2):028301, 2007.

[15] P. Schall, D. A. Weitz et F. Spaepen : Structural rearrangements that govern flow in colloidal glasses. *Science*, 318:1895, 2007.

[16] C. Donati, J. F. Douglas, W. Kob, S. J. Plimpton, P. H. Poole et S. C. Glotzer : Stringlike cooperative motion in a supercooled liquid. *Phys. Rev. Lett.*, 80(11):2338–2341, Mar 1998.

[17] R. G. Larson : *The structure and rheology of complex fluids.* Oxford University press, New York, 1999.

[18] P. Oswald : *Rhéophysique ou comment coule la matière.* Belin, 2006.

[19] T. Burgess et M. Ferry : Nanoindentation of metallic glasses. *Materials today*, 12, 2009.

[20] M. F. Ashby et A. L. Greer : Metallic glasses as structural materials. *Scr. Mater.*, 54:321, 2006.

[21] Y. Shi et M. L. Falk : Stress-induced structural transformation and shear banding during simulated nanoindentation of a metallic glass. *ACTA MATERIALIA*, 55(13): 4317–4324, AUG 2007.

[22] S. Xie et E. P. George : Hardness and shear band evolution in bulk metallic glasses after plastic deformation and annealing? *Acta. Mater.*, 56:5202, 2008.

[23] J. Lu et K. Ravi-Chandar : Inelastic deformation and localization in polycarbonate under tension. *Int. J. Solids Struct.*, 36:391, 1999.

[24] R. Morbitzer et U. Eisele : *Introduction to polymer physics.* Springer, 1990.

[25] G. Strobl : *The physics of polymers.* Springer, 2007.

[26] P.-P. Cortet : *Croissance lente de fissures : de la fragilité à la complexité.* Thèse de doctorat, Ecole Normale Supérieure de Lyon, 2007.

[27] G. Ovarlez, S. Rodts, X. Chateau et P. Coussot : Phenomenology and physical origin of shear localization and shear banding in complex fluids. *rheol. acta*, 2009.

[28] J. D. Goddard : Material instability in complex fluids. *Annu. Rev. Fluid. Mech.*, 35:113, 2003.

[29] P. C. F. Moller, J. Mewis et D. Bonn : Yield stress and thixotropy : on the difficulty of masuring yield stresses in practice. *Soft Matter*, 2:274, 2006.

[30] P. Coussot : Rheophysics of pastes : a review of microscopic model approaches. *Soft Matter*, 3:528, 2006.

[31] S. M. Fielding : Complex dynamics of shear banded flows. *Soft Matter*, 3:1262, 2007.

[32] J. K. G. Dhont et W. J. Brick : Gradient and vorticity banding. *Rheol Acta*, 47:257, 2008.

[33] P. D. Olmsted : Perspectives on shear banding in complex fluids. *Rheol Acta Materialia*, 47:283, 2008.

[34] T. Gibaud, C. Barentin, N. Taberlet et S. Manneville : Shear-induced fragmentation of laponite suspensions. *Soft Matter*, 5:3026, 2009.

[35] S. Bénito, C.-H. Bruneau, T. Colin, C. Gay et F. Molino : An elasto-visco-plastic model for immortal foams or emulsions. *The European Physical Journal E: Soft Matter and Biological Physics*, 25:1292, 2008.

[36] C.-Y. David Lu, Peter D. Olmsted et R. C. Ball : Effects of nonlocal stress on the determination of shear banding flow. *Phys. Rev. Lett.*, 84(4):642–645, Jan 2000.

[37] S. Lerouge, M. Argentina et J. P. Decruppe : Interface instability in shear-banding flow. *Physical Review Letters*, 96(8):088301, 2006.

[38] L. Bécu, S. Manneville et A. Colin : Spatiotemporal dynamics of wormlike micelles under shear. *Phys. Rev. Lett.*, 93(1):018301, Jun 2004.

[39] J.-F. Berret et Y. Séréro : Evidence of shear-induced fluid fracture in telechelic polymer networks. *Phys. Rev. Lett.*, 87:048303, 2001.

[40] A. Aradian et M. E. Cates : Minimal model for chaotic shear banding in shear thickening fluids. *Physical Review E (Statistical, Nonlinear, and Soft Matter Physics)*, 73(4):041508, 2006.

[41] L. Bécu, D. Anache, S. Manneville et Annie Colin : Evidence for three-dimensional unstable flows in shear-banding wormlike micelles. *Physical Review E (Statistical, Nonlinear, and Soft Matter Physics)*, 76(1):011503, 2007.

[42] J. Sprakel, E. Spruijt, M. A. Cohen Stuart, M. A. J. Michels et J. van der Gucht : Intermittent dynamics in transient polymer networks under shear: Signs of self-organized criticality. *Physical Review E (Statistical, Nonlinear, and Soft Matter Physics)*, 79(5):056306, 2009.

[43] J. Sprakel : *Physics of associative polymers; bridging time and length scales.* Thèse de doctorat, van Wageningen Universiteit, 2009.

[44] M. Dennin : Discontinuous jamming transitions in soft materials: coexistence of flowing and jammed states. *J. Phys. Condens. Matter*, 16:283101, 2008.

[45] Y. Wang, K. Krishan et M. Dennin : Impact of boundaries on velocity profiles in bubble rafts. *Physical Review E (Statistical, Nonlinear, and Soft Matter Physics)*, 73(3):031401, 2006.

[46] E. Janiaud, D. Weaire et S. Hutzler : Two-dimensional foam rheology with viscous drag. *Physical Review Letters*, 97(3):038302, 2006.

[47] V. J. Langlois, S. Hutzler et D. Weaire : Rheological properties of the soft-disk model of two-dimensional foams. *Physical Review E (Statistical, Nonlinear, and Soft Matter Physics)*, 78(2):021401, 2008.

[48] Berhinger : *http://www.phy.duke.edu/ bob/.*

[49] F. Da Cruz : *Ecoulement de grains secs : frottement et blocage.* Thèse de doctorat, Ecole nationale des ponts et chaussées, 2004.

[50] Y. Forterre et O. Pouliquen : Flows of dense granular media. *Annu. Rev. Fluid. Mech.*, 40, 2008.

[51] C. Derec, A. Ajdari et F. Lequeux : Rheology and aging : a simple approach. *Eur. Phys. J. E*, 4:355, 2001.

[52] G. Picard, A. Ajdari, L. Bocquet et F. Lequeux : Simple model for heterogeneous flows of yield stress fluids. *Phys. Rev. E*, 66(5):051501, Nov 2002.

[53] P. Coussot, Q. D. Nguyen, H. T. Huynh et D. Bonn : Avalanche behavior in yield stress fluids. *Phys. Rev. Lett.*, 88(17):175501, Apr 2002.

[54] H. Eyring : Viscosity, plasticity, and diffusion as examples of absolute reaction rates. *The Journal of Chemical Physics*, 4(4):283–291, 1936.

[55] J. Rottler et M. O. Robbins : Shear yielding of amorphous glassy solids: Effect of temperature and strain rate. *Phys. Rev. E*, 68(1):011507, Jul 2003.

[56] C. Monthus et J.-P. Bouchaud : Models of traps and glass phenomenology. *Journal of Physics A: Mathematical and General*, 29:3847–3869(23), 1996.

[57] P. Sollich, F. Lequeux, P. Hébraud et M. E. Cates : Rheology of soft glassy materials. *Phys. Rev. Lett.*, 78(10):2020–2023, Mar 1997.

[58] P. Sollich : Rheological constitutive equation for a model of soft glassy materials. *Phys. Rev. E*, 58(1):738–759, Jul 1998.

[59] S. M. Fielding, M. E. Cates et P. Sollich : Shear banding, aging and noise dynamics in soft glassy materials. *Soft Matter*, 5:2378, 2008.

[60] M. H. Cohen et D. Turnbull : Molecular transport in liquids and glasses. *The Journal of Chemical Physics*, 31(5):1164–1169, 1959.

[61] F. Spaepen : A microscopic mechanism for steady state inhomogeneous flow in metallic glasses. *Acta Metallurgica*, 25(4):407 – 415, 1977.

[62] A. S. Argon et H. Y. Kuo : Plastic flow in a disordered bubble raft (an analog of a metallic glass). *Materials Science and Engineering*, 39:101–109, 1979.

[63] D. Srolovitz, K Maeda, K. Vitek et T. Egami : Structural defects in amorphous solids statistical analysis of a computer model. *Philosophical Magazine A*, 44:847, 1981.

[64] Anaël Lemaître : Rearrangements and dilatancy for sheared dense materials. *Phys. Rev. Lett.*, 89(19):195503, Oct 2002.

[65] L. Bocquet, A. Colin et A. Ajdari : Kinetic Theory of Plastic Flow in Soft Glassy Materials. *PHYSICAL REVIEW LETTERS*, 103(3), JUL 17 2009.

[66] K. Chen, P. Bak et S. P. Obukhov : Self-organized criticality in a crack-propagation model of earthquakes. *Phys. Rev. A*, 43(2):625–630, Jan 1991.

[67] G. Picard : *Hétérogénéités de l'écoulement de fluides à seuil : approche phénoménologique et modélisation élasto-plastique.* Thèse de doctorat, Université Paris 7 - Denis Diderot, 2004.

[68] J.-C. Baret, D. Vandembroucq et S. Roux : Extremal model for amorphous media plasticity. *Phys. Rev. Lett.*, 89(19):195506, Oct 2002.

[69] A. Kabla : *Désordre et plasticité dans les milieux divisés : mousses et matériaux granulaires.* Thèse de doctorat, Université Paris 7, 2003.

[70] J. S. Langer : Microstructural shear localization in plastic deformation of amorphous solids. *Phys. Rev. E*, 64(1):011504, Jun 2001.

[71] G. Picard, A. Ajdari, F. Lequeux et L. Bocquet : Slow flows of yield stress fluids: Complex spatiotemporal behavior within a simple elastoplastic model. *Phys. Rev. E*, 71(1):010501, 2005.

[72] P. Hébraud et F. Lequeux : *Phys. Rev. Lett.*, 81:2934, 1998.

[73] J. Goyon, A. Colin, G. Ovarlez, A. Ajdari et L. Bocquet : Spatial cooperativity in soft glassy flows. *NATURE*, 454(7200):84–87, JUL 3 2008.

[74] O. Pouliquen : Velocity correlations in dense granular flows. *Phys. Rev. Lett.*, 93(24):248001, Dec 2004.

[75] S. Deboeuf, E. Lajeunesse, O. Dauchot et B. Andreotti : Flow rule, self-channelization, and levees in unconfined granular flows. *Physical Review Letters*, 97(15):158303, 2006.

[76] F. Léonforte, A. Tanguy, J. P. Wittmer et J. L. Barrat : Inhomogeneous elastic response of silica glass. *PHYSICAL REVIEW LETTERS*, 97(5), AUG 4 2006.

[77] T. Hatano : Power law rheology and the dynamical heterogeneity in a sheared granular material. 2008.

[78] F. Ercolesi : A molecular dynamics primer. http://www.sissa.it/furio.

[79] D. Frenkel et B. Smit : *Understanding molecular dynamics simulation.* Academic press, 1996.

[80] M. P. Allen et D. J. Tildesley : *Computer simulation of liquids.* Oxford university press, 1987.

[81] S. J. Plimpton : Fast parallel algorithms for short range molecular dynamics. *J. Comp. Phys.*, 117:1, 1995.

[82] V Ruhle : Berendsen and nose-hoover thermostats.

[83] W. G. Hoover : Canonical dynamics: Equilibrium phase-space distributions. *Phys. Rev. A*, 31(3):1695–1697, Mar 1985.

[84] http://www.gnu.org/software/gsl/manual/html$_n$*ode/multimin − algorithms − with − derivatives.html.*

[85] http://portal.acm.org/citation.cfm?id=138359.

[86] http://portal.acm.org/citation.cfm?id=202407.

[87] http://www.wag.caltech.edu/home-pages/mario/dec.lammps2001/history.html.

[88] http://www.biomath.nyu.edu/index/software/tnpack/index.html.

[89] S. Kobayashi, K. Maeda et S. Takeuchi : Computer simulation of deformation of amorphous cu57zr43. *Acta Metallurgica*, 28(12):1641 – 1652, 1980.

[90] P. E. Frandsen et K. Jonasson : Unconstrained optimization. Lecture notes.

[91] R. S. Dembo et T. Steihaug : Truncated-newton algorithms for large-scale unconstrained optimization. *Math. Prog.*, 26:190, 1983.

[92] Y. Shi et M. L. Falk : Simulations of nanoindentation in a thin amorphous metal film. *THIN SOLID FILMS*, 515(6):3179–3182, FEB 12 2007. Symposium on Mechanical Behavior of Thin Films and Small Structures held at the 2005TMS Annual Meeting, San Francisco, CA, FEB 13-17, 2005.

[93] D. Deng, A. S. Argon et S. Yip : Simulation of plastic deformation in a two-dimensional atomic glass by molecular dynamics. *Phil. Trans. R. Soc. Lond. A*, 329:613, 1989.

[94] F. Delogu : Atomic mobility and strain localization in amorphous metals. *Phys. Rev. Lett.*, 100:075901, 2008.

[95] N. P. Bailey, J. Schiøtz et K. W. Jacobsen : Simulation of cu-mg metallic glass: Thermodynamics and structure. *Phys. Rev. B*, 69(14):144205, Apr 2004.

[96] David Rodney et Christopher Schuh : Distribution of thermally activated plastic events in a flowing glass. *Physical Review Letters*, 102(23):235503, 2009.

[97] P. Vashishta, Rajiv K. Kalia, José P. Rino et Ingvar Ebbsjö : Interaction potential for *sio*2: A molecular-dynamics study of structural correlations. *Phys. Rev. B*, 41(17):12197–12209, Jun 1990.

[98] C. L. Rountree, D. Vandembroucq, M. Talamali, E. Bouchaud et S. Roux : Plasticity-induced structural anisotropy of silica glass. *Physical Review Letters*, 102(19): 195501, 2009.

[99] B. W. H. van Beest, G. J. Kramer et R. A. van Santen : Force fields for silicas and aluminophosphates based on ab initio calculations. *Phys. Rev. Lett.*, 64(16):1955–1958, Apr 1990.

[100] M. J. Demkowicz et A. S. Argon : High-density liquidlike component facilitates plastic flow in a model amorphous silicon system. *Physical Review Letters*, 93(2):025505, 2004.

[101] M. J. Demkowicz et A. S. Argon : Autocatalytic avalanches of unit inelastic shearing events are the mechanism of plastic deformation in amorphous silicon. *Physical Review B (Condensed Matter and Materials Physics)*, 72(24):245206, 2005.

[102] M. J. Demkowicz et A. S. Argon : Liquidlike atomic environments act as plasticity carriers in amorphous silicon. *Physical Review B (Condensed Matter and Materials Physics)*, 72(24):245205, 2005.

[103] F. Varnik, L. Bocquet, J.-L. Barrat et L. Berthier : Shear Localization in a Model Glass. *Physical Review Letters*, 90(9):095702–+, mars 2003.

[104] F Varnik, L. Bocquet et J.-L. Barrat : A study of the static yield stress in a binary lennard-jones glass. *J. Chem. Phys.*, 120:2788, 2004.

[105] F. Varnik et O. Henrich : Yield stress discontinuity in a simple glass. *PHYSICAL REVIEW B*, 73(17), MAY 2006.

[106] T. Okuzono et K. Kawasaki : Intermittent flow behavior of random foams: A computer experiment on foam rheology. *Phys. Rev. E*, 51(2):1246–1253, Feb 1995.

[107] F. Bolton et D. Weaire : Rigidity loss transition in a disordered 2d froth. *Phys. Rev. Lett.*, 65(27):3449–3451, Dec 1990.

[108] D. J. Durian : Foam mechanics at the bubble scale. *Phys. Rev. Lett.*, 75(26):4780–4783, Dec 1995.

[109] W. Kob et H. C. Andersen : Testing mode-coupling theory for a supercooled binary lennard-jones mixture i: The van hove correlation function. *Phys. Rev. E*, 51(5):4626–4641, May 1995.

[110] K. N. Pham, A. M. Puertas, J. Bergenholtz, S. U. Egelhaaf, A. Moussaïd, P. N. Pusey, A. B. Schofield, M. E. Cates, M. Fuchs et W. C. K Poon : Multiple glassy states in a simple model system. *Science*, 296:104, 2002.

[111] N. Kiriushcheva et Peter H. Poole : Influence of mass polydispersity on dynamics of simple liquids and colloids. *Phys. Rev. E*, 65(1):011402, Dec 2001.

[112] R. K. Murarka et B. Bagchi : Diffusion and viscosity in a supercooled polydisperse system. *Phys. Rev. E*, 67(5):051504, May 2003.

[113] J. P. Wittmer, A. Tanguy, J.-L. Barrat et L. Lewis : Vibrations of amorphous, nanometric structures: When does continuum theory apply? *Europhysics Letters*, 57:423–429, février 2002.

[114] A. Tanguy, J. P. Wittmer, F. Léonforte et J.-L. Barrat : Continuum limit of amorphous elastic bodies: A finite-size study of low-frequency harmonic vibrations. , 66(17):174205, novembre 2002.

[115] F. Léonforte, A. Tanguy, J. P. Wittmer et J.-L. Barrat : Continuum limit of amorphous elastic bodies II: Linear response to a point source force. , 70(1):014203–+, juillet 2004.

[116] F. Varnik : *Some selected issues in computer simulation of complex systems : Structural relaxation, external forces and hydrodynamics.* Habilitationsschrift, 2006.

[117] F. Léonforte : *Vibrations et micromecanique de matériaux amorphes.* Thèse de doctorat, Université Claude Bernard Lyon1, 2005.

[118] F. Léonforte, R. Boissière, A. Tanguy, J. P. Wittmer et J.-L. Barrat : Continuum limit of amorphous elastic bodies. III. Three-dimensional systems. , 72(22):224206–+, décembre 2005.

[119] G. He et M. O. Robbins : Simulations of the static friction due to adsorbed molecules. *Phys. Rev. B*, 64(3):035413, Jun 2001.

[120] S. Alexander : Amorphous solids: their structure, lattice dynamics and elasticity. *Physics Reports*, 296:65–236, 1998.

[121] F. A. Z. Lindemann : The calculation of molecular vibration frequencies. *Physik. Z.*, 11:609, 1910.

[122] M. Born : Thermodynamics of crystals and melting. *The Journal of Chemical Physics*, 7(8):591–603, 1939.

[123] R. W. Cahn : Melting from within. *Nature*, 413:582, 2001.

[124] Z. H. Jin, P. Gumbsch, K. Lu et E. Ma : Melting mechanisms at the limit of superheating. *Phys. Rev. Lett.*, 87(5):055703, Jul 2001.

[125] N. W. Ashcroft et N. D. Mermin : *Solid state physics.*

[126] M. Born et K. Huang : *Dynamical Theory of Crystal Lattices.* Clarendon, Oxford, 1954.

[127] M. F. Thorpe et P. M. Duxbury : *Rigidity theory and applications.* Kluwer Academic/Plenum, 1999.

[128] C. Kittel : *Introduction to solid state physics.* John Wiley and Sons, Inc. New York, 1996.

[129] A. E. H. Love : *A treatise on the mathematical theory of elasticity.* 4th ed. Cambrodge University Press and Dover Publications, New York, 1927.

[130] L. D. Landau et E. M. Lifshitz : *Theory of elasticity.* Pergamon Press, Oxford, NY, 1970.

[131] J. R. Ray : Elastic constants and statistical ensembles in molecular dynamics. *Computer physics reports*, 8:109, 1988.

[132] J.-L. Barrat : Microscopic elasticity of complex systems. *private communication*, 2005.

[133] J. F. Lutsko : Stress and elastic constants in anisotropic solids: Molecular dynamics techniques. *J. Appl. Phys.*, 64:1152, 1988.

[134] J. F. Lutsko : Generalized expressions for the calculation of elastic constants by computer simulation. *J. Appl. Phys.*, 65:2991, 1989.

[135] Z. Zhou et B. Joós : Fluctuation formulas for the elastic constants of an arbitrary system. *Phys. Rev. B*, 66(5):054101, Aug 2002.

[136] D. C. Wallace : *Thermodynamics of crystals.* Wiley, New York, 1972.

[137] I. Goldhirsch et C. Goldenberg : On the microscopic foundations of elasticity. *Eur. Phys. Jour. E*, 9:245–251, 2002.

[138] W. Voigt : Uber die beziehung zwischen den beiden elastizitatsckonstanten isotroper korper. *Wied. Ann.*, 38:573, 1889.

[139] K. Walton : The effective elastic moduli of a random packing of spheres. *J. Mech. Phys. Solids.*, 35:213, 1987.

[140] H. A. Makse, N. Gland, D. L. Johnson et L. M. Schwartz : Why effective medium theory fails in granular materials. *Phys. Rev. Lett.*, 83(24):5070–5073, Dec 1999.

[141] K. Bagi : Stress and strain in granular assemblies. *Mech. Mater.*, 22:165, 1996.

[142] K. Bagi : Analysis of microstructural strain tensors for grain assemblies. *Int. J. Solids Struct.*, 43:3166, 2006.

[143] N. Kruyt et L. Rothenburg : Micromechanical definition of the strain tensor for granular materials. *J. Appl. Mech.*, 118:706, 1996.

[144] M. Kuhn : Structure deformation in granular materials. *Mech. Mater.*, 31:407, 1999.

[145] B. Cambou, M. Chaze et F. Dedecker : Change of scale in granular materials. *Eur. J. Mech. A/Solids*, 19:999, 2000.

[146] P. A. Cundall et O. D. L. Strackk : A discrete numerical model for granular assemblies. *Geotechniques*, 29:47, 1979.

[147] M. A. Koenders : *Mechanics of deformations and flow of part materials.* ASCE, New York, NY, 1997.

[148] C.-L. Liao, T.-P. Chang, D.-H. Young et C. S. Chang : Stress-strain relationship for granular materials based on the hypothesis of best fit. *Int. J. Solids Struct.*, 34:4087, 1997.

[149] G. E. Schroder-Turk, W. Mickel, K. Mecke, M. Schroter, G. Delanay, M. Saadaftar, T. J. Senden et T. Aste : Anisotropy in experimental and simulated disordered sphere packs. *private communication*, 2009.

[150] C. Goldenberg et I. Goldhirsch : Continuum mechanics for small systems and fine resolutions. *Handbook of theoretical and computational nanotechnology*, 4, 2006.

[151] A. Drescher et G. De Josselin de Jong : Photoelastic verification of a mechanical model for the flow of a granular material. *J. Mech. Phys. Solids.*, 20:337, 1972.

[152] O. D. L. Strack et P. A. Cundall : The distinct element method as a tool for research in granular media. *Report to the national science fondation*, 1978.

[153] L. Rothenburg et Selvadurain A. P. S. : A micro-mechanical definition of the cauchy stress for particulate media. *Proceedings od the international symposium on mechanical behaviour of structured media*, page 469, 1981.

[154] M. D. Kluge, D. Wolf, J. F. Lutsko et S. R. Philipot : Formalism for the calculation of local elastic constants at grain boundaries by means of atomic simulation. *J. Appl. Phys.*, 67:2370, 1990.

[155] I. Alber, J. L. Bassani, M. Khantha, V. Vitek et G. J. Wang : Grain boundaries as heterogeneous systems : atomic and continuum elastic properties. *Phil. Trans. R. Soc. A*, 339:552, 1992.

[156] K. Yoshimoto, T. S. Jain, K. V. Workum, P. F. Nealey et J. J. de Pablo : Mechanical heterogeneities in model polymer glasses at small length scales. *Phys. Rev. Lett.*, 93(17): 175501–+, octobre 2004.

[157] V. Ilyin, N. Makedonska, I. Procaccia et N. Schupper : Mechanical properties of glass forming systems. *PHYSICAL REVIEW E*, 76(5, Part 1), NOV 2007.

[158] V. Ilyin, I. Procaccia, I. Regev et N. Schupper : Aging and relaxation in glass-forming systems. *PHYSICAL REVIEW E*, 77(6, Part 1), JUN 2008.

[159] M. Tsamados, A. Tanguy, C. Goldenberg et J.-L. Barrat : Local elasticity map and plasticity in a model lennard-jones glass. *Physical Review E (Statistical, Nonlinear, and Soft Matter Physics)*, 80(2):026112, 2009.

[160] S. G. Mayr : Relaxation kinetics and mechanical stability of metallic glasses and supercooled melts. *Phys. Rev. B*, 79:060201, 2009.

[161] J. Li, K. J. Van Vliet, T. Zhu, S. Yip et S. Suresh : Atomistic mechanisms governing elastic limit and incipient plasticity in crystals. *NATURE*, 418(6895):307–310, JUL 18 2002.

[162] R. Lakes : http://silver.neep.wisc.edu/ lakes/vecmp.html.

[163] R. N. Christensen et K. H. Lo : Solutions for the effective properties of composite materials. *J. Mech. Phys. Solids*, 1979.

[164] S. Torquato : *Random heterogeneous materials.* Springer, 2005.

[165] T. Mura : *Micromechanics of defects in solids.* Martinus Nijhoff, 1987.

[166] J. H. Irving et J. G.Kirkwood : The statistical mechanical theory of transport processes. *J. Chem. Phys.*, 18:817, 1950.

[167] T. H. K. Barron et M. L. Klein : Second-order elastic constants of a solid under stress. *Proc. Phys. Soc.*, 85:523–532, 1965.

[168] J. Salençon : *Handbook of continuum mechanics. General concepts, thermoelasticity.* Springer Verlag, 2001.

[169] C. Goldenberg, A. Tanguy et Barrat J.-L. : Particle displacements in the elastic deformation of amorphous materials: Local fluctuations vs. non-affine field. *EPL*, 80:16003, 2007.

[170] A. Cemal Eringen : *Nonlocal continuum field theories.* Sringer, 2001.

[171] L. Berthier et R. L. Jack : Structure and dynamics of glass formers: Predictability at large length scales. *PHYSICAL REVIEW E*, 76(4, Part 1), OCT 2007.

[172] W. Kob, C. Donati, S. J. Plimpton, P. H. Poole et S. C. Glotzer : Dynamical heterogeneities in a supercooled lennard-jones liquid. *Phys. Rev. Lett.*, 79(15):2827–2830, Oct 1997.

[173] C. Donati, S. C. Glotzer, P. H. Poole, W. Kob et S. J. Plimpton : Spatial correlations of mobility and immobility in a glass forming lennard-jones liquid. *Phys. Rev. E*, 60:3107, 1999.

[174] S. C. Glotzer et C. Donati : Quantifying spatially heterogeneous dynamics in computer simulations of glass forming liquids. *J. Phys. : Condens. Matter*, 11:A285, 1999.

[175] J. Qian, R. Hentschke et A. Heuer : Dynamic heterogeneity of translational and rotational motion of a molecular glass former from computer simulations. *J. Chem. Phys.*, 110:4514, 1999.

[176] K. Vollmayr-Lee, W. Kob, K. Binder et A. Zippelius : Dynamical heterogeneity below the glass transition. *J. Chem. Phys.*, 116:5158, 2002.

[177] K. Binder et W. Kob : *Glassy materials and disordered solids.* World Scientific, Singapore, 2005.

[178] P. Lunkenheimr, U. Schneider, R. Brand et A. Loid : Glass dynamics. *Contemp. Phys.*, 41:15, 2000.

[179] J. P. Garrahan et D. Chandler : Geometrical explanation and scaling of dynamical heterogeneities in glass forming systems. *Phys. Rev. Lett.*, 89(3):035704, Jul 2002.

[180] G. H. Fredrickson et H. C. Andersen : Kinetic ising model of the glass transition. *Phys. Rev. Lett.*, 53(13):1244–1247, Sep 1984.

[181] K. Tarjus, S. A. Kivelson, Nussunovn Z. et P. Viot : The frustration-based approach of supercooled liquids and the glass transition: a review and critical assessment. *J. Phys. : Condens. Matter*, 17:R1143, 2005.

[182] G. Adam et J. H. Gibbs : *J. Chem. Phys.*, 43(1):139, 1965.

[183] T. R. Kirkpatrick et D. Thirumalai : Dynamics of the structural glass transition and the p-spin—interaction spin-glass model. *Phys. Rev. Lett.*, 58(20):2091–2094, May 1987.

[184] W. Gotze et L. Sjogren : Relaxation processes in supercooled liquids. *Rep. Prog. Phys.*, 55:241, 1992.

[185] W Brito et M. Wyart : On the rigidity of a hard-sphere glass near random close packing. *Europhys. Lett.*, 76:149, 2006.

[186] Asaph Widmer-Cooper, Heidi Perry, Peter Harrowell et David R. Reichman : Irreversible reorganization in a supercooled liquid originates from localized soft modes. *NATURE PHYSICS*, 4(9):711–715, SEP 2008.

[187] B. Doliwa et A. Heuer : Energy barriers and activated dynamics in a supercooled lennard-jones liquid. *Phys. Rev. E*, 67(3):031506, Mar 2003.

[188] F. H. Stillinger et T. A. Weber : Packing structures and transitions in liquids and solids. *Science*, 225:4666, 1984.

[189] J. C. Dyre : Colloquium: The glass transition and elastic models of glass-forming liquids. *Reviews of Modern Physics*, 78(3):953, 2006.

[190] E. Aharonov, E. Bouchbinder, H. G. E. Hentschel, V. Ilyin, N. Makedonka, I. Procaccia et N. Schupper : Direct identification of the glass transition : growing length scale at the onset of plasticity. *Europhys. Lett.*, 77:56002, 2007.

[191] M. T. Downton et M. P. Kennett : Following microscopic motion in a two-dimensional glass-forming binary fluid. *J. Phys.: Condens. Matter*, 20:244127, 2008.

[192] H. G. E. Hentschel, V. Ilyin, N. Makedonska, I. Procaccia et N. Schupper : Statistical mechanics of the glass transition as revealed by a voronoi tesselation. *Phys. Rev. E*, 75:050404, 2007.

[193] P. J. Steinhardt, D. R. Nelson et M. Ronchetti : Bond-orientational order in liquids and glasses. *Phys. Rev. B*, 28(2):784–805, Jul 1983.

[194] A. V. Mokshin et J.-L. Barrat : Shear-induced crystallization of an amorphous system. *Physical Review E (Statistical, Nonlinear, and Soft Matter Physics)*, 77(2):021505, 2008.

[195] A. V. Mokshin et J.-L. Barrat : Shear induced structural ordering of a model metallic glass. *The Journal of Chemical Physics*, 130(3):034502, 2009.

[196] T. Hamanaka et A. Onuki : Heterogeneous dynamics in polycrystal and glass in a binary mixture with changing size dispersity and composition. *Physical Review E (Statistical, Nonlinear, and Soft Matter Physics)*, 75(4):041503, 2007.

[197] Takeshi Kawasaki, Takeaki Araki et Hajime Tanaka : Correlation between dynamic heterogeneity and medium-range order in two-dimensional glass-forming liquids. *Physical Review Letters*, 99(21):215701, 2007.

[198] J. Rottler et M. O. Robbins : Yield conditions for deformation of amorphous polymer glasses. *Phys. Rev. E*, 64(5):051801, Oct 2001.

[199] C. A. Schuh et A. C. Lund : Atomistic basis for the plastic yield criterion of metallic glass. *Nat. Mater.*, 2:449 – 452, 2003.

[200] R. Hill : *The mathematical theory of plasticity.* Oxford University Press Inc., New York, 1950.

[201] V. V. Bulatov et A. S. Argon : A stochastic-model for continuum elastoplastic behavior .1. numerical approach and strain localization. *MODELLING AND SIMULATION IN MATERIALS SCIENCE AND ENGINEERING*, 2:185–202, 1994.

[202] V. V. Bulatov et A. S. Argon : A stochastic-model for continuum elastoplastic behavior .1. numerical approach and strain localization. *MODELLING AND SIMULATION IN MATERIALS SCIENCE AND ENGINEERING*, 2:167–184, 1994.

[203] V. V. Bulatov et A. S. Argon : A stochastic-model for continuum elastoplastic behavior .1. numerical approach and strain localization. *MODELLING AND SIMULATION IN MATERIALS SCIENCE AND ENGINEERING*, 2:203–222, 1994.

[204] K. J. Van Vliet, J. Li, T. Zhu, S. Yip et S. Suresh : Quantifying the early stages of plasticity through nanoscale experiments and simulations. *PHYSICAL REVIEW B*, 67(10), MAR 1 2003.

[205] C. E. Maloney et A. Lemaître : Amorphous systems in athermal, quasistatic shear. *Physical Review E (Statistical, Nonlinear, and Soft Matter Physics)*, 74(1):016118, 2006.

[206] S. G. Mayr : Activation energy of shear transformation zones: A key for understanding rheology of glasses and liquids. *Phys. Rev. Lett.*, 97:195501, 2006.

[207] C. E. Maloney et D. J. Lacks : Energy barrier scalings in driven systems. *Physical Review E (Statistical, Nonlinear, and Soft Matter Physics)*, 73(6):061106, 2006.

[208] F. H. Stillinger : Relaxation and flow mechanisms in "fragile" glass-forming liquids. *J. Chem. Phys.*, 89:6461, 1988.

[209] E. Vidal Russell et N. E. Israeloff : Direct observation of molecular cooperativity near the glass transition. *Nature*, 408:695–698, 2000.

[210] W. Schirmacher, G. Diezemann et C. Ganter : Harmonic vibrational excitations in disordered solids and the "boson peak". *Phys. Rev. Lett.*, 81(1):136–139, Jul 1998.

[211] S. N. Taraskin, Y. L. Loh, G. Natarajan et S. R. Elliott : Origin of the boson peak in systems with lattice disorder. *Phys. Rev. Lett.*, 86(7):1255–1258, Feb 2001.

[212] E. Duval, L. Saviot, A. Mermet, L. David, S. Etienne, V. Bershtein et A. J. Dianoux : Inelastic light, neutron, and x-ray scattering related to the heterogeneous elasticity of glasses. *J. Non-Cryst. Solids*, 307:103, 2002.

[213] R.C. Zeller et R.O. Pohl : Thermal conductivity and specific heat of noncrystalline solids. *Physical Review B*, 4:2029–2041, 1971.

[214] R.O. Pohl, X. Liu et E. Thompson : Low-temperature thermal conductivity and acoustic attenuation in amorphous solids. *Rev. Mod. Phys.*, 74:991–1013, 2002.

[215] J.J. Freeman et A.C. Anderson : Thermal conductivity of amorphous solids. *Phys. rev. B*, 34:5684–5690, 1986.

[216] D. J. Wales : *Energy landscapes.* Cambrodge University Press, Cambridge, England, 2003.

[217] P. G. Debenedetti et F. H. Stillinger : Supercooled liquids and the glass transition. *Nature*, 410:259, 2001.

[218] F. Delogu : Identification and characterization of potential shear transformation zones in metallic glasses. *Phys. Rev. Lett.*, 100:255901, 2008.

[219] W. L. Johnson et K. Samwer : A universal criterion for plastic yielding of metallic glasses with a $(t/tg)2/3$ temperature dependence. *Phys. Rev. Lett.*, 95(19):195501, Nov 2005.

[220] A. Widmer-Cooper et P. Harrowell : Predicting the long-time dynamic heterogeneity in a supercooled liquid on the basis of short-time heterogeneities. *Phys. Rev. Lett.*, 96: 185701, 2006.

[221] L. Berthier G. Biroli C. Toninelli, M. Wyart et J.-P. Bouchaud : *Phys. Rev. E*, 71(4):041505, 2005.

[222] O. Dauchot, G. Marty et G. Biroli : Dynamical heterogeneity close to the jamming transition in a sheared granular material. *Phys. Rev. Lett.*, 95(26):265701, Dec 2005.

[223] A. Furukawa, K. Kim, S. Saito et H. Tanaka : Anisotropic cooperative structural rearrangements in sheared supercooled liquids. *Phys. Rev. Lett.*, 102:016001, 2009.

[224] A. Lemaitre et C. Caroli : Rate-Dependent Avalanche Size in Athermally Sheared Amorphous Solids. *PHYSICAL REVIEW LETTERS*, 103(6), AUG 7 2009.

[225] F. Krzakala et L. Bocquet : *unpublished*, 2007.

[226] M. Tsamados : *Mechanical response of glassy materials : theoretical and numerical approach.* Thèse de doctorat, Université Claude Bernard Lyon 1, 2009.

[227] A. Lemaitre et C. Caroli : Plastic response of a 2d amorphous solid to quasi-static shear : Ii - dynamical noise and avalanches in a mean field model. 2007.

[228] S.V. Nemilov : Interrelation between shear modulus and the molecular parameters of viscous flow for glass forming liquids. *J. Non-Cryst. Solids*, 352:2715–2725, 2006.

[229] J. C. Dyre, N. B. Olsen et T. Christensen : Local elastic expansion model for viscous-flow activation energies of glass-forming molecular liquids. *Phys. Rev. B*, 53(5):2171–2174, Feb 1996.

[230] J. P. Sethna, K. A. Dahmen et C. R. Myers : Crackling noise. *Nature*, 410:242, 2001.

[231] P. Bak : *How nature works : the science of self-organized criticality.* Springer-Verlag New York, Inc, 1996.

[232] P. Bak, C. Tang et K. Weisenfeld : Self-organized criticality. *Phys. Rev. A*, 38:364, 1988.

[233] W. Losert, L. Bocquet, T. C. Lubensky et J. P. Gollub : Particle dynamics in sheared granular matter. *Phys. Rev. Lett.*, 85(7):1428–1431, Aug 2000.

[234] F. Da Cruz, F. Chevoir, Daniel Bonn et P. Coussot : Viscosity bifurcation in granular materials, foams, and emulsions. *Phys. Rev. E*, 66(5):051305, Nov 2002.

[235] J. Lauridsen, G. Chanan et M. Dennin : Velocity profiles in slowly sheared bubble rafts. *Physical Review Letters*, 93(1):018303, 2004.

[236] J.-B. Salmon, A. Colin, S. Manneville et F. Molino : Velocity profiles in shear-banding wormlike micelles. *Phys. Rev. Lett.*, 90(22):228303, Jun 2003.

[237] N. P. Bailey, J. Schiötz, A. Lemaître et K. W. Jacobsen : Avalanche size scaling in sheared three-dimensional amorphous solid. *Phys. Rev. Lett.*, 98:095501, 2007.

[238] J. Lauridsen, M. Twardos et M. Dennin : Shear-induced stress relaxation in a two-dimensional wet foam. *Phys. Rev. Lett.*, 89(9):098303, Aug 2002.

[239] Daniel W. Howell, R. P. Behringer et C. T. Veje : Fluctuations in granular media. *Chaos: An Interdisciplinary Journal of Nonlinear Science*, 9:559–572, 1999.

[240] T.S. Majmudar et R.P. Behringer : Contact force measurements and stress-induced anisotropy in granular materials. *Nature*, 435:1079, June 2005.

[241] E. Lerner et I. Procaccia : Locality and nonlocality in elastoplastic responses of amorphous solids. *PHYSICAL REVIEW E*, 79(6, Part 2), JUN 2009.

[242] M. Talamali, V. Petäjä, D. Vandembroucq et S. Roux : Path-independent integrals to identify localized plastic events in two dimensions. *Physical Review E (Statistical, Nonlinear, and Soft Matter Physics)*, 78(1):016109, 2008.

[243] J. D. Eshelby : *Proc. R. Soc. London, Ser A*, 241:376, 1957.

[244] A. D. Gopal et D. J. Durian : Nonlinear bubble dynamics in a slowly driven foam. *Phys. Rev. Lett.*, 75(13):2610–2613, Sep 1995.

[245] P. Hébraud, F. Lequeux, J. P. Munch et D. J. Pine : Yielding and rearrangements in disordered emulsions. *Phys. Rev. Lett.*, 78(24):4657–4660, Jun 1997.

[246] M. Dennin et C. M. Knobler : Experimental studies of bubble dynamics in a slowly driven monolayer foam. *Phys. Rev. Lett.*, 78:2485 – 2488, 1997.

[247] F. Lequeux G. Picard, A. Ajdari et L. Bocquet : Elastic consequences of a single plastic event: A step towards the microscopic modeling of the flow of yield stress fluids. *The European Physical Journal E - Soft Matter*, 15:371–381, 2004.

[248] J.-P. Hansen et I.. R. McDonald : *Theory of simple liquids.* Academic Press, 1976.

[249] W. Kob : Supercooled liquids and glasses. *arXiv:cond-mat/9911023v1*, 1999.

[250] B. Doliwa et A. Heuer : Cooperativity and spatial correlations near the glass transition: Computer simulation results for hard spheres and disks. *Phys. Rev. E*, 61:6898 – 6908, 2000.

[251] N. Lacevic, F. W. Starr, T. B. Schroder et S. C. Glotzer : Spatially heterogeneous dynamics investigated via a time-dependent four-point density correlation function. *The Journal of Chemical Physics*, 119(14):7372–7387, 2003.

[252] N. Lacevic : *Dynamical heterogeneity in simulated glass-forming liquids studied via a four-point spatiotemporal density correlation function.* Thèse de doctorat, Johns Hopkins University, 2003.

[253] G. Samorodnitsky et M. S. Taqqu : *Stable Non-Gaussian Random Processes: Stochastic Models with Infinite Variance.*

[254] P. A. Martin : Introduction aux processus stochastiques en physique. http://seminairetransalpin.in2p3.fr/2006/talks/martin.pdf.

[255] A. V. Lyulin, B. Vorselaars, M. A. Mazo, N. K. Balabaev et M. A. J. Michels : *Europhys. Lett.*, 71:618, 2005.

[256] A. Crisanti et F. Ritord : *Europhys. Lett.*, 66:253, 2004.

[257] S. Cohen-Addad et R. Hohler : *Phys. Rev. Lett.*, 86:4700, 2001.

[258] G. Marty et O. Dauchot : *Phys. Rev. Lett.*, 94:015701, 2005.

[259] Farhang Radjai et Stéphane Roux : Turbulent-like fluctuations in quasistatic flow of granular media. *Phys. Rev. Lett.*, 89(6):064302, Jul 2002.

[260] P. Chaudhuri, L. Berthier et W. Kob : Universal nature of particle displacements close to glass and jamming transitions. *PHYSICAL REVIEW LETTERS*, 99(6), AUG 10 2007.

[261] C. Song, P. Wang et H. A. Makse : *Proc. Natl. Acad. Sci. U.S.A.*, 102:2299, 2005.

[262] F. Lechenault, O. Dauchot, G. Biroli et J. P. Bouchaud : Critical scaling and heterogeneous superdiffusion across the jamming/rigidity transition of a granular glass. *EPL*, 83(4), 2008.

[263] A. Ajdari, L. Bocquet et F. Krzakala : private communication.

[264] C. Dalle-Ferrier, C. Thibierge, C. Alba-Simionesco, L. Berthier, G. Biroli, J.-P. Bouchaud, F. Ladieu, D. L'ôte et G. Tarjus : Spatial correlations in the dynamics of glassforming liquids: Experimental determination of their temperature dependence. *Phys. Rev. E*, 76:041510, 2007.

[265] D. J. Ashton et J. P. Garrahan : Relationship between vibrations and dynamical heterogeneity in a model glass former : extended soft modes but local relaxation. *arXiv:0808.2412*, 2008.

[266] F. Ritort et P. Sollich : Glassy dynamics of kinetically constrained models. *Adv. Phys.*, 52:219, 2003.

[267] M. E. Mobius, G. Katgert et M. van Hecke : Relaxation and flow in linearly sheared two-dimensional foams. *arXiv:0811.0534v2*, 2009.

[268] L. Berthier : Yield stress, heterogeneities and activated processes in soft glassy materials. *J. Phys. Condens. Matte*, 15:S933, 2003.

[269] M. Fuchs et M. E. Cates : Theory of nonlinear rheology and yielding of dense colloidal suspensions. *Phys. Rev. Lett.*, 89(24):248304, Nov 2002.

[270] A. Lemaître et C. Caroli : 2007.

[271] C. E. Maloney et M. O. Robbins : Evolution of displacements and strains in sheared amorphous solids, 2008.

[272] I. Ono, S. Tewari, S. A. Langer et Andrea J. A. J. Liu : Velocity fluctuations in a steadily sheared model foam. *Phys. Rev. E*, 67:061503, 2003.